

FY-09 Report: Experimental Validation of Stratified Flow Phenomena, Graphite Oxidation, and Mitigation Strategies of Air Ingress Accidents

Chang H. Oh
Eung S. Kim
Hyung S. Kang
Hee C. No
Nam Z. Cho

December 2009



The INL is a U.S. Department of Energy National Laboratory
operated by Battelle Energy Alliance



FY-09 Report: Experimental Validation of Stratified Flow Phenomena, Graphite Oxidation, and Mitigation Strategies of Air Ingress Accidents

Chang H. Oh
Eung S. Kim
Hyung S. Kang¹
Hee C. No²
Nam Z. Cho²

¹KAERI
²KAIST

December 2009

**Idaho National Laboratory
Next Generation Nuclear Plant Project
Idaho Falls, Idaho 83415**

<http://www.inl.gov>

Prepared for the
U.S. Department of Energy
Office of Nuclear Energy
Under DOE Idaho Operations Office
Contract DE-AC07-05ID14517

DISCLAIMER

This information was prepared as an account of work sponsored by an agency of the U.S. Government. Neither the U.S. Government nor any agency thereof, nor any of their employees, makes any warranty, expressed or implied, or assumes any legal liability or responsibility for the accuracy, completeness, or usefulness, of any information, apparatus, product, or process disclosed, or represents that its use would not infringe privately owned rights. References herein to any specific commercial product, process, or service by trade name, trade mark, manufacturer, or otherwise, does not necessarily constitute or imply its endorsement, recommendation, or favoring by the U.S. Government or any agency thereof. The views and opinions of authors expressed herein do not necessarily state or reflect those of the U.S. Government or any agency thereof.


Next Generation Nuclear Plant Project

FY-09 Report: Experimental Validation of Stratified Flow Phenomena, Graphite Oxidation, and Mitigation Strategies of Air Ingress Accidents

INL/EXT-09-16465
Revision 1

December 2009


Approved by:



Chang H. Oh
NGNP Design Methods and Validation

12-10-09

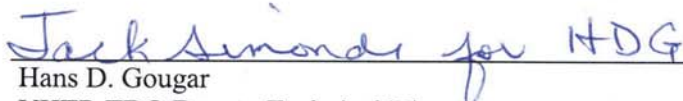
Date



Diane V. Croson
VHTR TDO Project Manager

12/10/2009

Date



Hans D. Gougar
VHTR TDO Deputy Technical Director

12/10/2009

Date

EXECUTIVE SUMMARY

Idaho National Laboratory (INL), under the auspices of the U.S. Department of Energy, is performing research and development that focuses on key phenomena important during potential scenarios that may occur in very high temperature reactors (VHTRs). Phenomena Identification and Ranking Studies to date have ranked an air ingress event, following on the heels of a VHTR depressurization, as important with regard to core safety. Consequently, the development of advanced air ingress-related models and verification and validation data are a very high priority.

Following a loss of coolant and system depressurization incident, air will enter the core through the break, possibly causing oxidation of the in-the core and reflector graphite structure. Simple core and plant models indicate that, under certain circumstances, the oxidation may proceed at an elevated rate with additional heat generated from the oxidation reaction itself. Under postulated conditions of fluid flow and temperature, excessive degradation of the lower plenum graphite can lead to a loss of structural support. Excessive oxidation of core graphite can also lead to the release of fission products into the confinement. Experimental validation of analytical and computational fluid dynamic (CFD) models of air ingress as undertaken in this study can thus improve understanding of this phenomenon. Validated models can in turn be used to estimate the probability and consequences of various air ingress events.

In an effort to estimate the proper safety margin during such events, computer simulations must include accurate multidimensional thermal-hydraulic and reactor physics, burn-off, and fracture models. Each of these components must be validated with experimental data. An understanding of the interplay between these models can lead to effective strategies to mitigate the effects of oxidation. The results from this research will answer key questions raised during the phenomena identification and ranking table (PIRT) process.

The second year of this three-year project (FY-08 to FY-10) was focused on (a) the analytical, CFD, and experimental study of air ingress caused by density-driven, stratified, countercurrent flow; (b) advanced graphite oxidation experiments and modeling; (c) the experimental study of burn-off in the core bottom structures, (d) the implementation of advanced graphite oxidation models into the GAMMA code, (f) air ingress and oxidation mitigation analyses of a class of air-ingress scenarios, (g) development of core neutronic models, (h) coupling of core neutronic and thermal hydraulic models, and (i) verification and validation of coupled models.

This executive summary highlights the accomplishments from this research project.

E-1. RESEARCH OBJECTIVES

The major goal of this project is to perform air-ingress-related analyses and experiments so the consequences of air-ingress in the Next Generation Nuclear Plant (NGNP) can be reliably predicted with a high degree of certainty. The research objectives are summarized in this section.

Analyses will be performed to simulate air-ingress accidents. The major objective of these analyses is to understand what will really happen in the air-ingress accident and to evaluate various methods for mitigating the effects of the air ingress.

Experiments will be conducted in this project to supply information needed to validate computer codes to model important phenomena during air-ingress accidents. These experiments will measure:

- the rate of air ingress into the reactor core because of density-driven, stratified flow,
- the internal pore area density of nuclear grade graphite, which is an important parameter for determining the oxidation rate,

- the variation in oxidation rate and density and their effects on burn-off in the bottom reflector,
- the effect of burn-off on the structural integrity of the core bottom structures.

Another important goal of this project is to develop coupled neutronics and thermal-hydraulic capability in the GAMMA code, which involves the:

- Development of core neutronics models
- Coupling of neutronic-thermal hydraulic tools
- Verification and validation (V&V) of the coupled core model.

This will allow the simulation of re-criticality in conduction cool-down without scram and accurate initial and transient power distribution, which are both essential for the accurate estimation of the safety margin.

E-2. REPORT CONTENT AND ORGANIZATION

This report highlights key accomplishments achieved in FY-09. Section 1 provides introductory information about the project's focus. Detailed information about the objectives and accomplishments from each task completed in this project can be found in Sections 2 through 10. Section 11 highlights the results and conclusions that can be drawn from each task.

E-3. PROJECT APPROACH AND ORGANIZATION

The proposed work was planned to be carried out over a 3-year period (FY-08–10). The proposed work plan consists of the following nine major tasks:

1. Density-difference induced stratified flow analysis (INL)
2. Experimental study of the stratified flow (INL)
3. Advanced graphite oxidation study (INL)
4. Air ingress mitigation study (INL)
5. Experiment of burn-off in the core bottom structures (KAIST)
6. Structural tests of oxidized core bottom structures (KAIST)
7. Coupling neutronic-thermal hydraulic tools (KAIST)
8. Core neutronic model (KAIST)
9. Coupled core model V&V (KAIST).

Figure E-1 shows more details of tasks involved in this project.

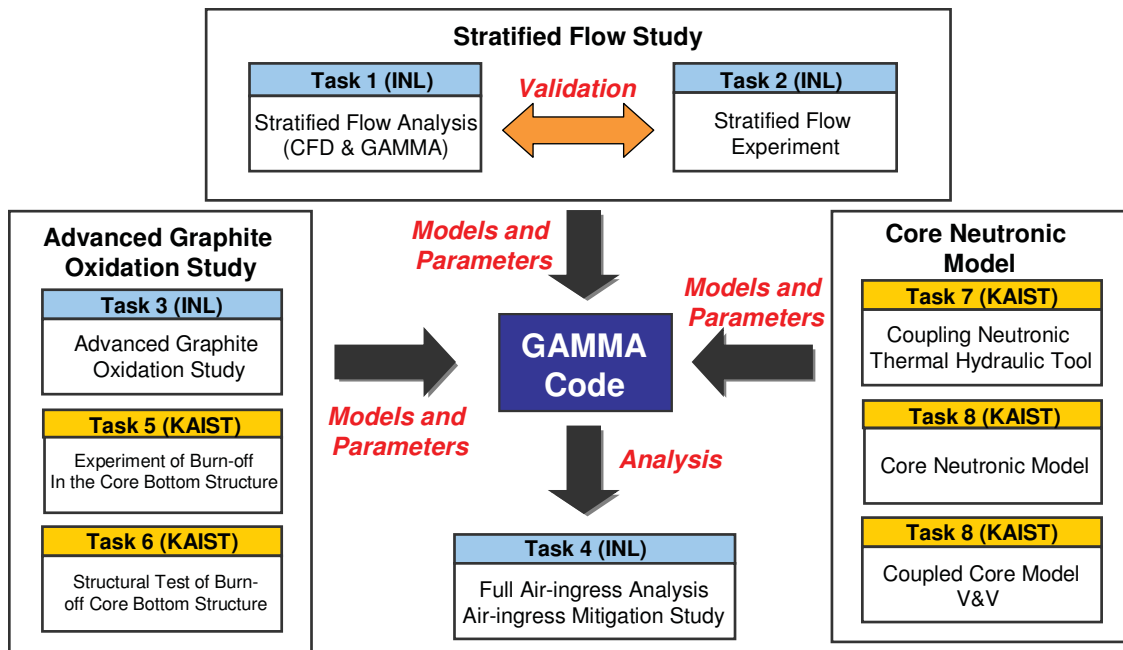


Figure E-1. Schematic diagram of all tasks involved.

E-4. KEY PROGRAM ACCOMPLISHMENTS

Highlights of key accomplishments during this fiscal year (FY-09) for the nine tasks are summarized in this section. These accomplishments include items required to meet task objectives outlined in the original proposal for this project and items that meet overall I-NERI objectives. As indicated below, this project not only advanced the state-of-art in research pertaining to the VHTR, but also provided hands-on experience to a number of graduate students studying complex flow phenomena in gas-cooled reactors.

E-4.1 Task 1—Density-difference Induced Stratified Flow Analysis (INL)

Various theoretical and computational tasks were accomplished in Task 1. First, previous gravity current studies which indicate qualitative agreement with air-ingress phenomena in HTRs have been extensively reviewed. Based upon this review, some analytical investigations have been completed. This analysis was focused on the identification and comparison of the important air-ingress mechanisms (molecular diffusion versus density gradient driven flow). In FY-09, a simple 2-D CFD model developed in FY-08 was upgraded to three-dimensional (3-D) CFD model which includes the confinement of the GTMHR, a reference design selected for this study.

Results of analytical models agree very well with those of 2-D and 3-D CFD simulations in terms of time scales and the recirculation pattern in the lower plenum. This recirculation pattern helps air to move up to the reactor core along with a recirculation flow pattern in the core established by the temperature difference in the reactor core and lower temperature near the outer wall.

3-D calculations have confirmed the current understanding of the phenomena of air-ingress based on density-gradient driven flow. In addition to the detailed 3-D model, some preliminary 2-D CFD analyses

included the heterogeneous chemical reaction which appears to be dominated by carbon monoxide (CO) in the higher temperature regions in the reactor core. All details are described in Section 2.6.

E-4.2 Task 2—Experimental Study on the Stratified Flow (INL)

An experimental plan for the density gradient driven stratified flow has been established in this fiscal year. Two isothermal experiments have been designed in order to understand stratified flow phenomena in the double-ended-guillotine-break (DEGB) situation and the partial break situation, respectively. The DEGB experiment will focus on visualization of stratified flow in the horizontal pipe, at the flow expansion, and around the supporting structures. This experiment is designed to measure local and global velocity and concentration data by using optical methods. The obtained data will be used for code validation. The partial break experiment will focus on the different flow regimes that occur in the different break orientations. In these experiments, the flow regimes will be simulated and measured to produce a flow regime map if possible. The measured local and global velocity and concentration data also will be used for code validations. For data comparisons, CFD models have been developed based on the final experimental design, and some sensitivity studies have been completed. This blind CFD analyses results will finally be compared to the experimental data for validation.

E-4.3 Task 3—Advanced Graphite Oxidation Study (INL)

In FY-09, the structural analyses on the graphite supporting structure that was performed in FY-08 has been upgraded under the new air-ingress scenario assuming that the flow is driven by density gradients in addition to molecular diffusion. In this analysis, the collapse of the graphite structure was estimated for a simplified model of the reference VHTR by two computer codes; GAMMA code (system analysis code) and ABAQUS code (stress analysis code). The graphite oxidation and corrosion were predicted by the GAMMA code, and the information was implemented into the ABAQUS code to estimate the core collapse. Aside from this analysis, further computations were performed with MATLAB to conservatively estimate the maximum allowable burn-off to maintain graphite structural integrity. A graphite oxidation models and algorithm, including graphite corrosion and failure, were constructed and implemented in the GAMMA code. Based on the advanced model, VHTR air-ingress analyses have been carried out for two different graphite structural materials (IG-110, H-451) under conservative assumptions.

E-4.4 Task 4—Air Ingress Mitigation Study (INL)

As part of the FY-09 scope, some preliminary studies were conducted to investigate air-ingress mitigation methods, providing some idea of the air-ingress mitigation or graphite oxidation mitigation methods proposed in this task.

E-4.5 Task 5—Experiment of Burn-off in the Bottom Structure (KAIST)

Various graphite oxidation and burn-off characteristics of IG-430 graphite were investigated in Task 5 as a continuation of FY-08 work. The experimental results were compared to those of IG-110 graphite obtained in FY-08. As a result, the kinetic parameters such as activation energy and order of reaction were experimentally measured to be 158.5 kJ/mol and 0.37 for IG-430, respectively, while the values are 218 kJ/mol and 0.75 for IG-110. Burn-off characteristics of the IG-430 and IG-110 were also compared at Zone I dominated by kinetics. The maximum reaction rates for both IG-430 and IG-110 graphite appeared at about 40% burn-off, but the trends were somewhat different. IG-110 showed rapid increase of reaction in the beginning with large internal surface area changes, but IG-430 showed only small changes of reaction with burn-offs. One interesting observation was that the presence of moisture in the reacting gas does not affect the oxidation or burn-off history during the whole time period.

E-4.6 Task 6—Structural Tests of Burn-off Bottom Structure (KAIST)

Mechanical testing for IG-430 graphite was carried out in Task 6 for various oxidized conditions, and the results were compared to those of IG-110 obtained in FY-08. The followings are the notable results. Compressive strength of original IG-430 was measured to be 88.99 MPa, which is about 13% higher than that of IG-110. The experiment for fracture of IG-430 showed that the graphite failure stress is a function of slenderness ratio only. Therefore, the failure strength of the graphite structure can be simply determined by the geometrical information and burn-off level. This experiment also showed that IG-430 is fractured by buckling at the slenderness ratio larger than 13.83, while IG-110 is fractured by buckling at the slenderness ratio larger than 11.76. They can be considered the transition point of the slenderness ratio showing different failure modes (compressive or buckling). The relation between graphite burn-off and buckling strength for IG-430 has been investigated by mechanical testing for the oxidized samples. The relationship has been expressed by a Knudsen type formula. This experiment showed that the mechanical degradation of IG-430 is quite a bit slower than that of IG-110, thus maintaining better structural integrity. Finally, mechanical testing of several graphite columns with different geometries and dimensions was performed for various burn-off levels considering general geometries. Based on the experimental results, the strength of graphite columns oxidized in Zone I is dependent on the initial strength and burn-off level, even though the graphite columns have different dimensions with different failure modes.

E-4.7 Task 7—Coupling Neutronic-Thermal Hydraulic Tools (KAIST)

KAIST proposed coupling neutronics-thermal hydraulic tools in Task 7 to analyze VHTR thermal hydraulics behavior. KAIST therefore developed a multidimensional gas multicomponent mixture analysis code (GAMMA) and multigroup 3-D hexagonal geometry neutronics code (COREDAX). These codes were coupled into a system code, GAMMA/COREDAX, so the VHTR core could be analyzed. During FY-09, the parameters for neutronic/thermal-hydraulic coupling were set up between the GAMMA and COREDAX codes. Since the calculation nodes between the two codes are quite different, a node mapping subroutine was developed in the COREDAX code and tested. By replacing the 'point kinetics' subroutine in GAMMA code with the 'COREDAX_coupling' subroutine, the coupling GAMMA and COREDAX codes were finally completed. To test GAMMA/COREDAX code coupling, a simplified GTMHR 600 MWth was tested. As a result, the calculation results between GAMMA with COREDAX results and GAMMA/COREDAX code are exactly matched.

E-4.8 Task 8—Core Neutronic Model (KAIST)

KAIST developed the COREDAX code in Task 8 based on the analytic function expansion nodal (AFEN) method in 3-D hexagonal geometry. The AFEN method includes the use of node-interface flux moments as nodal unknowns. These nodal unknowns increase the accuracy of 3-D calculation results. Multigroup extension based on matrix function theory and coarse group rebalance (CGR) acceleration were applied into the COREDAX code. The COREDAX code implementing the AFEN method was verified by testing the VVER-440 benchmark problem, a simplified VVER-1000 benchmark problem, and the SNR-300 benchmark problem. The benchmark results showed that the COREDAX results are in good agreement with the reference results calculated by PARCS (for VVER-400), VENTURE (for VVER-1000), and DIF3D (for SNR-300).

E-4.9 Task 9—Coupled Core Model V&V (KAIST)

This task involves the verification of GAMMA code coupled with COREDAX code and the validation of prediction results of thermal power distribution in the hexagonal reactor core. This task will be performed in FY-10.

E-5. STUDENT AND OTHER PARTICIPATION

List of Students (U.S.):

Jong Bin Lim (University of Wisconsin)

Nathaniel Salpeter (Texas A&M)

List of Students (ROK):

Ho Joon Yoon (KAIST)

Hyeonil Kim (KAIST)

Jong Woon Kim (KAIST)

Hyung Gon Jin (KAIST)

Jae-Jun Lee (KAIST)

Sung-Hwan Yoon (KAIST)

Young Soo Kim (KAIST)

Byung Ha Park (KAIST)

Han Jong Ryu (KAIST)

Jae Hoon Song (KAIST)

Others:

Hyung S. Kang (Korea Atomic Energy Research Institute)

Jim Liou (University of Idaho)

Thibaut Simond (Ecole des Mines de Paris-Paristech)

CONTENTS

EXECUTIVE SUMMARY	vi
ACRONYMS	xxiv
1. INTRODUCTION.....	1-1
1.1 Objectives	1-1
1.2 Background.....	1-2
1.3 R&D Plan	1-2
1.3.1 Task 1: Density-Difference Induced Stratified Flow Analysis—FY-08 and FY-09 Task.....	1-2
1.3.2 Task 2: Experimental Study on the Stratified Flow—FY-09 and FY-10 Task	1-3
1.3.3 Task 3: Advanced Graphite Oxidation Study—FY-08 and FY-09 Task	1-3
1.3.4 Task 4: Air Ingress Mitigation Study—FY-10 Task.....	1-3
1.3.5 Task 5: Experiment of Burn-off in the Core Bottom Structures (KAIST).....	1-4
1.3.6 Task 6: Structural Tests of Oxidized Core Bottom Structures (KAIST)— FY-09 and FY-10 Task	1-4
1.3.7 Task 7: Coupling Neutronic-Thermal Hydraulic Tools (KAIST)—FY-09 Task.....	1-4
1.3.8 Task 8: Core Neutronic Model (KAIST) –FY-08 and FY-09 Task.....	1-4
1.3.9 Task 9: Coupled Core Model V&V (KAIST) – FY-10 Task	1-5
1.4 Research and Development Collaboration.....	1-5
2. TASK 1: DENSITY-DIFFERENCE INDUCED STRATIFIED FLOW ANALYSIS (INL)	2-1
2.1 Introduction.....	2-1
2.2 Review on the Previous Gravity Current Flow Studies.....	2-4
2.3 Analytical Estimations for VHTR Air-ingress Accident.....	2-18
2.3.1 Time Scale Comparisons in Stratified Flow—Stage 1.....	2-18
2.3.2 Time Scale Comparisons in Stratified Flow—Stage 2.....	2-25
2.4 2-D Preliminary Partial Break Analyses by FLUENT Code	2-33
2.5 3-D DEGB Analyses by CFX Code	2-38
2.5.1 3-D Grid Model	2-39
2.5.2 Initial, Boundary, Porous Media Conditions and Properties	2-41
2.5.3 Flow Field models and Numerical Models for the 3-D CFX Analysis	2-44
2.5.4 Discussion on the CFD Analysis Results	2-45
2.5.5 Conclusions and Further Works	2-53
2.6 2-D Preliminary Analyses on the Effect of Chemical Reaction.....	2-53
3. TASK 2: EXPERIMENTAL STUDY ON THE STRATIFIED FLOW (INL)	3-1
3.1 Introduction.....	3-1
3.2 Plan for Stratified Flow Experiment (Isothermal).....	3-1
3.2.1 Isothermal DEGB Experiment.....	3-2
3.2.2 Isothermal Partial-Break Experiment.....	3-9
3.3 CFD Analyses of Isothermal Stratified Flow Experiment	3-13
3.3.1 Lock Exchange Simulations.....	3-13
3.3.2 DEGB Simulations	3-19
3.3.3 Conclusions	3-24

3.3.4	Preliminary CFD Analyses on the Partial Break	3-24
3.4	Isothermal Wedge Flow Experiment in University of Idaho	3-28
3.4.1	<i>Apparatus and Procedure</i>	3-28
3.4.2	<i>Results</i>	3-29
3.4.3	<i>Discussion</i>	3-29
3.5	Validations on the CFD code for Density Gradient Driven Stratified Flow	3-30
3.5.1	Description on the Experiment	3-30
3.5.2	<i>Numerical Simulations and Comparisons</i>	3-33
4.	TASK 3: ADVANCED GRAPHITE OXIDATION STUDY (INL)	4-1
4.1	Introduction	4-1
4.2	Modeling of Graphite Oxidation and Fracture in Air-ingress	4-1
4.2.1	Stress Analysis Strategy	4-1
4.2.2	Structural Dimensions	4-4
4.2.3	Change of Temperature, Burn-off, and Corrosion Thickness	4-6
4.2.4	Material Database	4-7
4.2.5	Treatment of Material Properties during Analysis	4-12
4.2.6	Initial Un-oxidized State Results	4-12
4.2.7	Oxidized State Results	4-15
4.3	Estimation of Conservative Burn-off Criteria for Graphite Structure	4-19
4.4	Implementation of Advanced Graphite Oxidation Model into GAMMA code and Analyses	4-28
5.	TASK 4: AIR INGRESS MITIGATION STUDY (INL)- FY-10 Task	5-1
6.	TASK 5: EXPERIMENT OF BURN-OFF IN THE BOTTOM STRUCTURE (KAIST)	6-1
6.1	Graphite Selection	6-1
6.2	Kinetics	6-2
6.3	Mass Diffusion	6-5
6.4	Combined Effect of Kinetics and Mass Diffusion	6-5
6.5	Effect of Burn-off	6-6
6.6	Effect of Moisture	6-9
7.	TASK 6: STRUCTURAL TESTS OF BURN_OFF BOTTOM STRUCTURE (KAIST)	7-1
7.1	Graphite Support Column	7-1
7.1.1	Graphite Oxidation and Failure Mechanisms	7-1
7.1.2	Materials	7-2
7.1.3	Strength Measurements	7-2
7.1.4	Oxidation Treatments	7-3
7.1.5	Measurements of Compressive and Buckling Strength of Fresh Graphite Column	7-4
7.1.6	Compressive and Buckling Strength Degradation of Graphite Column Oxidized in Zone 1	7-5
7.1.7	Buckling Strength Graphite Column Oxidized in Zone 3	7-8
7.2	Graphite Support Column	7-9
7.2.1	Buckling Strength Graphite Column Oxidized in Zone 3	7-10
7.2.2	Strength Degradation of Various Columns Oxidized in Zone 1	7-11

8.	TASK 7: COUPLING NEUTRONICS-THERMAL HYDRAULIC TOOLS (KAIST)	8-1
8.1	Coupling Procedure.....	8-1
8.1.1	Set-up Parameters for Neutronics/Thermal-Hydraulics Code Coupling.....	8-1
8.1.2	Calculation Node Mapping between the COREDAX and GAMMA Code	8-2
8.1.3	Code coupling of COREDAX with GAMMA	8-2
8.1.4	Calculation procedure in a coupling system.....	8-4
8.2	Homogenized Cross-Section Table	8-5
8.3	GAMMA/COREDAX Test Calculation.....	8-6
9.	TASK 8: CORE NEUTRONICS MODEL.....	9-1
9.1	Basic Theory and Method.....	9-1
9.1.1	Nodal Unknowns and Nodal Equations	9-1
9.1.2	Multigroup Extension	9-4
9.1.3	Coarse Group Rebalance Acceleration	9-4
9.2	Verification of the COREDAX code.....	9-6
9.2.1	VVER-440 benchmark problem	9-6
9.2.2	A Simplified VVER-1000 Benchmark Problem	9-8
9.2.3	SNR-400 benchmark problem	9-9
9.2.4	VVER-1000 benchmark problem	9-11
9.3	Test on GTMHR Core Model	9-14
9.3.1	Description	9-14
9.3.2	Test results.....	9-16
10.	TASK 9: COUPLED CORE MODEL V&V (KAIST)—FY-10 Task	10-1
11.	SUMMARY	11-1
11.1	Task 1 (INL)	11-1
11.2	Task 2 (INL)	11-1
11.3	Task 3 (INL)	11-2
11.4	Task 4 (INL)	11-3
11.5	Task 5 (KAIST)	11-3
11.6	Task 6 (KAIST)	11-4
11.7	Task 7 (KAIST)	11-4
11.8	Task 8 (KAIST)	11-4
11.9	Task 9 (KAIST)	11-5
12.	REFERENCES.....	12-1
	Appendix A—DEGB Experiment Facility Schematics.....	1

FIGURES

Figure E-1.	Schematic diagram of all tasks involved.	viii
Figure 2-1.	Density-driven induced stratified flow.	2-1
Figure 2-2.	Air-ingress Scenario (INL's current understanding).	2-3

Figure 2-3. Gravity current produced by lock-exchange in a rectangular channel (Shin et al. 2004).	2-5
Figure 2-4. Diagram of idealized gravity current in the rest frame of the current (Shin et al. 2004).	2-6
Figure 2-5. Dimensionless net energy flux plotted against dimensionless current depth h/H (Shin et al. 2004).	2-7
Figure 2-6. Wave speed plotted versus density ratios ($r=\rho_B/\rho_A$) (Keller & Chyou 1991).	2-8
Figure 2-7. Gravity current of low-density fluid penetrating into a channel that initially contained high-density fluid (Keller & Chyou 1991).	2-9
Figure 2-8. Loss-free gravity current of high density fluid penetrating into a horizontal channel originally filled with low density fluid (Keller & Chyou 1991).	2-9
Figure 2-9. Fractional depth (ξ) versus density ratio (r) (Keller & Chyou 1991).	2-10
Figure 2-10. Typical gravity current front advancing along a horizontal plane (Mok et al. 2003).	2-11
Figure 2-11. Full depth lock exchange experiment with the lock gate at an angle (Shin et al. (2004)).	2-12
Figure 2-12. Schematic of a partial-depth lock exchange in a channel (a) before release and (b) after release (Shin et al. [2004]).	2-13
Figure 2-13. Lock exchange experiment for non-Boussinesq cases ($\gamma = 0.681$).	2-14
Figure 2-14. Schematic of two lock exchange configuration for non-Boussinesq flow.	2-14
Figure 2-15. Speed of the light current for various density ratios (Lowe et al. (2005)).	2-15
Figure 2-16. Speeds of the heavy currents (Lowe et al. 2005).	2-16
Figure 2-17. Flow depth of the heavy current (Lowe et al. 2005).	2-16
Figure 2-18. Nondimensional vorticity maps for the steady flow by DNS (Etienne et al. 2005).	2-17
Figure 2-19. Schematics of Stage 1 (post-depressurization).	2-18
Figure 2-20. Speeds of the heavy currents (Lowe et al. 2005).	2-21
Figure 2-21. Flow depth of the heavy current (Lowe et al. 2005).	2-21
Figure 2-22. Schematics of GTMHR 600 MWth.	2-22
Figure 2-23. Correlation between length scale and relative time scales.	2-25
Figure 2-24. Schematics of Stage 2 air-ingress.	2-25
Figure 2-25. Schematics of the VHTR reactor for analytical modeling.	2-29
Figure 2-26. Circulation pattern in the location 3 (lower plenum).	2-30
Figure 2-27. A sketch of the phenomena in Stage 2.	2-31
Figure 2-28. Calculated y-velocity profile in the reactor core during Stage 2 (FLUENT 6.3).	2-32
Figure 2-29. VHTR partial break schematic.	2-34
Figure 2-30. Fluent simulation of partial break situation (20 sec).	2-35
Figure 2-31. Velocity profile at the break location (10 sec).	2-35
Figure 2-32. Air-mass fractions in the VHTR in the partial break situation (FLUENT results).	2-36

Figure 2-33. Average air mass fraction in the core and the lower plenum.	2-37
Figure 2-34. FLUENT models for wall thickness effect.	2-37
Figure 2-35. Effect of wall thickness in the partial break.	2-38
Figure 2-36. 3-D grid model for the DEGB analysis.....	2-39
Figure 2-37. Initial air mass fraction, temperature, and pressure conditions for 3-D CFX analysis.	2-41
Figure 2-38. Wall temperature conditions for the core blocks, support blocks and reactor vessel.	2-42
Figure 2-39. Pressure distribution results with the porous conditions under the normal operation conditions.	2-43
Figure 2-40. Binary diffusion coefficient between air and helium.....	2-43
Figure 2-41. Variation of the air mass fraction according to time.	2-46
Figure 2-42. Velocity profile, density, and pressure distribution at 0.0 seconds and 0.18 seconds.	2-47
Figure 2-43. Air mass fraction of upper plenum, coolant riser, cold duct header, and reactor bottom.	2-48
Figure 2-44. Air mass fraction of the hot and cold duct (front view).....	2-49
Figure 2-45. Air mass fraction and velocity profile in the lower plenum at 5.96 seconds.	2-49
Figure 2-46. Volume averaged air mass fraction of the lower plenum, the reactor bottom, the cold duct header and the coolant riser (Maximum value of the air mass fraction is 0.5).	2-50
Figure 2-47. Volume averaged velocity of the core blocks.	2-51
Figure 2-48. Volume and area averaged air mass fraction of the lower plenum, core blocks, and core inlet (maximum value of the air mass fraction is 0.5).	2-51
Figure 2-49. Volume and area averaged air temperature of the lower plenum, core blocks, and core inlet.....	2-51
Figure 2-50. Temperature distribution on the plane of $z = 6.7$ m in the lower plenum (LP bottom: $z = 7.624$ m, LP top: $z = 7.624$ m, temperature and air mass fraction are averaged over the area of the plane at $z = 6.7$ m).....	2-52
Figure 2-51. Ratio of CO/CO_2 with temperature (Oh et al. 2006).	2-54
Figure 2-52. Effect of temperature on the graphite oxidation rates and oxidation regimes.....	2-54
Figure 2-53. Species concentration profiles in the VHTR at 13 seconds.	2-56
Figure 2-54. Comparisons of with and without chemical reaction models.....	2-57
Figure 3-1. Flows of interest in the isothermal full-break experiment.	3-2
Figure 3-2. Comparisons between previous gravity current studies and VHTR air-ingress condition.....	3-3
Figure 3-3. Schematics of the isothermal DEGB experiment.	3-4
Figure 3-4. Estimated accidental flow regime and experimental conditions.	3-5
Figure 3-5. Pipe and tank wall thicknesses vs. maximum stress in the wall.....	3-6
Figure 3-6. Set-up of combined PIV/PLIF system.	3-7
Figure 3-7. Flow Regime of Air Intrusion in the Partial Break (Orientation Effect).	3-10

Figure 3-8. Effect of Break Orientation and Flow Rate (Partial Break).	3-10
Figure 3-9. Schematics of the partial break experiment.	3-11
Figure 3-10. Set-up of combined PIV/PLIF system.	3-12
Figure 3-11. Counter current flow in a rectangular channel at $t = 0$ (a), 0.5 (b), 1 (c), and 2.5 (d) seconds.	3-14
Figure 3-12. Counter current flow species interface with velocity mapping in a rectangular channel at $t = 0.5$ (a), 1 (b), and 2.5 (c) seconds.	3-15
Figure 3-13. X- velocity component in a rectangular channel at $t = 2.5$ seconds.	3-15
Figure 3-14. NaCl species volume fraction along horizontal line probe through flow front at $t = 2.5$ seconds.	3-16
Figure 3-15. X-velocity component along horizontal line probe through flow front at $t = 2.5$ seconds.	3-16
Figure 3-16. Counter current flow in a cylindrical channel at $t = 0$ (a), 0.5 (b), 1(c), and 2.5 (d) seconds.	3-17
Figure 3-17. Counter current flow species interface with velocity mapping in a cylindrical channel at $t = (a)0.5$, (b)1, and (c)2.5 seconds.	3-17
Figure 3-18. X- velocity component in a cylindrical channel at $t = 2.5$ seconds.	3-18
Figure 3-19. NaCl species volume fraction along horizontal line probe through flow front at $t = 2.5$ seconds.	3-18
Figure 3-20. X-velocity component along horizontal line probe through flow front at $t = 2.5$ seconds.	3-18
Figure 3-21. Facility model (a) from which the fluid domain (b) was extracted	3-20
Figure 3-22. Mass fraction of CO ₂ at $t = 0$ (a) and 0.5 (b) seconds.	3-21
Figure 3-23. X-velocity component at $t = 0.5$ seconds.	3-21
Figure 3-24. Velocity vectors and density gradient at $t = 0.5$ seconds.	3-21
Figure 3-25. Isosurface of flow interface with velocity mapping at $t = 0.5$ seconds.	3-22
Figure 3-26. Mass fraction along horizontal line probe through flow front at $t = 0.5$ seconds; the red line indicates the initial break location.	3-22
Figure 3-27. Plot of x-velocity component along horizontal line probe through flow front at $t = 2.5$ seconds; the red line indicates the initial break location.	3-23
Figure 3-28. Plot indicating flow height with mass fraction ($mf = 0.5$ at interface) at $t = 0.5$ seconds.	3-23
Figure 3-29. Three different regimes created depending on the break angle of the hole.	3-25
Figure 3-30. Diffusion regime (break angle = 0 deg).	3-25
Figure 3-31. Stratified flow regime (break angle = 112.5 deg).	3-26
Figure 3-32. Intermittent flow regime (break angle = 180 deg).	3-27
Figure 3-33. Break angle vs. maximum volumetric flow rate.	3-27
Figure 3-34. Air-water-brine test loop.	3-28

Figure 3-35. Dynamic intrusion of a gravity driven flow.	3-29
Figure 3-36. Quasi-static wedge intrusion of a gravity driven flow.	3-29
Figure 3-37. Onset of intrusion by momentum principles.	3-30
Figure 3-38. Experimental arrangement (Grobelbauer et al. 1993).	3-31
Figure 3-39. Propagation velocities of dense gas and light gases (Grobelbauer et al. 1993).	3-32
Figure 3-40. Geometry and FLUENT mesh.	3-33
Figure 3-41. Initial Air mass fractions.	3-34
Figure 3-42. FLUENT simulation (air mass fraction (fine mesh)).	3-35
Figure 3-43. FLUENT simulation (air mass fraction (normal mesh)).	3-35
Figure 3-44. FLUENT simulation (air mass fraction (coarse mesh)).	3-36
Figure 3-45. Air mass fraction at the bottom plate (current locations).	3-36
Figure 3-46. Comparisons between different mesh sizes.	3-37
Figure 3-47. Simulated front speeds and estimated front speed at zero grid spacing.	3-38
Figure 3-48. FLUENT simulation (air mass fraction, k-w model, fine mesh).	3-39
Figure 3-49. FLUENT simulation (air mass fraction, standard k-e model, fine mesh).	3-39
Figure 3-50. FLUENT simulation (air mass fraction, RSM model, fine mesh).	3-40
Figure 3-51. Comparisons between CFD results and experimental data (front location).	3-40
Figure 3-52. Initial air mass fraction for light gas intrusion (helium).	3-41
Figure 3-53. FLUENT simulation for light gas intrusion (air mass fraction, realizable k-e model, fine mesh).	3-42
Figure 3-54. Helium mass fraction at the upper plane for light gas intrusion.	3-42
Figure 3-55. Comparisons between CFD results and experimental data (light gas intrusion).	3-43
Figure 4-1. GTMHR core side view (Shenoy 2007).	4-2
Figure 4-2. Top cutaway view of the core (Cocheme 2004).	4-2
Figure 4-3. ABAQUS generated whole and cut view of the support block and plenum.	4-3
Figure 4-4. The dimensions of a General Atomics' GTMHR fuel block. (GA 1997, Cocheme 2004, GA 2003).	4-4
Figure 4-5. Plenum (a) side views (with dimensions), and (b) wireframe top view.	4-5
Figure 4-6. Corrosion depth and section assignments.	4-6
Figure 4-7. GAMMA result temperature over the time.	4-7
Figure 4-8. GAMMA result burn-off over the time.	4-7
Figure 4-9. (a) Tensile strength as function of the burn-off; (b) compressive strength as function of the burn-off (Ishihara et al. 2004).	4-8
Figure 4-10. Tensile strength as function of temperature (Eto et al. 1986).	4-9

Figure 4-11. (a) The change in Young's modulus because of oxidation as a function of temperature (best fit of experiment data), and (b) the correlations for the Young's modulus as a function of temperature and burn-off (Eto et al. 1986).	4-10
Figure 4-12. Young's modulus (a) and mechanical strength (b) as function of dpa caused by irradiation (Burchell et al. 1996).	4-11
Figure 4-13. (a) Compressive stress-strain curve for UNS31803 Steel (Rasmussen 2001), and (b) Compressive stress-strain curve for IG-110 (Fuji et al. 1997).	4-12
Figure 4-14. Compressive stress distribution on an unoxidized support block and plenum.	4-13
Figure 4-15. The principal stress components (Beer et al. 2006).	4-14
Figure 4-16. (a) Upper part of support block with triangular prism; (b) Mesh and temperature distribution; (c) Compressive stress; and (d) Tensile stress.	4-15
Figure 4-17. Modification of plenum head's height block by 25 cm.	4-16
Figure 4-18. Assumed 1/6 cyclic symmetry units of the modified plenum head for each day.	4-16
Figure 4-19. Maximum compressive stress over time.	4-17
Figure 4-20. Maximum compressive tensile stress over time.	4-18
Figure 4-21. Compressive stress distribution of non-uniform corrosion model, 12.25 days after LOCA.	4-18
Figure 4-22. Tensile stress distribution of non-uniform corrosion model, 12.25 days after LOCA.	4-19
Figure 4-23. Unit block schematics.	4-20
Figure 4-24. Relation between local burn-off and normalized compressive strength (IG-110).	4-23
Figure 4-25. Relation between local burn-off and normalized compressive strength (H-451).	4-23
Figure 4-26. Modeling of graphite fracture by corrosion damage (constant f).	4-24
Figure 4-27. Modeling of graphite fracture by corrosion damage (randomly sampled f [uniform]).	4-25
Figure 4-28. Modeling of graphite fracture by corrosion damage (randomly sampled f [Gaussian]).	4-25
Figure 4-29. Relations between f-value (f) vs. fractured total burn-off (IG-110).	4-26
Figure 4-30. Fractured burn-off (Random f) vs. fractured burn-off (constant f) – IG-110.	4-27
Figure 4-31. Relations between f-value (f) vs. fractured total burn-off (H451).	4-27
Figure 4-32. Fractured burn-off (random f) vs. fractured burn-off (constant f) – H451.	4-28
Figure 4-33. Overall graphite oxidation rate (Oh et al. 2006).	4-28
Figure 4-34. Relationship between burn-off (%) and multiplication factor (Oh et al. 2008).	4-30
Figure 4-35. Flowchart of the advanced oxidation model.	4-32
Figure 4-36. GTMHR 600 MWth code nodalization (GAMMA).	4-33
Figure 4-37. Time vs. core maximum temperature.	4-34
Figure 4-38. Time vs. Total Burn-off (Bottom Reflector – IG-110).	4-35
Figure 4-39. Time vs. Total Burn-off (Lower Plenum – IG-110).	4-35
Figure 4-40. Comparisons of IG-110 and H-451 for fracture at the bottom reflector.	4-36

Figure 5-1. Graphite oxidation regime map.....	5-1
Figure 5-2. GT-HTR 300 (or GTHTR-300) Geometry and CFD model.	5-3
Figure 5-3. Injection of Helium in the Lower Plenum via three Defuel Chutes.	5-3
Figure 6-1. Schematic of experimental facility.....	6-2
Figure 6-2. Experimental facility.	6-3
Figure 6-3. Effect of temperature on oxidation rate (IG-430).....	6-4
Figure 6-4. Effect of oxygen concentration on oxidation rate (IG-430).....	6-4
Figure 6-5. Experimental facility for burn-off tests.	6-7
Figure 6-6. Changes of burn-off with time for different conditions.....	6-8
Figure 6-7. Changes of reaction rate with burn-off.....	6-8
Figure 6-8. relation between burn-off and ratio of reaction rate.	6-9
Figure 6-9. Moisture effect on the graphite oxidation in Zone 1.	6-10
Figure 6-10. Moisture effect on the graphite oxidation in Zone 3.	6-11
Figure 7-1. Schematic of oxidation in a graphite column.....	7-1
Figure 7-2. Experimental facility for oxidation tests.....	7-4
Figure 7-3. Buckling strength of IG-110 graphite columns.....	7-4
Figure 7-4. Buckling strength of IG-430 graphite columns.....	7-5
Figure 7-5. Normalized compressive strength of IG-110 oxidized in Zone 1.....	7-6
Figure 7-6. Normalized compressive and buckling strength of graphite columns oxidized in Zone 1.....	7-6
Figure 7-7. Comparison of the experimental results for the compressive strength degradation.	7-7
Figure 7-8. Normalized compressive strength of IG-430 oxidized in Zone 1.....	7-8
Figure 7-9. Strength of graphite columns oxidized in Zone 3.	7-9
Figure 7-10. One-sixth of a graphite support block and its simplified modeling.....	7-9
Figure 7-11. Normalized compressive and buckling strength of IG-430 columns.....	7-11
Figure 8-1. Sample Input of Calculation Node Mapping.	8-2
Figure 8-2. Example of calculation node mapping.....	8-3
Figure 8-3. COREDAX calling in the GAMMA code.	8-3
Figure 8-4. Calculation procedure in neutronics code.....	8-4
Figure 8-5. Homogenized cross-section form in the COREDAX code.....	8-5
Figure 8-6. Homogenized cross-section sample in the COREDAX code.	8-5
Figure 8-7. Simplified GTMHR 600 benchmark problem.	8-6
Figure 8-8. Calculation results of GAMMA/COREDAX code.	8-7
Figure 9-1. Coordinates in a hexagon.....	9-2
Figure 9-2. Interface flux moments on six radial interfaces.	9-2

Figure 9-3. Rebalance factors.	9-5
Figure 9-4. Core configuration of 3-D VVER-440.	9-7
Figure 9-5. Radial core geometry of simplified 3-D VVER-100.	9-8
Figure 9-6. Axial core geometry of 3-D VVER-1000.	9-9
Figure 9-7. Radial core geometry of 3-D SNR-300.	9-10
Figure 9-8. Axial core geometry of 3-D SNR-300.	9-10
Figure 9-9. Core configuration of 3-D VVER-100 benchmark problem.	9-11
Figure 9-10. Results of VVER-100 benchmark problem.	9-12
Figure 9-11. Control rod position in VVER-1000.	9-13
Figure 9-12. Total power change in time.	9-13
Figure 9-13. Arrangement of active core and its components.	9-14
Figure 9-14. Fuel block cell, type 1 fuel assembly.	9-15
Figure 9-15. Fuel block with cavity for control rod or reserve shutdown system, type 2 fuel assembly.	9-15
Figure 9-16. Radial core configuration of simplified 3-D GTMHR.	9-16
Figure A-1. DEGB facility assembly with knife gate valve.	3
Figure A-2. Horizontal pipe dimensions.	3
Figure A-3. Flanged tank dimensions; tanks have covers on both top and bottom to facilitate cleaning.	4
Figure A-4. Bottom tank cover.	4
Figure A-5. Top tank cover.	5

TABLES

Table 1-1. Organization responsibilities by task.	1-5
Table 2-1. Comparisons of pressure build-up and static head for GTMHR and NACOK experiment.	2-27
Table 2-2. Comparisons of time scales for the GTMHR and NACOK experiment (Stage 2).	2-33
Table 2-3. Number of mesh and volume data for each region in the 3-D grid model.	2-40
Table 2-4. Pressure drop results using the porous media conditions.	2-43
Table 2-5. NASA format correlation for specific heat of helium.	2-44
Table 3-1. Previous and current validation data for air-ingress analyses.	3-1
Table 3-2. Test matrix of isothermal DEGB experiment.	3-5
Table 3-3. Gas combinations used for Grobelbauer et al. (1993)'s experiment.	3-32
Table 3-4. Grid information and front speed.	3-37
Table 3-5. Comparisons between CFD results and experimental data (current speed).	3-40
Table 3-6. Comparisons between CFD results and experimental data (light gas intrusion).	3-43

Table 4-1. Basic thermo mechanical properties of IG-110 at standard conditions. (Ishihara et al. 2004, Burchell 1991).	4-8
Table 4-2. Comparison of the analytical solution to the ABAQUS result.....	4-14
Table 4-3. Material properties at each day.....	4-17
Table 4-4. Input parameters for graphite oxidation and structural integrity.	4-25
Table 6-1. Graphite selection matrix (Robert and Timothy 2005).	6-1
Table 6-2. Properties of IG-110 and IG-430 manufactured by Toyo Tanso in Japan.	6-1
Table 6-3. Test conditions.	6-3
Table 6-4. Activation energy and order of reaction.....	6-5
Table 6-5. Experimental results on kinetics parameters for IG-110.....	6-5
Table 6-6. Experimental results on kinetics parameters for IG-430.....	6-5
Table 6-7. Conditions for burn-off tests.	6-7
Table 6-8. Conditions for effect of moisture tests.....	6-9
Table 7-1. Test matrix.	7-3
Table 7-2. Comparison of the Knudsen relation.	7-7
Table 7-3. Dimensions of graphite specimens for fresh graphite tests.	7-10
Table 7-4. Experimental results of IG-110 columns.	7-10
Table 7-5. Experimental results of IG-430 columns.	7-10
Table 9-1. Results of VVER-440 benchmark problem ^a	9-6
Table 9-2: Results on CGR acceleration of VVER-440 benchmark problem ^a	9-7
Table 9-3. Results on k_{eff} of simplified VVER-1000 benchmark problem.	9-9
Table 9-4. Results of SNR-300 benchmark problem.....	9-11
Table 9-5. Relative power deviation from mean (%).	9-12
Table 9-6. Results on k_{eff} of simplified GTMHR benchmark problem.	9-16

ACRONYMS

AFEN	analytic function expansion nodal
CFD	computational fluid dynamics
DEGB	double-ended guillotine break
DP	differential pressure
GA	General Atomics
GTMHR	gas turbine modular helium reactor
HGTR	high temperature gas reactor
INL	Idaho National Laboratory
LIF	laser-induced fluorescence
LOCA	loss-of-coolant accident
LWR	light water reactor
NACOK	an acronym of German words that stand for “Natural Convection in the Core with Corrosion”
NASA	National Aeronautics and Space Administration
NGNP	Next Generation Nuclear Plant
PIV	particle image velocimetry
PLIF	planar laser-induced fluorescence
R&D	research and Development
RSM	Reynolds’s Stress Model
V&V	verification and validation
VHTR	very high temperature gas-cooled reactor

FY-09 Report: Experimental Validation of Stratified Flow Phenomena, Graphite Oxidation, and Mitigation Strategies of Air Ingress Accidents

1. INTRODUCTION

A loss-of-coolant accident (LOCA) is considered as a critical event for a very high temperature gas-cooled reactor (VHTR). Following helium depressurization, it is anticipated that unless countermeasures are taken, air will enter the core through the break leading to oxidation of the in-core graphite structure. Thus, without mitigation features, a LOCA will lead to an air ingress event, which may lead to exothermic chemical reactions of graphite with oxygen. Under extreme circumstances, a loss of core structural integrity may occur along with excessive release of radiological inventory. The rate of graphite oxidation and the likelihood of extensive structural damage can be assessed with a combination of analytical investigation, simulations of simplified core models, and experimental validation.

Idaho National Laboratory under the auspices of the U.S. Department of Energy is performing research and development (R&D) that focuses on key phenomena important during challenging scenarios that may occur in the VHTR. Phenomena Identification and Ranking Table (PIRT) studies to date have identified the air ingress event, following on the heels of a VHTR depressurization, as very important (Oh et al. 2006, Schultz et al. 2006). Consequently, the development of advanced air ingress-related models and verification and validation (V&V) requirements are part of the experimental validation plan.

1.1 Objectives

The major goal of the second year effort of the 3-year study was first to perform air-ingress-related experiments and validate the computer codes, such as computational fluid dynamics (CFD) and GAMMA, in order to make them reliable for use in predicting the consequences of air-ingress in a VHTR.

This research was conducted to supply information needed by the codes that will model the important phenomena during air-ingress accidents. The following information was obtained:

- The effects of density-driven, stratified flow on air ingress in the reactor core
- The internal pore area density of nuclear grade graphite, an important parameter for determining the oxidation rate
- the oxidation and density variation in terms of burn-off in the core bottom structures
- The effects of the burn-off on the structural integrity of the core bottom structures.

The second objective of this study was to simulate air-ingress accidents by validated methods for estimating the consequence of a LOCA, and evaluating various methods for the mitigation of the effects of air ingress.

The final objective was to develop a coupled neutronics and thermal-hydraulic capability in the GAMMA code, which involved:

- The development of core neutronics models
- Coupling neutronic-thermal hydraulic tools
- Coupled core model V&V.

These objectives are pursued to allow the simulation of recriticality in conduction cool-down accidents without scram and to determine initial and transient power distribution, which are essential for the accurate estimation of the safety margin.

1.2 Background

The VHTR is a graphite-moderated, uranium-fueled, helium-cooled reactor using a direct or indirect gas cycle to convert the heat generated by nuclear fission into other forms of energy suitable for driving industrial processes. High temperature gas reactor (HTGR) technology has been researched and developed since the 1950s. The VHTR produces a higher outlet temperature than the HTGR. VHTRs work on the principle of passing a cooling gas through the core, then running the heated gas directly to a steam generator or a gas turbine. VHTRs have been built in Japan and China for their nuclear research. VHTRs have several advantages over light water reactors (LWRs), including fuel integrity, proliferation resistance, a relatively simple fuel cycle, easy refueling, and modularity to supply electricity to remote areas and energy-starved underdeveloped countries with a smaller power generation infrastructure. The characteristics of the VHTR are (1) helium coolant, (2) higher than 900°C outlet temperature, and (3) a modularity of 600 MWth. Benefits of the VHTR concept are (1) high thermal efficiency compared to other concepts, (2) process heat production at temperatures suitable for a range of industrial applications, and (3) a high degree of passive safety. The plant design should be streamlined to be technically sound, robust, proliferation-resistant, and economical. Even though gas reactors have been developed in the past with some success, the innovations of modularity and integrated state-of-the-art safety systems make the VHTR design attractive from a technical and economic perspective.

The very high temperatures of this reactor concept can degrade structural graphite in the event of leak in the primary loop leads to depressurization and introduction of air into the core. This LOCA may lead to the oxidation of the in-core graphite structure and heat-up of the fuel that can lead to release of fission products. If such events are found to be likely, design changes or other countermeasures may be required.

To resolve these concerns, a well-validated tool on safety and design analysis is needed. As part of an International Nuclear Energy Research Initiative project (Oh et al. 2006), the GAMMA code has been developed. GAMMA has a capability to analyze the air-ingress accident under a VHTR LOCA. The GAMMA code is being further improved and validated in order to simulate transient and chemical phenomena associated with the VHTR LOCA.

Two important new issues are associated with air-ingress in a VHTR. One concerns the potential for core degradation caused by weakening of the graphite support structure following oxidation. The other is associated with stratified flow caused by density differences that will accelerate the air-ingress into the lower plenum of the reactor. Excessive graphite oxidation and density-driven stratified flow have been observed in simple geometries and flow regimes but it is yet to be determined whether they play a significant role in the VHTR LOCA accident sequence. To determine if these phenomena are of licensing concern, further investigation is warranted.

1.3 R&D Plan

1.3.1 Task 1: Density-Difference Induced Stratified Flow Analysis—FY-08 and FY-09 Task

Task 1 involved computational analyses to validate the density-difference induced air ingress phenomena postulated in the VHTR following a pipe break. After the hypothesized break in the hot duct of the VHTR, air present in the reactor cavity will enter the reactor vessel via density-driven stratified flow. Because of the significantly higher molecular weight and lower initial temperature of the reactor cavity air, the air-helium mixture in the cavity is heavier than the helium discharging through the break. In the later stages of the helium blow-down, the momentum of the helium flow decreases enough that the

heavier cavity air can flow into the lower plenum of the reactor vessel through the lower portion of the broken hot duct while helium is escaping in the opposite direction through the upper portion of the hot duct. Once it enters the reactor, the heavier gas (air) will pool at the bottom of the lower plenum and begin to diffuse upwards into the core. This condition (based on the countercurrent stratified flow assumption) is considerably different from the standard assumption used in calculations to date in which the air is assumed to diffuse into the lower plenum through the hot duct. Preliminary calculations performed as part of the FY-08 task showed that countercurrent stratified flow occurs and significantly accelerates air ingress, rather than the assumed molecular diffusion. In this task, the characteristics and behaviors of these phenomena have been analyzed and estimated by computational and theoretical methods. The following activities were carried out in this study:

- CFD analysis of the stratified flow
- Development of a stratified flow model for GAMMA (if necessary)
- Air-ingress analyses, including stratified flow phenomena.

1.3.2 Task 2: Experimental Study on the Stratified Flow—FY-09 and FY-10 Task

Task 2 involves experimental data collection to provide a baseline for validation of CFD and GAMMA codes based on experimental results. In this task, a test flow loop is set up to mimic the density-difference induced air ingress phenomena. The following parameters are being investigated:

- Test flow loop setup
- Flow visualization
- Parametric study
- Total break versus partial break.

1.3.3 Task 3: Advanced Graphite Oxidation Study—FY-08 and FY-09 Task

Task 3 measures the transient graphite oxidation with burn-off, and the internal pore surface area density of nuclear-grade graphite—a parameter found to be a very important in the early stage of graphite oxidation. The results of these measurements will be implemented into the upgraded GAMMA code. The following activities are being carried out in this task:

- Measurement of surface area density of nuclear graphite using Brunaur-Emmett-Teller method
- Measurement of transient graphite oxidation with burn-off
- Implementation of the advanced graphite material parameters into GAMMA code.

1.3.4 Task 4: Air Ingress Mitigation Study—FY-10 Task

This task will develop potential methods of air-ingress mitigation and evaluate the effects of those methods by computational means. Full air-ingress analyses will be performed by upgraded GAMMA code. These analyses will consider all the possible physical phenomena expected in an air-ingress accident including: gas diffusion, natural convection, stratified flow, radiation, conduction, convection, porous media, etc. The following activities will be carried out in this task:

- Set up the advanced air-ingress analysis
- Develop air-ingress mitigation methods (Conceptual study)
- Analyze full air-ingress and evaluate mitigation methods.

The progress being made on each of these tasks is discussed in the rest of this report.

1.3.5 Task 5: Experiment of Burn-off in the Core Bottom Structures (KAIST)

This task will measure the oxidation rate and density of the nuclear graphite and developed oxidation models of the core bottom structures, which would be exposed to air in a LOCA. The main parameters that affect the rate of oxidation and density of the graphite of the core bottom are kinetics, mass diffusion, combined effect of kinetics and mass diffusion, moisture, shape and size, and degree of burn-off. The following activities will be carried out in this task:

- Measurement of oxidation rate of nuclear graphite
- Measurement of density of nuclear graphite with burn-off.

1.3.6 Task 6: Structural Tests of Oxidized Core Bottom Structures (KAIST)—FY-09 and FY-10 Task

This task involves the fracture model regarding the oxidation of the nuclear graphite. Because of the density changes in the nuclear graphite, structural characteristics will be investigated and the fracture model of the core bottom structures will be developed by fracture test, including the internal pressure test, uniaxial compression test, diametrical compression test, and fracture toughness test. The following activities will be carried out in this task:

- Fracture test of nuclear graphite with burn-off
- Development of fracture model of burnt-off bottom reflector.

1.3.7 Task 7: Coupling Neutronic-Thermal Hydraulic Tools (KAIST)—FY-09 Task

This task involves enhancing the thermal-hydraulic capability of GAMMA code. Thermal power distribution in the reactor core is needed to improve the reliability of thermal-hydraulic analysis. The knowledge of accurate thermal distribution is also needed to generate an exact cross-section of nuclei. Neutronics/thermal-hydraulics feedback effects will be therefore investigated and the feedback parameters will be implemented into an upgraded GAMMA code. The following activities will be carried out in this task:

- Set up parameters for neutronics/thermal-hydraulics code coupling
- Code coupling of COREDAX with GAMMA.

1.3.8 Task 8: Core Neutronic Model (KAIST) –FY-08 and FY-09 Task

This task involves an advanced neutronics code for both steady and transient analysis of a VHTR core. Korea Advanced Institute of Science and Technology (KAIST) developed COREDAX code to analyze the hexagonal-z three-dimensional (3-D) geometry. The COREDAX code is based on analytic function expansion nodal (AFEN) method, which does not use the transverse-integration procedure, but uses analytic basis functions to represent solution with upmost accuracy. The COREDAX and GAMMA coupled code will provide accurate analysis of initial condition power distribution of VHTR via feedback calculation with each other. In this task, the COREDAX code will be developed to deal with the hexagonal-z 3-D geometry. COREDAX code will be used to investigate the feedback between neutronics and thermal-hydraulics. The following activities will be carried out in this study:

- Development of a VHTR core neutronics analysis code in hexagonal 3-D geometry
- Investigation of neutronics/thermal-hydraulics feedback effects.

1.3.9 Task 9: Coupled Core Model V&V (KAIST) – FY-10 Task

This task involves the verification of GAMMA code coupled with COREDAX code and the validation of prediction results of thermal power distribution in the hexagonal reactor core. The following activities will be carried out in this task:

- Verification of GAMMA and COREDAX coupling
- Validation of coupled code with reference data.

1.4 Research and Development Collaboration

The research proposed in this report was carried out as collaboration between Idaho National Laboratory (INL) in the United States and KAIST in Korea. Both INL and KAIST provided project management and integration in addition to performing work on technical tasks. This collaboration exploited unique capabilities and resources available at these organizations.

The individual task responsibilities of INL and KAIST are indicated in Table 1-1. All tasks where INL and KAIST shared the leadership and technical performance responsibilities, each of the activities were planned and executed with a high degree of coordination between the organizations.

Table 1-1. Organization responsibilities by task.

Task No.	Lead	INL Responsibilities	KAIST Responsibilities
0.0	Shared	Project management at INL	Project management at KAIST
0.1	Shared	Prepare annual reports	Prepare annual reports
1.0	INL	Analysis of stratified flow	Review and comments
2.0	INL	Experiment on stratified flow	Review and comments
3.0	INL	Experiment and analysis on graphite oxidation	Review and comments
4.0	INL	Full air ingress analysis for reference reactor Method development for air-ingress mitigation	Modeling and method validation Review and comments
5.0	KAIST	Review and comments	Experiment on burn-off of bottom reflector graphite
6.0	KAIST	Review and comments Generating backup data	Fracture test and analysis
7.0	KAIST	Review and comments	Coupling neutronic-thermal hydraulic tool
8.0	KAIST	Review and comments	Development of core neutronic model
9.0	KAIST	Review and comments	Validation of coupled code

2. TASK 1: DENSITY-DIFFERENCE INDUCED STRATIFIED FLOW ANALYSIS (INL)

2.1 Introduction

The potential for air to ingress into the VHTR vessel stems from consideration of postulated LOCAs. The VHTR is located in a reactor cavity that is filled with air under normal operational conditions. If a LOCA occurs, air may be able to move into the reactor vessel. It is presently thought that the worst-case scenario will occur if a double-ended guillotine break (DEGB) in the hot duct is postulated. The probability of a DEGB is still a subject of discussion as to whether it can and should be considered a licensing basis event. This issue is not addressed in this study and is arguably treated more appropriately using probabilistic methods but, as a worst-case event, simulation of the DEGB may provide useful information about the trajectory of a 'cliff-edge' air ingress sequence. The hot duct is a large pipe (exact dimensions presently not defined, but the outer diameter is over a meter) that connects the reactor vessel with the vessel housing the power conversion equipment.

For a DEGB, the transient will commence with a depressurization from operating pressure (assumed to be approximately 7 to 9 MPa) as helium is discharged into the reactor cavity. During the depressurization phase hot helium from the vessel will mix with the air in the reactor cavity. Hence, a helium-laced air mixture will be available to move into the reactor vessel once the pressure gradient across the break has been equalized, thus changing the flow behavior at the break from a momentum-driven flow out of the reactor vessel into the reactor cavity to a density-gradient driven stratified countercurrent flow with helium moving out of the reactor vessel into the cavity while helium-laced air moves into the reactor vessel from the reactor cavity.

The potential for density-gradient governed stratified air to ingress into the VHTR following a large-break LOCA was first described in the Next Generation Nuclear Plant Methods Technical Program Plan (Schultz et al. 2006) based on stratified flow studies performed with liquid (Liou et al. 1997, 2005). Studies on density gradient driven stratified flow in advanced reactor systems has been the subject of active research for well over a decade because density-gradient dominated stratified flow is an inherent characteristic of passive systems used in advanced reactors.

The work done on Generation 3+ systems, although for LWRs, is conceptually identical and directly applicable to the phenomenological behavior that will occur in the Next Generation Nuclear Plant (NGNP). Even though the earlier studies were based on Generation 3+ systems using water as the working fluid, the governing equations are identical. The boundary conditions change to reflect the differences in the working fluid and the reactor vessel geometry. Recently a simple computational fluid dynamic calculation was made to mimic the LOCA between two tanks filled with helium and oxygen, respectively, as shown in Figure 2-1.

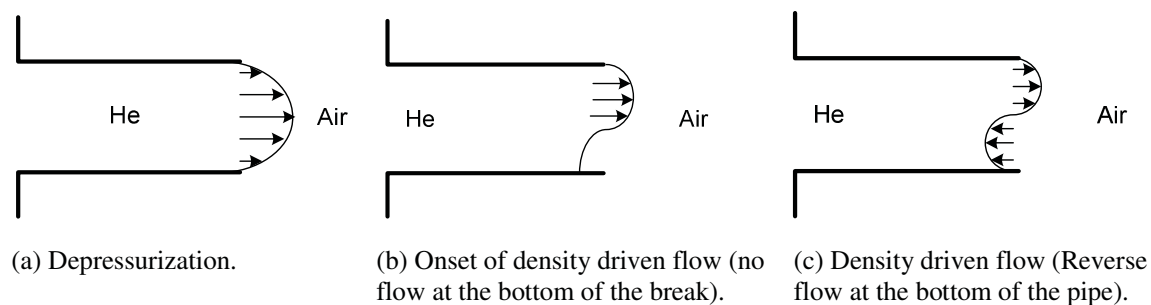


Figure 2-1. Density-driven induced stratified flow.

Earlier studies of the mechanisms leading to air ingress into the reactor vessel focused on diffusion as described by Fick's Law (Takeda 1997, Takeda and Hishida 1996, Oh et al. 2006, Kim et al. 2007, NO et al. 2007) and ignored the effects of density gradients on the interactions between helium (low density) and air or helium-laced air (high density) flows.

Air ingress into the reactor vessel stemming from density gradient driven stratified flow occurs over a shorter time scale than diffusion and results in a depressurized conduction cooling scenario with a different set of boundary conditions than previously assumed. Hence, experiments are needed to study these phenomena as noted in the NGNP Methods Thermal-Fluids Experiment Plan (Schultz et al. [2006]). Subsequent to the break in the hot duct hypothesized in depressurized conduction cool-down, air present in the reactor cavity will enter the reactor vessel. Because of the significantly higher molecular weight and lower initial temperature of the reactor cavity air, the air-helium mixture in the cavity is always heavier than the helium discharging from the reactor vessel via the break into the reactor cavity. Once the air-helium mixture enters the reactor vessel, it will pool at the bottom of the lower plenum then move from the lower plenum into the core via diffusion and the density-gradient induced by heating. When density gradient driven stratified flow is considered as a contributing phenomena for air ingress into the reactor vessel, the following factors contribute to a much earlier natural circulation-phase in the reactor vessel: (a) density gradient driven stratified flow is a much more rapid mechanism (at least one order of magnitude) for moving air into the reactor vessel lower plenum than diffusion, and consequently, (b) the diffusion dominated phase begins with a much larger flow area and a much shorter distance for air to move into the core than earlier scenarios that attribute all air ingress from the reactor cavity into the core to diffusion only.

In essence, the stratified flow assumption is based on the formation of a wedge of air at the lower portion of the hot duct break which will advance into the reactor vessel as a function of the density-gradients once the blow down has depressurized. Such flows are well characterized by the densimetric Froude number F , which correlates the densities of helium and the air mixture to a constant value representative of the flow condition at different times in the scenario.

$$F = \frac{u}{\sqrt{g'd}} \quad (2-1)$$

where u = discharge velocity of air, d = hydraulic depth of air, and g' = reduced gravity defined by

$$g' = \frac{g(\rho_2 - \rho_1)}{\frac{\rho_2 + \rho_1}{2}} \quad (2-2)$$

The buoyancy induced by the density difference of the two fluids necessitates the use of reduced gravity g' instead of the standard gravity g . The magnitude of F indicates the magnitude of inertia force relative to the buoyancy created by stratification, and is a controlling parameter in stratified flows. This idea and experimental confirmation can be found in Liou et al. (1997) and Yih (1980).

A stratified flow experiment is required to better understand this phenomenon and provide data for validation of codes that will be used in conjunction with systems analysis codes to model this inherently multidimensional phenomenon. It is expected that the densimetric Froude number will be found to be a function of

$$F = f\left(\alpha, L/D, \frac{V_{vessel}}{V_{vault}}, P_R, R\right) \quad (2-3)$$

where α = orientation of the break with respect to the vertical, L = length of the separated hot duct on the reactor vessel side, D = diameter of the hot duct, V = volume, Pr = Pressure coefficient, and R = Reynolds number.

Thus, as shown in Figure 2-1(a), outward flow of helium into the reactor cavity from the reactor vessel continues until the reactor pressure is sufficiently reduced such that the blow-down flow subsides. Thereafter, air begins to intrude into the pipe through the lower portion of the break as depicted in Figure 2-1(b) and Figure 2-1(c). In a rectangular flow cross section, it can be shown theoretically that the volumetric flow rates of the two fluids through the break are the same (Liou 1997). It is therefore assumed that the helium volumetric flow and air volumetric flow are equal. The heavy air will enter the vessel and collect (allowing dome turbulent mixing) at the bottom of the VHTR in the lower plenum. The air in the lower plenum will heat up and create a density gradient that causes a buoyancy force that drives the air further up into the reactor core. This density gradient will trigger a natural circulation in the reactor with the potential for subsequent oxidation of the graphite structures, perhaps leading to loss of structural integrity. If the stratified air flow induces the natural circulation flow to begin earlier than previously thought, graphite oxidation will occur earlier and at a more rapid rate. Earlier predictions from the GAMMA code (NO et al. 2007) predict oxidation between 150 and 200 hours following pipe rupture, depending on the initial air volume in the containment. Calculations using MELCOR code predict that oxidation begins at 220 hours (Yih 1980) following pipe rupture. However, recent CFD calculations (Oh et al. 2008), using the stratified flow approach, predict that natural circulation commences much sooner than 150 hours, emphasizing the importance of clarifying the understanding of this phenomena and its effect on reactor safety.

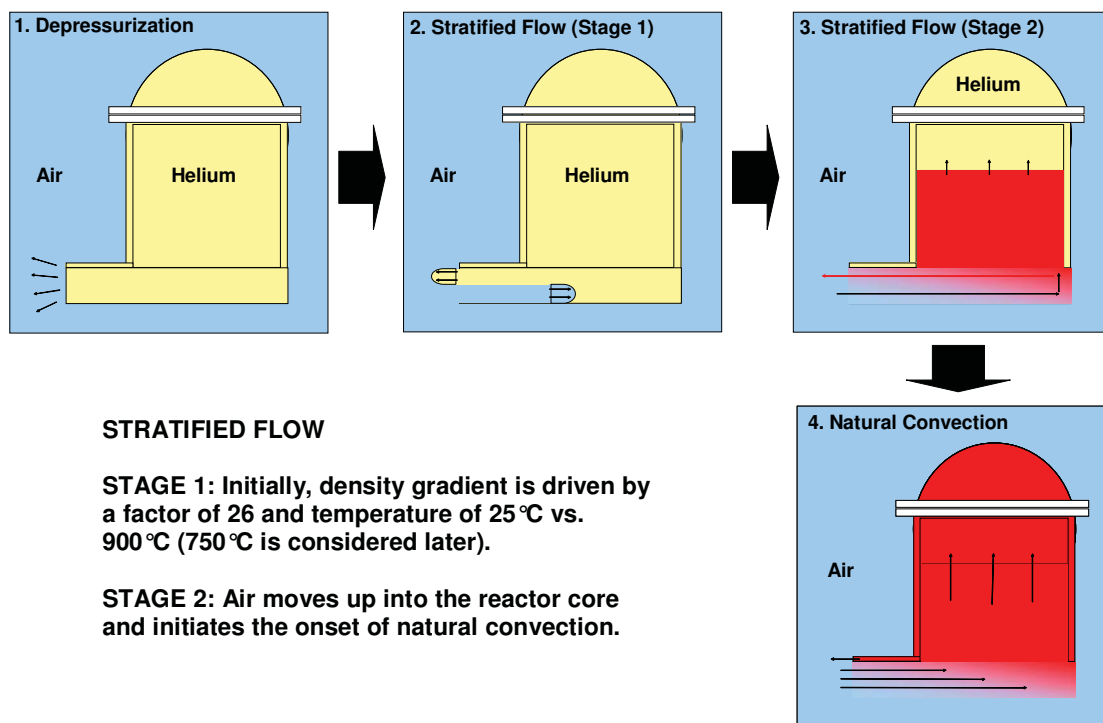


Figure 2-2. Air-ingress Scenario (INL's current understanding).

Some preliminary CFD analyses were performed in FY-08 for DEGB situations that focused on stratified flow. In these analyses, sensitivities and their relative importance for various parameters, including molecular mass, temperature, pressure, scale, turbulence model etc., were roughly estimated. These analyses indicated that molecular mass and temperature differences are the most important parameters affecting the stratified flow in the air-ingress accident. According to recent findings, the temperature gradient appears to be more important than the molecular diffusion during the whole air-ingress process. In addition to this preliminary CFD work, the whole air-ingress scenario was analyzed by using FLUENT and GAMMA code sequentially, which considered various air-ingress scenarios. Finally, the effects of these scenarios on the air-ingress consequences were compared to each other. As a result, the core maximum temperature, one of the most important safety parameters, appears to be insensitive to the air-ingress scenarios or the onset-natural-circulation time, while the supporting graphite corrosion and structural integrity were significantly influenced by the scenarios. These conclusions prompted graphite experiments, including oxidation and fracture, which produced valuable results and parameters. Based on those experimental results and parameters, the failure of supporting graphite structures caused by corrosion was estimated using GAMMA system analysis code and ABAQUS structure analyses code.

Recently, a new air-ingress scenario was established based on the density gradient driven flow as illustrated in Figure 2-2. According to this scenario, after the pipe break, the coolant (helium) in the vessel is rapidly blown into the reactor confinement with depressurization because the inside vessel pressure is much higher than the outside (Figure 2-2 (a)). After depressurization, if the overall pressures between inside and outside vessel is equilibrated, the outside air (or air/helium mixture) will move into the inside vessel forming stratified flow by density gradient (Figure 2-2 (b)), which was named “Stage 1 stratified flow.” In Stage 1, the density gradient is generated mainly by molecular mass differences between helium coolant and air, and secondly by temperature gradient. After the helium-air mixture fills up the reactor bottom, “Stage 2 stratified flow” begins (See Figure 2-2(c)). In Stage 2, the density gradient flow is generated solely by the temperature gradient between the inside and outside of the reactor. The temperature gradient drives cold air into the lower plenum, and the cold air expands by heating. Once the air is heated in the lower plenum, it (air or air-helium mixture) will have a buoyancy force to push the helium coolant up into the reactor core. The air will then slowly flow into the inside of the core. Once the reactor top is full, global natural circulation will begin (See Figure 2-2 (d)). It appears, from the FY-08 preliminary CFD analyses, to only take several minutes from post-depressurization to onset-of-global-natural-circulation.

2.2 Review on the Previous Gravity Current Flow Studies

This section summarizes previous investigations on the gravity current, which appears to have similar flow mechanisms to those of air-ingress accidents. The gravity current, also known as density gradient driven stratified flow, is the flow of one fluid through another by density differences that are caused by temperature differences, dissolved materials, or suspended particles. This type of stratified flow happens when a heavy fluid intrudes into a lighter fluid or vice versa. This gravity current flow is easily seen in the natural surroundings. Thermal stratification during the emergency coolant injection in advanced reactors, thunderstorm outflows, growth of lava domes, and avalanches are widely known natural examples of gravity currents. Wastewater discharge into rivers, oil spills in the ocean, accidental release of toxic industrial gases, and smoke movement are some examples of man-made gravity current (Simpson 1999). Figure 2-3 depicts the controlled lock-exchange experiment performed by Shin et al (2004) for small density differences (Boussinesq flow). This figure clearly shows that a dense gravity current of salted water (dark side) travels to the right along the lower boundary while the lighter current of pure water (light side) travels to the left along the upper boundary.

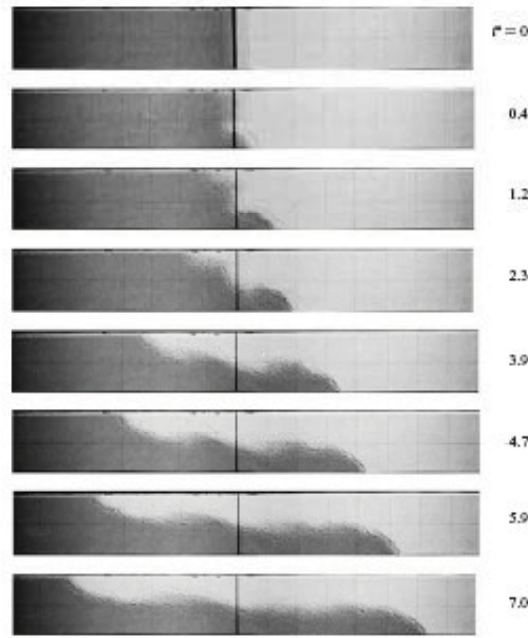


Figure 2-3. Gravity current produced by lock-exchange in a rectangular channel (Shin et al. 2004).

The study of gravity currents has a long history. The first modeling for the gravity current flow was carried out by von Karman (1940), who was one of the pioneers in the fluid dynamics field. He considered energy conserving current in his derivation, which is propagated in an ambient fluid of infinite depth, and proposed a theoretical correlation predicting the frontal speed (U) of the current flow as

$$F_h = \frac{U}{\sqrt{g'h}} = \frac{\sqrt{2}}{\gamma} \quad (2-4)$$

where

g' = reduced gravity ($g' = g(1 - \gamma)$)

h = depth of the current (m)

γ = density ratio (ρ_1 / ρ_2 , the low density / the higher density fluid)

In 1958, Keulegan indicated that the speed of the current was independent of the ratio of the channel width (w) and depth (h) from his lock-exchange experiment. He also observed a small increase of Froude number (F_H) with increase of Reynolds number (Re). Based on his experiment, he proposed the correlation

$$F_H = \frac{U}{\sqrt{g'H}} = 0.42 \quad (\text{at } Re = 600) \quad (2-5)$$

$$F_H = \frac{U}{\sqrt{g'H}} = 0.48 \quad (\text{at } Re > 150000) \quad (2-6)$$

where

H = channel depth (m).

The Reynolds number in Equations (2-5) and (2-6) was defined by

$$Re = \frac{UH}{\nu} \quad (2-7)$$

where

ν = kinematic viscosity (m^2/s).

Yih (1965) proposed that the depths of the two currents are equal and have the value of half the channel depth along their entire lengths, and that the speeds of both gravity currents are the same for the Boussinesq flow ($\gamma \sim 1$) where the density difference between two fluids is very small, like water and salted water.

Bar (1967) carried out experiments for both a free and a rigid upper surface. In separate tests, temperature and salinity were used to provide a density difference. His results showed that F_H increases with Reynolds number. The variations were significant for low Re numbers between 200 and 1,000, but the change was slight for higher Re numbers ($Re > 1,000$). He also found that the free-surface cases have higher values of F_H .

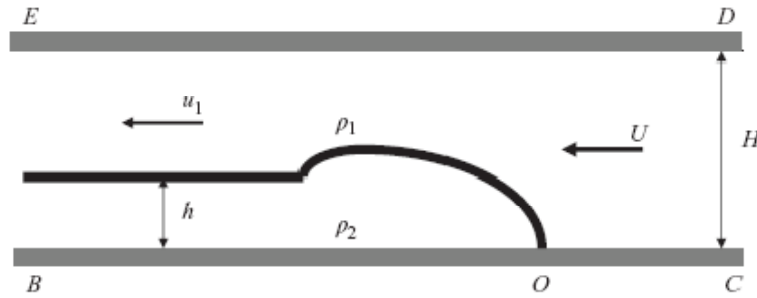


Figure 2-4. Diagram of idealized gravity current in the rest frame of the current (Shin et al. 2004).

Benjamin (1968) first developed a theory for the propagation of a steadily advancing current by using conservation of mass and momentum flux in a frame of reference moving with the current (Figure 2-4). Therefore, the front was set to be at rest in this reference frame. His derivation assumed inviscid flow where the Grashof number (Gr) is infinite. His derivation showed that there were various possible solutions, depending on the depth of the current as follows:

$$\frac{U^2}{gH} = \frac{h(2H-h)(H-h)(\rho_2/\rho_1-1)}{H^2(H+h)} = \left(\frac{1-\gamma}{\gamma} \right) \left(\frac{h(2H-h)(H-h)}{H^2(H+h)} \right). \quad (2-7)$$

Benjamin (1968) also showed that if there is no dissipation in the flow (if the energy fluxes into and out of the control volume is the same), the solution reduced to

$$\frac{h}{H} = 0 \text{ or } \frac{h}{H} = \frac{1}{2}. \quad (2-8)$$

The first solution is reduced to the exactly same solution derived by von Karman (Equation (2-4)) in the limit $h/H \rightarrow 0$ obtained as $H \rightarrow 0$. The second solution leads to the nondimensional front speed correlation from Equation (2-7)

$$\frac{U^2}{gH} = \frac{1}{4} \frac{(1-\gamma)}{\gamma}. \quad (2-9)$$

For Boussinesq case ($\gamma \sim 1$), Equation (2-9) shows the Froude number defined in terms of the reduced gravity, as Equation (2-5) is

$$F_H = \frac{U}{\sqrt{g'H}} = \frac{1}{2}. \quad (2-10)$$

He also argued that the gravity current occupying less than half the channel depth do not conserve energy and the maximum energy flux is reached when $h = 0.347H$. Figure 2-5 shows the dimensionless net energy flux based on Benjamin's theory. This figure shows that the energy flux increases from 0 with h , reaches a maximum when $h = 0.347$, and then decreases to 0 when $h = 0.5H$. For the case $h > 0.5H$, the energy leaving the downstream section is greater than that entering from upstream. This flow is clearly impossible unless there is an alternative energy supply within the control volume. Therefore, Benjamin (1968) argued that the depth of the gravity current should be less than half of the channel depth (H).

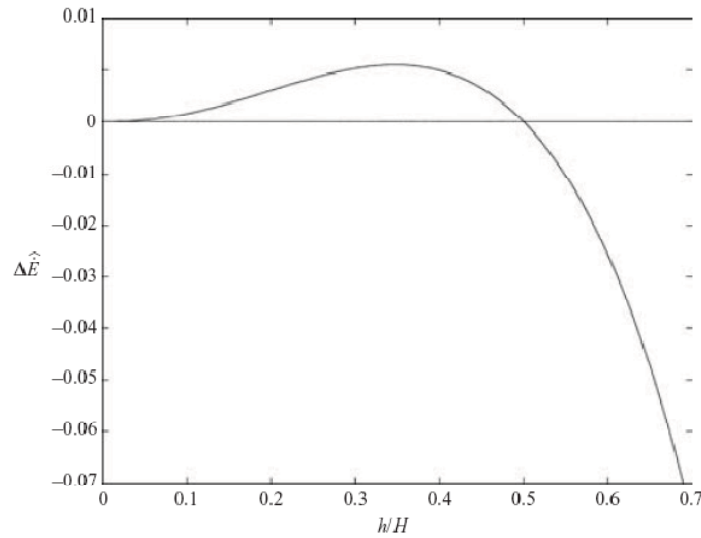


Figure 2-5. Dimensionless net energy flux plotted against dimensionless current depth h/H (Shin et al. 2004).

Britter & Simpson (1978) observed that most of the mixing took place along the interface between the two fluids behind the head, and the Kelvin-Helmholtz billows were shed behind the head. Hopper & Simpson (1980) developed an empirical model that incorporates mixing at the front. The correlations suggested from their experiments are

$$F_h = \frac{U}{\sqrt{g'h}} = 1.19 \quad (h/H < 0.075)$$

and (2-11)

$$F_h = \frac{U}{\sqrt{g'h}} = \frac{1}{2} \cdot \left(\frac{h}{H} \right)^{1/3} \quad (0.075 < h/H < 0.5) \quad (2-12)$$

Gardner & Crow (1970) and Wilkinson (1982) showed the existence of half-depth by their experiments with air cavities intruding into a water filled channel (large density differences and immiscible flow). They also observed that the cavities could occupy half the depth and the free surface is smooth without energy loss, when the surface tension effects are small. They extended Benjamin's analysis to account for surface tension effects and showed that surface tension slows the cavity.

Linden & Simpson (1986) showed that mixing behind the head significantly affects the dynamics of the current.

Keller & Chyou (1991) formulated a hydraulic theory for the entire density ratio range (from 0 to 1.0). They assumed that for the small density differences, both gravity currents are energy conserving and they are connected by a combination of a long wave of expansion and an internal bore. But, they assumed that for large density differences, the light current is energy conserving, the heavy current dissipative, and the gravity currents connected only by a long wave of expansion. Figure 2-6 summaries their models for various density ratios.

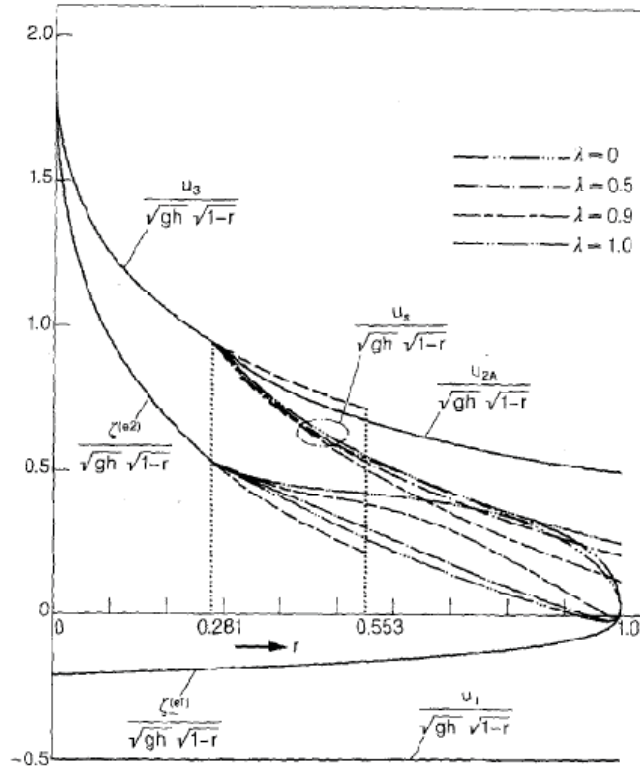


Figure 2-6. Wave speed plotted versus density ratios ($r = \rho_B / \rho_A$) (Keller & Chyou 1991).

For density ratio ($r > 0.281$), Keller & Chyou (1991) described the complete lock exchange flow as shown in Figures 2-7 and 2-8. The velocities of relevant waves were expressed as:

- (a) Front speed of the left-running gravity (loss-free) current (u_l : See Figure 2-7)

$$F_1 = \left(\frac{u_1}{\sqrt{g'h}} \right) = \frac{1}{2} \quad (2-13)$$

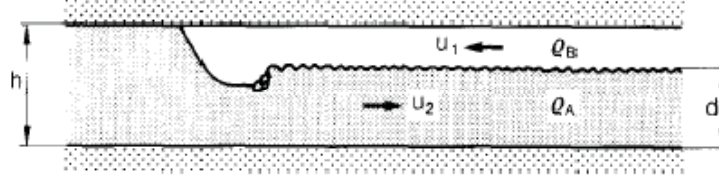


Figure 2-7. Gravity current of low-density fluid penetrating into a channel that initially contained high-density fluid (Keller & Chyou 1991).

- (b) Front of the right running (dissipative) gravity current (u_{2A} : See Figure 2-8)

$$F_{2A} = \left(\frac{u_{2A}}{\sqrt{g'h}} \right) = \left(\frac{\xi \cdot (1-\xi)^2}{2-\xi} \right) \cdot \frac{1}{\sqrt{r}} \quad (2-14)$$

where

$$\xi = \text{fractional depth } (h/H)$$

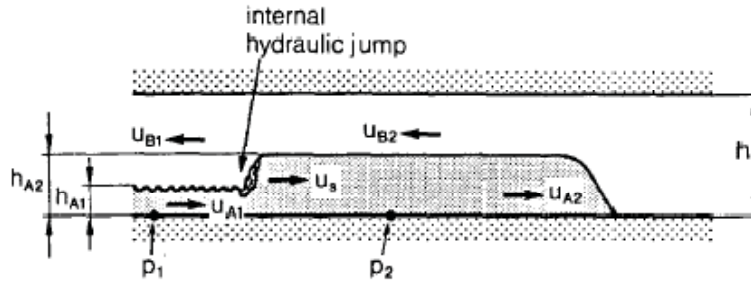


Figure 2-8. Loss-free gravity current of high density fluid penetrating into a horizontal channel originally filled with low density fluid (Keller & Chyou 1991).

In the Equation (2-13) and (2-14), the value of ξ is determine by Figure 2-9. In this figure, the coefficient λ represents the relative amount of energy loss. The mathematical representation where Case $\lambda = 1$ corresponds to a loss-free flow in the lower layer and case $\lambda = 0$ to the special case of no recovery of kinetic energy is

$$p_2 - p_1 = \lambda \cdot \frac{\rho_A}{2} ((u_{1A} - u_s)^2 - (u_{2A} - u_s)^2). \quad (2-15)$$

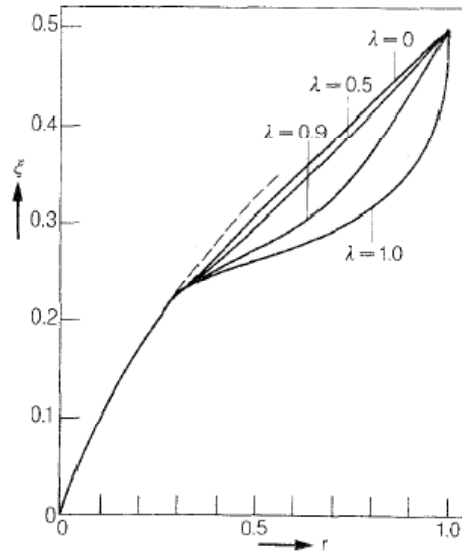


Figure 2-9. Fractional depth (ξ) versus density ratio (r) (Keller & Chyou 1991).

Grobelbauer et al. (1993) conducted lock-exchange flow experiments with gases of density ratios down to 0.046. They used an unevenly divided horizontal channel of half height ($h = 0.15$ m). They used various combinations of helium, air, argon and CO_2 gases for their experiment.

Klemp et al. (1994) calculated the behavior of lock exchange gravity current using both shallow-water theory and two-dimensional (2-D) numerical simulation. They argued that dissipation must be included in the modeling and an energy conserving gravity current cannot be physically realized based on their theory. They also argued that the maximum achievable depth of the heavier current is $0.347H$, which Benjamin (1968)'s theory gives for the current with the maximum speed and the maximum dissipation. They also explained that the inviscid gravity depth can never be greater than 0.347 of the channel depth. However, Gardner & Crow (1970), Wilkinson (1982), and Keller & Chyou (1991) clearly showed that the air cavity has both the shape and speed predicted by Benjamin's energy conserving gravity current. They argued about the fact that the differences in speeds between the fastest allowable current and Benjamin's energy conserving current are too small to discriminate in an experiment. However, the measurement of the current depth showed that their observations are much closer to the energy conserving value than to the fastest allowable gravity current. In addition, recent research by Shin et al. (2004) showed that there is very slight dissipation in the gravity current.

Parson & Garcia (1998) showed the importance of the Grashof/Reynolds' numbers on the evolution of the gravity current. They found that mixing is intensified at large Reynolds numbers.

Chen & Lee (1999) used Reynolds-averaged Navier-Stokes (RANS) model for lock release flows. The challenge related to the use of RANS models to the gravity current is that practically all these models (RANS) are calibrated for fully developed turbulent flow and are not capable of accurately predicting transition and relaminarization, which is essential for simulating gravity current flow.

Simpson (1999), who extensively reviewed the gravity current, explains that the current moves at an almost constant speed, depending on the depth of the water and the density difference. According to his summary, as the gravity current advances, the current front is formed at the leading edge of the flow and is slightly raised above the bottom surface with intense mixing between the front of the current and its

surrounding. He also explained that the head of the current is approximately two times as deep as the following flow depth. He also said that the characteristic head would control the mixing behavior, current velocity, and current profile. The current induced mixing is considered to be caused by two types of instabilities; (a) billows, and (b) lobes and clefts as shown in Figure 2-10. Billows roll up in the region of velocity shear above the front of the dense fluid, and lobes and clefts are formed by the influence of the ground on the lower part of the leading edge.

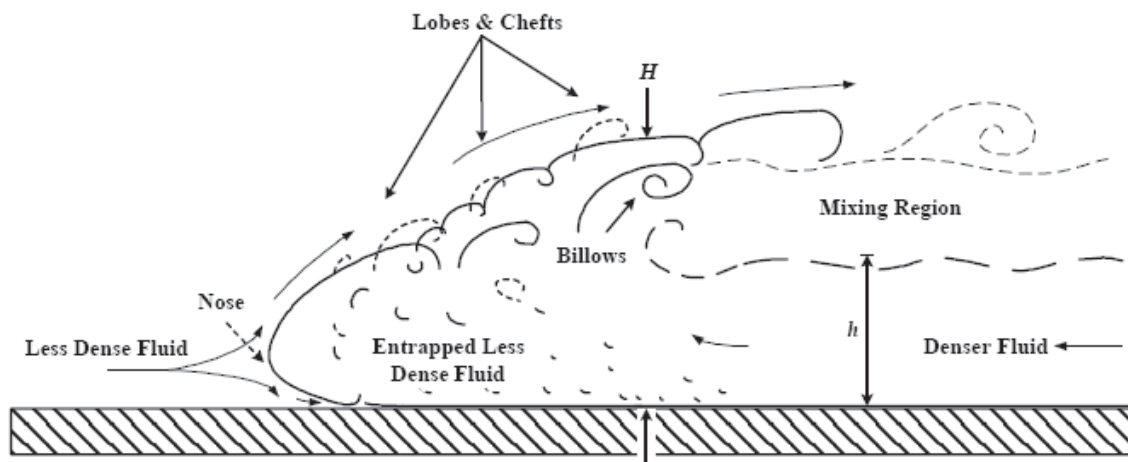


Figure 2-10. Typical gravity current front advancing along a horizontal plane (Mok et al. 2003).

Hartel et al. (2000) showed that the current can be explained using shallow-water theory if sufficiently accurate front conditions are prescribed for the nonhydrostatic flow at the head of the current.

Recently, Lowe et al. (2002) repeated experiments on symmetric intrusions propagating along a sharp density interface conducted by Britter & Simpson (1981). They observed in their experiment that the shape and speed of the intrusion were in good agreement with Benjamin's theory. These experiments suggest that Benjamin's energy conserving gravity currents are observed for Boussinesq, miscible fluids.

Shin et al. (2004) performed experiment with freshwater and sodium chloride for both full and partial lock exchange ($Re > 1,000$, $\gamma > 0.9$, $0.11 < h/H < 1$). In the experiment, they found that the speed of the front head is constant and the shapes of the light and heavy currents are symmetric about the centerline. They measured the speed of the current head and current depth and concluded that Benjamin's energy conserving theory predicts their experiments very well. The measured F_H for the full depth experiment was 0.5 within 5–10% maximum error. The depth of the current ranged between $0.35H$ and $0.5H$. The $0.35H$ represents the maximum dissipation depth predicted by Benjamin's theory, which was obtained by changing gate-valve slope and giving initial disturbance in the flow (See Figure 2-11). Their experiment showed lots of evidence that Benjamin's previous theory describes the phenomena satisfactorily.

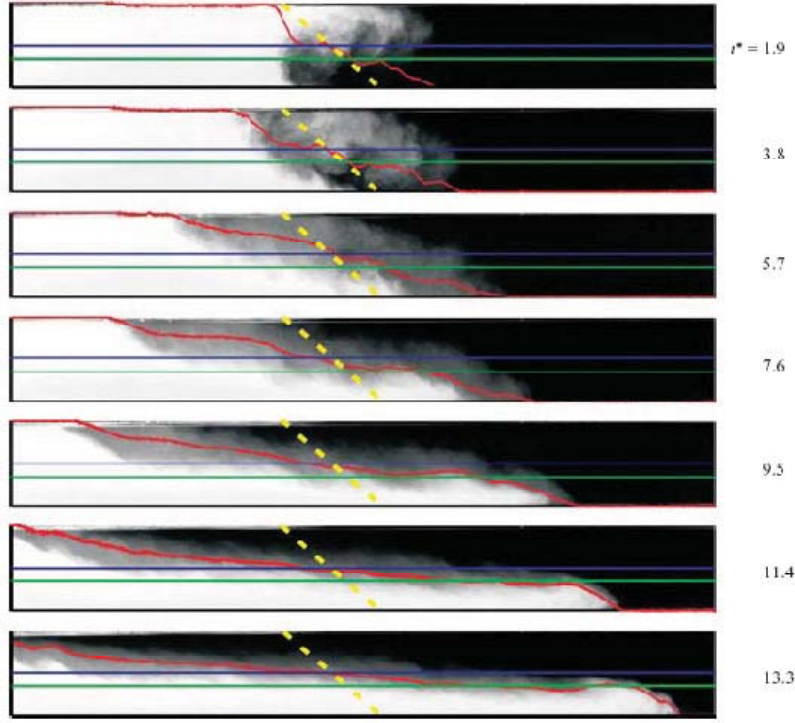


Figure 2-11. Full depth lock exchange experiment with the lock gate at an angle (Shin et al. (2004)).

Shin et al. (2004) also expanded Benjamin's model to the partial lock exchange cases. In their theory, they argued that energy and momentum can be transferred along the interface by internal waves. They showed that energy and momentum can be transferred towards the current front for partial depth locks less than about $0.76H$, but for deeper locks, the current travels faster than long interfacial waves. So, he suggested that for lower fractional depths, Benjamin's theory be modified to allow energy transfer. For partial depth cases (See Figure 2-12), based on the mass and momentum conservation, he obtained the expression

$$\frac{U^2}{gH} = \left(\frac{(\rho_2 - \rho_1)D(D-h)(H-h)}{2hH(\rho_2(H-h) + \rho_1h)} \right). \quad (2-16)$$

By applying energy conservation assumption, they obtained the solution

$$h = \frac{D}{2}. \quad (2-17)$$

Substituting Equation (2-17) into Equation (2-16) gives

$$\frac{U^2}{gH} = \left(\frac{(\rho_2 - \rho_1)D(2H-D)}{2H(\rho_2(2H-D) + \rho_1D)} \right). \quad (2-18)$$

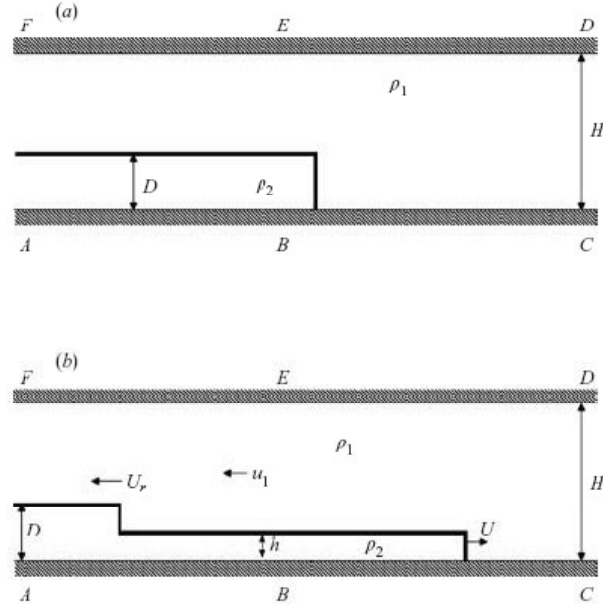


Figure 2-12. Schematic of a partial-depth lock exchange in a channel (a) before release and (b) after release (Shin et al. [2004]).

The above energy-conservation solution was derived without using the Boussinesq approximation. Therefore, it is theoretically valid for any pair of densities; however, Shin et al. (2004) was not sure if it is valid for non-Boussinesq cases. For the Boussinesq cases, Equation (2-18) can be rearranged as

$$F_H = \frac{U}{\sqrt{g'H}} = \frac{1}{2} \sqrt{\frac{D}{H} \left(2 - \frac{D}{H} \right)}. \quad (2-19)$$

In the limit of full depth case ($D=H$), Equation (2-19) reduces to Benjamin's theory (Equation (2-10)). Shin et al. (2004) compared their experimental data with the model, and showed very good agreement between them. They also argued that Benjamin's theory cannot apply for partial depth problem with $D < 0.76H$. For the gravity current in a deep ambient fluid, they suggested

$$F_h = \frac{U}{\sqrt{g'h}} = 1. \quad (2-20)$$

Lowe et al. (2005) performed experiments and modeling for the entire density ratio range. They also repeated Keller & Chyou's (1991) theory, and derived another solution that involves only an expansion wave connecting the two gravity currents. To validate the models, they used their experimental data and Birman et al. (2005)'s computational solutions employing a combination of spectral and compact finite-difference methods. Their comparisons indicated that the theory without the bore gives the best agreement. They showed that the speeds of the current front were still constant for the non-Boussinesq cases, but the heavier current traveled faster than the light current (see Figure 2-13). The light non-Boussinesq current traveled at about the same speed as the Boussinesq current. The symmetry was also lost for the Boussinesq cases. But the depths of the leading parts of the two currents were close to the half depth of the fluid.

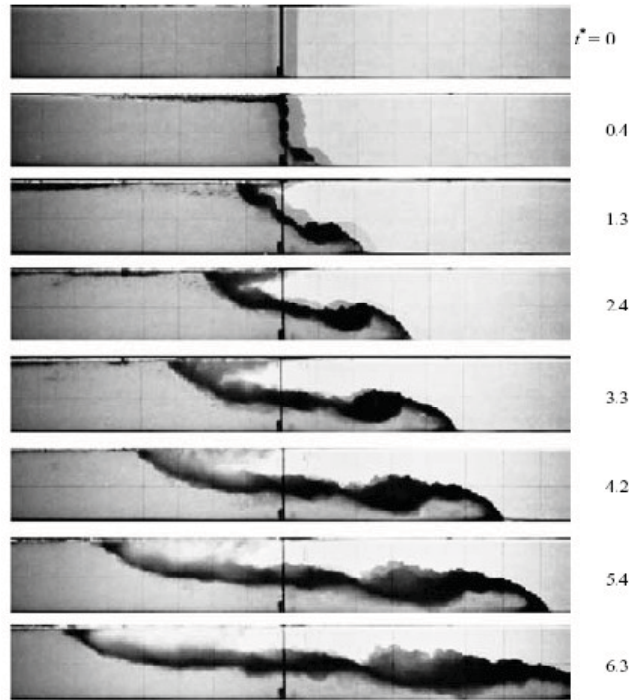


Figure 2-13. Lock exchange experiment for non-Boussinesq cases ($\gamma = 0.681$).

Based on Keller & Chyou's (1991) observations and suggestions, there are two possible flow configurations for the non-Boussinesq lock-exchange flow (Lowe et al. (2005)). Figure 2-14 shows the schematics of the flow configurations. The flow configuration of Figure 2-14(a) occurs when $\gamma^* < \gamma < 1$ and that of Figure 2-14(b) occurs when $0 < \gamma < \gamma^*$. The speeds of the front are summarized below for each case (Lowe et al. (2005)). Lowe et al. (2005) suggested the critical density ratio (γ^*) has the value 0.281.

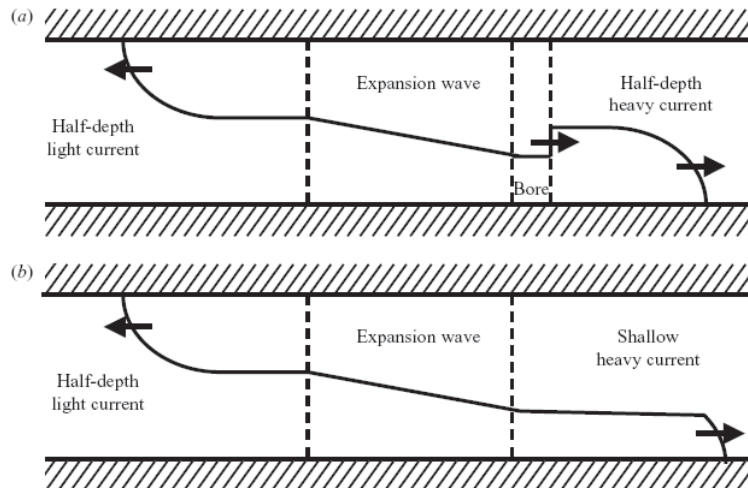


Figure 2-14. Schematic of two lock exchange configuration for non-Boussinesq flow.

(a) $\gamma^* < \gamma < 1$.

The speed and height of the left-propagating current are given by Benjamin's energy conserving current theory as

$$U_L = \frac{1}{2} \sqrt{(1 - \gamma) g H} \quad (2-21)$$

$$h_L = \frac{1}{2} H. \quad (2-22)$$

Figure 2-15 shows the comparisons of the light current for various density ratios (Lowe et al. (2005)). In this figure, solid line is the value calculated by Equation (2-21), and the points are experimental data obtained by previous investigations (Grobelaue et al. (1993), Keller & Chyou (1991), Birman et. al (2005)). The Reynolds numbers of the experiments varies from 10,000 to 100,000. Therefore, the results of Figure 12 shows that the speeds of the speeds of light current is independent of Re number and the model is in good agreement with the experimental data.

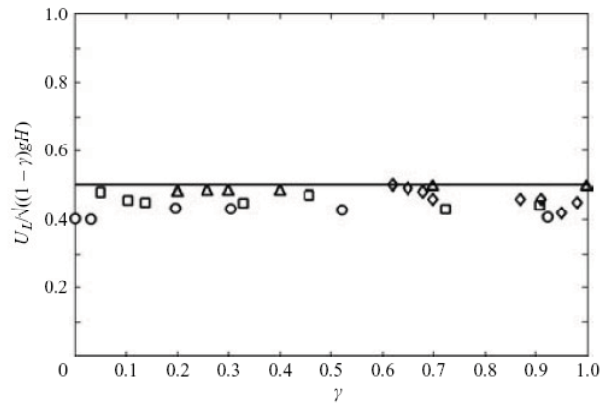


Figure 2-15. Speed of the light current for various density ratios (Lowe et al. (2005)).

(b) $0 < \gamma < \gamma^*$

For the right-propagating current, the speed and the depth are expressed by

$$U_H = \frac{1}{2} \sqrt{\frac{(1 - \gamma)}{\gamma} g H} \quad (2-23)$$

$$h_H = \frac{1}{2} H \quad (2-24)$$

The speed of the left-propagating current is the same as that expressed by Equation (2-21). However, the heavy current has the different speeds calculated as

$$U_H = \sqrt{(1 - \gamma) g H} \left[\frac{1}{\gamma} \frac{h_H}{H} \left(2 - \frac{h_H}{H} \right) \frac{1 - h_H / H}{1 + h_H / H} \right]^{1/2}. \quad (2-25)$$

Figure 2-16 shows the comparisons of the speeds of the heavy currents for various density ratios. The theory in this figure shows good predictions for $\gamma > 0.281$, but for less than that, the model over-predicts the experimental results a little bit. Figure 2-17 shows the comparisons of the theoretical front height and the experimental data (Lowe et al. 2005).

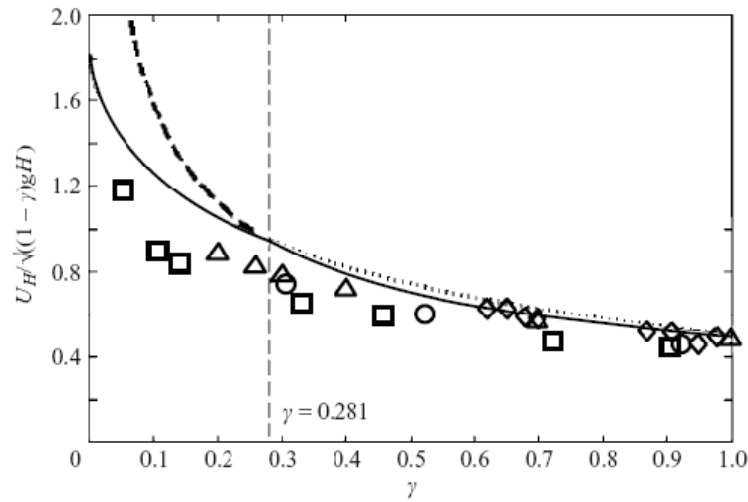


Figure 2-16. Speeds of the heavy currents (Lowe et al. 2005).

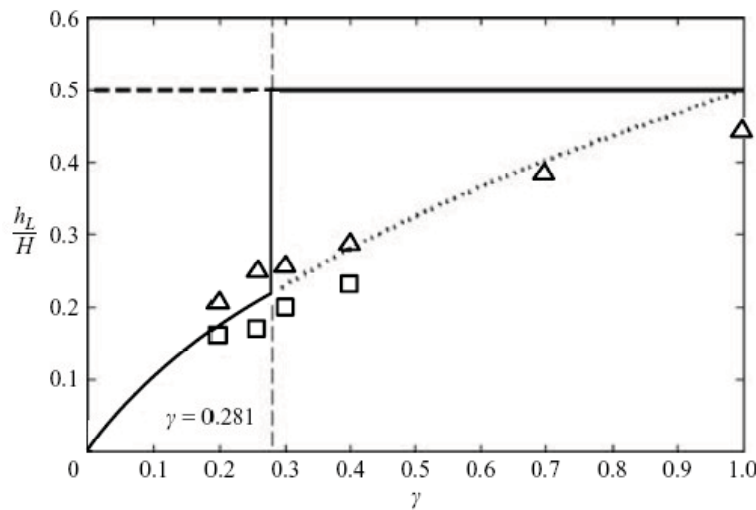


Figure 2-17. Flow depth of the heavy current (Lowe et al. 2005).

Etienne et al. (2005) performed direct numerical simulation for the exchange flow of large density ratios (See Figure 2-18), and they compared the calculation results with the experimental data provided by Grobelbauer et al. (1993). Their simulation using a dynamic mesh adaptation covered the whole density ratio of the experiments and showed very good agreement with the experimental front velocities and Froude number variations.

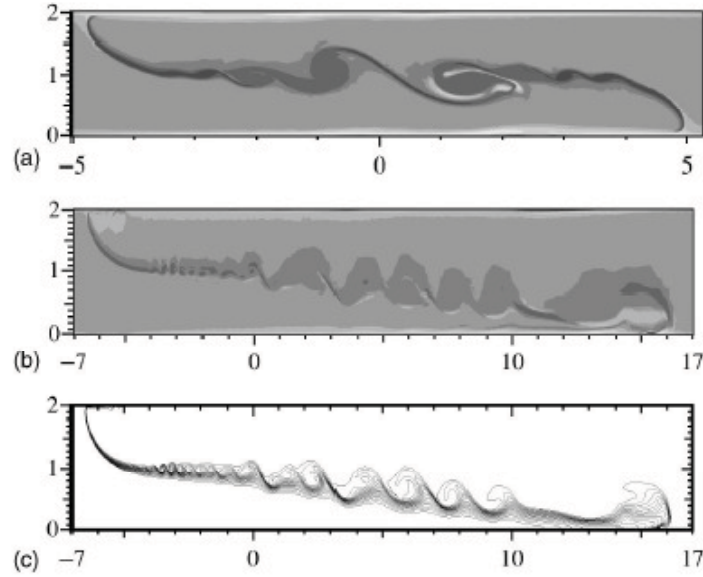


Figure 2-18. Nondimensional vorticity maps for the steady flow by DNS (Etienne et al. 2005).

Eugeniy et al. (2007) argued that the solution by Shin et al. (2004) is valid only at sufficiently large values of the Reynolds number in which the viscous effect is not important. They carried out some experiments on the propagation speed of gravity currents at moderate values of gravity Reynolds numbers ($1,600 < \text{Re} < 28,000$), and developed a semi-empirical model to predict the front propagation speed for various Re number ranges. Their model showed good agreement with the experimental results, but the applicability of such approach to general cases of decelerating flows with dissipation is still an open issue. They recommend

$$Fr(\alpha, \xi, \text{Re}) = \frac{U_H}{(g'h)^{1/2}} = \left[\left(\frac{C\xi}{\text{Re}} \varphi(\alpha) \right)^2 + (1 - \alpha) \right]^{1/2} - \frac{C\xi}{\text{Re}} \varphi(\alpha) \quad (2-26)$$

$$\varphi(\alpha) = \frac{1 - \alpha}{\alpha^{5/2}} \left[1 + \left(\frac{\alpha}{1 - \alpha} \right)^3 \right] \quad (2-27)$$

where

$$\alpha = h / H \quad (2-28)$$

$$\text{Re} = \left(\frac{g'H^3}{\nu^2} \right)^{1/2} \quad (2-29)$$

$$\xi = L / H \quad (2-30)$$

$$C = 2.4 \text{ (recommended by Eugeniy et al. (2007)).} \quad (2-31)$$

2.3 Analytical Estimations for VHTR Air-ingress Accident

One of the main objectives of Task 2 is to identify what is the most important mechanism in the air-ingress process. As already described in Section 2.1, the air-ingress scenario is divided into four steps: (1) depressurization, (2) stratified flow in pipe (Stage 1), (3) stratified flow into reactor core (Stage 2), and (4) overall natural circulation (See Figure 2-2). The depressurization process is dominated by forced convection driven by large pressure difference. There is no argument that the dominant mechanism in the depressurization step is forced convection. However, for two stratified flow steps (Stage 1 and Stage 2), there are still some disagreement among the researchers about the detailed understandings and interpretations of the phenomena. This section therefore focuses on the post-depressurization process.

As previously mentioned in this report, there are two important physical mechanisms mainly affecting air-ingress process after depressurization: molecular diffusion and density gradient driven stratified flow. To compare the relative importance of these mechanisms, time scales were calculated for each at the different air-ingress steps. First, the relative time scales were estimated for molecular diffusion and density gradient driven stratified flow, and then they were compared to each other. If the time scale is larger, it indicates that the mechanism is relatively slower and thus less important than the other. If the time scale is smaller, it indicates that the mechanism is faster and can be considered more important. The time scale comparisons thus provide a qualitative indication of which mechanism is more important. All the analytical calculations in this section are based on a simplified version of the gas turbine modular helium reactor (GT-MHR) 600 MW ‘reference’ design.

2.3.1 Time Scale Comparisons in Stratified Flow—Stage 1

Figure 2-19 shows the schematics of Stage 1, which follows the depressurization process. In Stage 1 there are two air-ingress mechanisms: density gradient driven stratified flow and molecular diffusion. The density gradient driven stratified flow, known as gravity current, is driven by the density differences between air (reactor outside) and helium (reactor inside) in the VHTR. In this case, the heavy gas (air) intrudes into a light gas (helium) along with the hot-leg bottom. On the other hand, molecular diffusion is generated by concentration gradient of air between the reactor’s inside and outside.

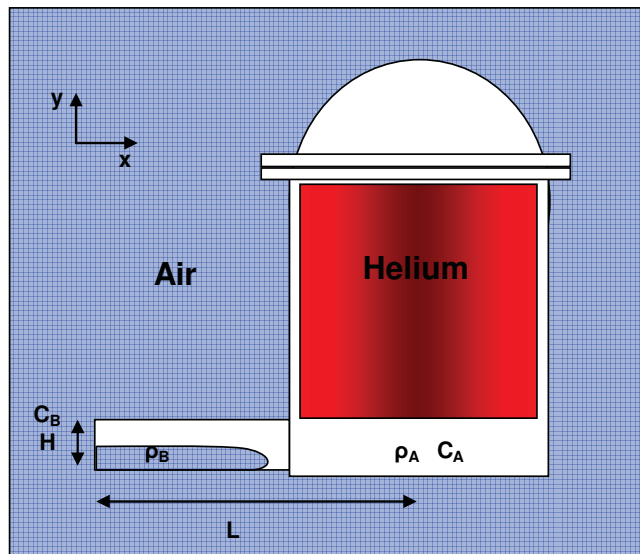


Figure 2-19. Schematic of Stage 1 (post-depressurization).

To compare the time scales of the stratified flow and the diffusion process, the species transport equation was adopted (Welty et al. 1984) as

$$\frac{\partial C_A}{\partial t} = -v \cdot \nabla C_A + D_{AB} \nabla^2 C_A \quad (2-32)$$

where

C_A = gas concentration (k-moles/m³)

t = time (sec)

v = velocity (m/s)

D_{AB} = diffusion coefficient (m²/s).

Since the y-directional flow is ignorable compared to x-direction in Figure 2-19, only x-directional flow were taken into consideration. Then, Equation (2-32) is reduced to

$$\frac{\partial C_A}{\partial t} = -U_x \frac{dC_A}{dx} + D_{AB} \frac{d^2 C_A}{dx^2} \quad (2-33)$$

where

U_x = velocity in x-direction (m/s).

In Equation (2-33), the term in the left-hand side represents the concentration variations with time. The first term and the second term in the right-hand side represent contributions of convection and diffusion for species transport, respectively.

From Equation (2-33), the scaling formula can be obtained

$$\frac{C_A}{\Delta t} \sim U \cdot \frac{C_A}{L_1} + D_{AB} \frac{C_A}{L_2^2} \quad (2-34)$$

where

Δt = overall time scale (sec)

L_1 = length scale of convection (m)

L_2 = length scale of diffusion (m)

In this equation, the symbol, (\sim) means that the left-hand side and the right-hand side have the same order of magnitude. Equation then (2-34) reduces to

$$\frac{1}{\Delta t} \sim \frac{1}{L_1 / U_x} + \frac{1}{L_2^2 / D_{AB}} \quad (2-35)$$

Therefore, the time scales for the convection (stratified in this case) and the diffusion can be defined by

$$\Delta t_{gc} \sim L_1 / U_x, \quad (2-36)$$

and

$$\Delta t_d \sim L_2^2 / D_{AB}. \quad (2-37)$$

(a) Estimation of Stratified Time Scale (Δt_{gc}) in Stage 1

In this section, the time scale for the stratified flow has been estimated in Stage 1. According to Equation (3-36), the velocity (U_x) and the length (L_l) should be first determined in order to estimate the stratified flow time scale in Stage 1. The speed of the gravity current in the heavy side is generally determined by the following two equations as described in Section 2.2 (Lowe et al. 2005).

(i) $\gamma^* < \gamma < 1$

$$U = \frac{1}{2} \sqrt{\frac{(1-\gamma)}{\gamma} gH} \quad (2-38)$$

where

U = speed of heavy gravity current (m/s)

γ = density ratio (ρ_1 / ρ_2)

γ^* = critical density ratio (= 0.281 (suggested by Lowe et al. (2005)))

H = channel depth (m).

g = gravity constant (9.8 m²/s).

(ii) $0 < \gamma < \gamma^*$

$$U = \sqrt{(1-\gamma)gH} \left[\frac{1}{\gamma} \frac{h}{H} \left(2 - \frac{h}{H} \right) \frac{1-h/H}{1+h/H} \right]^{1/2} \quad (2-39)$$

where

h = current depth (m).

For the GTMHR reactor design, the maximum density ratio between inside (helium, 900°C, 1 atm) and outside (air, 25°C, 1 atm) of the vessel is estimated to be 0.036 in the air-ingress situation. It means that this flow is in the highly non-Boussinesq flow regime and therefore it will follow Equation (2-39) or Figures 2-20 and 2-21. The channel depth (H) was determined to be 1.5 m based on the GTMHR cross duct design (See Figure 2-22).

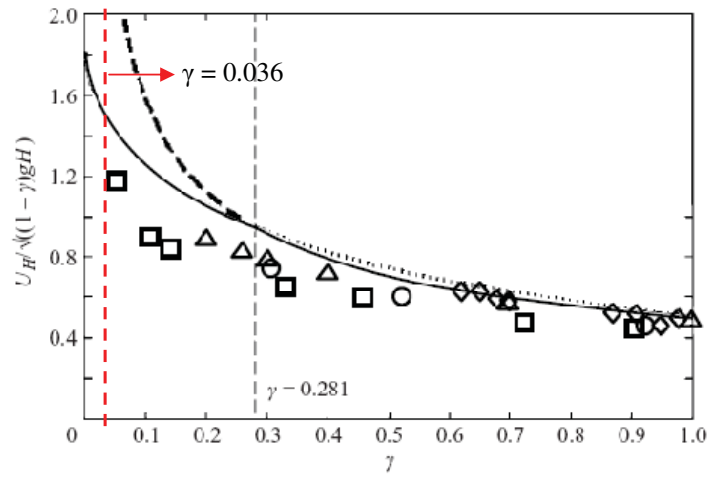


Figure 2-20. Speeds of the heavy currents (Lowe et al. 2005).

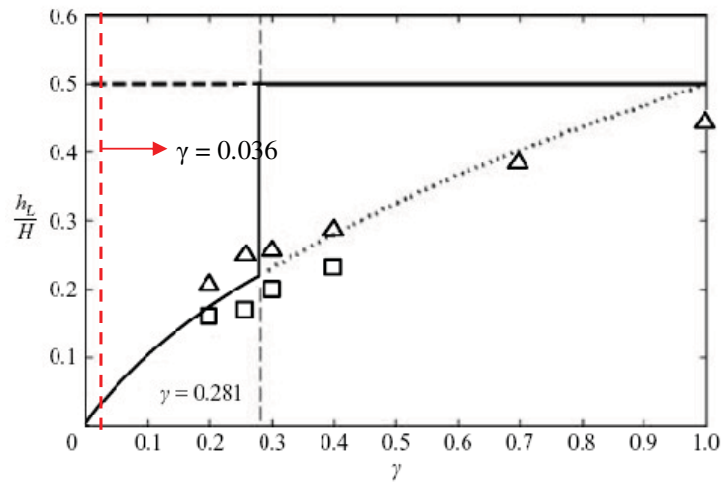


Figure 2-21. Flow depth of the heavy current (Lowe et al. 2005).

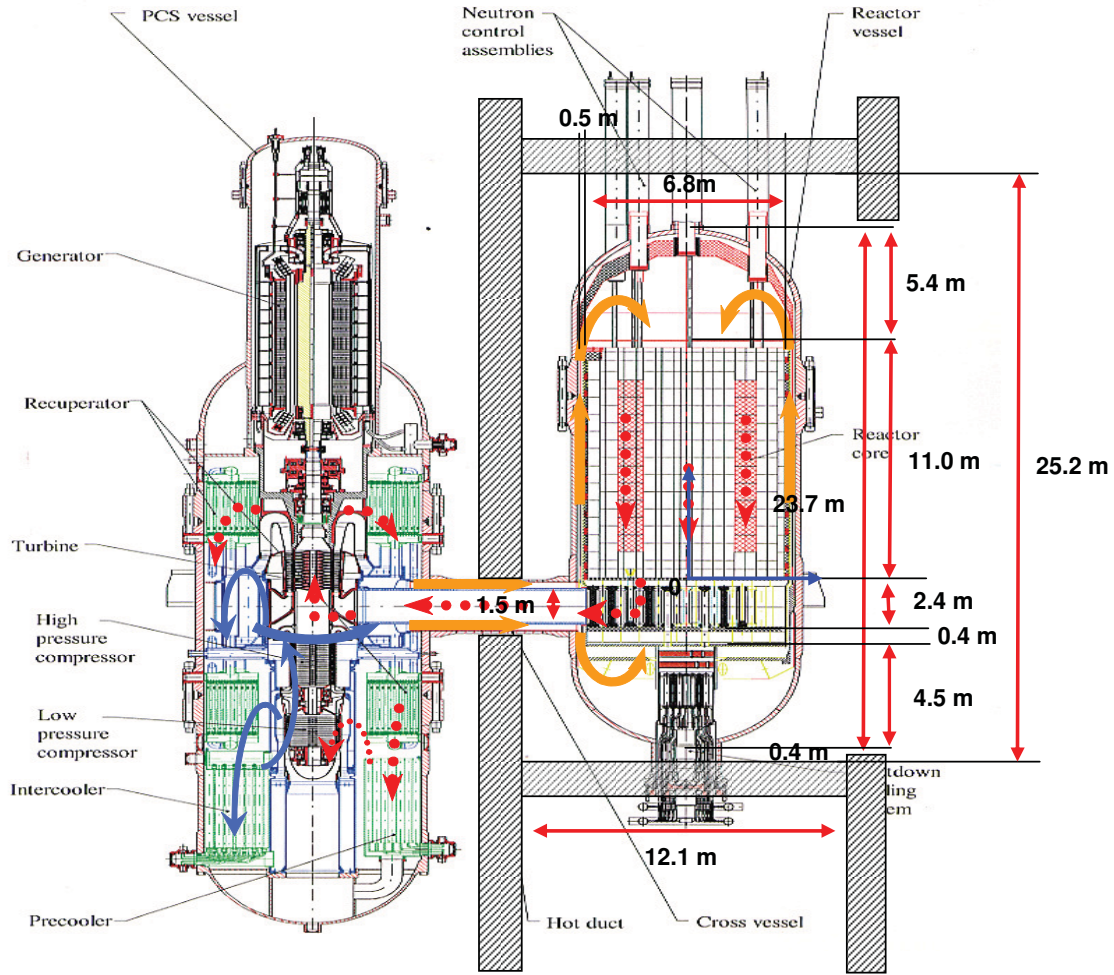


Figure 2-22. Schematics of GTMHR 600 MWth.

To estimate the air current speed (U) and depth (h), the interpolation of the experimental data in Figures 2-21 and 2-22 were used rather than analytical model Equation (3-39). The estimated current speed and depth in the GTMHR design are as follows.

$$U = 5.269 \text{ m/s}, \quad (2-40)$$

and

$$h = 0.06 \text{ m}. \quad (2-41)$$

The Reynolds number of this flow is estimated and the result is

$$\text{Re} = \frac{\rho U h}{\mu} = \frac{5.269 \text{ kg/m}^3 \cdot 5.269 \text{ m/s} \cdot 1.5 \text{ m}}{1.78 \times 10^{-5} \text{ Pa} \cdot \text{s}} = 5.08 \times 10^5. \quad (2-42)$$

The estimated Reynolds number, 5.08×10^5 is quite high value in the gravity current flow, and in these high Re numbers, the viscous effect is not generally important since the inertia force is much larger than

the viscous force. Therefore, the previous model assumptions (energy conservation and inviscid) are valid (Eugeniy et al. 2007) in this high Reynolds number regime ($Re > 10,000$).

To estimate the stratified flow (convection) time scale, the length scale (L_I) was determined to be a distance between the pipe break point and the center of the lower plenum. In this section, a minimum length scale of 3.4 m which is a half of the lower plenum total length in the GTMHR reactor has been arbitrarily determined to be the reference value. However, because the exact break point is flexible in the real situation, the sensitivity of length scales was taken into consideration in the parametric studies. In the parametric studies, the length scale, L_I , was varied from 3.4 m to 8 m. Examples of the time scale calculation for the base case ($L_I = 3.4$ m) include:

- The length scale is

$$L_I = 3.4 \text{ m} \quad (2-43)$$

- The superficial velocity of the air-ingress can be calculated by

$$U_x = \frac{U \cdot h}{H} = 0.21 \text{ m/s} \quad (2-44)$$

- Base on the above numbers, the calculated stratified flow time scale is

$$\Delta t_{gc} \sim L_I / V = 3.4 \text{ m} / 0.21 \text{ m/s} = 19.5 \text{ sec} . \quad (2-45)$$

The physical meaning of this time scale is the duration for the air convective flow to fill one-half of the lower plenum in Stage 1.

(b) Estimation of Diffusion Time Scale (Δt_d) in Stage 1

To calculate the diffusion time scale, the diffusion coefficient (D_{AB}) and length scale (L_2) should be determined. The theoretical expression for the diffusion coefficient for gas pairs of nonpolar, nonreacting molecules (Welty et al. 1984) is

$$D_{AB} = \frac{18.58 \cdot T^{3/2} \left[\frac{1}{M_A} + \frac{1}{M_B} \right]}{P \cdot \sigma_{AB}^2 \Omega_D} \text{ (m/s)} \quad (2-46)$$

where

T = temperature (K)

M = molecular weight (kg/kmol)

P = absolute pressure (atm)

σ_{AB} = collision diameter (Lennard-Jones parameter) (Angstroms)

Ω_D = collision integral.

For air and helium molecules, the diffusion coefficient can be calculated as

$$D_{air-helium} = 7.92 \times 10^{-4} \text{ m}^2 / \text{s} \text{ (at } 900^\circ\text{C, 1 atm).} \quad (2-47)$$

Since the diffusion length scale is not constant during the diffusion process, it is difficult to determine as a single number. For this reason, a different method to calculate the diffusion time scale was used. The main idea is to obtain the equivalent time scale, which has the same physical meaning as the convection time scale. The time scale of the diffusion is physically equivalent to that of the convection, when the average air concentration in the lower plenum becomes one-half of the external air concentration. The local air concentration (C_{Air}) in the lower plenum is mathematically expressed (Welty et al. 1984) as

$$\frac{C_{Air}(z, t) - C_{Air,0}}{C_{Air,s} - C_{Air,0}} = 1 - \operatorname{erf}\left(\frac{z}{2\sqrt{D_{air-helium}t}}\right) \quad (2-48)$$

where

z = distance from air source (m)

t = time (sec)

$C_{Air}(z, t) = C_{A,0}$ at $t = 0$, for all z

$C_{Air}(z, t) = C_{A,s}$ at $z = 0$, for all t

$C_{Air}(z, t) = C_{A,0}$ as $z \rightarrow \infty$, for all t .

The definition of the error function in Equation (2-48) is

$$\operatorname{erf}(x) = \frac{2}{\pi} \int_0^x e^{-t^2} dt. \quad (2-49)$$

From Equation (2-48), the average concentration in the lower plenum can be expressed as

$$\left(\frac{C_{Air}(z, t) - C_{Air,0}}{C_{Air,s} - C_{Air,0}} \right)_{\text{average, LowerPlenum}} = \frac{1}{D_{LP}} \int_{\text{LowerPlenum}} 1 - \operatorname{erf}\left(\frac{z}{2\sqrt{D_{AB}t}}\right) \cdot dz \quad (2-50)$$

where

D_{LP} = diameter of the lower plenum (m).

Therefore, the time scale of the diffusion can be calculated by solving the following equation.

$$\frac{1}{D_{LP}} \int_{\text{LowerPlenum}} 1 - \operatorname{erf}\left(\frac{z}{2\sqrt{D_{AB}t}}\right) \cdot dz = 0.5 \quad (2-51)$$

In this work, the solution of Equation (2-51) was calculated using MATLAB. The result of the diffusion time scale is as

$$t = \Delta t_d = 1.29 \times 10^4 \text{ sec} \quad (2-52)$$

(c) Comparisons of Time Scales

Based on the results of Equation (2-45) and Equation (2-52), the convection time scale ($=19.5$ sec) is estimated to be about 785 times larger than the diffusion time scale ($=1.29 \times 10^4$ sec), which means that the convection process is at least about 785 times faster than the diffusion process. If the overall time scale is calculated by using Equation (2-35), it is

$$\Delta t \sim 19.5 \text{ sec} . \quad (2-53)$$

Figure 2-23 shows the relation between length-scales and relative time scales ($\Delta t_d/\Delta t_{gc}$). The relative time scale increases linearly with the length scale indicating that the stratified flow is the dominant mechanism in Stage 1, allowing the diffusion mechanism to be neglected.

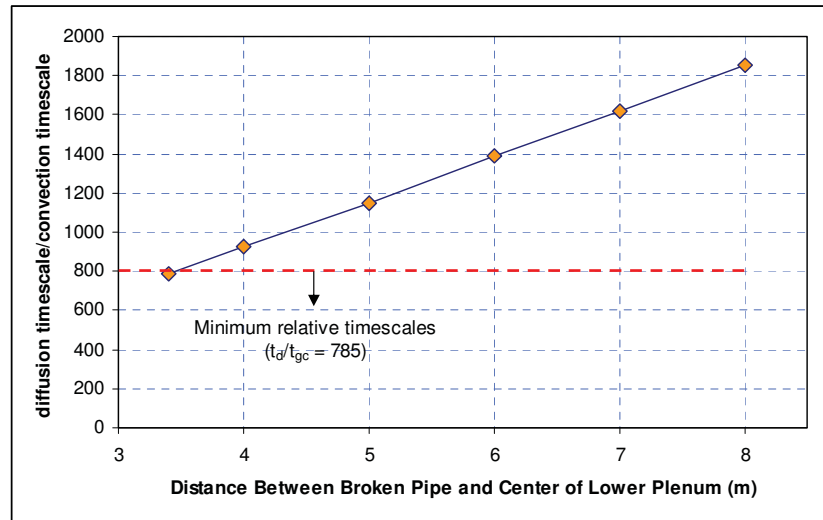


Figure 2-23. Correlation between length scale and relative time scales.

2.3.2 Time Scale Comparisons in Stratified Flow—Stage 2

After air flows into the reactor in Stage 1 by density gradient driven flow, the lower part of the core (lower plenum) is filled with air as shown in Figure 2-24. Once the air occupies the lower plenum, the main driving force which was generated by molecular mass differences (between air and helium) will disappear; however, temperature gradient between inside and outside reactors will still maintain density gradient even though the driving force is weaker than in Stage 1. It finally leads to another stratified flow or a local natural circulation flow. Since the temperature gradient is maintained during the whole air-ingress process, this stratified flow (Stage 2) will be continued until the overall on-set of natural circulation starts.

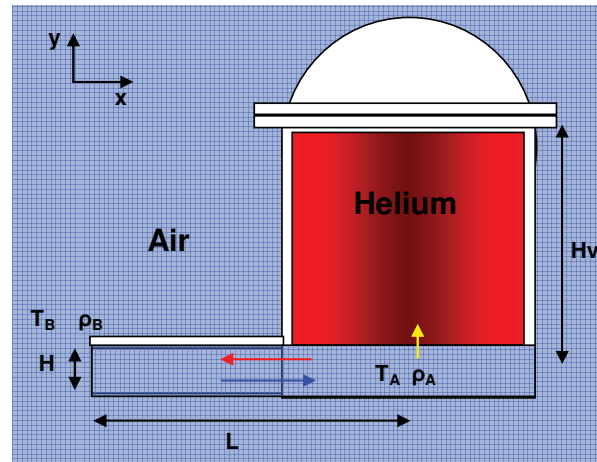


Figure 2-24. Schematics of Stage 2 air-ingress.

In Stage 2, the majority of the inflow (blue arrow in Figure 2-24) is expected to return to the reactor outside (red arrow) through the channel upper part. However, some portion of the flow is expected to be moved into the reactor core (yellow arrow) slowly by a buoyancy force. This buoyancy force is generated when the cold air moves into the lower plenum. If the cold air ingresses into the inside of the reactor, the air will interact with hot supporting structures. The air will be heated and expand, making it less dense than the unexpanded air, giving it a buoyancy force. If the buoyancy force is sufficient to overcome the static head in the core, the air will be able to move into the reactor core. If not, the air-ingress into the core will be controlled solely by molecular diffusion and turbulence mixing. Therefore, pressure build-up in the lower plenum and the static head was compared in the core to estimate the main air-ingress mechanism in Stage 2. It can be simply described as:

- Pressure Build-up (Buoyancy Force) > Hydrostatic Head : Convection Dominant
- Pressure Build-up (Buoyancy Force) < Hydrostatic Head : Molecular Diffusion Dominant.

The pressure build-up was estimated by energy conservation law and previous gravity current correlations described in Section 2.1. In this estimation, the friction loss and local heat transfer were not considered. The temperatures inside the reactor were assumed to be constant throughout the whole core. The temperatures inside and outside of the reactor were assumed to be 900°C and 25°C, respectively. In this temperature condition, the density ratio is estimated to be 0.25 in non-Boussinesq flow regime.

The total kinetic energy of the flow in the lower plenum is defined by

$$K.E._1 = \frac{1}{2} \rho_A \cdot u_A^2 \quad (J/m^3) \quad (2-54)$$

where

ρ_A = density of the flow in the lower plenum (kg/m^3)

u_A = velocity of the flow in the lower plenum (m/s).

In this derivation, it was assumed that the air has enough time to be heated up to the same temperature as the reactor inside. Therefore, the Kinetic energy of the air in the lower plenum can be derived by inserting Equation (2-38) into Equation (2-54) and the mass conservation law as

$$K.E._1 = \frac{1}{2} \rho_A \cdot \left(\frac{1}{4} \cdot \left(\frac{1-\gamma}{\gamma} \right) \cdot g \cdot H \right) / \gamma^2. \quad (2-55)$$

Therefore, Equation (2-55) reduces to

$$K.E._1 = \frac{\rho_A \cdot g \cdot H}{8} \cdot \left(\frac{1-\gamma}{\gamma^3} \right). \quad (2-56)$$

The Kinetic energy of the returning flow in the horizontal pipe can then be estimated by Equation (2-21) as

$$K.E._2 = \frac{1}{2} \rho_A \cdot \left(\frac{1}{4} \cdot (1-\gamma) \cdot g \cdot H \right). \quad (2-57)$$

Therefore, Equation (2-57) reduces to

$$K.E._2 = \frac{\rho_A \cdot g \cdot H}{8} \cdot (1 - \gamma). \quad (2-58)$$

The pressure build-up can be estimated by energy conservation equation

$$\Delta P = K.E._1 - K.E._2 = \frac{1}{8} \cdot (\rho_A \cdot g \cdot H \cdot (1 - \gamma)) \cdot \left(\frac{1}{\gamma^3} - 1 \right). \quad (2-59)$$

In this estimation, effects of viscous dissipation and potential head were neglected.

The static head of the core can be calculated by the following hydraulic head equation.

$$\text{Hydrostatic Head} = (\rho_{core} - \rho_{riser}) \cdot g \cdot H_v \quad (2-60)$$

where

$$\rho_{core} = \text{density of the coolant in the core (kg/m}^3\text{)}$$

$$\rho_{riser} = \text{density of the coolant in the riser (kg/m}^3\text{)}.$$

In this section pressure build-up and static head was estimated for two different designs, one being the GTMHR 600 MWth reactor and the other is the NACOK (an acronym of German words that stand for “Natural Convection in the Core with Corrosion”) experiment (Schaaf et al. [1998])). Table 2-1 summarizes the results. In the GTMHR, the pipe diameter is 1.5 m and the core height is 11 m. It has quite large pipe diameter but relatively shorter core height; however, the NACOK experiment has a 0.125 m pipe diameter and 7.334 m core height, which is a relatively large height compared to the pipe diameter. The pipe diameter is closely related to the pressure build-up as shown in Equation (2-59). As the diameter increases, the pressure build-up increases proportionally. On the other hand, the core height is related to the static head (See Equation (2-60)) where if the core height is increased, the static head is increased as well. According to the estimation in Table 2-1, the pressure build-up (24.18 Pa) in a GTMHR is larger than the average static head (10.01 Pa), indicating that the air will move into the core in Stage 2 for the GTMHR design. On the other hand, the pressure build-up (1.101 Pa) in the NACOK experiment is much smaller than the average static head (9.6 Pa), indicating that the air won’t be able to move into the NACOK ‘core’. The process therefore appears to be controlled by molecular diffusion in the NACOK experiment, even though there is a small stratified flow generated by the temperature gradient. This physical interpretation is consistent with previous NACOK experimental data.

Table 2-1. Comparisons of pressure build-up and static head for GTMHR and NACOK experiment.

Parameters	GTMHR	NACOK
Air Density Ratio (γ)	0.253	0.323
Pipe Diameter (D)	1.5 m	0.125 m
Core Height (H_v)	11 m	7.334 m
Pressure Build-up (dP)	24.18 Pa	1.101 Pa
Static Head	10.01 Pa	9.6 Pa

The criteria of air movement into the core in Stage 2 was developed based on Equation (2-59) and Equation (2-60). According to the previous description, the criterion for the air movement into the core is

$$\Delta P > \text{Hydrostatic Head} \quad (2-61)$$

Therefore, Equation (2-61) can be rewritten as

$$\frac{\Delta P}{\text{Hydrostatic Head}} > 1. \quad (2-62)$$

If Equation (2-59) and (2-61) are inserted into Equation (2-62), the result is

$$\Pi_2 = \frac{1}{8} \left(\frac{H}{H_v} \right) \cdot \left(\frac{\rho_A}{\rho_{Core} - \rho_{Riser}} \right) \left(\frac{(1-\gamma)(1-\gamma^3)}{\gamma^3} \right) > 1. \quad (2-63)$$

The physical meaning of nondimensional parameter, Π_2 in Equation (2-63) is the ratio of the buoyancy force (pressure build-up) to the static head in Stage 2. If this value is larger than 1, the air will have enough buoyancy force to generate flow into the core. On the other hand, if the value is less than 1, the air will not have enough buoyancy force to generate flow into the core. The implication of this with respect to air-ingress mitigation is that decreasing the Π_2 value is beneficial in the mitigation of the air-ingress process. The following modifications can, in theory, be shown to decrease the Π_2 value,

- Decreasing the diameter of the horizontal pipe (H),
- Increasing the height of the core (H_v),
- Increasing the $\rho_{Core} - \rho_{Riser}$ which can be achieved by increasing the riser temperature in the accident conditions or decreasing the core temperature in the accident conditions, and
- Increasing the density ratio (γ), which can be achieved by increasing cavity temperature or decreasing lower plenum temperature.

(a) Calculation of Convection Time Scale (Δt_c)

From the comparisons between buoyancy force and static head, it was found that the air will move into the reactor core by convective force. However, to estimate the relative importance of the mechanisms between molecular diffusion and the convective flow, the speed of the air movement into the core should be quantified. To estimate this velocity, three equations were set up for the following three flow paths (See Figure 2-25).

- Path-1: from core top to reactor outside
- Path-2: from core bottom to core top
- Path-3: circulation flow in the lower plenum

The Path-1 (See Figure 2-25) can be expressed by the following Bernoulli's equation if the heat transfer effect in the riser is ignored.

$$P_1 + \frac{1}{2} \rho_1 \cdot u_1^2 = P_2 + \frac{1}{2} \rho_2 \cdot u_2^2 + \rho_A \cdot g \cdot H_v \quad (2-64)$$

Since there are no heat-transfer and very slight pressure differences between locations 1 and 2, the densities can be assumed to be almost the same between those two locations.

$$\rho_1 \approx \rho_2 \quad (2-65)$$

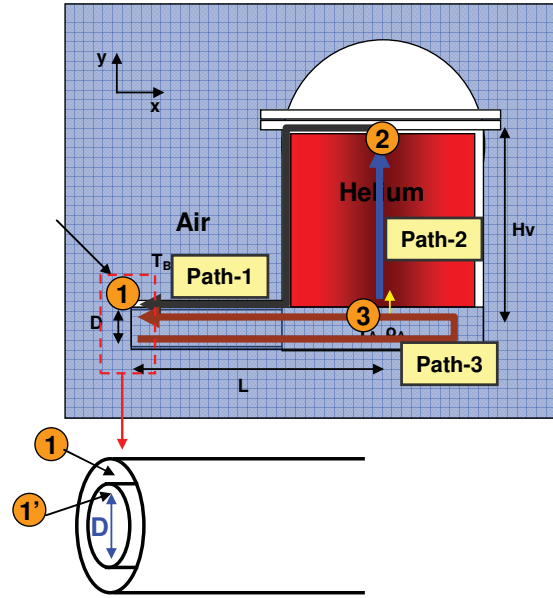


Figure 2-25. Schematics of the VHTR reactor for analytical modeling.

Therefore, through mass conservation, the following can be obtained:

$$u_1 A_1 = u_2 A_2 \quad (2-66)$$

Since the friction effect cannot be ignored in the core, Path-2 (See Figure 2-25) can be expressed by

$$P_3 - P_2 = 32 \frac{\mu \cdot u_{avg} \cdot H_v}{D^2} + \text{hydrostatic head} \quad (2-67)$$

Since it was assumed no heat transfer in the core region (uniform temperature), the velocities in the core and location 2 (core top) may be considered to be the same as

$$u_{avg} \approx u_2 \quad (2-68)$$

Depending on the core density (ρ_c), which is an average density of the core fluids, the hydrostatic head can be expressed by

$$\text{hydrostatic head} = \rho_c \cdot g \cdot H_v \quad (2-69)$$

Path-3 was modeled very carefully. Figure 2-26 shows the assumed flow pattern in the lower plenum where there is a counter current flow between upper and lower parts of the region and the lower flow changes its direction at the right side of the core. The contour plot in this figure shows the flow angle in the lower plenum. Blue indicates a flow in the x direction, red indicates the negative x direction. This plot supports that the flow direction in the modeling is reasonably assumed.

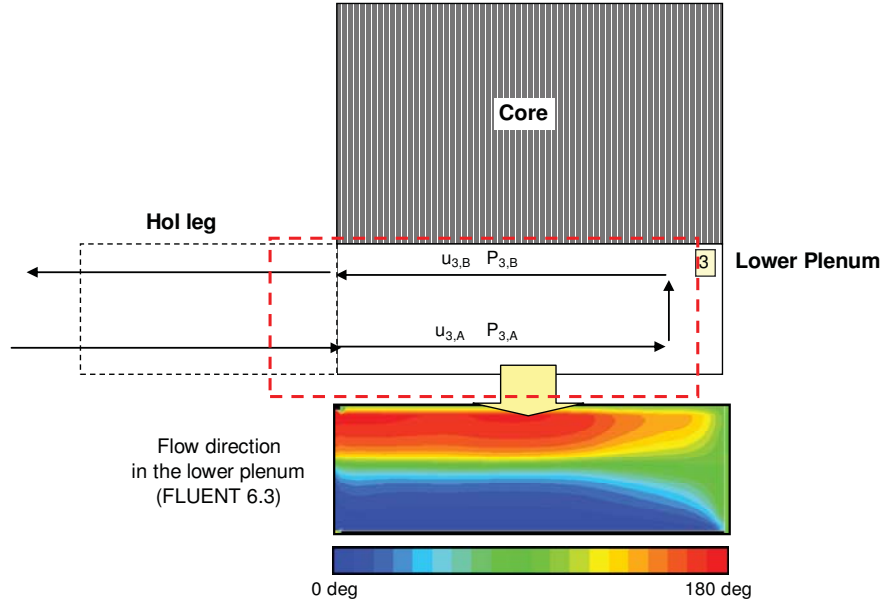


Figure 2-26. Circulation pattern in the location 3 (lower plenum).

This modeling assumes that the kinetic energy difference between the lower and upper flows is converted to the pressure energy with negligible static head differences. The concept of this method is basically the same as that of pressure build-up modeling. The derivation provides

$$P_1' - P_3 = P_1 + \frac{1}{8} \rho_3 \cdot g \cdot D \cdot (1 - \gamma) \cdot \left(\frac{1}{\gamma^3} - 1 \right). \quad (2-70)$$

In this derivation, the hydrostatic head differences between location 1 and location 1' (See Figure 2-25) was ignored. Therefore it cannot be assumed that the static pressure in location 1 and location 1' will be the same. If the effect of the energy loss for turning the direction of the fluid (See Figure 2-26) is considered, Equation (2-70) can be expressed as

$$P_1 - P_3 = \frac{1}{8} \rho_3 \cdot g \cdot H \cdot (1 - \gamma) \cdot \left(\frac{1}{\gamma^3} - 1 \right) \cdot \eta. \quad (2-71)$$

In this equation, the symbol η represents the efficiency of energy conversion. From Equations (2-67), (2-69), and (2-71), to obtain

$$\begin{aligned} P_3 - P_2 &= 32 \frac{\mu \cdot u_2 \cdot H_v}{D^2} + \rho_c \cdot g \cdot H_v \\ &= \frac{1}{8} \rho_3 \cdot g \cdot H \cdot (1 - \gamma) \cdot \left(\frac{1}{\gamma^3} - 1 \right) \cdot \eta - \frac{1}{2} \rho_2 \cdot \left(\left(\frac{A_2}{A_1} \right)^2 - 1 \right) \cdot u_2^2 + \rho_A \cdot g \cdot H_v. \end{aligned} \quad (2-72)$$

Equation (2-72) can be arranged as

$$C_1 \cdot u_2^2 + C_2 \cdot u_2 + C_3 = 0, \quad (2-73)$$

where

$$C_1 = \frac{1}{2} \rho_2 \cdot \left(\left(\frac{A_2}{A_1} \right)^2 - 1 \right) \quad (2-74)$$

$$C_2 = 32 \frac{\mu \cdot H_v}{D^2} \quad (2-75)$$

$$C_3 = \frac{1}{8} \rho_3 \cdot g \cdot H \cdot (1 - \gamma) \cdot \left(1 - \frac{1}{\gamma^3} \right) \cdot \eta + (\rho_c - \rho_A) \cdot g \cdot H_v \quad (2-76)$$

The core average density (ρ_c) in Equation (2-76) can be defined as (See Figure 2-27):

$$\rho_c = \left(\frac{H_{air}}{H_v} \right) \cdot \rho_{air} + \left(1 - \left(\frac{H_{air}}{H_v} \right) \right) \cdot \rho_{helium} \quad (2-77)$$

where

ρ_{air} = density of air (or heavy) gas

ρ_{helium} = density of helium

H_{air} = height of the air (or heavy gas) in the core

H_v = total core height.

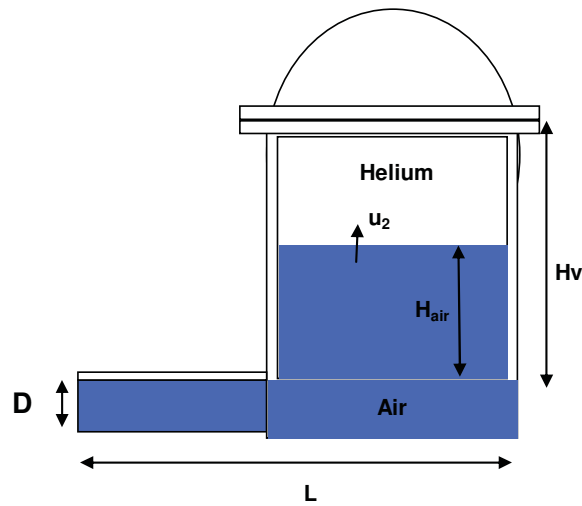


Figure 2-27. A sketch of the phenomena in Stage 2.

Therefore, the speed of the flow in the core can be calculated by

$$u_2 = \frac{-C_2 + \sqrt{C_2^2 - 4C_1 \cdot C_3}}{2C_1} \quad (2-78)$$

If Equation (2-78) is applied to the GTMHR 600 MWth core dimensions, the initial and average speeds of the core flow are calculated to be 0.487 m/s and 0.26 m/s, respectively when the initial core is filled with only helium coolant and $A_2/A_1 = 1$. This speed is decreased with an increase of air height in the core. Figure 2-28 shows a sketch of the phenomena in Stage 2 and the velocity profile calculated by FLUENT 6.3 in the reactor core in the Stage 2 period of the stratified flow. Even though the temperature in the core is not uniform in the model (varying 500 to 950°C), the average velocity (0.3 m/s) in this calculation is the same order as estimated by the simplified analytic solution (~0.26 m/s). Still, further validation work is required afterward.

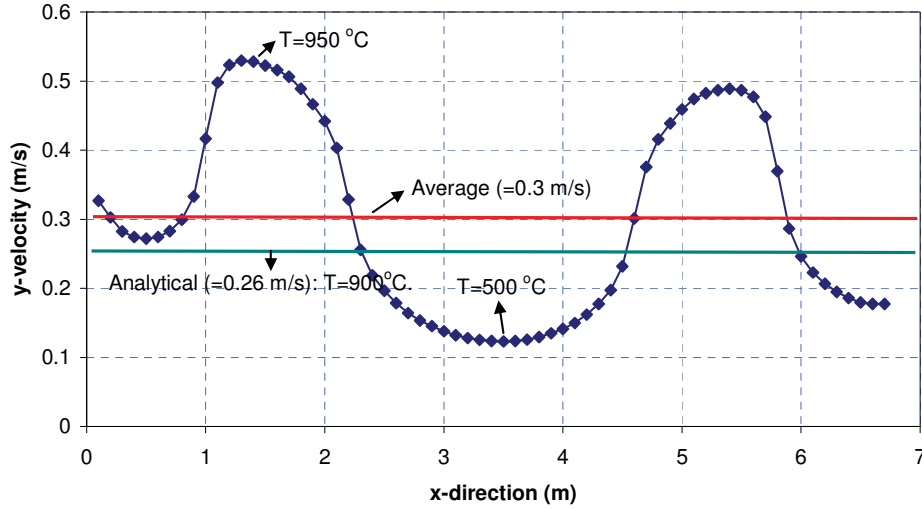


Figure 2-28. Calculated y-velocity profile in the reactor core during Stage 2 (FLUENT 6.3).

Based on the estimated core flow velocity (= 0.26 m/s), the convection time scale by density gradient flow in Stage-2 was estimated as follows:

$$\Delta t_c \sim 42 \text{ sec} \quad (2-79)$$

(b) Calculation of Diffusion Time Scale (Δt_d)

To calculate the diffusion time scale, the diffusion coefficient (D_{AB}) and length scale (L_2) should be determined as done in the previous section. For air and helium molecules, the diffusion coefficient is

$$D_{\text{air-helium}} = 7.92 \times 10^{-4} \text{ m}^2 / \text{s} \text{ (at } 900^\circ\text{C, 1 atm).} \quad (2-80)$$

The diffusion time scale in Stage 2 was calculated by the same method as carried out in Equations (2-50) and (2-51) in the previous section. The calculated time scale of the diffusion process to deliver the same amount of air into the core as the convection did during the convection time scale (= 42 sec) is

$$\Delta t_d \sim 2.7 \times 10^4 \text{ sec (at } 900^\circ\text{C, 1 atm).} \quad (2-81)$$

(c) Comparisons of Time Scales

Based on Equation (2-79) and Equation (2-88), the convection time scale is estimated to be approximately 642-times larger than the diffusion time scale. It means that the convection process is about 642-times faster than the diffusion process. If calculated, the overall time scale is

$$\Delta t \sim 42 \text{ sec .} \quad (2-82)$$

This time scale is the same as the convection time scale, which means that Stage 2 is dominated by a stratified flow process. The diffusion effect may therefore be neglected. The results are summarized in Table 2-2.

Table 2-2. Time scales for the GTMHR (Stage 2).

Parameters	Values
Channel depth (D) (m)	1.5
Core height (H _v) (m)	11
Average core flow velocity by buoyancy force (sec)	0.26
Convection time scale (t _c) (sec) (within H _{air})	42
Diffusion time scale (t _d) (sec)	2.70e4
t _d /t _c	642

2.4 2-D Preliminary Partial Break Analyses by FLUENT Code

The air-ingress caused by a small pipe break is an important issue because it has a higher probability of occurrence than the DEGB. The purpose of this simulation is to (1) determine what mechanism dominates the initiation of air ingress, whether by molecular diffusion or density-gradient induced flow and to (2) find the timing of the natural convection that fills the reactor with air. It is strongly believed that the air ingress mechanism is dependent on the geometry and conditions of the break. This calculation pursues an interest in the air ingress mechanism, the flow path, and the timing of natural convection.

A design basis event (DBE-10) for the failure of a release valve that is less than 10 inch² was investigated. Air ingress analysis of a small pipe break (82 cm²) on the top of the steam generator was assumed (See Figure 2-29). This event has a higher probability of occurrence than other accident scenarios related to the depressurization LOCA and is considered by the General Atomics to be a Design Basis Event.

This analysis is also based on a single failure of the check valve, which can happen when the corrosion materials and graphite particles are stuck into the hinge of the check valve. A 2-D FLUENT model was developed based on the gas turbine modular helium reactor, GTMHR design. The simulation continues, and some preliminary results are presented in this section.

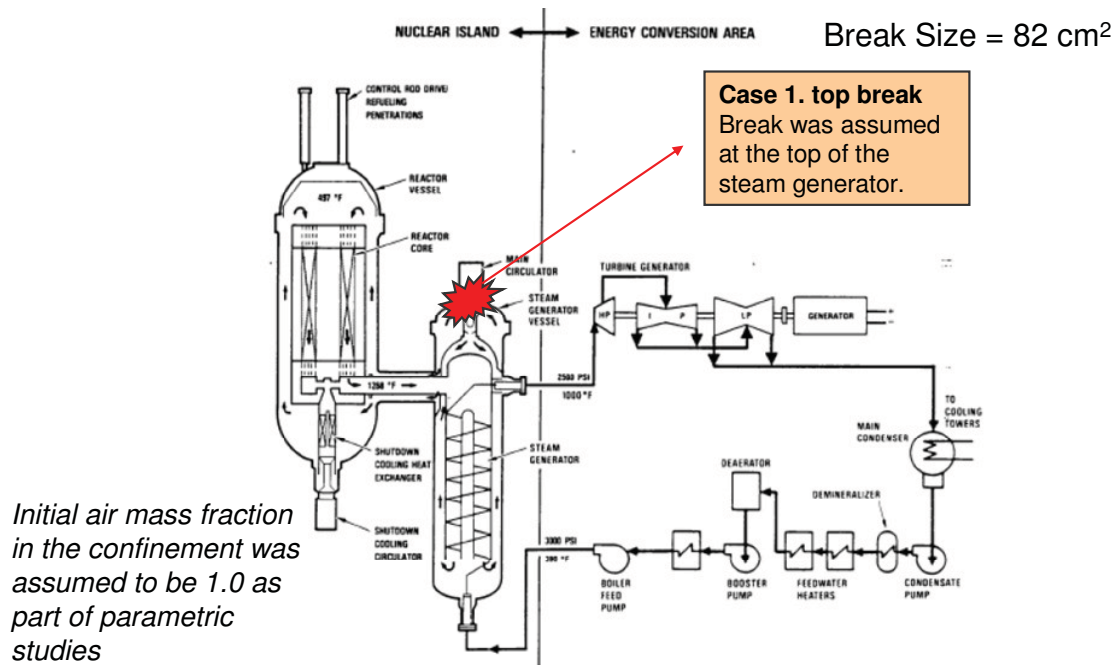


Figure 2-29. VHTR partial break schematic.

FLUENT (Version 6.3) was used with a simplified (2-D) model of the GTMHR into a 2-D geometry that includes GTMHR confinement, a reactor pressure vessel, and a steam generator. The break was assumed to occur at the top of the steam generator, which mimics a small break of the relief valve failure. Initial pressures at the break location were assumed to be the same between reactor inside and outside. The initial temperature distribution was obtained by GAMMA code calculation for depressurization. The options and models adopted in the analyses are summarized as:

- 2-D
- Unsteady
- Segregated solver
- 2nd order accuracy in time and space
- Noniterative time advancement
- Absolute velocity formulation
- Cell based gradient
- Physical velocity (in the porous media formulation)
- Laminar viscous model
- Energy equation solving
- Species transport equation solving
 - Two gas species: Air/Helium
 - Multicomponent diffusion model (same as binary diffusion model in this case)
 - No consideration for thermal diffusion

- Pressure-velocity coupling method : PISO
- Pressure discretization method : PRESTO!
- Momentum : 2nd order upwind
- Species : 2nd order upwind

Figure 2-30 shows the fluent simulation result (10 sec) of the partial break simulation. In this simulation, it was visualized that the air-flow entered into the steam generator by density gradient. The flow, however, was not quite stratified because of the conflict between inflows (air) and outflows (helium). Figure 2-31 shows the velocity profile in the break location; the x-axis represents horizontal locations, and the y-axis represents y-directional velocity. A positive velocity indicates upward flow (helium outflow) and a negative velocity indicates downward flow (air inflow). According to the FLUENT calculation, the average air inflow velocity is about 0.2 m/s while helium outflow is about 0.6 m/s. This velocity gets slower with time, owing to the decrease of density gradient by mixing.

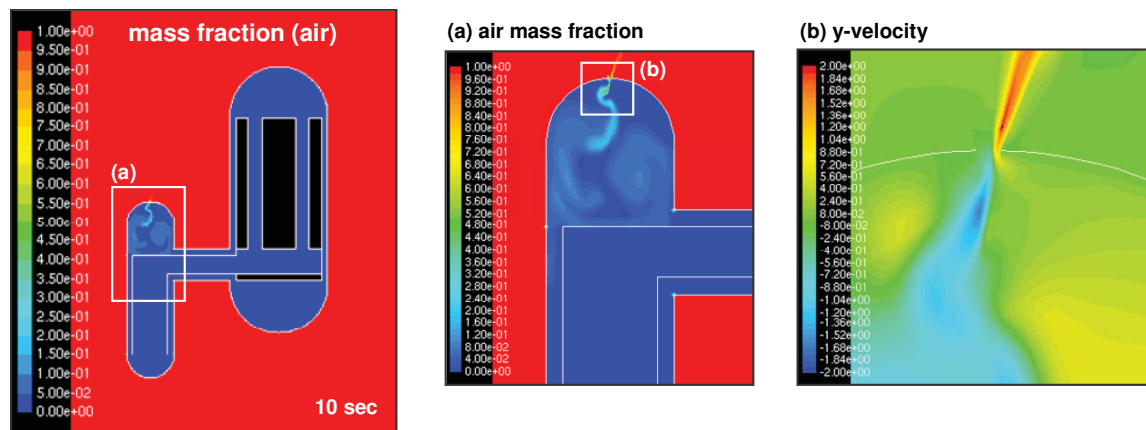
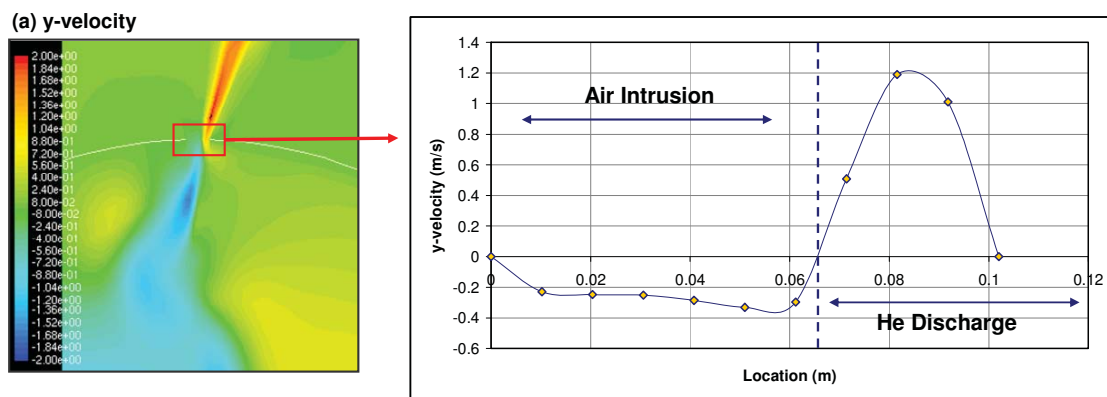


Figure 2-30. Fluent simulation of partial break situation (20 sec).



Flow velocity at the break location

Figure 2-31. Velocity profile at the break location (10 sec).

Figure 2-32 shows the air mass fractions in the VHTR calculated by FLUENT code. According to this figure, the air (1) enters the steam generator through the broken section located at the top of the steam generator; (2) moves to the steam generator bottom by gravity force (30 sec); (3) moves through the steam generator core and hot-leg, and finally (4) moves into the lower plenum and core (100 sec). Once the air goes into the reactor core, it is heated and easily moved up to the top (200 sec). The air ultimately goes back to the steam generator through the cold-leg, which is the outer channel of the horizontal coaxial duct (200 sec ~). This FLUENT simulation shows that the air-ingress process in the partial break situation is still very fast and highly dominated by density gradient flow rather than molecular diffusion.

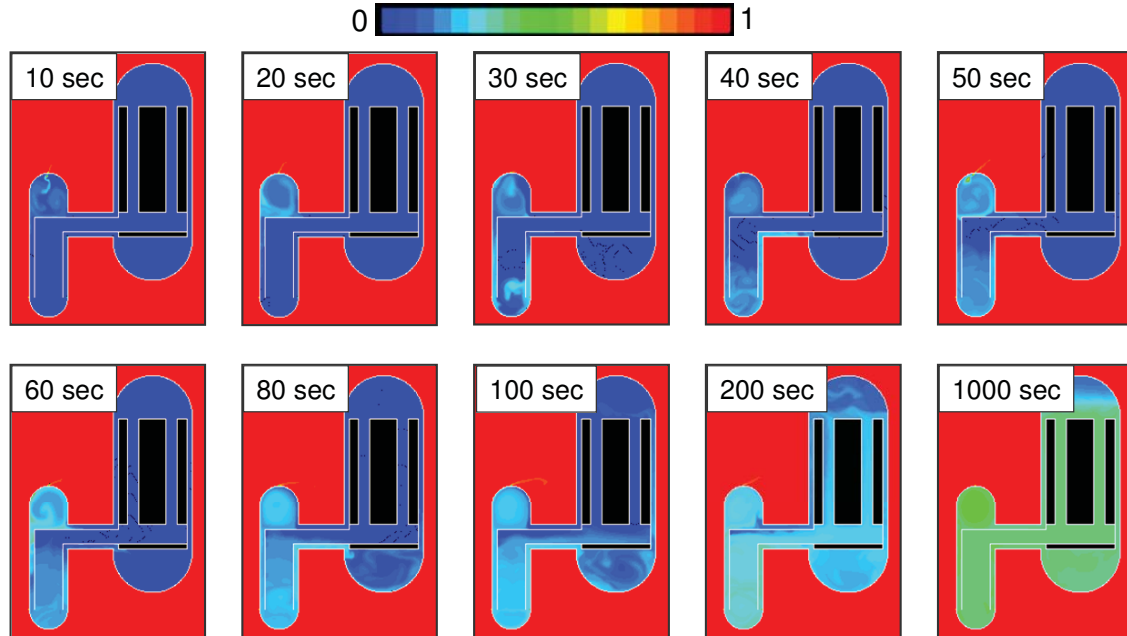


Figure 2-32. Air-mass fractions in the VHTR in the partial break situation (FLUENT results).

Figure 2-33 shows averaged air mass fractions in the reactor lower plenum and the core. For the initial 200 seconds, air moves from the broken part to the lower plenum. From 200 to 500 seconds, the air mass fractions in the core and the lower plenum rapidly increased. After 500 seconds, the air mass fractions slowly increase with a global natural circulation. According to this result, after the global natural circulation starts, the air ingress speed decreases with time. This is because the density difference between the inside and outside of the reactor at the broken part also decreases. It is also possible that the global convective motion is preventing the air from coming in through the break at a significant rate.

The wall thickness effect in the FLUENT model in Figure 2-33 was ignored because considering the small wall will make the model size unnecessarily huge. In this section, the effect of the wall thickness was estimated by using two different FLUENT models as shown in Figure 2-34. These FLUENT models basically consist of two tanks in vertical arrangement. Between the two tanks, there is a small hole with 10 cm. The upper tank is initially filled with air and the lower tank with helium. One model has the wall with 10 cm thickness, the other does not. The pressure and the temperature in the models were assumed to be 1.0 atm and 25°C, respectively.

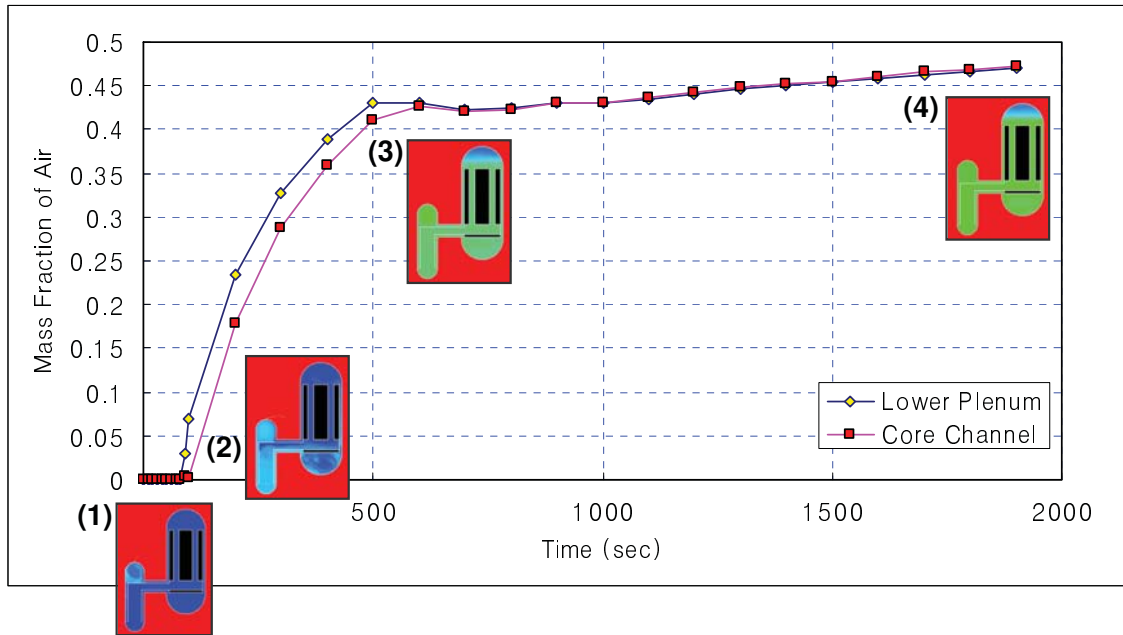


Figure 2-33. Average air mass fraction in the core and the lower plenum.

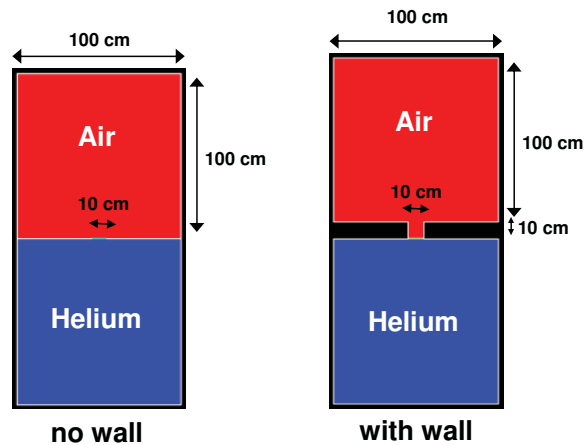


Figure 2-34. FLUENT models for wall thickness effect.

Figure 2-35 shows the results of the FLUENT calculations by plotting the averaged air mass fractions in the lower tank during 10 second simulations. This plot shows three different data sets: no-wall, with-wall, and diffusion. The diffusion case was calculated by deactivating the gravity force in the FLUENT model. As shown, the averaged mass fractions of the with-wall case showed a similar trend to those of the no-wall case, even though specific flow distributions and patterns are not exactly the same. The diffusion case showed very different results from the other two cases. According to the estimation, the air-ingress speeds in the density gradient flows (no-wall and with-wall cases) were much faster than the diffusion case, even in the small hole. This indicates that even in the partial break situation, the density gradient effect is much more dominant than molecular diffusion.

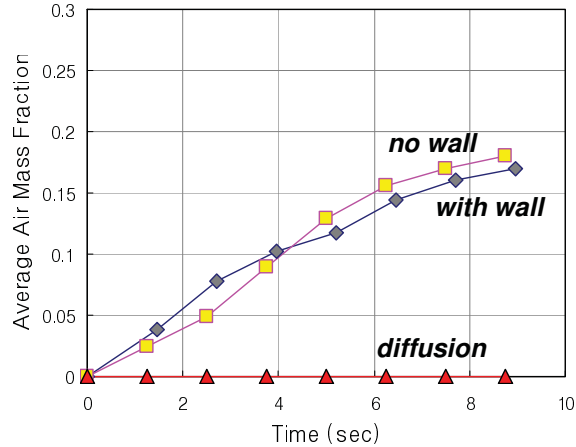


Figure 2-35. Effect of wall thickness in the partial break.

2.5 3-D DEGB Analyses by CFX Code

A 3-D CFD analysis with CFX-12 was performed for the air ingress accident of the GTMHR 600 MWth reactor under the assumption of a DEGB in order to understand the air ingress behavior in detail and estimate the onset of natural circulation time. According to previous research, FLUENT 2-D results show that the onset of natural circulation time is about 200 seconds, which differs greatly from the 1-D GAMMA results of about 150 hours (Oh et al. 2008). The 1-D option of the GAMMA code was not able to capture the stratified flow and the flow recirculation in the lower plenum. The FLUENT 2-D analysis used a simplified porous model with a friction factor correlation and an approximated thermal equilibrium model to simulate the hydraulic resistance because of a friction and form loss and the heat transfer between the air and the solid structure in the lower plenum and the core block. The 3-D CFD analysis with the real grid model, especially for the lower plenum, was introduced to verify the 2-D FLUENT results.

The air ingress phenomenon is usually driven by the stratified flow (Liou et al. 2005) and the pressure build-up in the lower plenum during air heat up and reduced inertia in the recirculation pattern. Air ingress may also be interrupted by the hydraulic resistance that takes place when the air passes a complicated geometry in the reactor. Therefore, it is not expected that an exactly simulated grid model for the complicated geometry of the lower plenum and core block can accurately predict the propagation of the air ingress inside the reactor. A grid interface function that connects two nonconformal meshes was used to complete the 3-D grid model because of the complicated nature of combining the consecutive mesh generation for the lower plenum, core blocks, and coolant riser within a single model.

The grid interface implemented in the CFX-12 (ANSYS 2009) is superior to that of other CFD codes (Kang 2006); however, the 3-D DEGB analysis by CFX-12 cannot simulate the helium blow-down phase with a decay heat generation in the core blocks. This is because CFX-12 has trouble obtaining fully converged solutions for the large pressure difference between the reactor and the confinement in the blow-down phase, and there is presently no implemented model for decay heat generation. The CFD calculations were therefore made at the pressure equalization between the confinement and the reactor vessel following the high pressure helium blow down to the confinement. The 3-D CFX analysis should therefore be carefully used to only predict the air ingress behavior because of the density driven stratified flow, buoyant flow by heat transfer, and hydraulic flow interrupted by complicated geometry. If the 3-D CFX analysis is able to predict the physical characteristics of an air ingress accident, the 3-D CFX analysis may also be used to find a mitigation method for the air ingress accident.

2.5.1 3-D Grid Model

In order to calculate the air inflow from the confinement into the reactor vessel through the broken pipes, a half symmetric grid model (see Figure 2-36, (a)) simulating the confinement and the reactor vessel internal was generated based on the design data of the GTMHR 600 MWth (Oh et al. 2008). The inner and outer reflector was also modeled to simulate the solid heat structure and the flow path formed from the core block upper region to the coolant riser upper region in the air ingress accident. A hexahedral mesh was separately generated by ICEM-CFD software (ANSYS 2008) for all regions in the reactor and confinement except the lower plenum, and then all separated models were connected by using the grid interface function of CFX-12. The lower plenum grid model was initially generated by using GAMBIT with hexahedral, tetrahedral, and pyramidal meshes (Johnson 2008). It was transformed to the grid model for CFX-12 by ICEM-CFD.

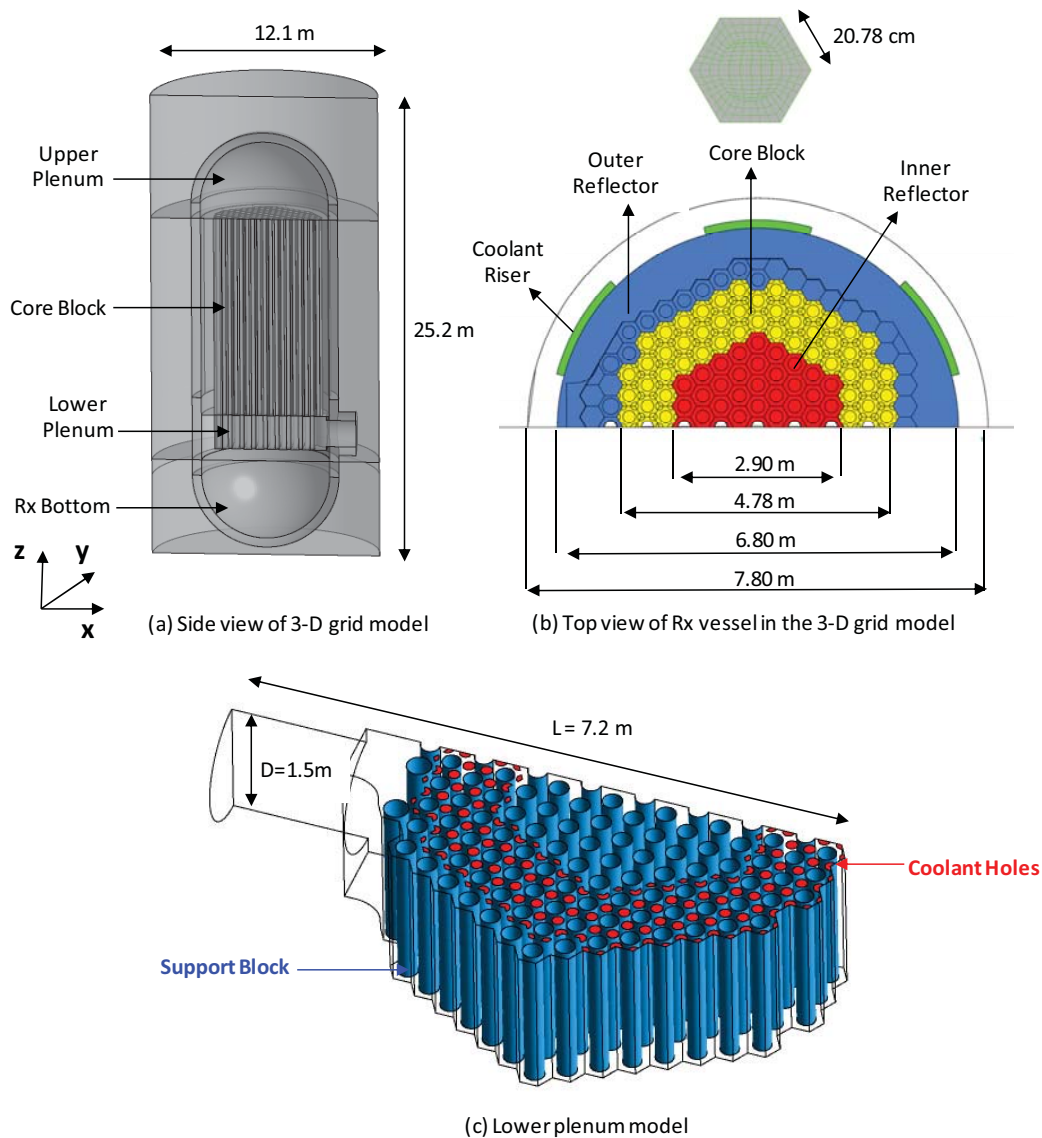


Figure 2-36. 3-D grid model for the DEGB analysis.

All meshes were densely distributed in a fluid region of the grid model, except the confinement, to prevent numerical diffusion and assure a low courant number (Equation (2-83)). About two millions mesh cells were generated for all the core blocks to predict the air ingress more accurately because the expected flow regime in the core blocks is a buoyant flow because of heat transfer between the core block walls and the air. The 2-mm bypass gaps between the core blocks were neglected to avoid the large number of cells required to resolve a 2-mm gap. The expected CFD results with the bypass gap are not expected to differ greatly from those without the bypass gap. In the confinement, a coarse mesh distribution was used, except around the broken pipes and the reactor vessel wall, because locally precise CFD results are not necessary for the regions far from the broken pipes and the reactor vessel walls. Thirty CFX parallel licenses are being used to compute the air ingress phenomena in the HTGR reactor and the confinement with a total of 8.5 million meshes.

$$\text{Courant Number} = V \Delta t / \Delta x \quad (2-83)$$

where

V = Fluid velocity (m/s)

Δt = Time step (sec)

Δx = Mesh length (m).

The shutdown cooling system located in the reactor bottom region and several guide tubes in the upper plenum were neglected in the grid model because the anticipated advantages of those models are not essential in predicting the air ingress from the confinement into the core blocks and the coolant riser. The detailed information of the mesh distribution and the geometry are shown in Table 2-3.

Table 2-3. Number of mesh and volume data for each region in the 3-D grid model.

Reactor Internal		Confinement
Core Blocks	Volume : 60.35 m ³ (Volume Porosity : 0.185) Height : 10.82 m Hexahedral mesh : 2,248,560	Volume : 961.05 m ³ Hexahedral mesh : 621,183 Fluid volume ration the confinement to the reactor internal : 3.81 Total meshes number : 8,517,835
Lower Plenum	Volume : 15.29 m ³ Height : 1.84 m Hexahedral mesh : 677, 917 Tetra mesh : 25,940 Pyramids mesh : 1,103	
Upper Plenum	Volume : 66.27 m ³ Radius : 3.4 m Hexahedral mesh : 712,023	
Coolant Riser	Volume : 6.98 m ³ (2.328 m ³ × 3) Height : 9.87 m Hexahedral mesh : 287,820 (2.328 m ³ × 3)	
Rx Bottom	Volume : 82.33 m ³ Hexahedral mesh : 651,963	
Reflector and Solid Regions	Volume : 204.58 m ³ Hexahedral mesh : 3,075,831	

2.5.2 Initial, Boundary, Porous Media Conditions and Properties

This 3-D DEGB CFX analysis assumed that the helium discharge from the reactor into the confinement through the broken pipes is already complete and that global pressure equilibrium has occurred between the confinement side and inside the reactor. All initial conditions of the concentration, temperature, and pressure were computed using the GAMMA code and those values were used in CFD calculations as initial conditions. This was done because a large computation time would be necessary to get a well converged solution for the helium blow-down phase.

Initial conditions (see Figure 2-37) for the air mass fraction, the temperature, and the pressure for the confinement and reactor, including the inner and outer reflectors, were given according to the GAMMA results and hand calculation results for the blow-down phase (Oh et al. 2008). The air mass fraction of 0.5 for the confinement was simply calculated by considering the pressure and volume difference between the confinement and the reactor with the ideal gas law during the blow-down phase. The initial pressure distribution along an elevation was automatically calculated by CFX-12 with a gravitational direction and a density value.

Based on the GAMMA results, a constant temperature condition (see Figure 2-38) for the wall boundary condition was applied along the core block walls, the surface of the core support block, and the surface of the reactor vessel. In the core wall temperature condition, the temperature of the core upper region (see Figure 2-38, A) is lower than that of the core lower region (see Figure 2-38, B) because the helium passes from the upper region into the lower region at the normal operation. The constant wall temperature conditions may be verified because the solid structure temperature is not changed, at least for several minutes. The symmetric condition is also applied on the 180 degree cut plane of the grid model.

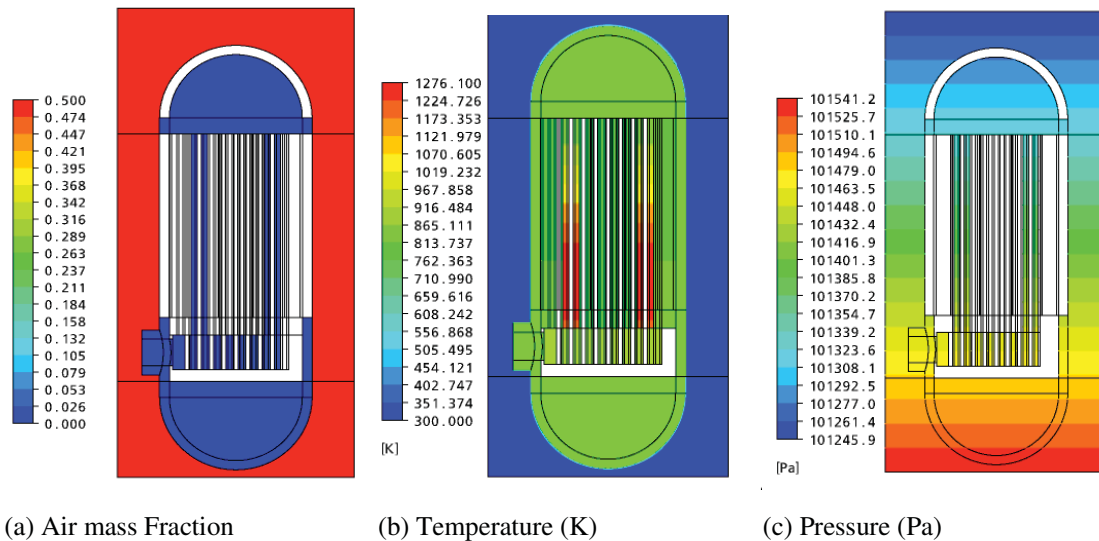


Figure 2-37. Initial air mass fraction, temperature, and pressure conditions for 3-D CFX analysis.

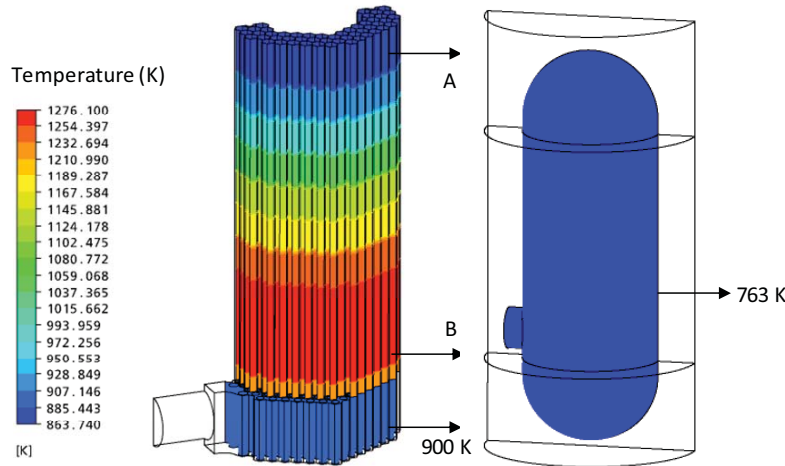


Figure 2-38. Wall temperature conditions for the core blocks, support blocks and reactor vessel.

A porous media condition was applied to the core blocks to simulate a pressure drop through the core blocks when helium or air flows along the core blocks. This was done to simulate 108 coolant channels with diameters of 12.7 and 15.8 mm per core block (Oh et al. 2008). The porous media condition was given in terms of a permeability (K_{perm}), a loss coefficient (K_{loss}) and a volume porosity (Equation (2-84)). The velocity (V_i) used in the Equation (2-84) is a true velocity that can be obtained by dividing the superficial velocity with the volume porosity (Equation (2-85)). The true velocity concept of the porous media model may be important in the air ingress accident. The calculated turbulent viscosity based on the true velocity gradient can have an effect on the diffusion term of the species transport equation.

$$-\frac{\partial p}{\partial x_i} = \frac{\mu}{K_{perm}} V_i + K_{loss} \frac{\rho}{2} |V| V_i \quad (2-84)$$

$$\text{True Velocity} = \text{Superficial Velocity} / \text{Volume Porosity} \quad (2-85)$$

Experimental data are needed to give the accurate porous conditions simulating the core pressure drop under the air ingress accident because no other test data is available. Thus, conceptual design data regarding the core pressure drop (GA 1996) at a normal operation condition were introduced to generate the porous condition values. A theoretically obtained porous condition should also be verified by the comparison of the calculated pressure drop values and the conceptual design data before applying it to the air ingress accident analysis. A steady-state calculation was performed using normal GTMHR operating conditions (GA 1996) to show the pressure drop of the core blocks and the reactor vessel from the cold duct to the hot duct. The calculated pressure distribution is shown in Figure 2-39 and the comparison results of the core pressure drop and reactor pressure drop between the conceptual design data and CFD results (Table 2-4) show good agreement (within 10%). Therefore, it is not possible to judge that these porous conditions may be used for the air ingress accident analysis.

The properties of the air and helium, such as thermal conductivity, molecular viscosity, and specific heat used for the 3-D CFX analysis, were cited from those of the FLUENT 2-D analysis, except for helium specific heat (ANSYS 2009). The National Aeronautics and Space Administration (NASA) format correlations in Table 2-5 were used for the helium specific heat property in the 3-D CFX analysis. The binary molecular diffusivity shown in Figure 2-40 was calculated by Equation (2-46). The air and helium density was obtained by the ideal gas law. The graphite properties for thermal conductivity and specific heat for the inner and outer reflectors were quoted from the FLUENT 2-D analysis.

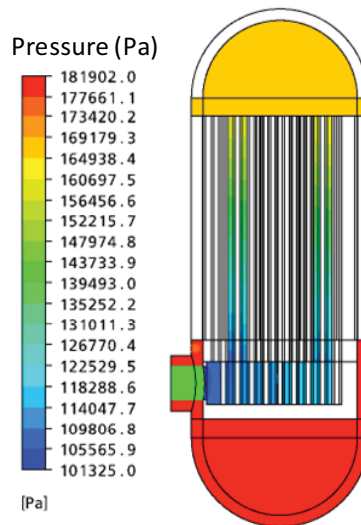


Figure 2-39. Pressure distribution results with the porous conditions under the normal operation conditions.

Table 2-4. Pressure drop results using the porous media conditions.

Porous Conditions: <ul style="list-style-type: none"> • Volume porosity : 0.185 • Permeability : $9.706 \times 10^{-4} \text{ m}^2$ • Resistance loss coefficient : 1.367 m⁻¹ 		
GTMHR 600 MWth Normal Operation Conditions [GA 2006]: <ul style="list-style-type: none"> • He mass flow rate : 320 kg/s • He average temperature through the core block : 743.65 K 		
	Conceptual Design Data	CFD Results
Pressure drop of Rx vessel (Cold Duct to Hot Duct)	71 kPa	78.8 kPa
Pressure drop of active core	51 kPa	50.9 kPa

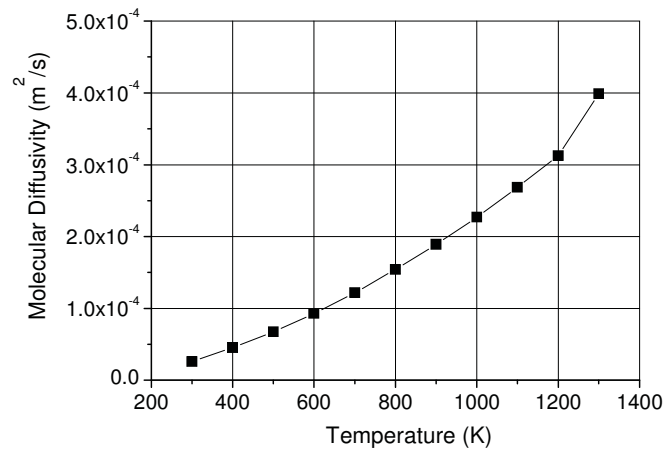


Figure 2-40. Binary diffusion coefficient between air and helium.

Table 2-5. NASA format correlation for specific heat of helium.

- $C_p / R = a_1 + a_2T + a_3T^2 + a_4T^3 + a_5T^4$
- $R = 2077 \text{ [J/kg K]}$ for helium
- Lower temperature = 300 [K], Midpoint temperature = 1000 [K], Upper temperature = 5000 [K]
- Lower interval coefficient:
 $a_1 = 0.02500000E+02$ [], $a_2 = 0.0E+00 \text{ [K}^{-1}\text{]}$, $a_3 = 0.0E+00 \text{ [K}^{-2}\text{]}$, $a_4 = 0.0E+00 \text{ [K}^{-3}\text{]}$,
 $a_5 = 0.0E+00 \text{ [K}^{-4}\text{]}$, $a_6 = -0.07453750E+04 \text{ [K]}$, $a_7 = 0.09153488E+01$ []
- Upper interval coefficient:
 $a_1 = 0.02500000E+02$ [], $a_2 = 0.0E+00 \text{ [K}^{-1}\text{]}$, $a_3 = 0.0E+00 \text{ [K}^{-2}\text{]}$, $a_4 = 0.0E+00 \text{ [K}^{-3}\text{]}$,
 $a_5 = 0.0E+00 \text{ [K}^{-4}\text{]}$, $a_6 = -0.07453750E+04 \text{ [K]}$, $a_7 = 0.09153489E+01$ []

2.5.3 Flow Field models and Numerical Models for the 3-D CFX Analysis

The air ingress accident under the DEGB was treated as a convective flow, a compressible flow, a turbulent flow, a species flow, a buoyant flow, and a transient flow. The governing equations (Equation (2-86)–(2-92)) used in this study are the continuity, Navier-Stokes, energy, and the species transport equations with a coupled solver algorithm (ANSYS 2009). Turbulent flow was modeled by the standard k- ϵ turbulent model with the scalable wall function, and the buoyancy flow was modeled by the density difference (see Equation (2-87)) (ANSYS, 2009). The governing equations used for the porous media are changed to Equation (2-93) by adding the volume porosity (λ) and area porosity tensor (K) into the general governing equations as follows:

$$\frac{\partial \rho}{\partial t} + \nabla \cdot (\rho \vec{V}) = 0 \quad (2-86)$$

$$\frac{\partial (\rho \vec{V})}{\partial t} + \nabla \cdot (\rho \vec{V} \otimes \vec{V}) = -\nabla p + \nabla \cdot [\mu_{eff} (\nabla \vec{V} + (\nabla \vec{V})^T)] + (\rho - \rho_{ref}) \vec{g} \quad (2-87)$$

$$\frac{\partial (\rho h_{tot})}{\partial t} - \frac{\partial p}{\partial t} + \nabla \cdot (\rho \vec{V} h_{tot}) = \nabla \cdot \left(\lambda \nabla T + \frac{\mu_t}{Pr_t} \nabla h \right) + \nabla \cdot (\vec{V} \cdot \tau) \quad (2-88)$$

$$\frac{\partial (\rho k)}{\partial t} + \nabla \cdot (\rho \vec{V} k) = \nabla \cdot \left[\left(\mu + \frac{\mu_t}{\sigma_k} \right) \nabla k \right] + P_k - \rho \epsilon \quad (2-89)$$

$$\frac{\partial (\rho \epsilon)}{\partial t} + \nabla \cdot (\rho \vec{V} \epsilon) = \nabla \cdot \left[\left(\mu + \frac{\mu_t}{\sigma_\epsilon} \right) \nabla \epsilon \right] + \frac{\epsilon}{k} (C_{\epsilon 1} P_k - C_{\epsilon 2} \rho \epsilon) \quad (2-90)$$

$$\mu_{eff} = \mu + C_\mu \rho \frac{k^2}{\epsilon} \quad (2-91)$$

$$\frac{\partial (\rho \phi)}{\partial t} + \nabla \cdot (\rho \vec{V} \phi) = \nabla \cdot \left(D_{AB} + \frac{\mu_t}{Sc_t} \right) \nabla \phi \quad (2-92)$$

$$\frac{\partial(\gamma\rho\phi)}{\partial t} + \nabla \cdot (\rho K \cdot \vec{V}\phi) - \nabla \cdot (\Gamma K \cdot \nabla \phi) = rS \quad (2-93)$$

where

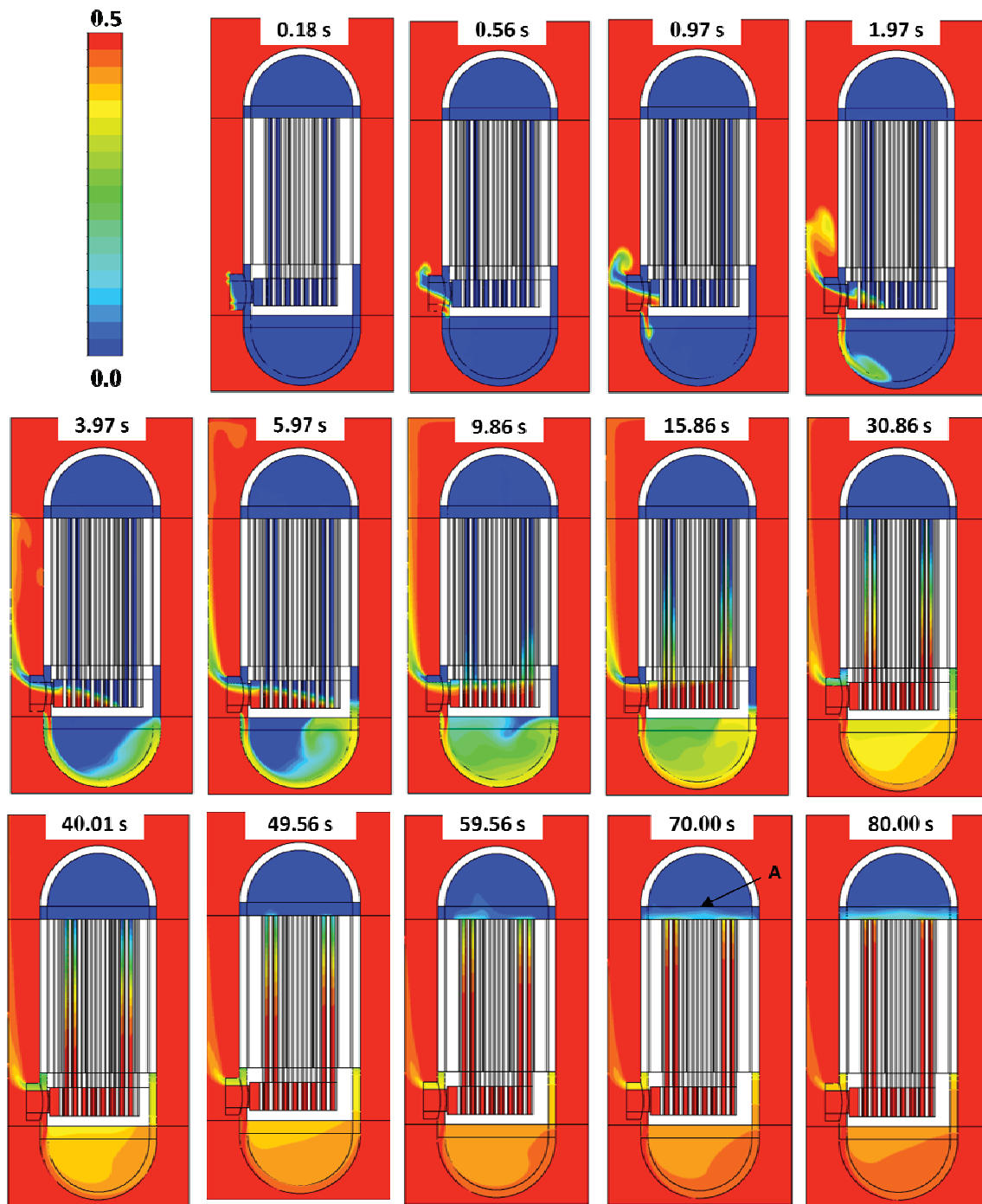
- \vec{V} = Velocity vector (m/s)
- \vec{g} = Gravitation vector (m/s²)
- h_{tot} = Total enthalpy (J/kg)
- D_{AB} = Binary diffusion coefficient (m²/s)
- k = Turbulent kinetic energy (m²/s²)
- ε = Turbulent dissipation rate (m²/s³)
- λ = Thermal conductivity (W/m K)
- μ_{eff} = Effective viscosity (Pa sec)
- ϕ = Variable
- Γ = Diffusion coefficient.

The transient calculation for a total time of 80 seconds with a time step of 0.001–0.005 seconds was performed to carefully simulate the buoyant flow behavior because of the heat transfer from the solid structures into the air and helium. As a calculation method, about 3–10 iterations were performed per the time step until the mass, enthalpy, and velocity residual of the air reached a value below 1.0×10^{-4} . The RMS Courant number was maintained below 2.5. The numerical models used for the 3-D CFX analysis are summarized as:

- Pressure-velocity coupling
- Linear equation solver: Algebraic Multigrid
- Convection scheme: Upwind 1st: $\phi_{ip} = \phi_{up}$
- Transient scheme: Backward Euler 1st: $\frac{\partial}{\partial t} \int_V \rho \phi dV = V \left(\frac{\rho \phi - \rho^o \phi^o}{\Delta t} \right)$
- Reynolds analogy: $Pr_t = 0.9$, $Sc_t = 0.9$
- 30 CPU parallel computation.

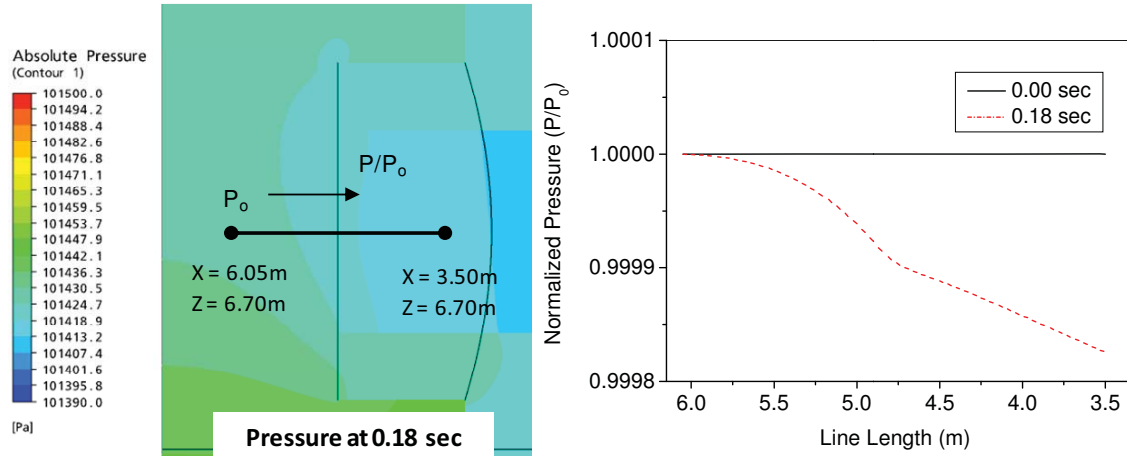
2.5.4 Discussion on the CFD Analysis Results

The 3-D CFD results of the air ingress accident are shown in Figures 2-41–2-43. The air mass fraction contours according to time (see Figure 2-41) show the air inflow pattern from the confinement side into the reactor internal side. Figure 2-41 shows the air entering into the hot and cold duct as soon as the CFD calculation starts. This is because the static head of the confinement side is slightly larger than that of the reactor internal side at the same elevation as much as the density difference between the air and the helium (see Figure 2-42, (a) and (b)). Figure 2-42 (a) shows the normalized pressure from the confinement (6.05 m from the center of the lower plenum) to the inlet point to the lower plenum (3.5 m from the center of the lower plenum) while $z=6.7$ m represents the midpoint of the broken pipe height. The vertical line in Figure 2-42 (a) is the pipe breach point and the curved line represents the curvature of

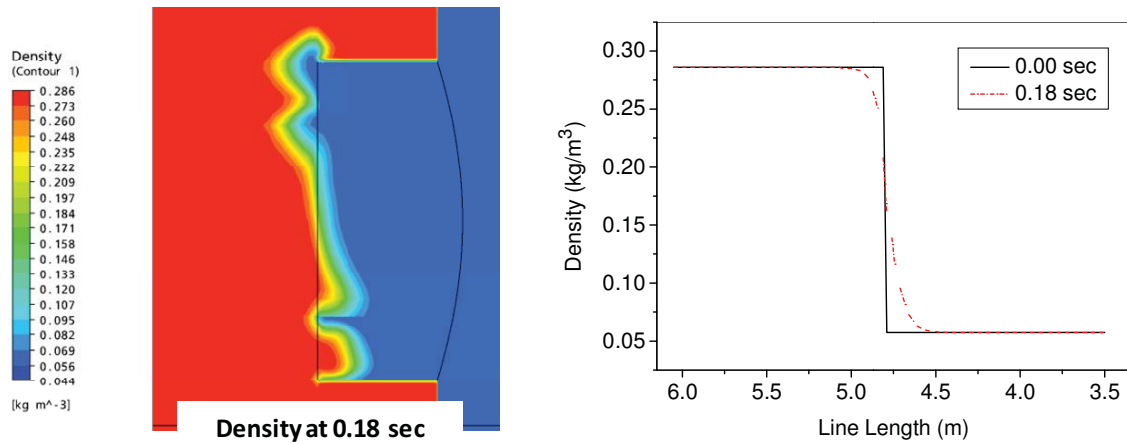


(Contours are plotted on the plane of $y = 0.01\text{m}$. Symmetry plane is $y = 0.0\text{ m}$)

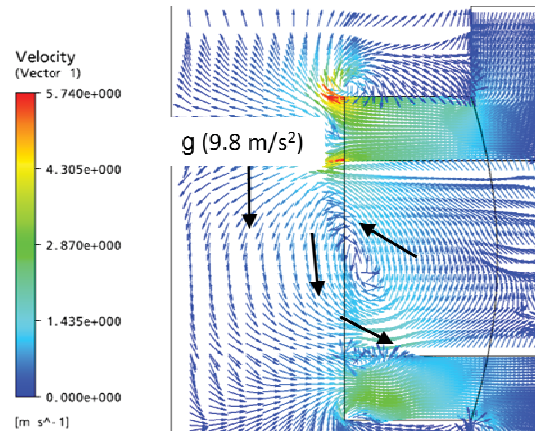
Figure 2-41. Variation of the air mass fraction according to time.



(a) Pressure contours and normalized pressure distribution along the line between $x=6.05$ m and $x=3.50$ m



(b) Density contours and normalized density distribution along the line between $x=6.05$ m and $x=3.50$ m.



(c) Velocity profile on the plane of $y = 0.01$ m at 0.18 seconds

(Contours are plotted on the plane of $y = 0.01$ m. Symmetry plane is $y = 0.0$ m)

Figure 2-42. Velocity profile, density, and pressure distribution at 0.0 seconds and 0.18 seconds.

the inlet pipe to the reactor vessel. Figure 2-42 (b) shows a sudden density change at the breach point. Figure 2-42 (c) shows the recirculation flow pattern at the breach point. Gravitational force directs the air inflow downward (see Figure 2-42, (c)). Finally, an instability may be developed on the interface between the air and helium when the air flows into the helium by Rayleigh-Taylor instability (Lowe et al. 2005).

As seen in Figure 2-41, the air arrives on the right end of the lower plenum at about 6 seconds and, after filling up the lower plenum and being heated by the support block, starts up into the core blocks right side at about 10 seconds. It takes approximately 50 seconds for the air in the lower part of the core block to move upward to the upper part by the buoyancy force generated by the density variation because of the heat transfer from the core block wall into the air. The air then arrives at the top of the coolant riser about 70 seconds after filling up the volume of the upper plenum near the core upper region (see Figure 2-41 and Figure 2-43; see A). The air that fills the upper plenum flows up through the reactor core, shown as two blank boxes in Figure 2-43. The air then moves downward along the coolant riser at about 80 seconds (see Figure 2-43, A), and is also located at the lower part of the coolant riser (Figure 2-43, B).

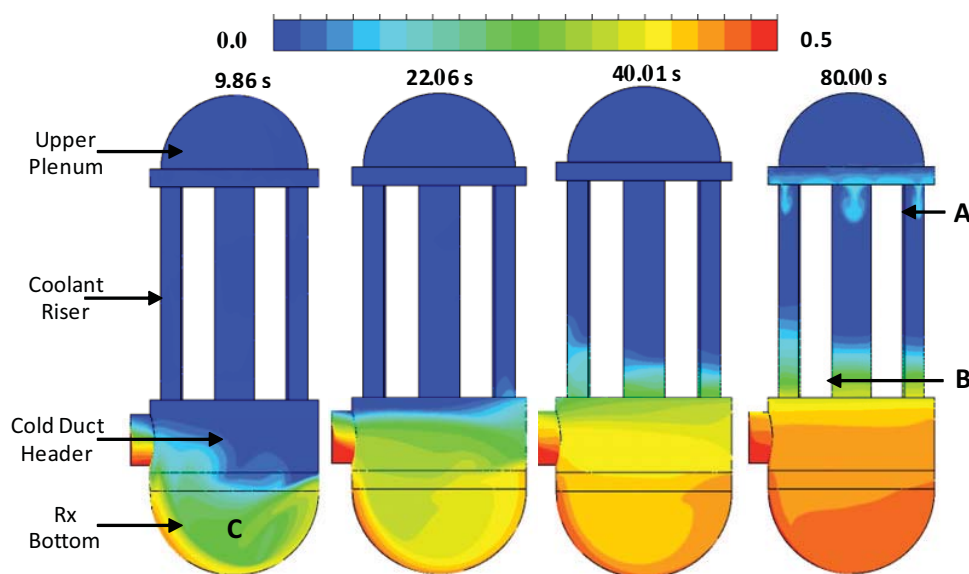


Figure 2-43. Air mass fraction of upper plenum, coolant riser, cold duct header, and reactor bottom.

It is believed that this air came from the confinement through the cold duct after filling up the reactor bottom region by the gravitation force effect (see Figure 2-43, C). From the air mass fraction contours, it can be expected that the air located on the upper region of the coolant riser can sufficiently reach the lower region of the coolant riser just 100–200 seconds after mixing with the air in the lower region.

Figure 2-44 shows the air mass fraction distribution on the hot and cold duct surface from a front view point. The air flows into the cold duct header through the lower region of the broken cold duct at the same time the helium counter-currently discharges through the upper region of the cold duct during the whole period. As time passes, the helium (blue color) in the helium discharge cold duct area steadily decreases. Figure 2-45 (a) and (b) show air mass fractions and velocity vectors in the lower plenum at 5.96 seconds. As can be seen, a portion of air velocity vector moves to the reactor core. When the flow is recirculated at the end of the plenum wall, it loses the momentum, resulting in pressure build-up, which makes the air move upward, if the hydrostatic force is less than the pressure build-up.

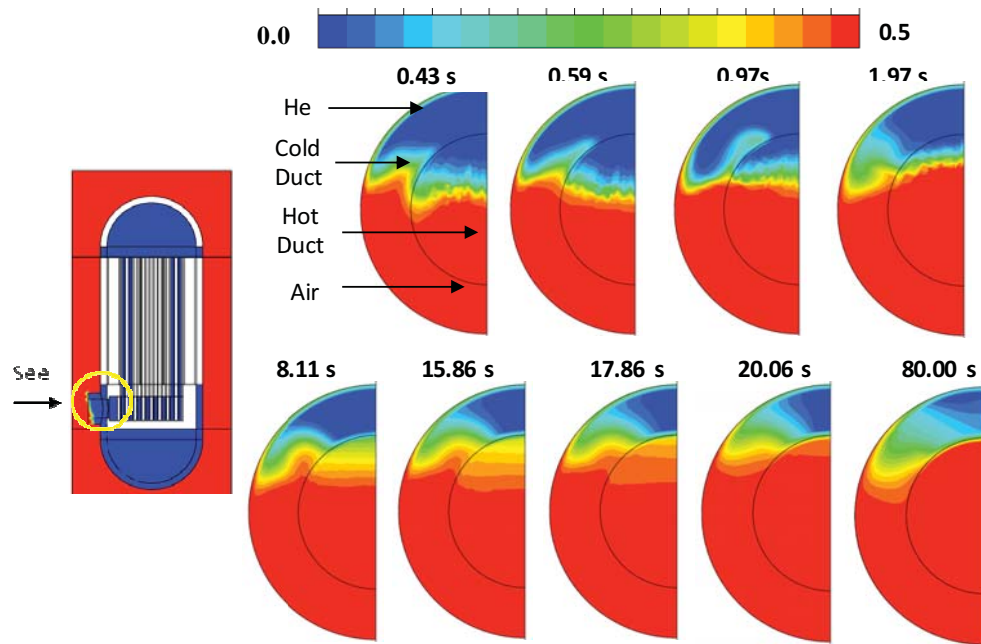


Figure 2-44. Air mass fraction of the hot and cold duct (front view).

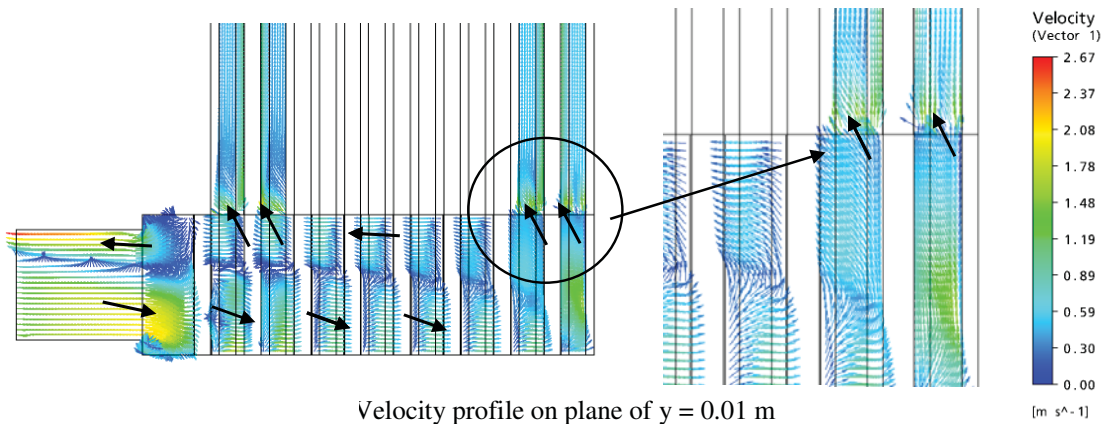
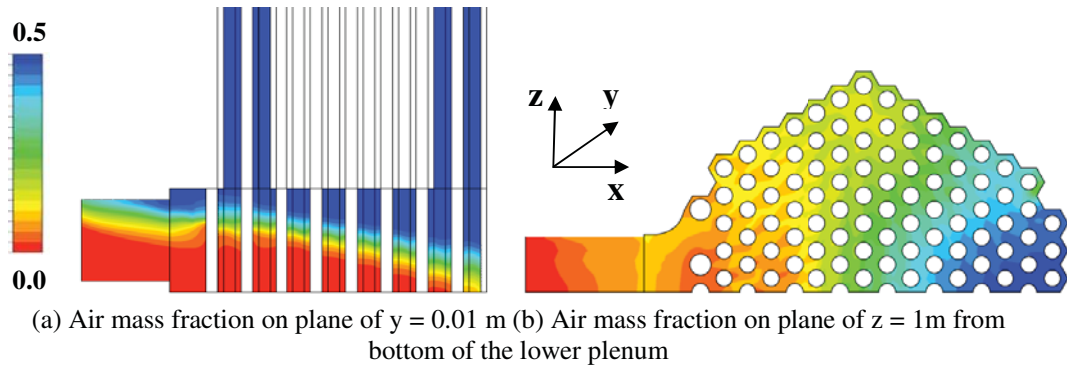


Figure 2-45. Air mass fraction and velocity profile in the lower plenum at 5.96 seconds.

The rate at which the helium area decreases is proportional to the helium inventory volume in the reactor vessel and the velocity of the air inflow. In the hot duct side, the same situation of the counter-current flow driven by the density occurs just as on the cold duct side. The helium discharge through the upper region of the hot duct (see Figure 2-45, (c)) continues until about 20 seconds. These different time scales for the discharge of helium through the cold and hot duct can be certified in terms of the volume averaged air mass fraction of the lower plenum, the reactor bottom, and the cold duct header as shown in Figure 2-46. The filling of the lower plenum with air is completed by about 20 seconds, whereas those of the reactor bottom and the cold duct are not completed until 80 seconds because the air through the cold duct moves downward and fills up the reactor bottom first.

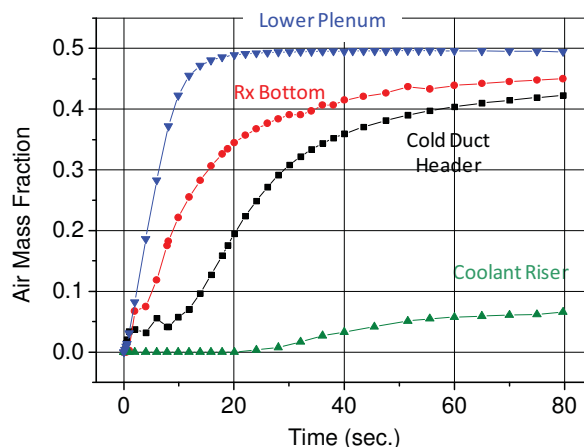


Figure 2-46. Volume averaged air mass fraction of the lower plenum, the reactor bottom, the cold duct header and the coolant riser (Maximum value of the air mass fraction is 0.5).

The complete time of the helium discharge is very short when considering the lower plenum volume of 15.29 m^3 and the helium discharge velocity of about $1.0\text{--}2.67 \text{ m/s}$ (see Figure 2-45). This situation may be caused from the helium located in the lower plenum at early stages that moves upward into the core blocks by the effect of the natural circulation along the core blocks. The development of the helium natural circulation along the core block because of the initial temperature difference (see Figure 2-38, (b)) may be confirmed in terms of the volume averaged velocity of the core block (see Figure 2-47). The velocity value shown in Figure 2-46 rapidly increases to about 1.1 m/s for $3.0\text{--}7.0$ seconds, and then decreases to about 0.2 m/s at about 30.0 seconds. This natural circulation at an early stage may entrain the helium located in the lower plenum, and accelerate the helium circulation from the upper plenum region into the coolant riser.

Figure 2-48 shows the air mass fraction variation of the lower plenum, core, and core lower region according to time. An interested phenomenon is that the air mass fraction of the core starts to increase from about 10 seconds, even though about 80% of the lower plenum volume was already filled with air in the first 10 seconds. This may be caused by the discharging helium stream along the lower plenum upper region, thus preventing air penetration into the core blocks, or the air buoyancy force developed by the heat transfer from the support blocks being weak compared to the momentum of the helium discharging flow. However, it is possible to know from the volume averaged temperature variation results of the lower plenum and the cold duct header (see Figure 2-49) that the starting time of the air flowing into the core block is closely related to the lower plenum temperature variation. The temperature graph of the lower plenum starts to increase at about 11 seconds from its continuous decreasing trend (see Figure 2-49, A), whereas the temperature of the cold duct header steadily decreased to the end of the CFD calculation

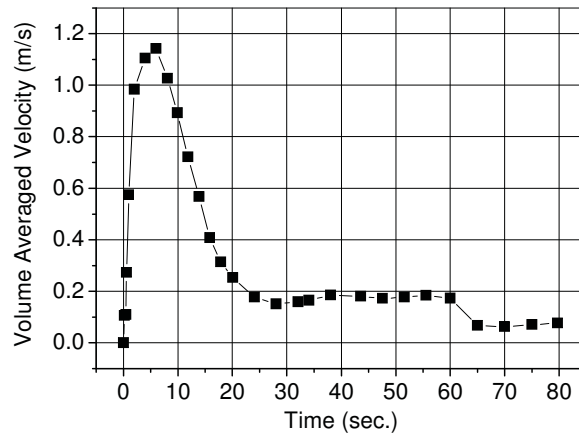


Figure 2-47. Volume averaged velocity of the core blocks.

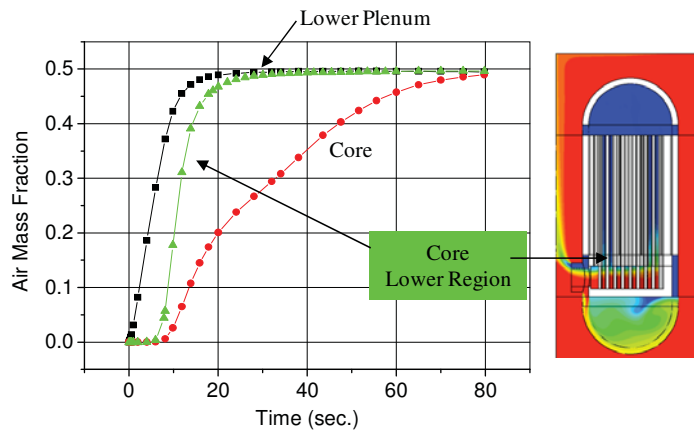


Figure 2-48. Volume and area averaged air mass fraction of the lower plenum, core blocks, and core inlet (maximum value of the air mass fraction is 0.5).

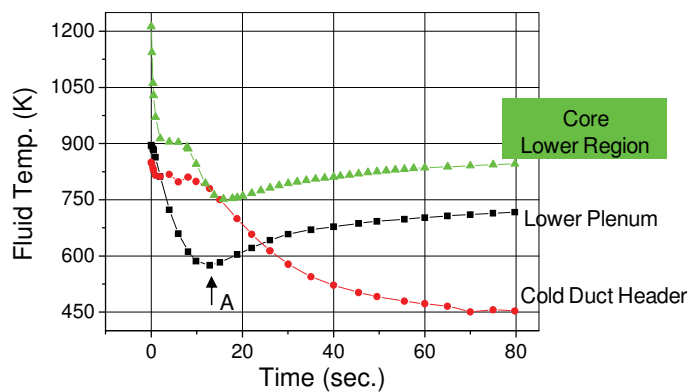


Figure 2-49. Volume and area averaged air temperature of the lower plenum, core blocks, and core inlet.

because it did not have the heat structure of the support block in the lower plenum. The temperature increase from the decreasing trend can also be confirmed by the temperature contours at the plane of $z = 6.7$ m in the lower plenum (see Figure 2-50, (g)). This may mean that the air heating time by the support block is an essential period for the air to have the buoyancy force because the buoyancy force can be developed by the density difference between a local value and an averaged value. It can therefore be expected that the starting time of the air flowing into the core block may be delayed if the air temperature of the lower plenum is maintained at a lower value.

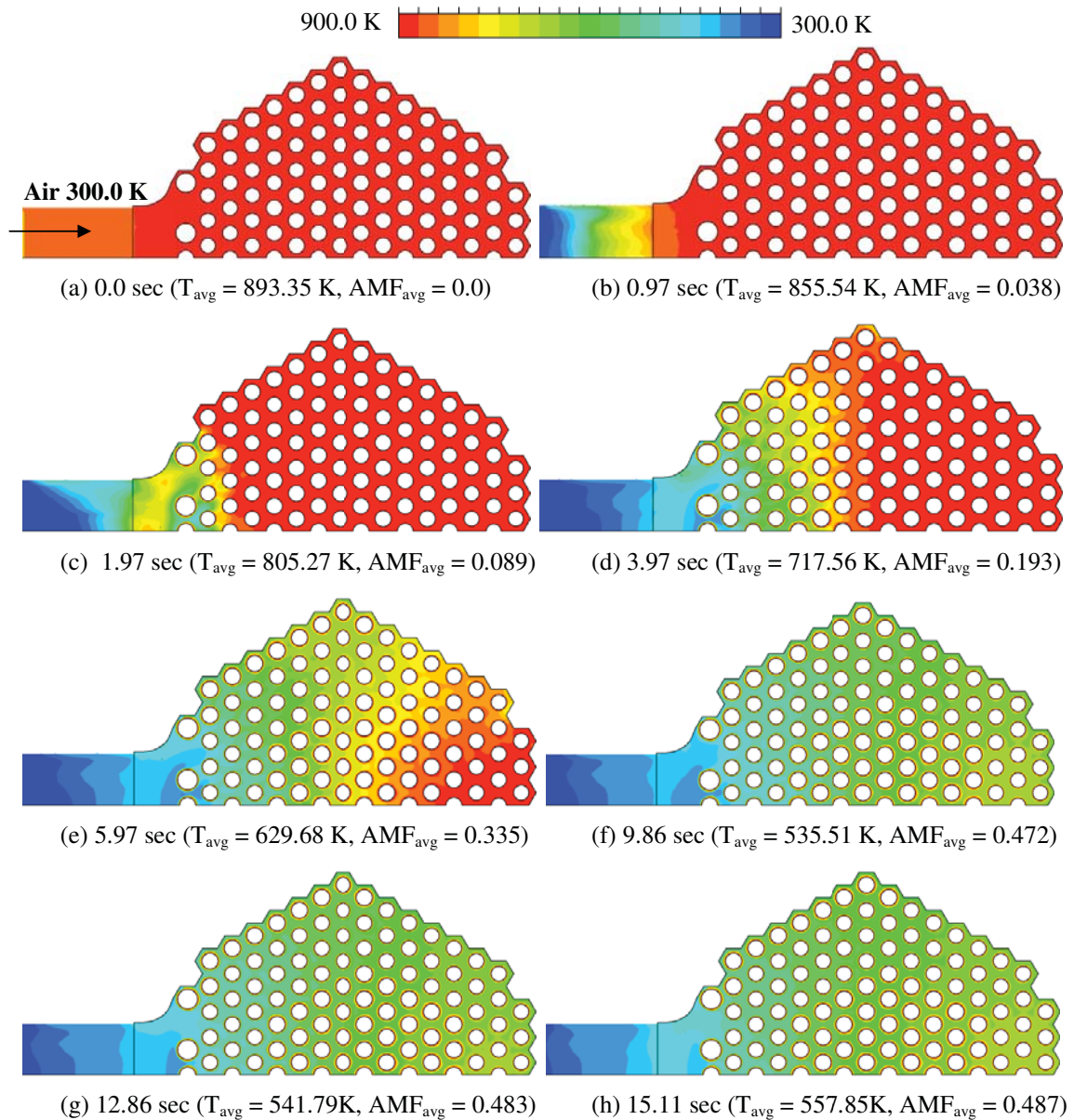


Figure 2-50. Temperature distribution on the plane of $z = 6.7$ m in the lower plenum (LP bottom: $z = 7.624$ m, LP top: $z = 7.624$ m, temperature and air mass fraction are averaged over the area of the plane at $z = 6.7$ m)

2.5.5 Conclusions and Further Works

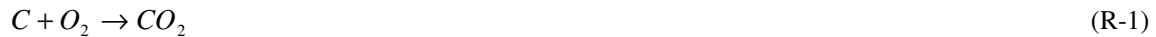
The 3-D CFX results of the 3-D DEGB analysis by CFX-12 show that air can actively ingress the reactor vessel because the air inflow momentum generated by the stratified flow and the buoyant flow because of the heat transfer from the solid structures inside the reactor vessel sufficiently overcome the hydraulic resistance when the air passes the lower plenum and core blocks. This confirms that the previous FLUENT 2-D results with the porous media model are reasonable. The expected onset of natural circulation time estimated by 3-D CFX analysis is approximately 100 seconds, which is 50% of that of FLUENT 2-D analysis results.

To confirm the starting time of the air flowing into the core blocks, a supplemental CFD calculation should be performed by changing the support block temperature. To reduce the uncertainty of the 3-D CFX results, several sensitivity calculations should be conducted by changing the numerical model for the convection term, the turbulent model, and the reference density value for the buoyant flow. The effect of the reference density value in the buoyant flow should also be carefully examined because the buoyant flow is a main driving force in the air ingress accident and its model is simply calculated by the density difference value based on the reference density value and the gravitational vector.

The qualitative results of the 3-D CFX analysis may not be changed because a lot of the heat structures definitely existed in the lower plenum and the density driven counter-current flow of air and helium is already verified by these experiments.

2.6 2-D Preliminary Analyses on the Effect of Chemical Reaction

Large amounts of graphite materials are used in VHTR cores, reflectors, and supporting structures. These graphite materials are very reactive to oxygen. The two main reactions between graphite and oxygen are



The R-1 reaction is dominant in low temperatures (<750°C). The R-2 reaction is dominant in high temperatures (See Figure 2-51). In the low temperature, the reaction is controlled by reaction kinetics and in the high temperature it is controlled by mass transfer rate (See Figure 2-52). In this work, the following equations were implemented into the FLUENT code by a user defined function.

(1) Overall graphite oxidation rate (Oh et al. 2006).

$$\frac{1}{R_g} = \frac{1}{R_k} + \frac{1}{R_m} \quad (2-94)$$

where

R_g = Overall graphite oxidation rate (kg/s)

R_k = Graphite oxidation rate estimated by Arrhenius model (kg/s)

R_m = Graphite oxidation rate estimated by mass transfer (kg/s).

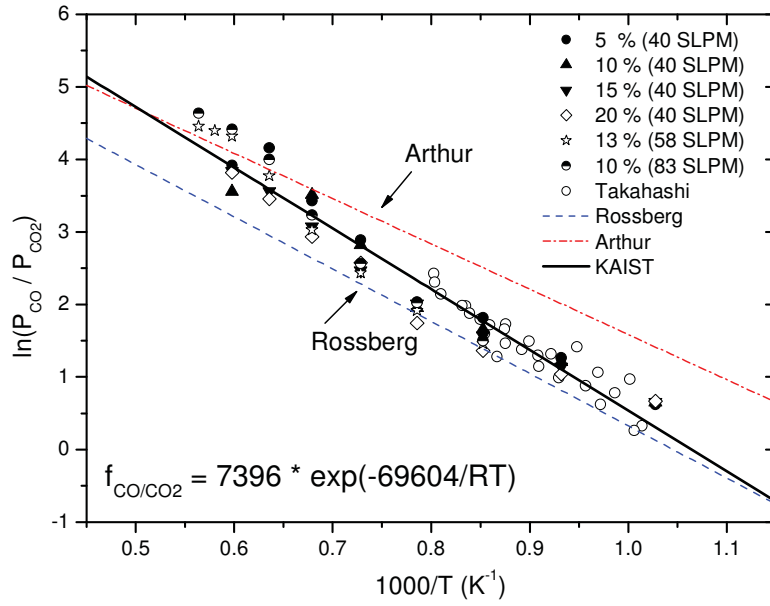


Figure 2-51. Ratio of CO/CO₂ with temperature (Oh et al. 2006).

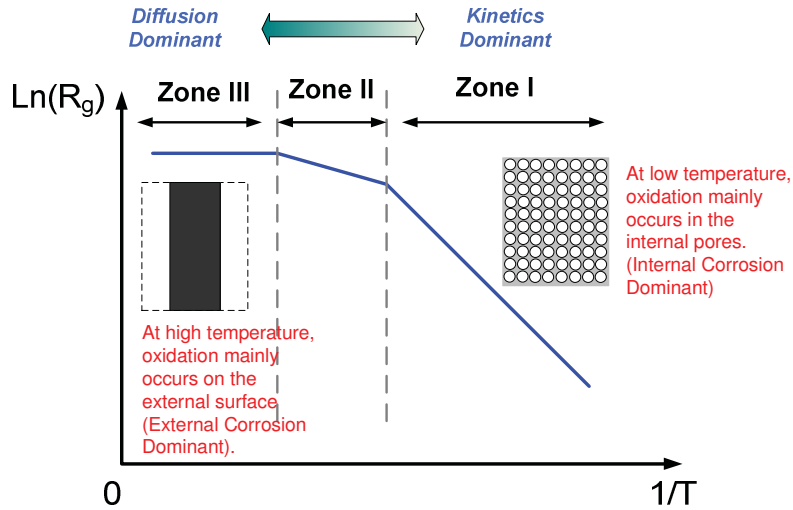


Figure 2-52. Effect of temperature on the graphite oxidation rates and oxidation regimes.

(2) Kinetics effect (Arrhenius model) (Oh et al. 2006).

$$R_k = 2552000 \cdot \exp\left(-\frac{218,000}{R \cdot T}\right) \cdot p_{O_2}^{0.75} \cdot \theta_0 \cdot V \quad (2-95)$$

where

R = Gas constant (8.315 kJ/kmol K)

- T = Graphite surface temperature (K)
 P_{O_2} = Oxygen partial pressure (Pa)
 θ_0 = Graphite initial surface density (m²/m³)
 V = Apparent volume of the graphite structure.

(3) Mass transfer.

$$R_m = 2M_c \cdot K_m (C_{O_2,\infty} - C_{O_2,0}) \cdot A \quad (2-96)$$

where

- M_c = Molecular mass of carbon, C (12 kg/kmol)
 K_m = Mass transfer coefficient of oxygen (m/s)
 $C_{O_2,\infty}$ = Oxygen concentration in the bulk flow (kmol/m³)
 $C_{O_2,0}$ = Oxygen concentration at the graphite surface (kmol/m³).

(4) CO/CO₂ ratio (Oh et al. 2006).

$$f_{CO/CO_2} = 7,396 \exp\left(-\frac{69,604}{R \cdot T}\right). \quad (2-97)$$

The effect of burn-off in the FLUENT model was neglected because the time scale in the FLUENT simulation was several minutes in which the effect of burn-off on the reaction rate was negligible. For consideration of the chemical reaction, six gas species in total were taken into consideration in the species conservation model. The chemical species include O₂, N₂, CO, CO₂, H₂O, and He. The model therefore solved five more equations than the previous FLUENT model, which did not consider chemical reactions. In this analysis, the computational speed significantly slowed down, even in the 2-D simplified geometries. The following summarizes the options and the models adopted in this calculation:

- 2-D
- Unsteady
- Segregated solver
- 2nd order accuracy in time
- Noniterative time advancement
- Absolute velocity formulation
- Cell based gradient
- Physical velocity (in the porous media formulation)
- Laminar viscous model
- Energy equation solving
- Species transport equation solving:

- Six gas species: O₂, N₂, CO, CO₂, H₂O, He
- Multicomponent diffusion model
- No consideration for thermal diffusion
- Pressure-velocity coupling method: PISO
- Pressure discretization method: PRESTO!
- Momentum: 2nd order upwind
- Species: 2nd order upwind.

The GTMHR was selected to be the reference reactor and DEGB was assumed. The geometry and mesh are the same as that used in the preliminary 2-D analyses in FY-08. Initial air mass fraction in the confinement was assumed to be 0.5. The results of the FLUENT simulation are briefly summarized in this section. Figure 2-53 shows the species concentration profiles in the reactor 13 seconds after depressurization, at which time the air has already filled the lower plenum and started to move into the reactor core by buoyancy force. The oxygen in the core is consumed by chemical reactions, resulting in CO and CO₂ species being generated. This result also shows that the chemical reactions are mainly generated at the core bottom region, while little chemical reaction is generated in the lower plenum. This is because the temperature in the lower plenum is relatively much lower than it is in the core. The generated CO and CO₂ gases move up through the core.

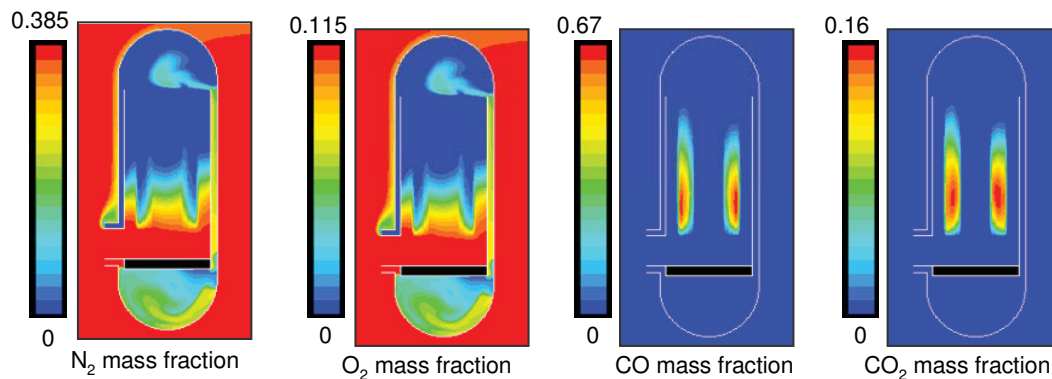
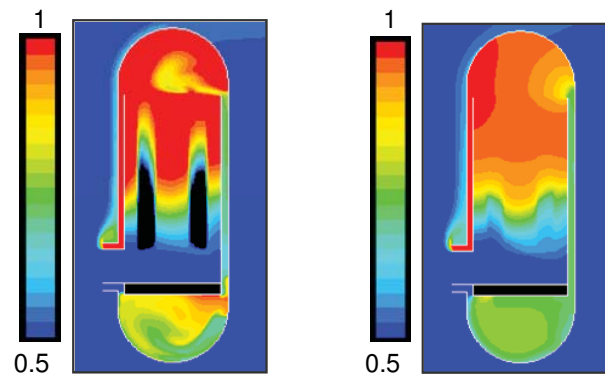


Figure 2-53. Species concentration profiles in the VHTR at 13 seconds.

Figure 2-54 shows the comparisons of the FLUENT calculations both with and without chemical reactions; helium concentrations are plotted in this figure for comparison. The chemical reaction accelerated the air-ingress process by moving more gases to the top. This occurred because the temperature in the reactor core is higher than 900°C. CO generation (reaction R-1) is therefore the dominant reaction in which one oxygen molecule is consumed and two CO molecules are generated. Therefore, a single gas species is generated by this reaction. Once CO is generated in the core, it will increase the pressure in the channel under the same temperature conditions. Graphite oxidation is an exothermic reaction, which increases the temperature at the reaction spot and generates more buoyancy force in the gases.

This preliminary calculation qualitatively indicates that the chemical reaction will accelerate the air-ingress process. However, for getting quantitative results, a detailed 3-D model is required as described in Section 2.5. The chemical reaction models and the user defined functions developed in this section can be directly implemented into the detailed 3-D CFD model. And, this detailed model will provide a more realistic and meaningful result. The detailed 3-D calculation for air-ingress with chemical reactions is currently planned.



(a) with reaction model

(b) without reaction model

Figure 2-54. Comparisons of with and without chemical reaction models.

3. TASK 2: EXPERIMENTAL STUDY ON THE STRATIFIED FLOW (INL)

3.1 Introduction

A LOCA that allows air to ingress the reactor core will result in oxidation of VHTR structural graphite. This can occur when a pipe breaks inside the reactor, allowing the air surrounding the reactor to rapidly ingress into the reactor vessel. This accident scenario will result in chemical reactions between oxygen and the core graphite structures, which will further heat up the reactor core and if unmitigated could, damage its structural integrity, resulting in the release of toxic gases such as CO and CO₂.

Lots of computational and theoretical work has been done to understand what will happen to a VHTR in the event of an actual air-ingress accident, but validation data is needed to support the theory and computational results. Table 3-1 shows the previous and current experimental data used to validate the computer codes for air-ingress analyses. This table lists 14 different experimental sets covering diffusion, natural convection, radiation, chemical reaction, and porous media models in the code; however, there are no good data for validation of stratified flow at this time.

Table 3-1. Previous and current validation data for air-ingress analyses.

	Test Facility	D	NC	R	C	P	etc
1	Pipe Network, NWU						O
2	Blowdown, NWU	O					O
3	Buncan & Toor's Experiment	O					
4	Inverse U-tube single/multiple channel test	O	O				
5	Ogawa's circular tube test				O		
6	Takahashi's annular tube test				O		
7	VENTURA pebble bed test				O	O	
8	Inverse U-tube air ingress experiment	O	O		O		
9	HTTR simulated air ingress experiment	O	O		O		O
10	Vertical slot experiment	O	O				
11	NACOK natural convection test		O			O	
12	SANA-1 afterheat removal test					O	
13	HTTR RCCS mockup test		O	O			
14	SNU RCCS test		O	O			

D: Diffusion NC: Natural Convection R: Radiation C: Chemical Reaction
P: Porous Media

Two sets of experiments were planned to understand stratified flow phenomena and validate the computer codes with physical models. This experimental work covers a separate effort to couple effects related to the stratified flow.

3.2 Plan for Stratified Flow Experiment (Isothermal)

The current section describes some separate-effect experiments for understanding stratified flow phenomena in the air-ingress accident and for generating data for validation of computer codes, including CFD codes or system analysis codes. As a first step, two isothermal experiments are presented: a DEGB experiment to analyze the phenomena that occurs in the DEGB situation, and a partial break experiment to analyze a partial break on the cross-duct of a VHTR. Since both experiments are designed to be

isothermal, i.e. heating or heat-exchange effects will not be considered at this stage. Heating effects will be considered later in separate non-isothermal experiments.

The density gradient driven flow is a new issue in the VHTR safety analysis field. The detailed mechanisms for the whole scenario have not been fully understood or validated in previous safety analyses. In addition, because previous studies were highly focused on numerical simulation, experimental data is required to validate these calculations and other systems codes used to analyze these events. All of the planned experiments will be performed to the appropriate quality standards.

3.2.1 Isothermal DEGB Experiment

3.2.1.1 Objectives

The DEGB experiment planned at INL has two main objectives: observe and understand phenomena driven by a density gradient in the broken pipe, and provide data for the validation of computer codes such as CFD or a system analysis codes that will eventually be used for VHTR safety analyses.

To meet the first objective, the characteristics of the flow phenomena will be investigated (See Figure 3-1). The following characteristics are typical to the VHTR DEGB scenario:

- Gravity current in the horizontal pipe
- Gravity current at the expansion point from the pipe to the vessel
- Gravity current around obstacle rods.

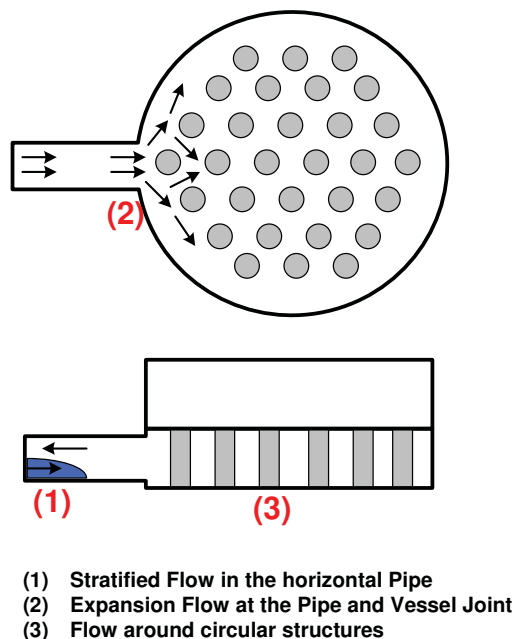


Figure 3-1. Flows of interest in the isothermal full-break experiment.

Section 2.1 mentions that the previous gravity current studies are quite similar to the air-ingress situation. Still, there are also differences between them, the biggest one being the shapes of channel cross-sections. Figure 3-2 (a) shows the channel shape in previous studies on gravity current, which were carried out using rectangular channels. In the rectangular channel, the channel height is not changed along

the horizontal axis, indicating that the current speed will be consistent along the axis and the flow regime in each horizontal location will be the same. In this configuration it is possible to visualize 2-D flow; therefore, the experimental results were well matched to the previous theoretical models derived in the 2-D axis. However, in the air-ingress condition, which consists of a circular channel, the channel height changes along the horizontal axis (See Figure 3-2 (b)). At the center, the height is large, and at the side, the height is small. Therefore, at the center, the current speed will vary from the speed near the sides, providing different flow regimes for different locations in the circular pipe. Thus, the circular pipe appears to see some 3-D effects on the gravity current flow. It is presently unclear if the previous models based on 2-D are still valid for the circular geometry.

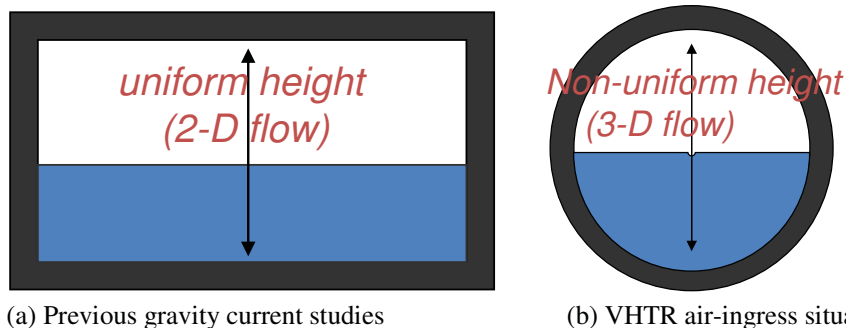


Figure 3-2. Comparisons between previous gravity current studies and VHTR air-ingress condition.

In these experiments, 2-D velocity field and species distributions will be directly measured by particle image velocimetry (PIV) and laser induced fluorescence (LIF). The measured local velocities and concentrations will be used to validate computer codes.

3.2.1.2 Experimental Parameters

Based on previous investigations (Von Karman 1940, Yih 1965, Benjamin 1968, Gardner 1970, Britter & Simpson 1978, Klemp et al. 1994, Keller and Chyou 1991, Simpson 1999, Hartel et al. 2000, Lowe et al. (2002, 2005), Shin et al. 2004, Birman et al. 2005), the most important parameter in the gravity currents is the density ratio between two fluids. In most of the cases, the current speed or the current depth are direct functions of the density ratios, satisfying energy conservation. If, however, the channel height is too small or the viscosity of the fluid is too high, the Reynolds number becomes important because the frictional loss is no longer negligible (Eugeniy and Gavrilov 2007). The four main parameters of interest for the DEGB isothermal experiment are:

- Density ratio
- Reynolds number
- Initial pressure differences between the inside and outside of the vessel
- Existence of obstacle rod (diameter).

The importance of the density ratios and the Reynolds number were already described in the above paragraph. The initial pressure difference was selected for the purpose of estimating the effect of initial momentum inertia on the gravity current. The existence of obstacle rods was selected to be the main parameters for visualizing the effect of the lower plenum post on the gravity current.

3.2.1.3 Experimental Setup

The DEGB isothermal experiment consists of two tanks and a horizontal pipe (See Figure 3-3). The horizontal pipe connects the two tanks as shown. A sliding gate valve is installed along the horizontal pipe to separate the tanks. Initially, both tanks are filled with different fluids having different densities, and the valve is closed. Once the predetermined initial conditions are achieved, the experiments are started by quickly opening the valve. After the valve opens, a counter-current stratified flow is formed in the test-section where the heavy fluid intrudes into the light fluid at the bottom and the light fluid intrudes into the heavy fluid at the top. At the bottom of the two tanks is a port that is linked to the differential pressure (DP) transmitter to be used for setting up the initial pressure equilibrium and stabilization. Each tank also has a pressure transducer for independent pressure monitoring. The tanks and the pipe will be made of transparent acrylic for optical measurements and flow visualization. Both PIV and LIF will be employed for simultaneous measurement of velocity fields and concentration profiles.

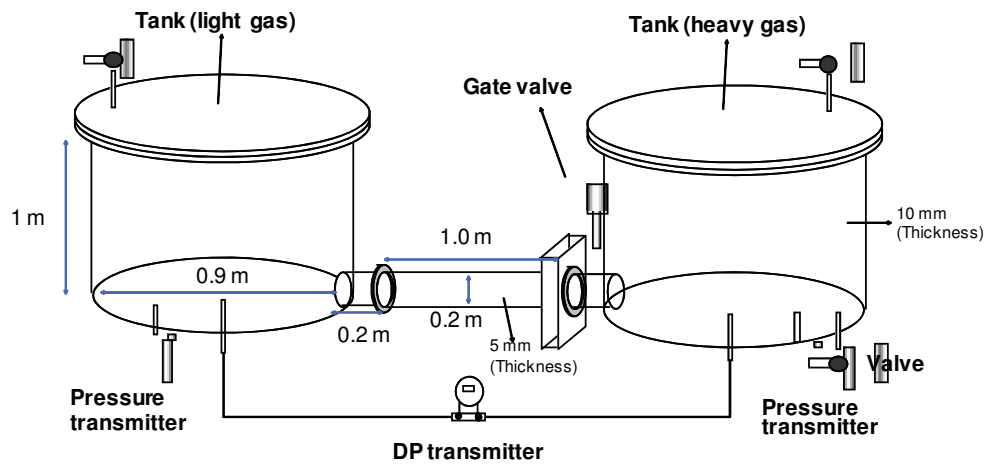


Figure 3-3. Schematics of the isothermal DEGB experiment.

The GTMHR 600 MWth reactor was selected as a reference reactor for the test-section design. As shown in Figure 3-3, the pipe diameter (0.2 m) is approximately 0.13 times smaller than the actual GTMHR hot-duct size. The tank diameter (0.9 m) is scaled to maintain the expansion ratios between the hot duct and the reactor vessel diameters ($d_{\text{hot duct}}/D_{\text{vessel}} = 0.22$) in the reference (GTMHR) reactor. The pressure will range between 1 atm and 3 atm. The working fluids in consideration are He, Air, CO₂, and SF₆. Various combinations of those fluids will be considered.

Table 3-2 displays the Test-Matrix. These experiments cover the range of density ratios from 0.03 to 0.46, and Reynolds numbers from 2.3×10^4 to 6.93×10^5 . Therefore, the main flow regimes are in the non-Boussinesq (large density differences) and turbulent flow (low viscous effect) regimes, which are the same flow regimes predicted in the actual air-ingress accident.

Figure 3-4 shows the experimental regime (Blue Region) and the actual accident regime (Yellow Region). The actual accident conditions were calculated by assuming and changing the air mass fractions (0.1–1.0) and temperatures (25–200°C) in the confinement. The pressure was assumed to be ambient pressure (1 atm) in all cases. This figure shows that the experimental test matrix in Table 3-2 (Blue Region in Figure 3-4) covers most of the actual accident regime (Yellow Region).

Table 3-2. Test matrix of isothermal DEGB experiment.

Light Fluid	Heavy Fluid	γ	Re	P (Light) [atm]	P (Heavy) [atm]
Air	SF ₆	0.19	1.17E+05	1	1
Air	SF ₆	0.19	2.39E+05	2	2
Air	SF ₆	0.19	3.66E+05	3	3
He	SF ₆	0.03	3.40E+05	1	1
He	SF ₆	0.03	6.93E+05	2	2
He	SF ₆	0.03	1.06E+06	3	3
He/ SF ₆ (5.5:4.5)	SF ₆	0.46	5.10E+04	1	1
He/ SF ₆ (5.5:4.5)	SF ₆	0.46	1.03E+05	2	2
He/ SF ₆ (5.5:4.5)	SF ₆	0.46	1.57E+05	3	3
CO ₂	SF ₆	0.3	7.29E+04	1	1
CO ₂	SF ₆	0.3	1.48E+05	2	2
CO ₂	SF ₆	0.3	2.25E+05	3	3
CO ₂ /He (2:8)	CO ₂	0.27	2.30E+04	1	1
CO ₂ /He (2:8)	CO ₂	0.27	4.67E+04	2	2
CO ₂ /He (2:8)	CO ₂	0.27	7.06E+04	3	3
He	SF ₆	0.03	3.40E+05	1	1
He	SF ₆	0.03	6.93E+05	2	1
He	SF ₆	0.03	1.06E+06	3	1

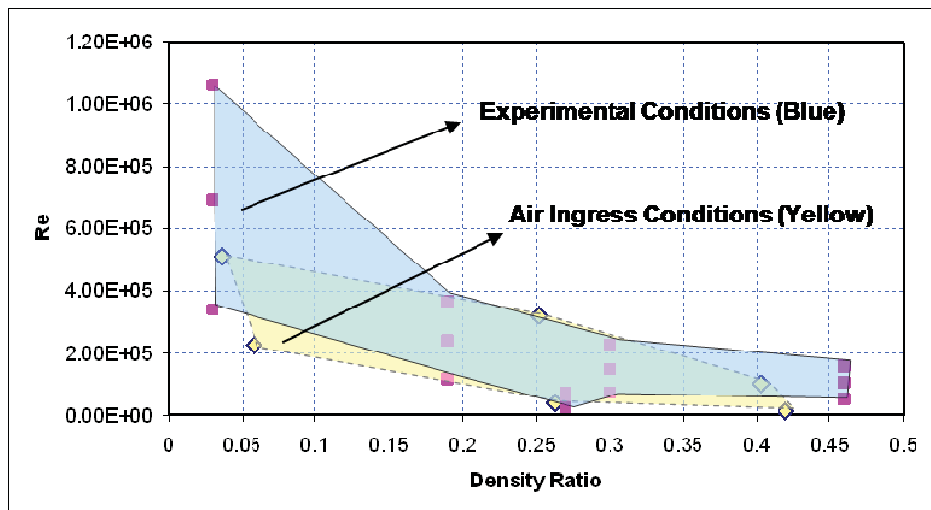


Figure 3-4. Estimated accidental flow regime and experimental conditions.

Since the DEGB experiment will be operated in the pressurized conditions, the pipe and tank thicknesses must be carefully determined with adequate safety margins. The wall thicknesses of the pipe and the tanks that provide adequate safety were determined to be 2 mm (0.002 m) and 10 mm (0.01 m), respectively. Figure 3-5 shows the relations between the wall thickness and the maximum stress. This calculation assumes that the maximum inside pressure of the pipe and the tanks are 4 atm (experimental ranges: 1–3 atm). The estimations for maximum stress were based on the stress in a general thick-walled pipe or cylinder (Crandall et al. 1972). As shown in this figure, maximum stress decreases exponentially with wall thickness. In the figure, the red-line (at 464 atm) represents the minimum allowable tensile stress data for acrylic glass. Therefore, if the maximum stress is higher than the red-line, the structure will be fractured. This figure confirms that the thicknesses determined for this experimental apparatus are sufficient. The safety factors estimated in the pipe and the tanks are 3.07 and 3.41, respectively.

The obstacle rod was determined to be 0.046 m in diameter, which maintains the Reynolds numbers scaling between the prototype (actual reactor conditions) and the experiment. The arrangement of the rods will be determined later.

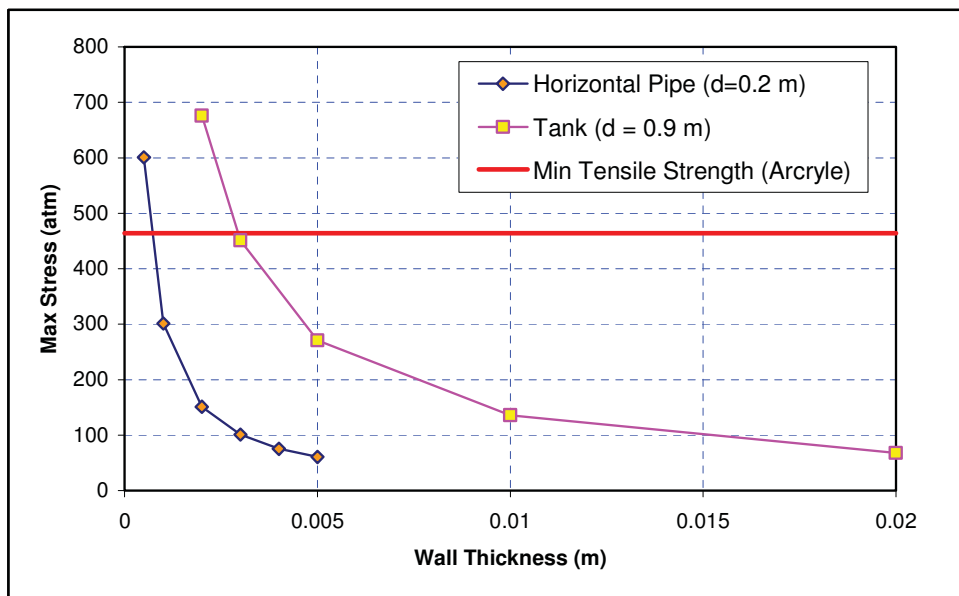


Figure 3-5. Pipe and tank wall thicknesses vs. maximum stress in the wall.

3.2.1.4 Experimental Procedure

The procedure for the DEGB isothermal experimental is as follows:

1. Open the sliding gate valve.
2. Remove all air in the test-section (both tanks and pipe) using a vacuum pump.
3. Close the sliding gate valve.
4. Fill the two tanks separately with two different fluids up to the predefined pressures.
5. Install LIF/PIV facility at the measuring location.
6. Stabilize the system.
7. Open the sliding gate valve to initiate the experiment.

8. Measure velocities and concentration profiles in the pipe and the tanks.

3.2.1.5 Measurement

In the current experiment, the main measurement parameters are velocity field and species concentrations. To measure these parameters simultaneously, combined PIV/LIF methods introduced by Sadanandan et al. (2008), Martin and Garcia (2009), Sanada et al. (2003), Cowen et al. (2001), and Hishida and Sakakibara (2000) were considered. The combined PIV/LIF methods are designed to simultaneously measure 2-D velocity fields and species concentrations by using laser sheets and single or multiple digital cameras. In the current experiment, the method used will be based on a single laser and two CCD cameras (one for PIV and the other for LIF) proposed by Hishida (2000). Figure 3-6 shows the basic set-up of the laser and cameras. The laser sheet is movable along the test-section.

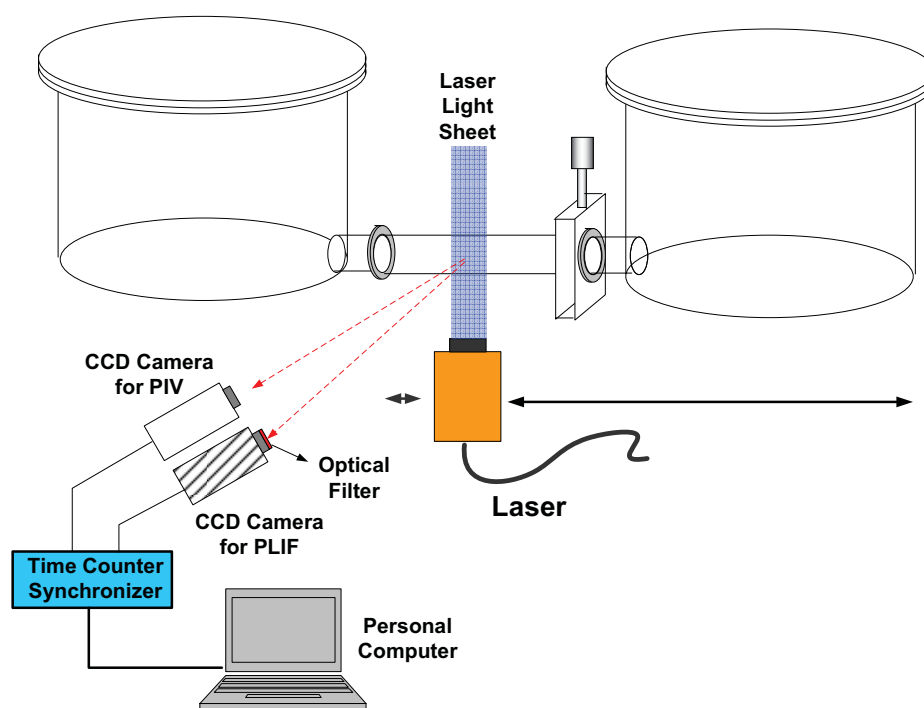


Figure 3-6. Set-up of combined PIV/PLIF system.

LIF is a powerful diagnostic tool for the investigation of nonreacting as well as reacting gas and liquid flows. LIF is a nonintrusive, instantaneous flow visualization technique with high spatial and temporal resolution and is applied to determine different flow-field variables in the plane of a laser light sheet; concentration (mole fraction), density, temperature and velocity fields can be derived from calibrated LIF images.

LIF applies to a large number of molecules and atoms for combustion, spray, and various fluid mechanical flow studies. The LIF detection of atomic species is also called laser excited atomic fluorescence. Combustion species like flame radicals and most fuel species can be visualized directly using LIF. If the flow itself contains no LIF-active species (like N_2 , CH_4 or water), fluorescing markers (tracers) are used to seed the flow for flow-field imaging (Tracer LIF).

The LIF emission is spread over many wavelengths (emission spectrum), with most of the emission red-shifted from the laser line. Because of this spectral shift of the LIF emission, unwanted interferences from stray light or Mie scattering can be effectively suppressed.

LIF is a technique with high selectivity. It is possible to selectively address species to emit light even in combustion environments where hundreds of different species are present. Single quantum states can be detected for small, typically diatomic molecules, which allow gas temperatures to be determined even under nonequilibrium conditions.

LIF imaging is particularly attractive because of the strength of the resonant absorption process compared with the nonresonant Rayleigh and Raman techniques. Because of this sensitivity, LIF has the capability to detect flame radicals and other species at the ppm or even sub-ppm level. Sensitivity and selectivity are the two main advantages of the LIF technique.

Principle of LIF Imaging

In a typical LIF experiment the flow is illuminated by a laser light sheet whose wavelength is tuned to excite a particular transition within the LIF-active molecule (atom). A fraction of the ground state molecules absorb the incident light, which are promoted to a higher (excited) electronic energy state. A fraction of these excited molecules emit light (fluorescence), those which are not dissociated return to the ground state by transferring the excess energy through nonradiative decay processes like collisional quenching or intramolecular deactivation.

For LIF imaging, the laser beam is spread into a sheet, passed through the fluid of interest, and the resulting fluorescence light from the light sheet is imaged through a filter onto a time-gated camera.

PIV, on the other hand, measures whole velocity fields in a laser light sheet by taking two images of the light sheet shortly after each other and calculating the distance individual particles travelled within this time. The velocity is calculated from the known time difference between the two images and the measured displacement. Since the flow can be quite fast, one has to avoid blurred images, which is one reason to use laser pulses. They are only 6–10 ns long and freeze any motion. The other reason is that only laser light can be focused into a thin enough light sheet so that only particles in that plane are imaged. Otherwise the scattered light from particles in other planes would make this measurement impossible. A special camera is used that it can store the first image (frame) fast enough to be ready for the second exposure. The dead time between the frames, when the camera is blind, is very short (down to 100 ns).

3.2.1.6 Comparisons of Experimental Data with CFD

The data obtained in the experiments will be used to validate CFD codes or safety analysis codes. This section summarizes the method and the procedure to be used for code validation.

Front Speed

The first piece of experimental data to be compared with the code results is a front speed, which is the most fundamental characteristic parameter in the gravity current. The front speed will be measured in various locations including the horizontal pipe, the tanks, the connections between the pipe and the tank, and the obstacle rods. Various viscous models (laminar, k-e, k-w, and Reynolds Stress Model [RSM]) will be considered in the code analyses. Conventional image processing techniques will be used to determine the front speed.

Current Depth

The second piece of experimental data to be compared to the code result is a current depth, which is another main characteristic of the gravity current. The current depth will be measured by PLIF with the front speed at the same time. Geometrical characteristics of the current will be also taken into consideration in visualization and assessment.

Concentration Profile

The third piece of experimental data to be used for comparisons is species concentration. The species concentration profiles will be measured in various local positions including the horizontal pipe, the junction between the pipe and the tank, and around the obstacle rods. For comparisons, the front locations of the currents will be matched between the experiment and the calculations. Viscous model effects (laminar, k-e, k-w, and RSM) on the calculation will be also taken into account. Finally, the average uncertainty and local uncertainty will be compared, and the best viscous model will be recommended. The error distributions will be also visualized by contour plots.

Velocity Field

The fourth piece of experimental data to be used for comparisons is velocity data in the test-section. The basic comparison method is the same as that used in the concentration comparisons. Two dimensional velocity magnitude and direction of the in plane velocity components (V_x , V_y) will be compared to the code calculations.

Mixing Parameters

The fifth piece of experimental data that will be compared are mixing parameters. The mixing parameters include Reynolds stress ($u'v'$) and turbulent scalar flux ($c'u'$). The basic method of comparisons is the same as the concentration and velocity comparisons. The comparison of mixing parameters is important, especially for validating the turbulence models.

3.2.2 Isothermal Partial-Break Experiment

3.2.2.1 Background and Objectives

In a VHTR, a partial break of the pipe has a much higher probability of occurrence than the DEGB. It is therefore important to understand air-ingress mechanisms in the partial break scenario for air-ingress safety analyses, even though the consequences of the partial break are less serious than that of the DEGB.

This section summarizes a newly designed isothermal partial-break experiment, which focuses on visualizing the gradient driven flow in the partial break conditions and on generating experimental data for code validation. According to preliminary CFD analyses, the partial break shows much different flow characteristics from those of the DEGB, despite both being governed by the same physical mechanism (density gradient). Computational analyses indicate that the flow pattern is highly dependent on the break orientation; therefore, depending on the break orientation, completely different regimes are encountered. Preliminary analyses indicated that there are three different regimes. Figure 3-7 shows the three flow regimes for three different break orientations. In a bottom break (angle = 0 degrees), the air-ingress is dominated by diffusion process because the heavy fluid is located lower than the lighter fluid (See Figure 3-7 (a)) with low air-ingress speeds. However, in a side break (angle = 90 degrees), a stratified flow is formed by the density gradient with the heavier fluid flowing into the lower part of the lighter fluid. In this case, the flow ingress speed is quite fast. In a top break (angle = 180 degrees), a stable stratified flow is not formed, instead, periodic and intermittent flow is formed at the break point. Air ingress speed is rapidly increased with the angle from 0 to 90 degrees. However, the speed is slowly

decreased for angles from 90 to 180 degrees. Figure 3-8 shows the general trend of the air-ingress flow rate with orientation angles. It shows that the break orientation is an important parameter for determining air-ingress speed. It is therefore necessary to investigate and understand these phenomena.

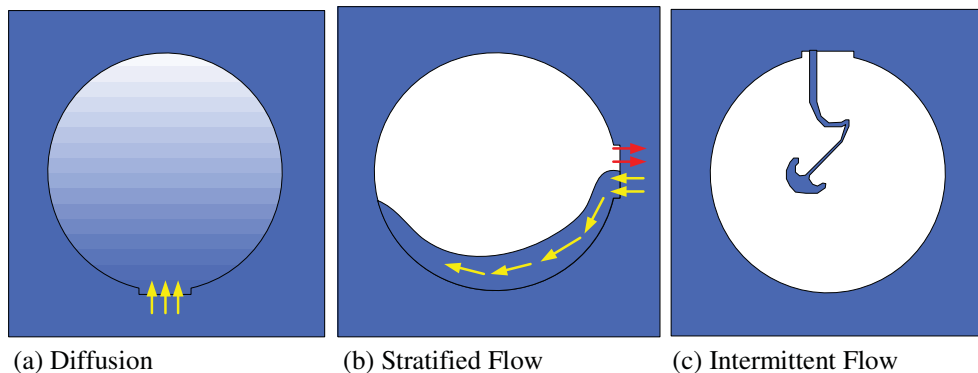


Figure 3-7. Flow Regime of Air Intrusion in the Partial Break (Orientation Effect).

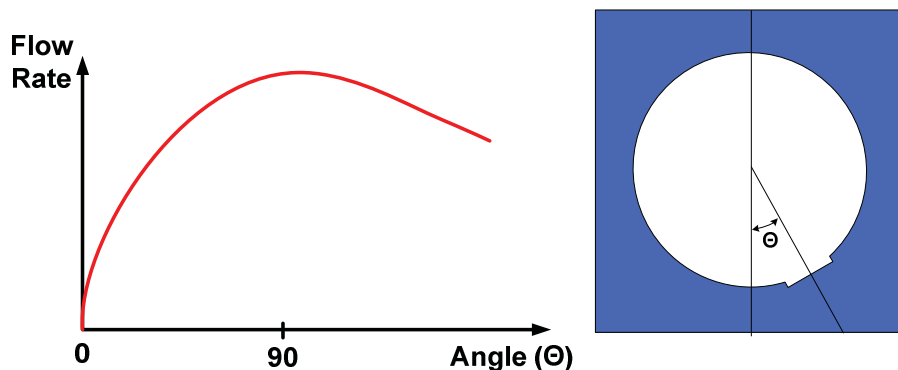


Figure 3-8. Effect of Break Orientation and Flow Rate (Partial Break).

A partial break experiment has three objectives: (1) identify and determine the main parameters affecting air-ingress mechanisms (flow regimes)—a flow regime map for air-ingress will be developed, if needed; (2) validate the computer codes (CFD and safety analysis codes) against the experimental data for the flow regimes or flow and concentration fields; (3) develop models (analytical or empirical) for quantitative prediction of air-ingress speeds in various conditions.

3.2.2.2 Experimental Parameters

In the partial break, the main parameters for the flow regimes and the flow ingress speeds are influenced by various factors such as break orientation, break size, density ratio, and wall thickness. For this reason, preliminary CFD analyses will be performed with parametric studies before the main experimental work starts. Through these analyses, the relative importance of each parameter will be estimated, and the results will be used for refining the test-section design and the detailed test matrix. The benefit of using preliminary CFD analyses is that it is can develop more efficient and higher quality results to the experiment by minimizing unnecessary activities and focusing on essential parts.

3.2.2.3 Experimental Setup

The concept of the partial break experiment is shown in Figure 3-9 where the test-section consists of two cylindrical tanks with different diameters. A smaller tank is located in the inside of the larger tank forming an annular shape. The two tanks are physically separated, and initially filled with different fluids with different densities. A sliding gate valve is installed at the side of the inside tank so when the valve is open, the materials can be exchanged between the inside and outside cylinders. The angle of the break location with the sliding valve can be adjusted by rotating the test-section. The inside and outside tanks are linked by a DP transmitter. The detailed sizes and dimensions of the test-section are to be determined. CFD will be used as a design aid tool. The main parameters that will be measured in this experiment are velocity fields and concentration profiles. For optical measurements, the test-section will be made of transparent materials such as acrylic or polycarbonate. The test-matrix also will be determined after preliminary calculations.

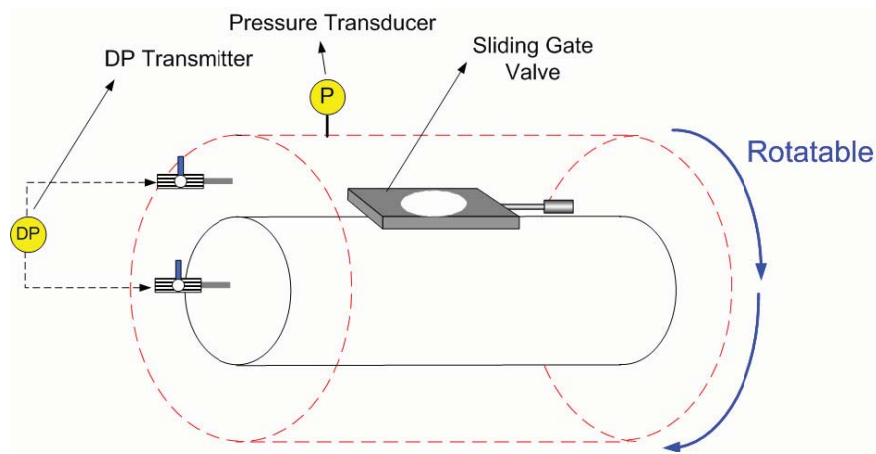


Figure 3-9. Schematics of the partial break experiment.

3.2.2.4 Experimental Procedure

The test procedure for the partial break experiment is as follows:

1. Determine break location in the test section.
2. Install LIF/PIV facility at the measuring location.
3. Remove air in the test section with a vacuum pump.
4. Close the sliding gate valve.
5. Fill the two tanks separately with two different fluids up to the pre-defined pressures.
6. Open the sliding gate valve.
7. Stabilize the two-fluid system.
8. Open the sliding gate valve to initiate the experiment.
9. Measure the velocities and concentration profiles in the pipe and the tanks.

3.2.2.5 Measurement

Velocities and concentration profiles will be measured simultaneously by a combined PIV/PLIF method proposed by Hishida (2000). His method consists of a single laser and two CCD cameras as shown in Figure 3-10. The basic measuring technique is the same as described in the DEGB experiment. The laser is also movable along the test-section.

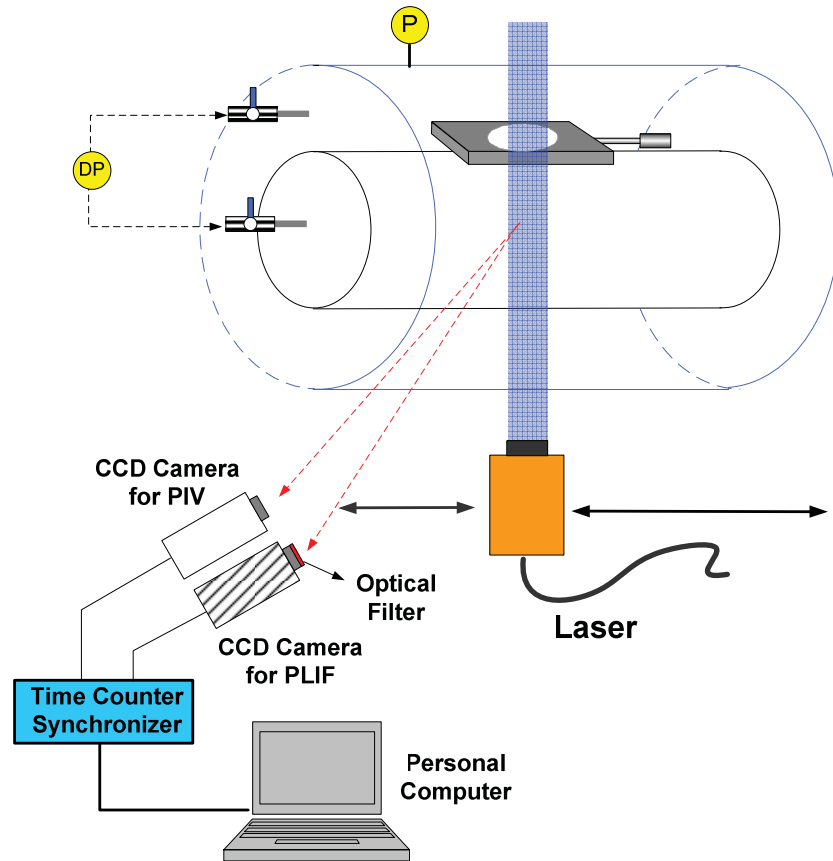


Figure 3-10. Set-up of combined PIV/PLIF system.

3.2.2.6 Experimental Data Assessment

Velocities and species concentration profiles in the partial break experiment, are measured in the inner cylinder. This data can be used to understanding air-ingress mechanisms and validate computer codes. The data assessment and code validation methods planned in the current experiment are summarized.

Observations on the Flow Patterns and Developing Flow Regime Map

The first thing to be done with the experimental data is observing flow patterns and understanding detailed air-ingress mechanisms. In this stage, the experimental data are qualitatively interpreted. After observation of the flow patterns, the experimental data can be used to develop a flow regime map that distinguishes diffusion, stratified, and intermittent flow regimes, if needed.

Comparisons of Average Concentrations with Calculated Results

The second task is to compare average species concentrations, which specifically investigates concentration variations with time. By comparing the average concentration data between the experiment and the code analyses, the capability of the code predictions on the partial break air-ingress scenario will be assessed for the different flow regimes. The various viscous models (laminar, k-e, k-w, RSM) will also be taken into consideration for code analyses.

Comparisons of Local Velocity Field and Concentration Profiles with Calculations

After comparing the averaged concentrations, some local variables, including velocities and species concentrations between the experiment and the calculations, will be compared. The local uncertainty will be estimated by comparisons, and the result will be used to assess if the codes or models apply to the partial break air-ingress analyses.

Comparisons of Mixing Parameters

Besides local velocities and concentrations, mixing parameters such as Reynolds stress ($u'v'$) and turbulent scalar flux ($c'u'$) will be compared. The comparison methods are the same as those described in the local concentration and velocity comparisons.

3.3 CFD Analyses of Isothermal Stratified Flow Experiment

The following section details the blind 3-D CFD analysis performed for the DEGB experiment in Star-CCM+ v4.02.011. One of the main objectives of the DEGB experiment is to provide validation data for comparison with the results from the numerical codes and to aid in the improvement of predictive models. In this section, results from simple lock exchange simulations in cylindrical and rectangular channel geometries are presented as well as preliminary simulation results of the DEGB experiment.

The simulation of different channel geometries for a lock exchange counter current flow allows a comparison between phenomena present in the different channel geometries. It also enables a comparison with the predictions of the analytical model for simple counter current lock exchange flows as described in Section 2.2.

3.3.1 Lock Exchange Simulations

3.3.1.1 Model and Initial Conditions

The model scale used for lock exchange simulations was chosen based on the height scale of the horizontal pipe of the DEGB experimental facility. The two different channels, one rectangular and the other cylindrical, had a maximum height (H) of 0.2 m and were 4 m long. The lock exchange interface was equidistant from the channel ends. The discretized mesh used for both channel models consisted of polyhedral cells with a base size of 0.005 m. Two prism layers were used along the wall and a high y^+ wall treatment was applied in the near-wall region. In total, 2.8 million and 1.6 million polyhedral cells were used to discretize rectangular and cylindrical models, respectively.

A simplified gate interface was used instead of simulating the thickness of the sliding gate. At $t = 0$, the gate interface between the two fluid species was removed and the species were allowed to interact. The two fluids for the simple lock exchange problem were H_2O and a saturated mixture of H_2O and $NaCl$. Atmospheric pressure was used for both fluids.

3.3.1.2 Numerical Models and Solver Criterion

Based on a literature review of previous work, the counter current stratified flow has significant turbulence in the form of Kelvin-Helmholtz billows. This turbulent regime, along with the transient nature of the problem, influenced the choice in models and solver technique.

The numerical models and solver schemes used for the following simulations are as follows:

- 3-D
- Mass, momentum, energy, multiple-component fluid, standard k- ϵ turbulence
- Segregated (for H₂O/NaCl, Coupled for He/CO₂) flow and energy solver algorithm
- 2nd Order up-winding scheme convection scheme
- Implicit unsteady with 2nd order temporal discretization scheme
- Global time step: 0.001–0.005 seconds
 - Total Calculation Time: 2.5 seconds
- Residual criteria for all variables $<10^{-4}$
- Density ratio (γ): 0.83 for H₂O and H₂O/NaCl solution.

3.3.1.3 Results

Rectangular Channel

The results from the first 2-1/2 seconds following the opening of the lock show a nearly constant result along the width of the channel and strong interfacial turbulence in the form of Kelvin-Helmholtz billows (see Figures 3-11 through 3-15).

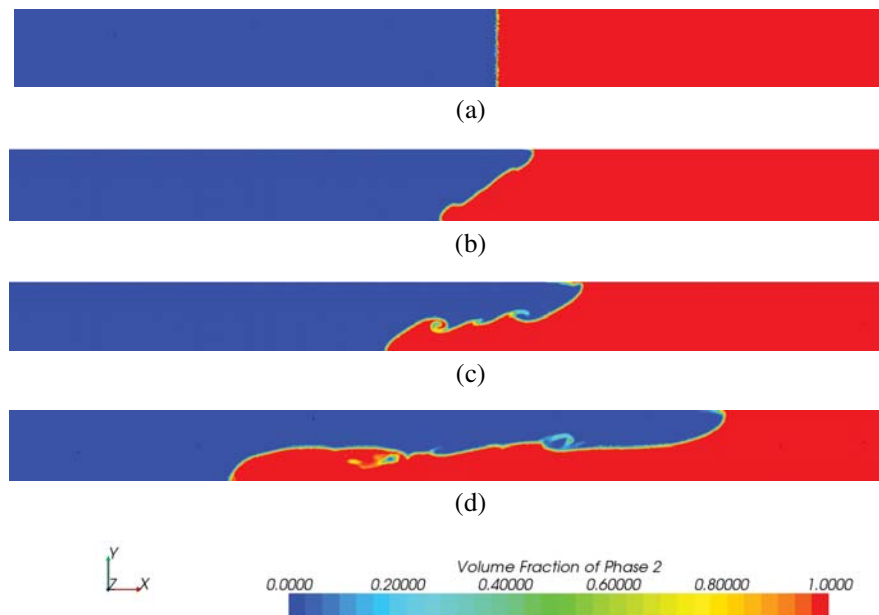


Figure 3-11. Counter current flow in a rectangular channel at $t=0$ (a), 0.5 (b), 1 (c), and 2.5 (d) seconds.

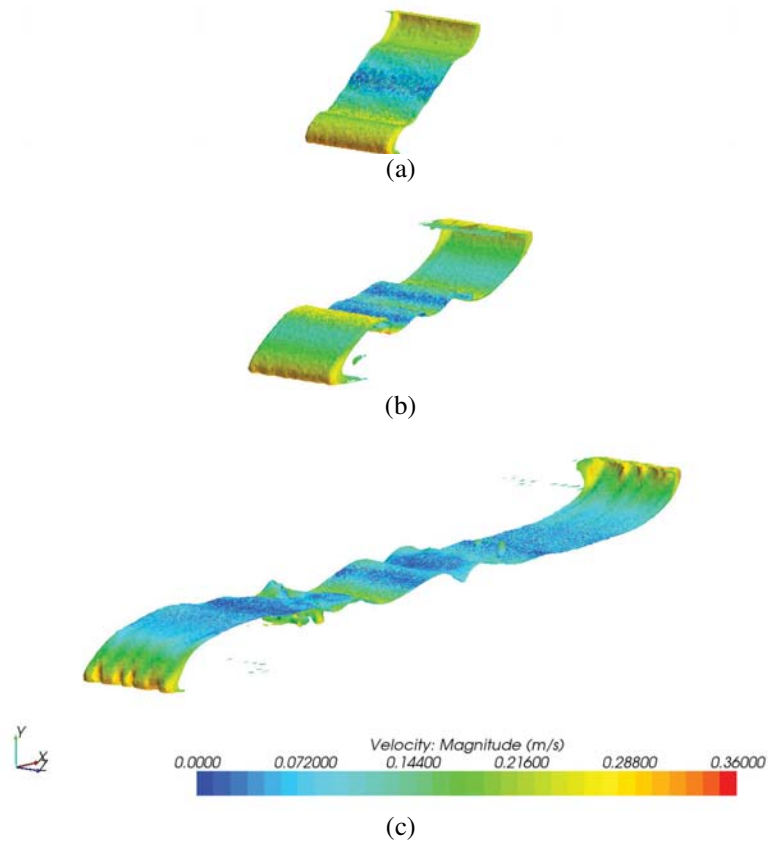


Figure 3-12. Counter current flow species interface with velocity mapping in a rectangular channel at $t = 0.5$ (a), 1 (b), and 2.5 (c) seconds.

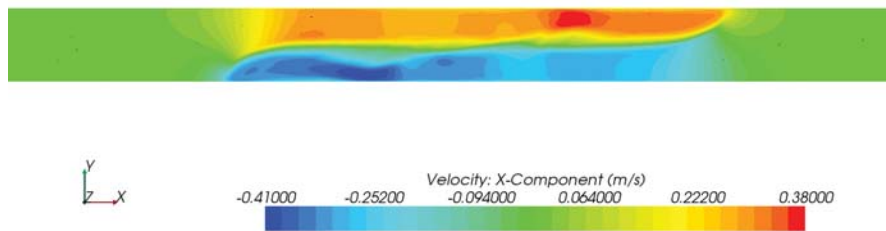


Figure 3-13. X- velocity component in a rectangular channel at $t = 2.5$ seconds.

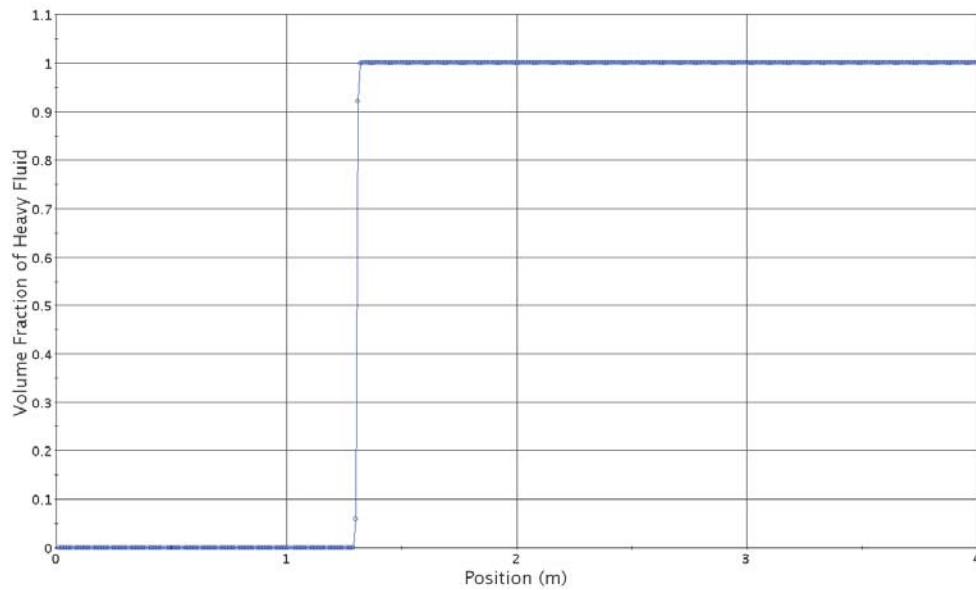


Figure 3-14. NaCl species volume fraction along horizontal line probe through flow front at $t = 2.5$ seconds.

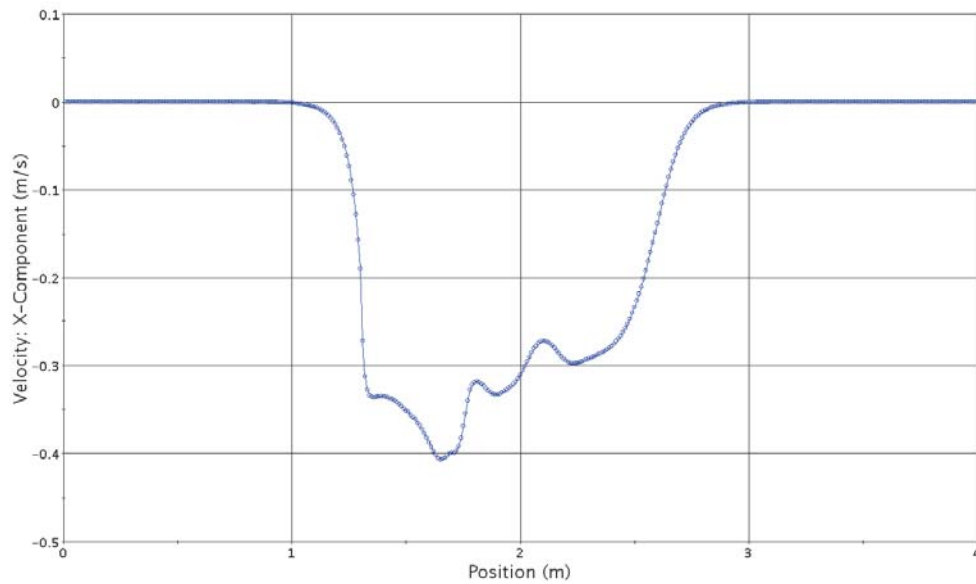


Figure 3-15. X-velocity component along horizontal line probe through flow front at $t = 2.5$ seconds.

Cylindrical Channel

The results from the cylindrical channel in the first 2-1/2 seconds following the opening of the lock differed slightly from those of the rectangular channel as shown in Figures 3-16 through 3-20. As seen in Figure 3-16, the interface velocities in the cylindrical channel do not have the uniformity in the z -direction as they do in the rectangular channel in Figure 3-11.

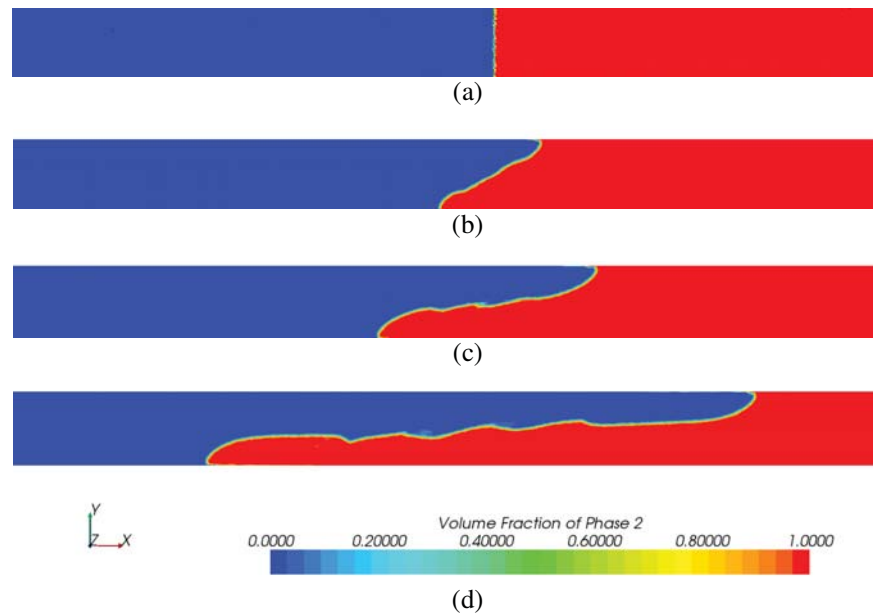


Figure 3-16. Counter current flow in a cylindrical channel at $t = 0$ (a), 0.5 (b), 1(c), and 2.5 (d) seconds.

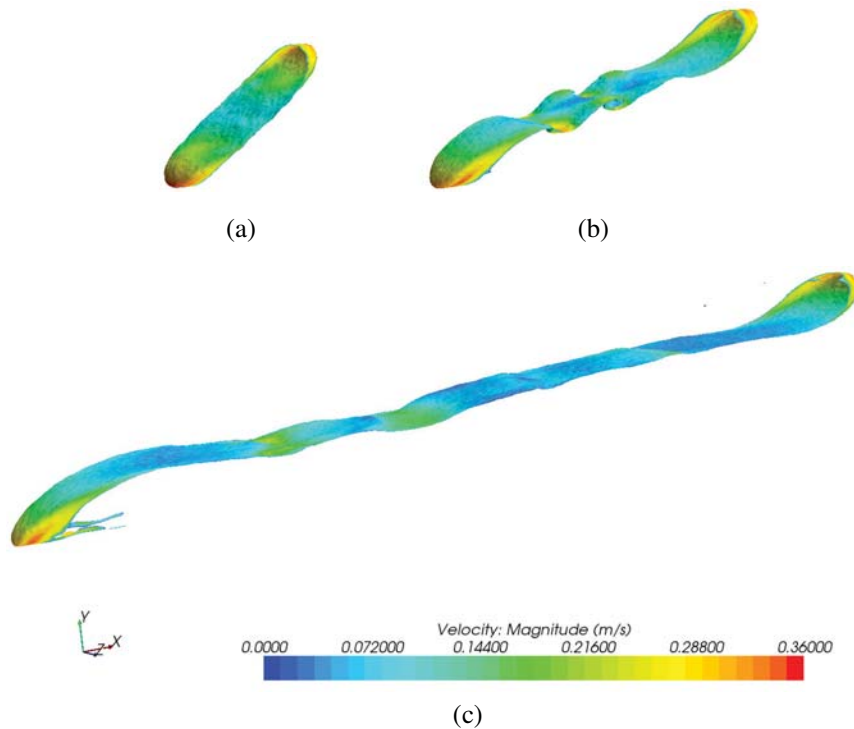


Figure 3-17. Counter current flow species interface with velocity mapping in a cylindrical channel at $t =$ (a)0.5, (b)1, and (c)2.5 seconds.

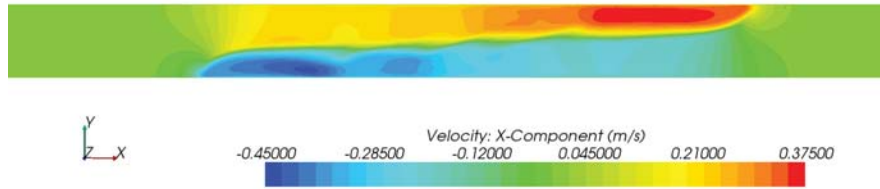


Figure 3-18. X- velocity component in a cylindrical channel at $t = 2.5$ seconds.

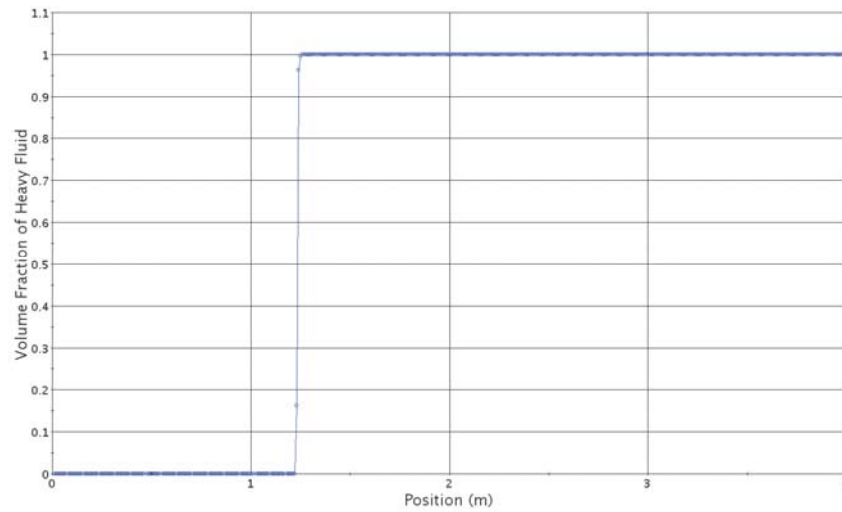


Figure 3-19. NaCl species volume fraction along horizontal line probe through flow front at $t = 2.5$ seconds.

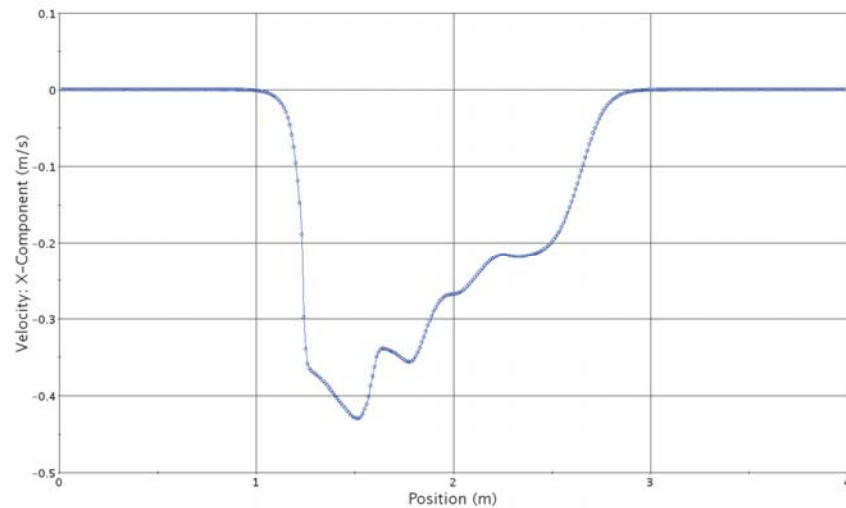


Figure 3-20. X-velocity component along horizontal line probe through flow front at $t = 2.5$ seconds.

3.3.1.4 Discussion

The results of the two different channel lock exchange flow configurations show good correlation with the analytic models presented in Section 2.2. As expected, the width of the rectangular channel had no effect on front velocity, but, in the case of the cylindrical channel, it is seen that there is a velocity gradient across the front. Near the lock location, higher velocities in both heavy and light fluids were located along the interface near the channel walls. This is thought to be the case because of the conservation of mass and the channel height being reduced in these locations. Towards the flow front, the maximum velocity shifts back to the center and into the front wedge.

The simulations produced Kelvin-Helmholtz billows, as seen in previous works, and velocity concentrations in both species were located at these sites. The size and definition of the instabilities in the rectangular channel were greater than in the cylindrical channel.

In the case of H₂O and a saturated NaCl mixture, the density ratio (γ) is approximately 0.83. The analytical predictions of Equations 2-21 and 2-23, respectively, for the case in which $\gamma^* < \gamma < 1$ are

$$U_L = \frac{1}{2} \sqrt{(1-\gamma)gH} = 0.29 \text{ m/s} \quad (3-1)$$

$$U_H = \frac{1}{2} \sqrt{\frac{(1-\gamma)}{\gamma} gH} = 0.31 \text{ m/s} . \quad (3-2)$$

The frontal speeds predicted by the code for the heavy fluid in the rectangular and cylindrical channels were 0.34 and 0.355 m/s, respectively. Comparing the front location and speed between the two channel configurations, it is predicted that the front in a cylindrical pipe would ingress at a faster rate than the analytical model suggests for a rectangular channel in the case where $\gamma^* < \gamma < 1$.

3.3.2 DEGB Simulations

3.3.2.1 Model and Initial Conditions

The model used for the DEGB simulations was the same as that of the DEGB experimental facility. The discretized mesh used for both models consisted of polyhedral cells with a base size of 0.0049m within the horizontal pipe and 3.5 cm within the large tanks. Three prism layers were used along wall interfaces within the tanks, and four were used within the horizontal pipe. In total, 688,000 polyhedral cells were used to discretize the model.

Just as in the lock exchange simulation, a simplified gate interface was used instead of simulating the thickness of the sliding gate. At $t = 0$, the gate interface between the two gas species is removed and the species are allowed to interact. The gate location can be seen in the facility model, in Figure 3-21(a), to be 1.55 m from the simulated lower plenum tank edge (right tank). Dimensions of the fluid domain satisfied the same dimensions outlined for the experiment in Figure 3-3 and full schematics may be found in Appendix A of this report.

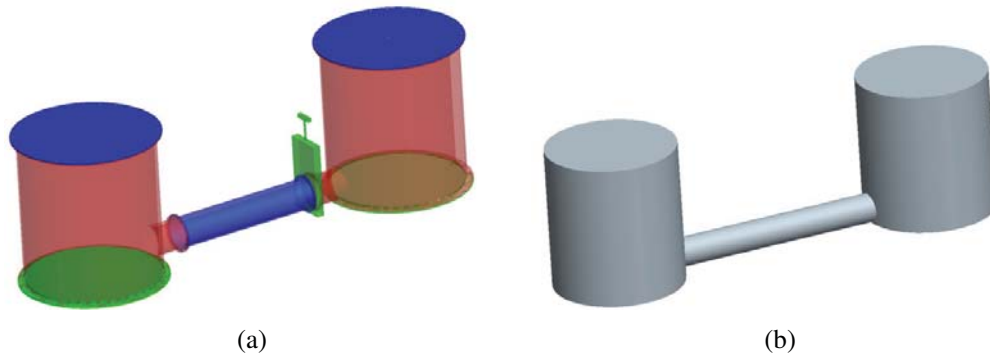


Figure 3-21. Facility model (a) from which the fluid domain (b) was extracted

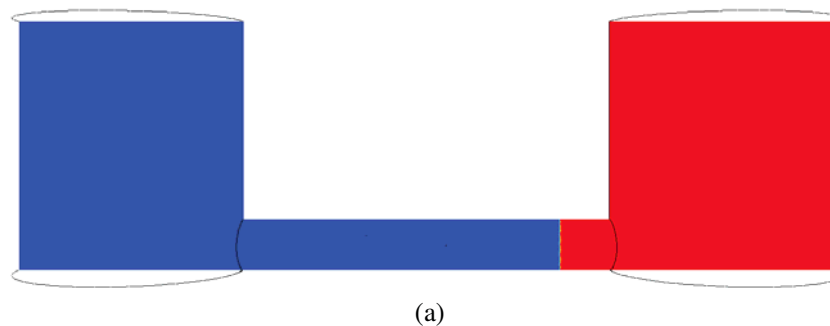
3.3.2.2 Numerical Models and Solver Criterion

The numerical models and solver schemes used for the following simulations are as follows:

- 3-D
- Mass, momentum, energy, multiple-component gas, standard k- ϵ turbulence
- Coupled flow and energy solver algorithm
- Ideal gas properties
- 2nd Order up-winding scheme convection scheme
- Implicit unsteady with 2nd order temporal discretization scheme
- Global time step: 0.001–0.005 seconds
 - Total calculation time: 2.5 seconds
- Residual criteria for all variables $<10^{-4}$
- Density ratio (γ): 0.091 for CO₂ and He.

3.3.2.3 Results

CFD results of the DEGB experiment have been obtained for the first 0.5 seconds following the opening of the valve. The results shown in Figures 3-22 through 3-28 are the initial results to be used in the validation of the code and models with the DEGB experiment.



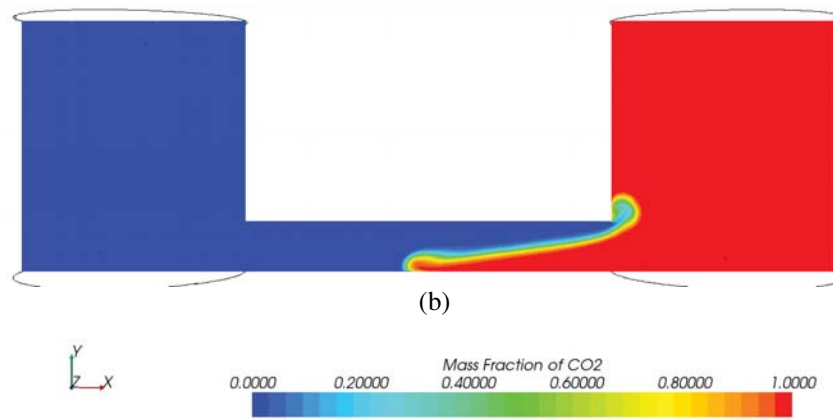


Figure 3-22. Mass fraction of CO2 at $t = 0$ (a) and 0.5 (b) seconds.

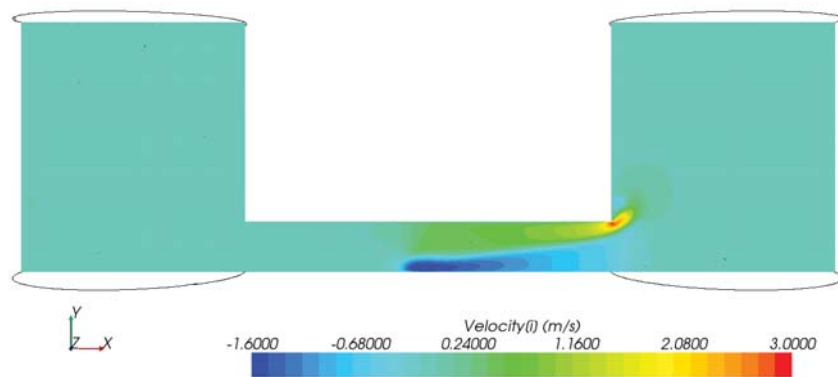


Figure 3-23. X-velocity component at $t = 0.5$ seconds.

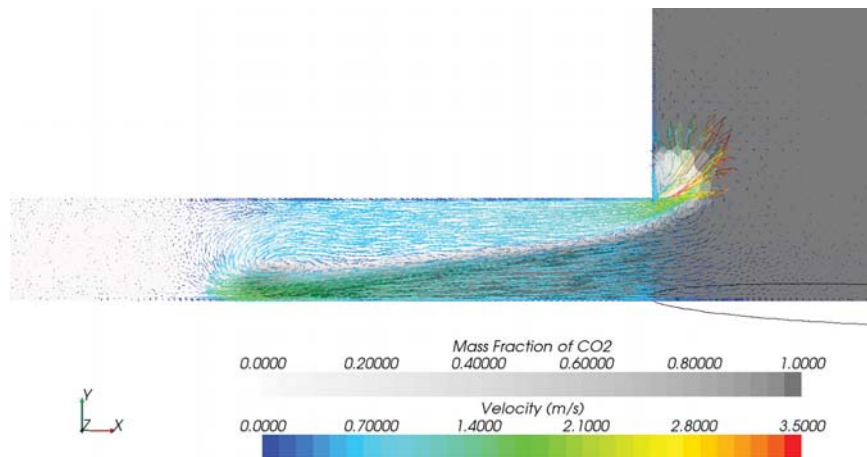


Figure 3-24. Velocity vectors and density gradient at $t = 0.5$ seconds.

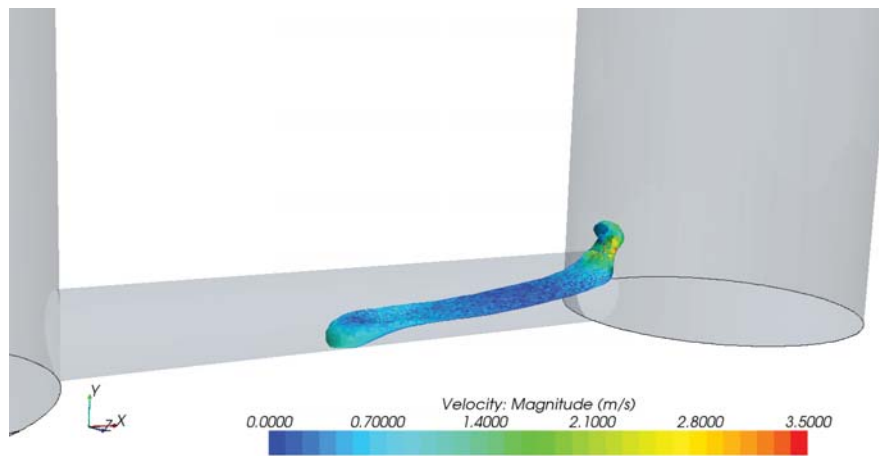


Figure 3-25. Isosurface of flow interface with velocity mapping at $t = 0.5$ seconds.

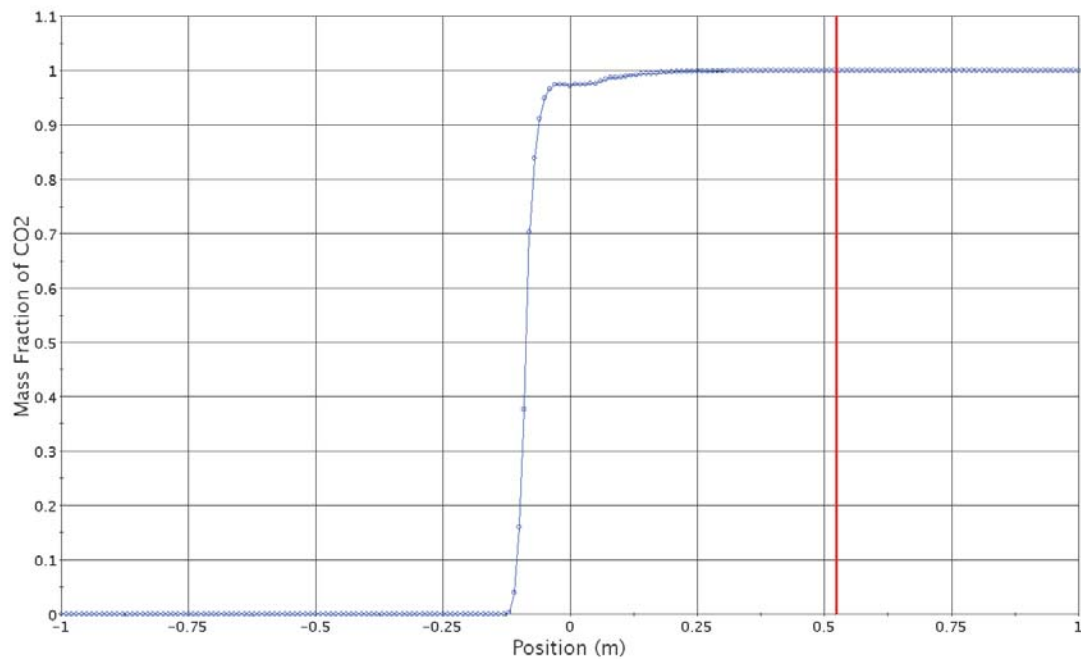


Figure 3-26. Mass fraction along horizontal line probe through flow front at $t = 0.5$ seconds; the red line indicates the initial break location.

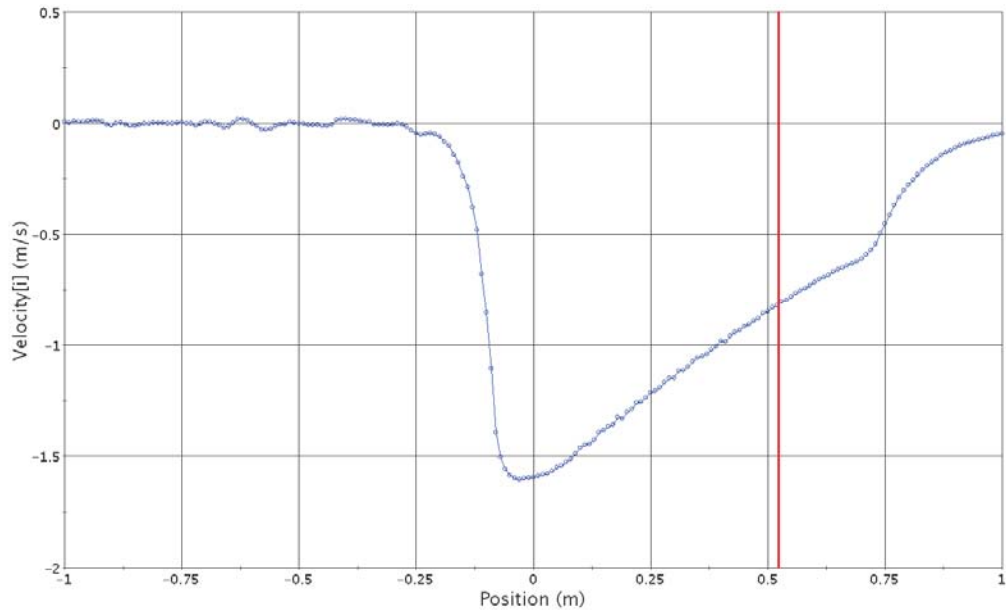


Figure 3-27. Plot of x-velocity component along horizontal line probe through flow front at $t = 2.5$ seconds; the red line indicates the initial break location.

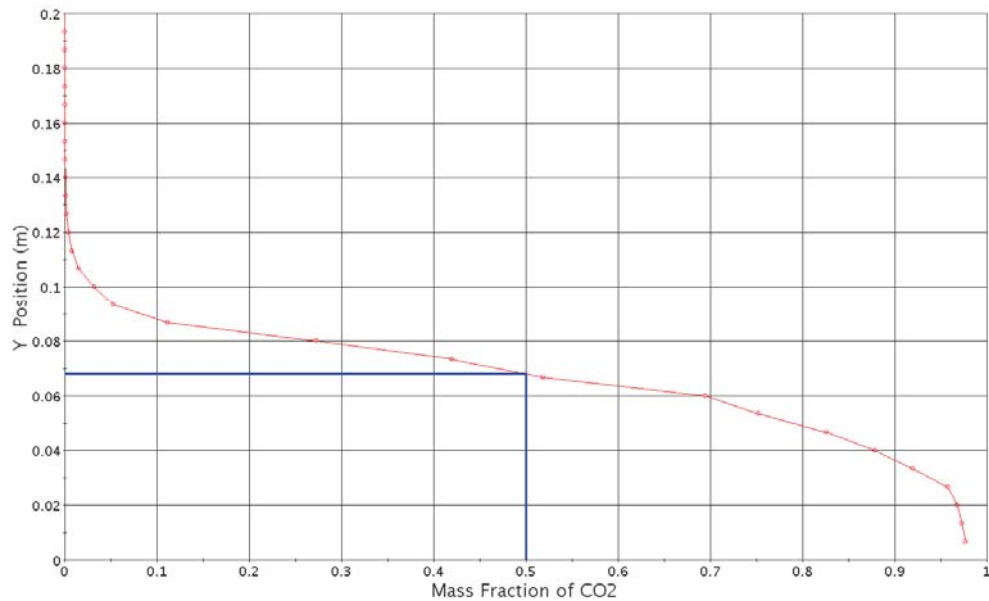


Figure 3-28. Plot indicating flow height with mass fraction ($mf = 0.5$ at interface) at $t = 0.5$ seconds.

The front height is taken to be approximately 0.068 m from the channel bottom, giving a fractional height (h/H) = 0.34.

3.3.2.4 Discussion

The results of the first 0.5 seconds following the simulated break of a pure He/CO₂ exchange clearly show that the flow follows the regime indicated in Figure 2-14(b) for flows in which the density ratio is below a critical density ratio. In this regime, limited instabilities are generated at the stratified interface, resulting in no Kelvin-Helmholtz billows being produced in the counter current flow.

In the case of He and CO₂, the density ratio (γ) is approximately 0.091. The analytical predictions of Equations 2-21 and 2-25, respectively, for the case in which $0 < \gamma < \gamma^*$ are

$$U_L = \frac{1}{2} \sqrt{(1-\gamma)gH} = 0.67 \text{ m/s} \quad (3-3)$$

$$U_H = \sqrt{(1-\gamma)gH} \left[\frac{1}{\gamma} \frac{h_H}{H} \left(2 - \frac{h_H}{H} \right) \frac{1 - h_H/H}{1 + h_H/H} \right]^{1/2} = 1.68 \text{ m/s}. \quad (3-4)$$

The frontal speed predicted by the current code and models for the CO₂ in the experimental facility was 1.60 m/s. The analytical prediction for a density driven counter current exchange in a rectangular channel was approximately 5% higher. The result of the fractional height matches within 3% of Benjamin's theory prediction of depth, 0.35, in a maximum dissipation lock exchange flow.

3.3.3 Conclusions

The results obtained using Star-CCM+ v4.02.011 and models for the lock exchange as well as the DEGB simulations show a level of consistency with analytical models developed in previous works. The variations in flow features in the differing channel geometries are readily seen in the lock exchange investigation, but they are still within a reasonable limit of previous works. The DEGB experiment consists of many variations in gases as well as pressures. Thus far, the simulation of one case on the lower end of the density ratios being tested has produced good results that are within 5% of predicted values; however, further simulations of the gravity driven flows inside the experimental lower plenum and other gas configurations are needed to verify that the results of air ingress incidents are accurate over a range of conditions.

3.3.4 Preliminary CFD Analyses on the Partial Break

Some preliminary CFD analyses have been performed to fully understand the partial break accidents before the detailed experimental design. One of the most important aspects in the partial break situation is that the flow characteristics are highly dependent on the break angle. Figure 3-29 shows the scheme of the general partial break situation. The cylinder is initially filled with helium (light fluid) while outside the cylinder is initially filled with air (heavy fluid.)

In this figure, the first regime is molecular diffusion. In the case where the break is at the bottom of the pipe, gravitational force keeps the air from mixing with the helium through either of the second two regimes. For this reason, only diffusion governs the exchange in this case. The second regime is gravity-driven flow. Heavier fluid goes into the lower part of the hole as a counter current flow that is stratified with the lighter fluid exiting in the upper portion. The last regime is an unstable gravity-driven flow for an angle of 180 deg. The helium exit flow is counter currently choked with the air inlet flow. The air flow rate is not constant and will be much smaller than in the second regime.

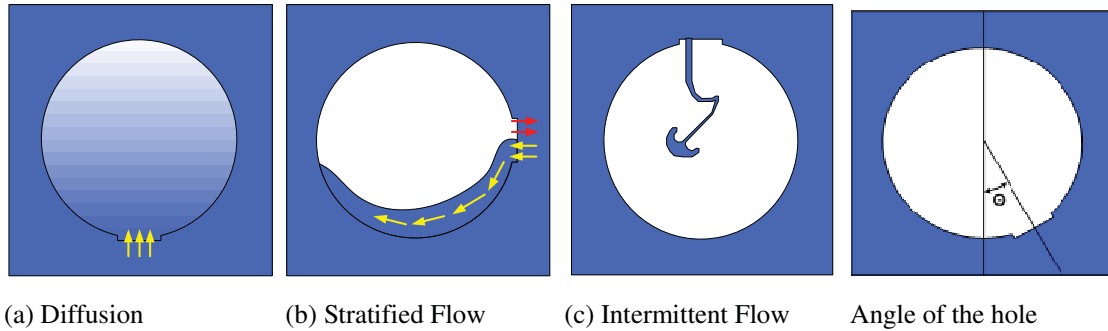


Figure 3-29. Three different regimes created depending on the break angle of the hole.

The objective of the CFD calculation is to observe these three different regimes, depending on the angle. These analyses adopted a simple 2-D geometry, which consists of two cylinders with annular arrangements. Since the zone of interest is the inner cylinder, mesh is more precise in it than in the outer cylinder. The diameter of the inner cylinder was assumed to be 2.4 m, which is the cold leg diameter in GTMHR 600 MWth design. The diameter of the outer cylinder was arbitrarily determined to be 7.2 m. The break size was assumed to be 0.76 m, which represents 10%. To model the presence of two different species, the multiphase model in FLUENT was adopted. For a preliminary study, a standard k- ϵ turbulent model was selected here. Second order accuracy in time and space was considered to minimize numerical diffusion. Initially, the inner cylinder was filled with helium (light fluid) and the outer cylinder with air. Seven cases were made for the analyses: 0, 45, 90, 112.5, 135, 157.5 and 180 degrees.

Figure 3-30 shows the simulation results for break angle = 0 deg, which represents the first regime (diffusion). The diffusion regime is very slow as predicted and no noticeable changes occur in a time scale of 10 seconds.

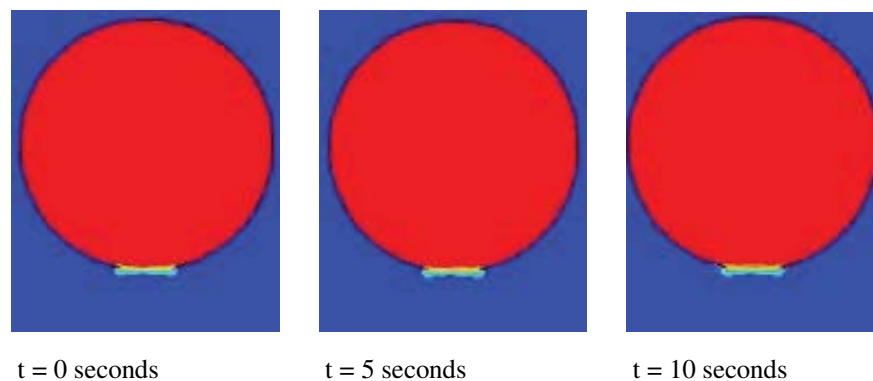


Figure 3-30. Diffusion regime (break angle = 0 deg).

Figure 3-31 shows the simulation results for break angle = 112.5 degrees, which represents the second regime (stratified flow). At the beginning, air enters the cylinder because of the density difference. Gravity forces the flow to follow the bottom part of the inner cylinder. It seems it doesn't lose so much energy, as it climbs at the altitude of the hole on the other side of the wall. Its momentum then forces it to spiral and mix with helium. After 6 seconds, a boundary begins to stabilize at the height of the hole. Wave motion can be seen on the interface. On the other hand, helium, which is lighter than the air, rises in the outer cylinder. A bubble of gas is created 1 second after the beginning and then mushrooms after 2 seconds. Next, the exiting plume straightens out.

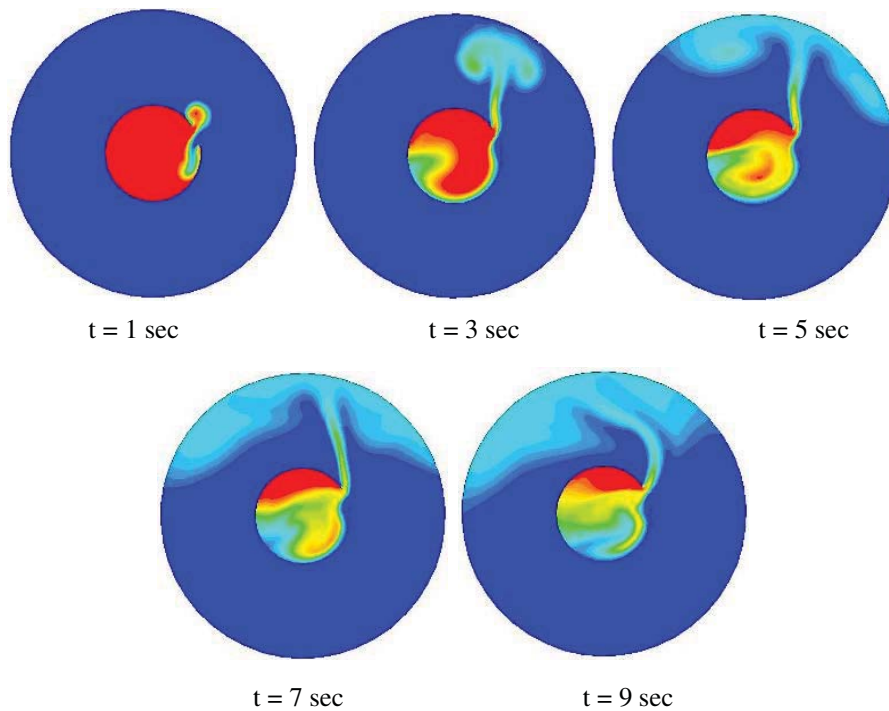


Figure 3-31. Stratified flow regime (break angle = 112.5 deg).

Figure 3-32 shows the simulation results for break angle = 180, which represents the intermittent flow regime. The 180 degree case is totally different from the previous one. Air cannot flow directly along the bottom of a helium flow because of the orientation of the hole. The initial interface is unstable and the interface will roll-up. This helium bubble created within the outer tank is mirrored by an air bubble within the inner volume. The process of this exchange creates a pulsed flow across the break.

Figure 3-33 shows the relations between break angles and maximum air flow rates. Air flow initially increases with break angle and peaks around 125 deg. The flow rate then rapidly drops with angle, owing to the flow conflict between inflows and outflows as seen in the intermittent flow regime. When the break angles reach 180 deg, the flow rate is decreased to 25% of the maximum flow rate.

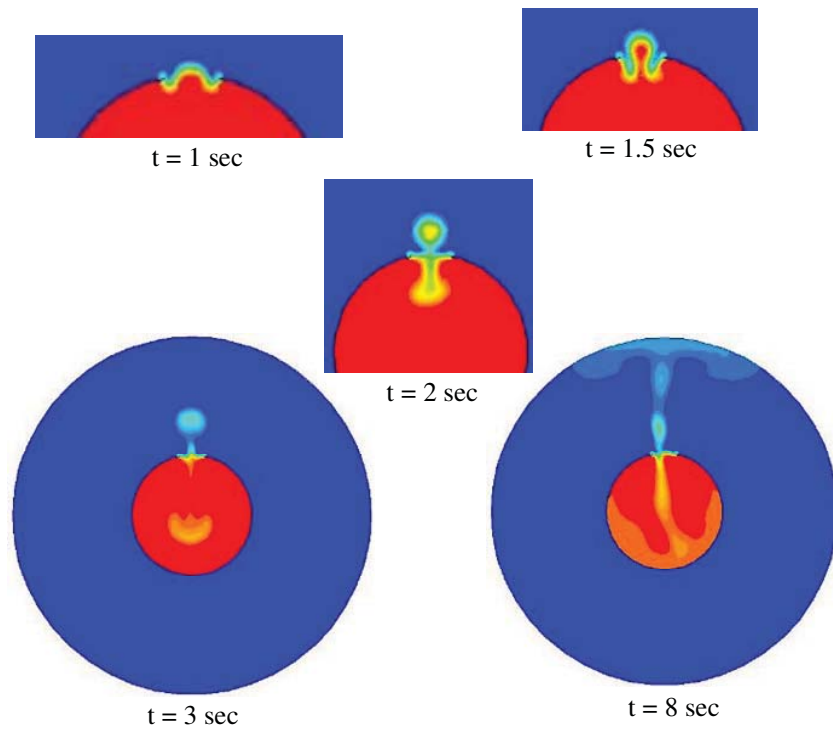


Figure 3-32. Intermittent flow regime (break angle = 180 deg).

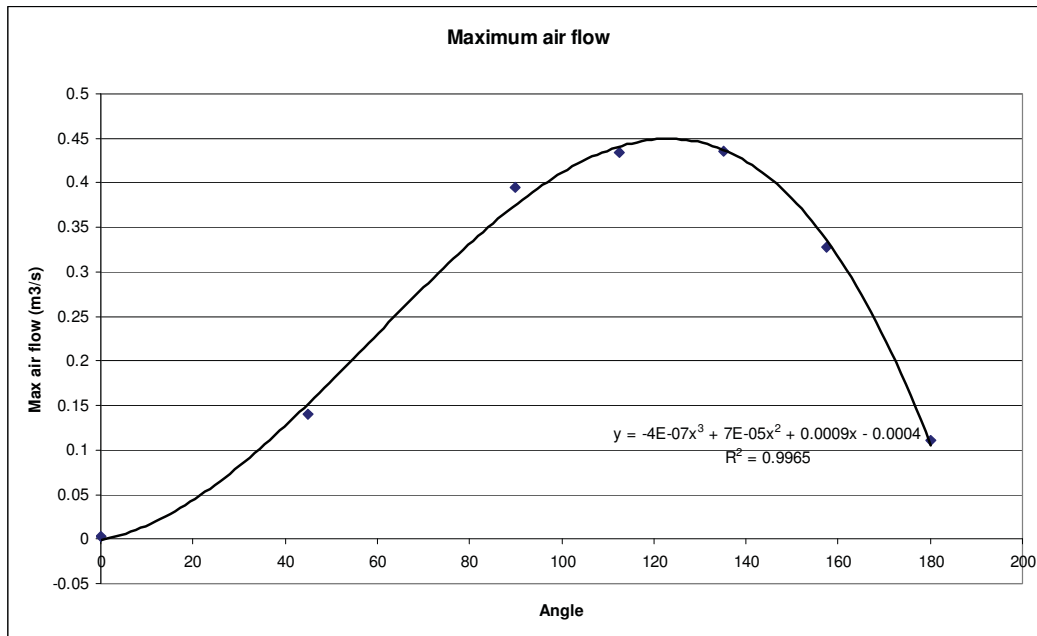


Figure 3-33. Break angle vs. maximum volumetric flow rate.

3.4 Isothermal Wedge Flow Experiment in University of Idaho

3.4.1 Apparatus and Procedure

An air-water-brine flow test loop was used to demonstrate the air ingress event under laboratory conditions as shown in Figure 3-34. A 38.1 mm (1.5 inch) internal diameter and 1,143 mm (45 inch) long clear glass pipe connects two reservoirs. The top of one of these reservoirs is open to the atmosphere while the other has a cap. Pressured air can be supplied to the level liquid surface in the capped reservoir. Both water-brine and, separately, oil-air were used for the demonstration; water and brine are miscible and the difference in specific gravity between them is small. Oil and air are not miscible and the difference in specific gravity between them is large. Intrusion of the heavier fluid underneath the counter flowing lighter fluid can be demonstrated as a moving wedge and a well defined head of a density current. Also observable are interfacial mixing and interfacial wave propagation.

Prior to initiating a water-brine test, the open reservoir is filled with brine, colored purple with potassium permanganate, to a level above the crown of the connecting pipe. The capped reservoir at atmospheric pressure is filled with fresh water to a level above the crown of the pipe, but below the level of the brine. The connecting pipe is closed at the brine end by placing the base of a paper cup against the pipe opening. The higher head on the brine side presses the cup base against the reservoir wall and keeps the two fluids separated. A test starts by applying air pressure to the water surface of the capped reservoir and drives the fresh water into the brine reservoir via the pipe. Upon the onset of the fresh water flow in the pipe, the cup is pushed away and the brine starts to intrude into the lower portion of the pipe cross-

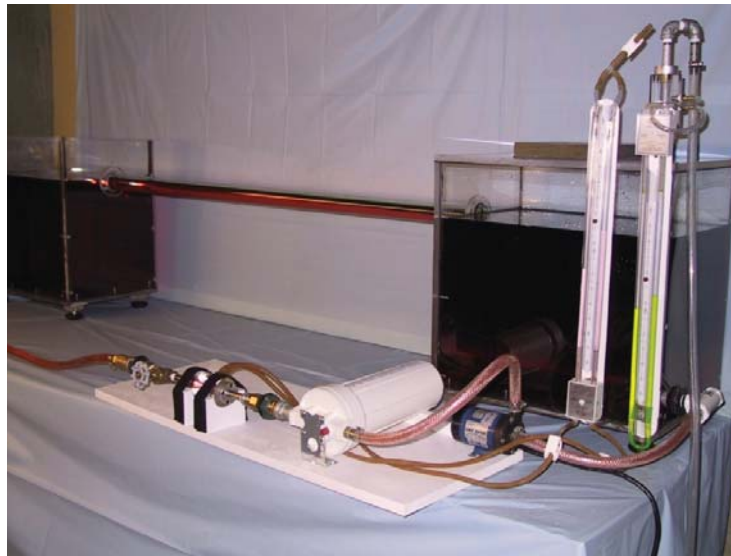


Figure 3-34. Air-water-brine test loop.

section against the fresh water flow. Subsequently, a wedge of brine is seen advancing toward the capped reservoir. Instability and mixing across the brine-water interface can be created by increasing the air pressure in the capped reservoir.

In oil-air tests, the open reservoir is filled with bio-diesel to a level above the pipe crown. The oil-end of pipe is closed by having the oil push the base of a cup against the reservoir wall. A test starts by supplying pressurized air to the capped reservoir. With sufficient air pressure, the cup base is pushed away by the air flow and oil starts to advance into the pipe as a wedge.

3.4.2 Results

Qualitative data has been obtained from the air-water-brine test loop. The formation of a distinctive head feature at the flow front was present in the case of dynamic intrusion. This head can be seen in Figure 3-35 followed by relatively steady flow. In Figure 3-36, quasi-static wedge intrusion takes place and the presence of faint Kelvin-Helmholtz billows are seen following the wedge front.



Figure 3-35. Dynamic intrusion of a gravity driven flow.

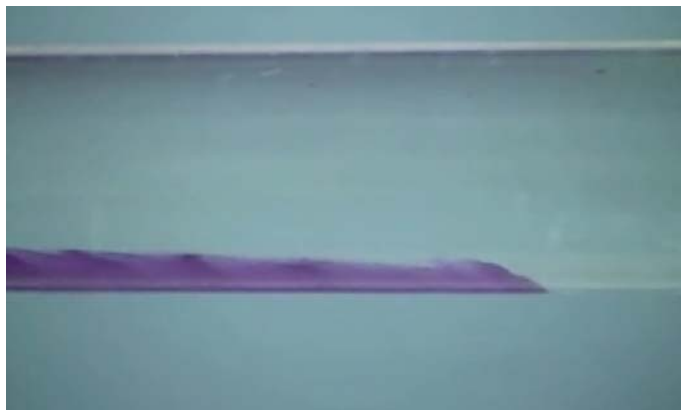
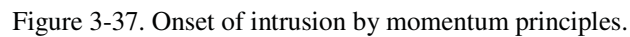


Figure 3-36. Quasi-static wedge intrusion of a gravity driven flow.

3.4.3 Discussion

In this study, University of Idaho has successfully constructed and tested flow loop designed to produce measurable gravity driven flows for both dynamic intrusion and wedge regimes. The onset of the intrusion principle, as seen in Figure 3-37, was tested and confirmed to reliably initiate an intrusion in the setup. The features seen in the preliminary set of data for the dynamic intrusion case confirmed the presence of the head phenomena described in Section 2.2.



3.5 Validations on the CFD code for Density Gradient Driven Stratified Flow

In this section, the CFD results are compared to the experimental results obtained by Grobelbauer et al. (1993) in ETH Zurich as a part of code validation works. Their experiments are based on both a series of lock-exchange flows with gases of different densities in a closed channel of a square cross-section. They focused on the quantitative measurement of front velocities of the gravity current flows. The experiment results cover the full range of gas intrusions, heavy as well as light, for the gravity current flows in the lock-exchange situations.

3-30

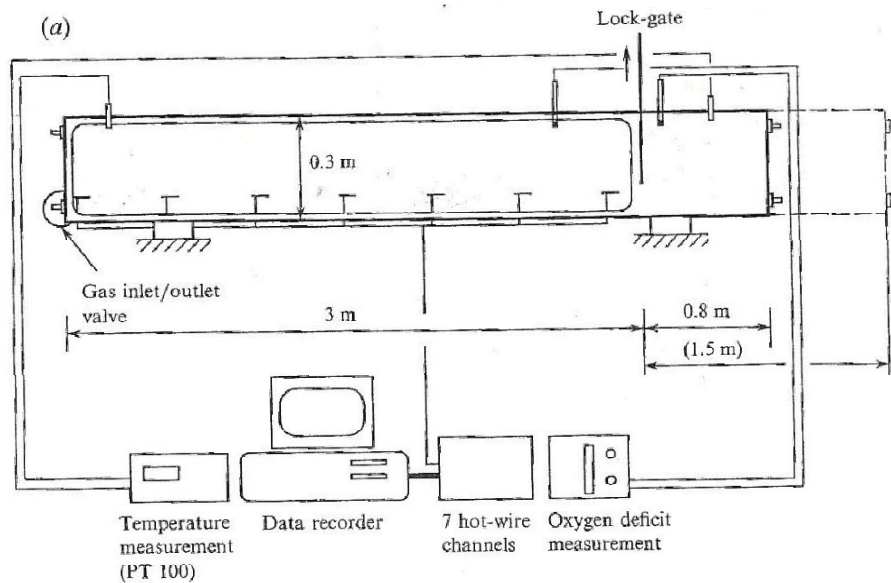


Figure 3-38. Experimental arrangement (Grobelbauer et al. 1993).

According to Grobelbauer et al. (1993), the experimental scatter is mainly contributed by the manually opened gate. However, the time required to open the gate was very short compared to the characteristic flow times. The gate velocity was reported to be 3–4 m/s, while flow velocity was reported to be 0.2–1.8 m/s. The velocity of the front was measured by using seven hot-wire probes placed along the floor (for heavy gas) or along the ceiling (for lighter gas). These probes were used as trip wires to give the signal of the arrival time of the current front. Figure 3-39 shows the propagation velocities of the fronts of heavy gas and light gas. The experiment was conducted with combinations of five different gases: air, argon, carbon dioxide, Freon 22, and helium, producing density ratios ranging from 0.046 to 0.9. Seven different gas combinations were taken into consideration (See Table 3-3). Each gas combination was tested in two configurations: first with the heavy gas in the smaller chamber and with the light gas in the larger, and then vice versa.

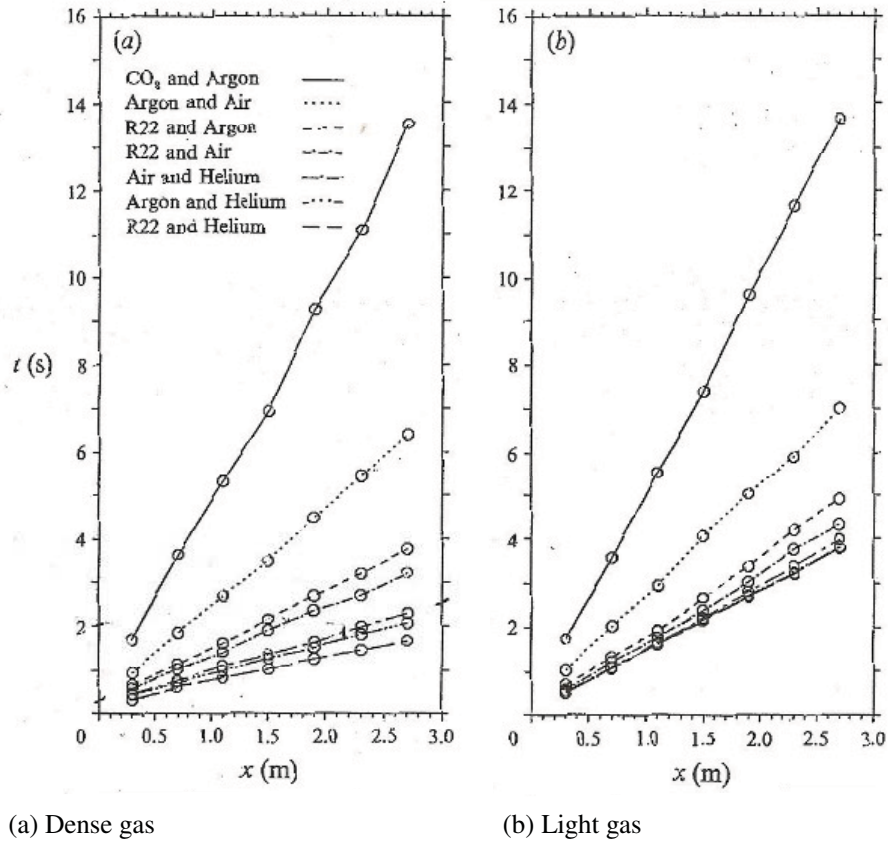


Figure 3-39. Propagation velocities of dense gas and light gases (Grobelbauer et al. 1993).

Table 3-3. Gas combinations used for Grobelbauer et al. (1993)'s experiment.

Gases	Density Ratio (ρ_l / ρ_H)
CO ₂ /Argon	0.90
Argon/Air	0.72
R22/Argon	0.46
R22/Air	0.33
Air/Helium	0.14
Argon/ Helium	0.1
R22 / Helium	0.046

The test-section was made of transparent material to allow visualization. The current depths were another interest in the experiment besides the current speed. Some initial visualization trials were made using smoke from commercial smoke pellets. These pallets, however, generated smoke by burning and the heat released changed the density distribution. A second trial has been performed by the method based on the evaporation of oil from a vertical wire. By this method, they obtained nice photos that visualize that the flow is not symmetric and that the light-gas front is less blunt and appear more stable than the heavy-gas fronts. However, they could not obtain the good quantitative data for the current depth.

3.5.2 Numerical Simulations and Comparisons

FLUENT 6.3, a general purpose CFD code, has been used for simulating the experiments. Figure 3-40 shows the geometry and mesh of the FLUENT model. Since the experiment by Grobelbauer et al. (1993) is based on the simple lock-exchange flows in the rectangular channel, the 2-D assumption is quite valid here. The model consists of two boxes of different sizes. The left one is 0.3 m high and 3.0 m long. The right one is 0.3 m high and 0.8 m long. The mesh type is hexagonal, and three different sizes of mesh were considered in the grid sensitivity study: coarse, normal, and fine. The mesh sizes are 0.04 m (coarse), 0.02 m (normal), and 0.01 m (fine) for each grid.

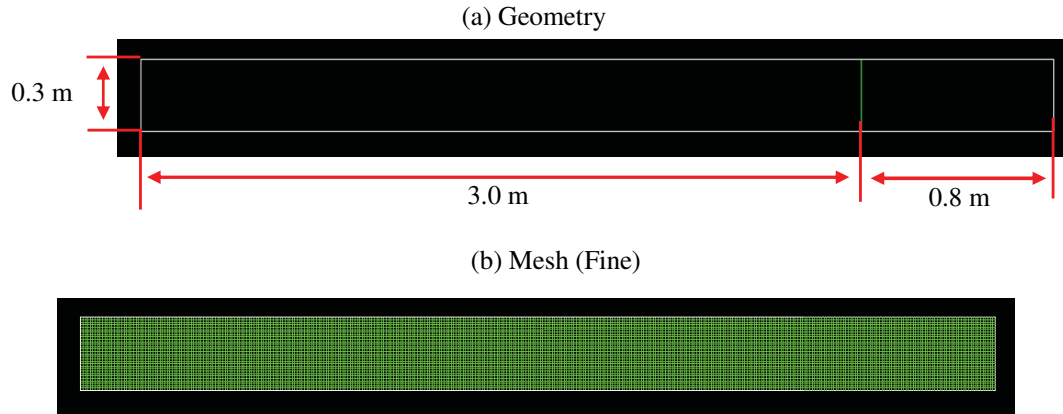


Figure 3-40. Geometry and FLUENT mesh.

The following summarizes the FLUENT options and models used for the base calculations.

- Solver:
 - Solver: Pressure Based
 - Formulation: Implicit
 - 2-D double precision
 - Unsteady
 - Velocity Formulation: Absolute
 - Gradient Option: Green-Gauss cell based
 - Pressure-Velocity Coupling: Simple
 - Pressure: Standard
 - Momentum: 2nd Order
 - Turbulence Kinetic Energy: 2nd Order
 - Turbulence Dissipation Rate: 2nd Order
 - Species: 2nd Order
 - Energy: 2nd Order
- Viscous Model:
 - Turbulence model: k-e realizable
 - Wall function: standard wall function
- Energy equation

- Species transport model:
 - 2 species: Air and Helium (for base case, see Table 1)
- Property Models
 - Density: Incompressible ideal gas
 - Heat capacity: mixing law
 - Thermal conductivity: mixing law
 - Viscosity: ideal gas mixing law.

Figure 3-41 shows the initial simulation condition. The left hand side was filled with helium and the right hand side with air. Therefore, this simulation demonstrates the heavy fluid intrusion into the light fluid. Initial temperature was set as 300 K and pressure as 1 atm.

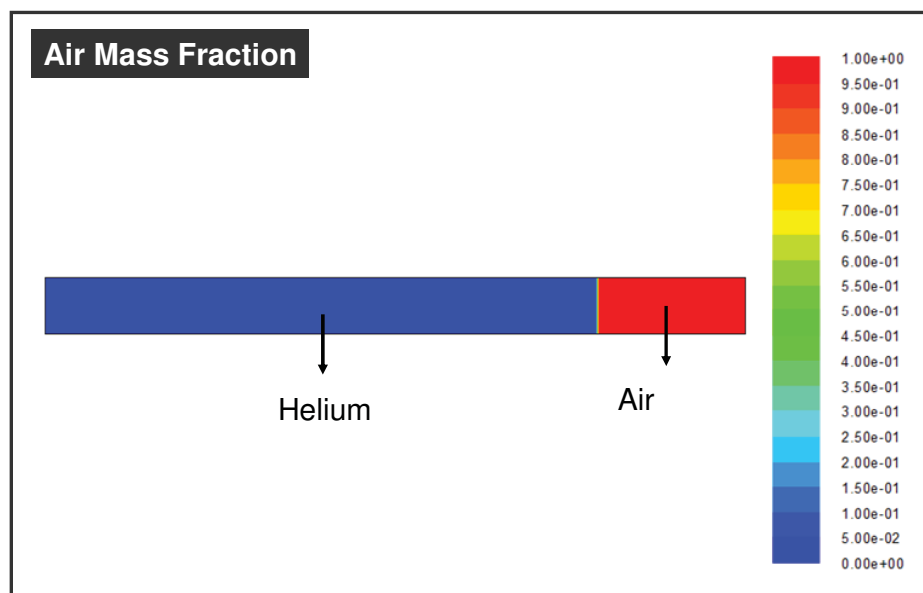


Figure 3-41. Initial Air mass fractions.

Figures 3-42, 3-43, and 3-44 show the contour plots of air mass fractions at different times for fine, normal, and coarse meshes, respectively. These figures clearly show that air rapidly intrudes into the helium side. According to these figures, the front speed of the air looks constant along with time. They show that air travels almost the same distance in the same time intervals. It strongly supports the inviscid flow assumptions used in the previous theoretical derivations.

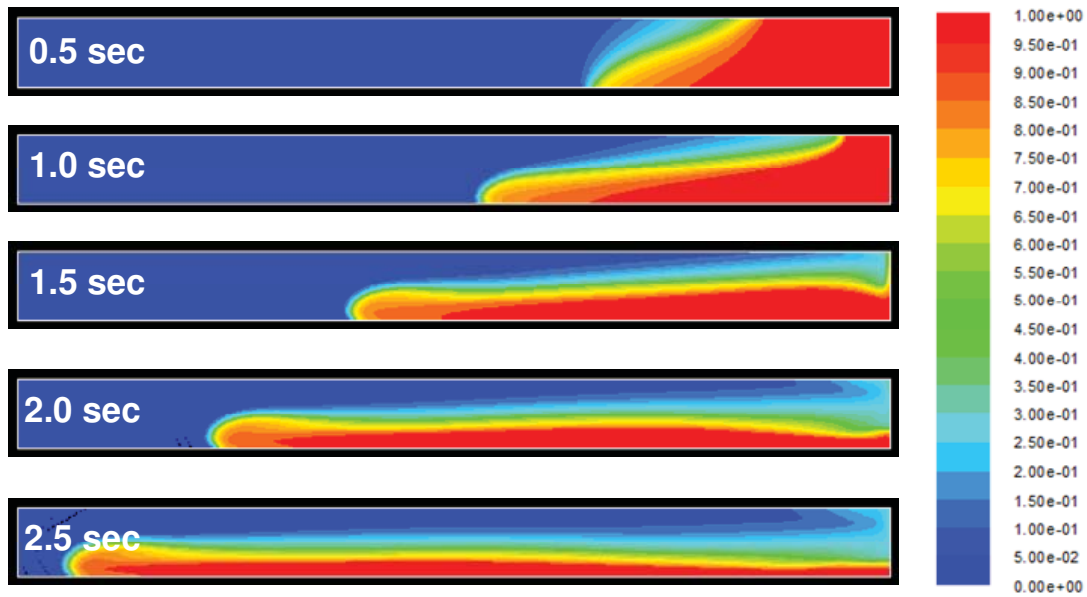


Figure 3-42. FLUENT simulation (air mass fraction (fine mesh)).

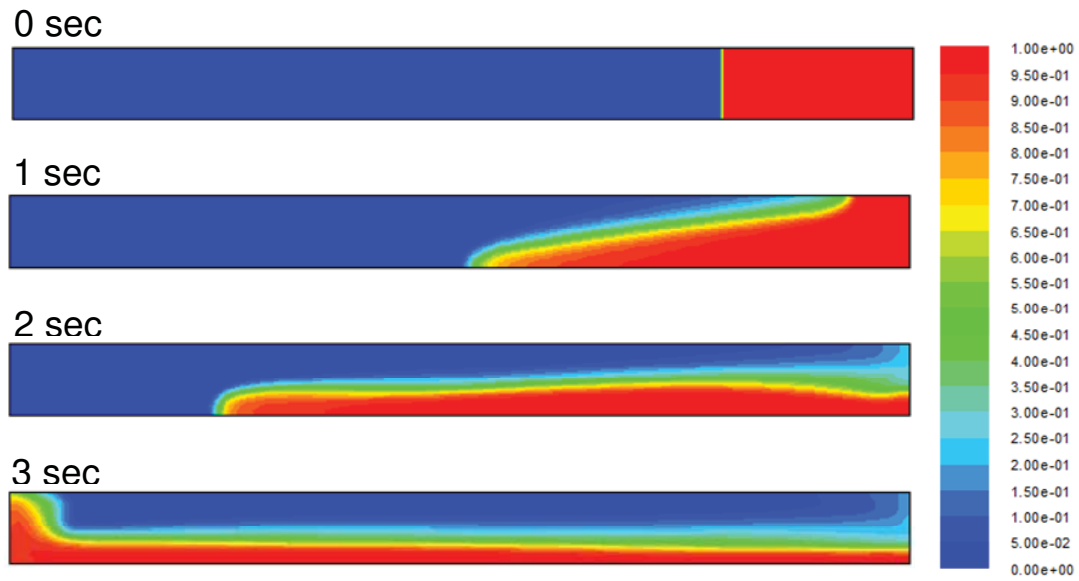


Figure 3-43. FLUENT simulation (air mass fraction (normal mesh)).

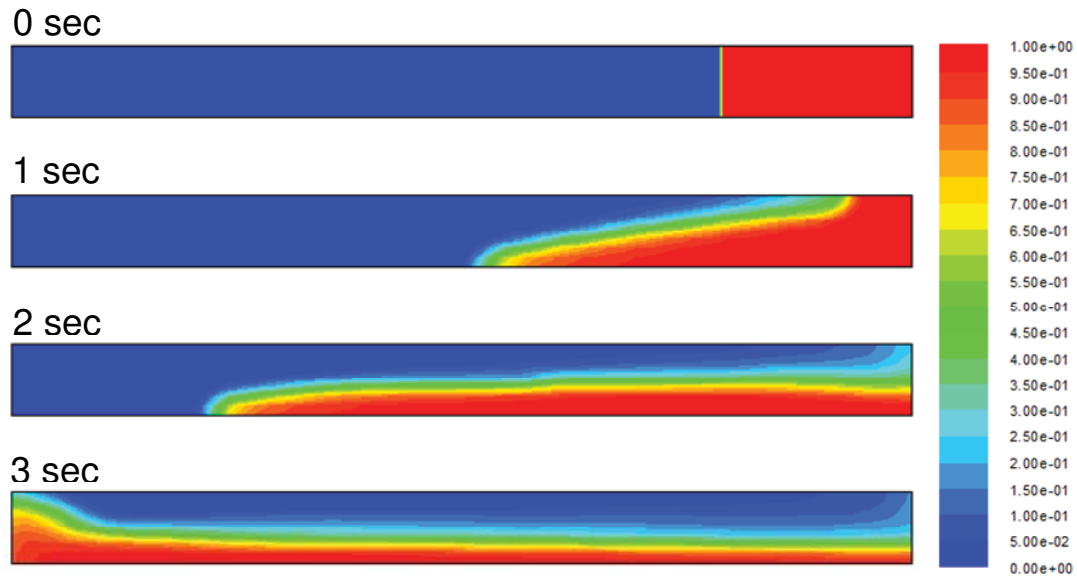


Figure 3-44. FLUENT simulation (air mass fraction (coarse mesh)).

A grid sensitivity study was performed for simulation. Since the front speed is the main comparison parameter in the current validation, the current speed in the simulation was first defined with the same method used in the experiment. In the experiment, the locations of the current were determined by hot-wires installed at the bottom of the test-section. So, the current locations in the simulations were also determined by the air concentrations at the bottom plane of the bottom. Figure 3-45 shows the air mass fractions at the bottom plane, and includes five different curves for different times: 0.5, 1.0, 1.5, 2.0, and 2.5 seconds. The current locations were determined to be the intersections between air mass fraction curves and x-axis.

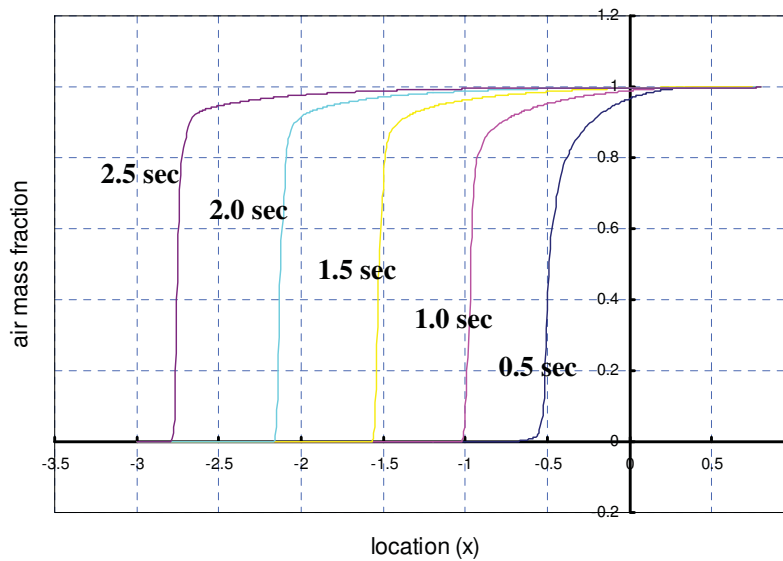


Figure 3-45. Air mass fraction at the bottom plate (current locations).

Based on Figure 3-45, the propagation distances were obtained for different times. Figure 3-46 compares the calculated propagation distances for three different quality meshes. As shown in this figure, the calculated propagation distances are quite close to each other, even though the quality of the meshes is different. Especially, if looking at the data at $t = 2.5$ seconds, three different models predict almost the same propagation distances (within 1%).

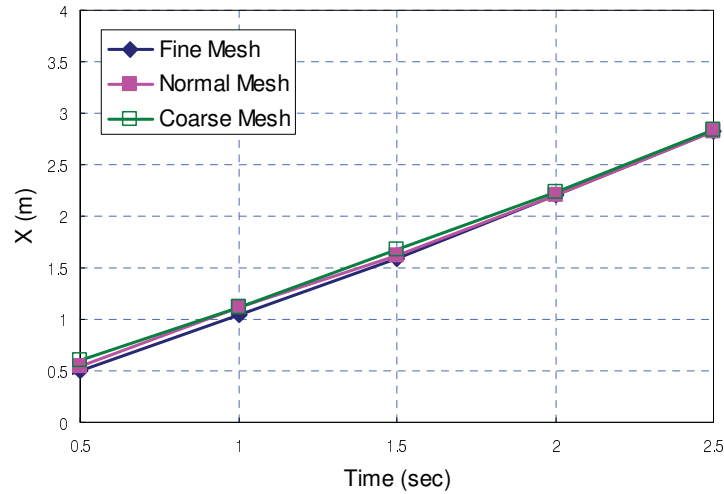


Figure 3-46. Comparisons between different mesh sizes.

A method based on the Richardson extrapolation (Roache et al. 1998) was used to quantitatively estimate the grid convergence. The objective of this CFD analyses was to determine the current front speed along with the channel. Table 3-4 indicates the grid information and the calculated front speeds by CFD calculations. Each solution was properly converged with respect to iterations. The column indicated by spacing is the spacing normalized by the spacing of the finest grid.

Table 3-4. Grid information and front speed.

Grid	Normalized Grid Spacing	Front Speed (m/s)
1 Fine	1	1.19
2 Normal	2	1.18
3 Coarse	4	1.16

From the above information, the order of convergence is calculated as

$$p = \ln((1.16 - 1.18)/(1.18 - 1.19)) / \ln(2) = 1. \quad (3-5)$$

Apply Richardson extrapolation using the two finest grids to obtain an estimate of the value of the front speed at zero grid spacing as

$$V_h = 1.19 + (1.19 - 1.18)/(2^1 - 1) = 1.2 \text{ m/s} . \quad (3-6)$$

Figure 3-47 plotted the simulated front speeds and the estimated front speed at zero grid spacing. The grid convergence index (GCI) for the fine grid solution was computed using a factor of safety of $F_s = 1.25$. The GCI for grids 1 and 2 is

$$GCI_{12} = 1.25 \times (1.19 - 1.18) / 1.19 / (2^1 - 1) \times 100 = 1.050\% \quad (3-7)$$

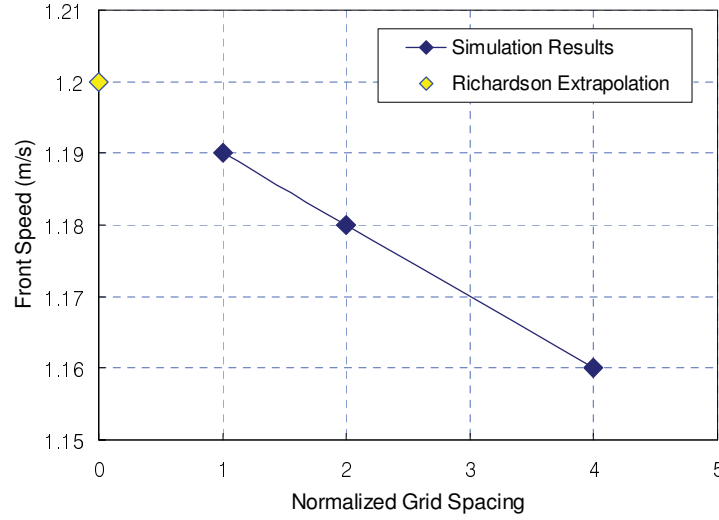


Figure 3-47. Simulated front speeds and estimated front speed at zero grid spacing.

and the GCI for grid 2 and 3 is

$$GCI_{23} = 1.25 \times (1.18 - 1.16) / 1.18 / (2^1 - 1) \times 100 = 2.119\% \quad (3-8)$$

The formula used to check that the solutions were in the asymptotic range of convergence is

$$2.119 / (2^1 \times 1.050) = 1.0085 \quad (3-9)$$

which is approximately one, indicating that the solutions are well within the asymptotic range of convergence.

Based on the calculation in Equations (3-5) through (3-9), the front speed is estimated to be 1.2 within an error of 1.050%. The front speed estimated in the fine mesh is only deviated from this value with an error of 0.84%, indicating that the simulated results by fine mesh are quite reliable.

More calculations were carried out to look at the turbulence model effect on the results. Figures 3-48, 3-49, and 3-50 show the contour plots on the air mass fractions for k-w, standard k-e, and RSM, respectively. All the simulations have been performed by using fine mesh grid and the same model setup as the base calculation except for turbulence models. The three figures show that the overall qualitative flow behaviors are not dependent on the different turbulence model. Figure 3-51 shows the comparisons between the CFD simulation results and the experimental data. The compared parameter is the front location of the heavy current (air). This figure shows that the realizable k-e and RSM models are well predicting the front locations and that the data in the beginning shows more deviations than those in the later. It is because in the actual experiment, the opening gate is not instantaneous, and the gate opening process disturbs the flow field. After 1 second, the experimental data and the CFD results show quite good agreement. Table 3-5 summarizes the comparisons of the front speed between the experiment and the CFD simulations. To estimate the front speeds correctly, only the data after 1.5 seconds were used by ignoring initial disturbed data. In the experiment, the air current speed was estimated to be 1.25 m/s. The calculated CFD results are 0.92 m/s (standard k-e), 1.19 m/s (realizable k-e), 1.12 m/s (k-w), and 1.20 m/s (RSM). As shown in the table, the realizable k-e and RSM models show good predictions of front speeds. The errors of the k-e model and the RSM model are 5.04% and 4.2%, respectively.

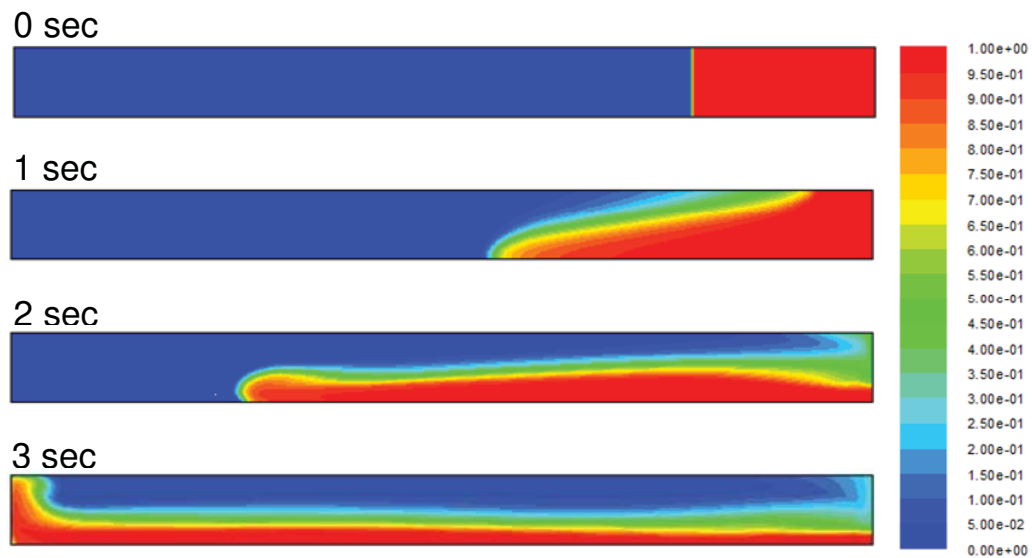


Figure 3-48. FLUENT simulation (air mass fraction, k-w model, fine mesh).

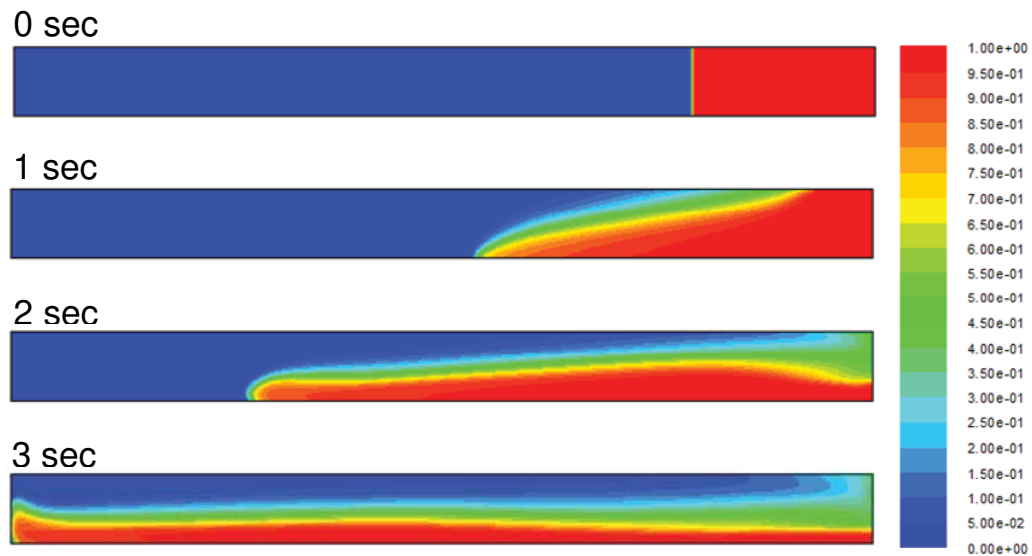


Figure 3-49. FLUENT simulation (air mass fraction, standard k-e model, fine mesh).

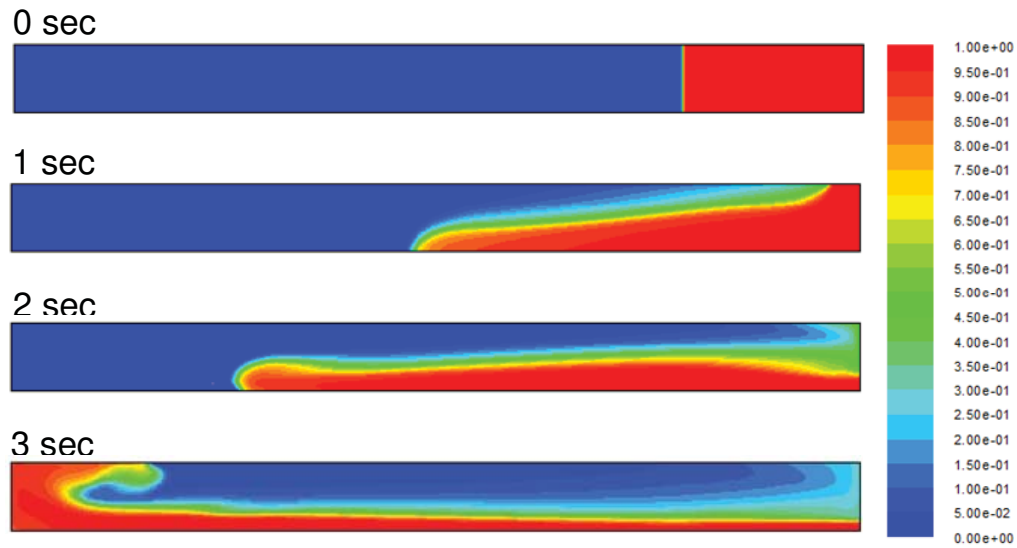


Figure 3-50. FLUENT simulation (air mass fraction, RSM model, fine mesh).

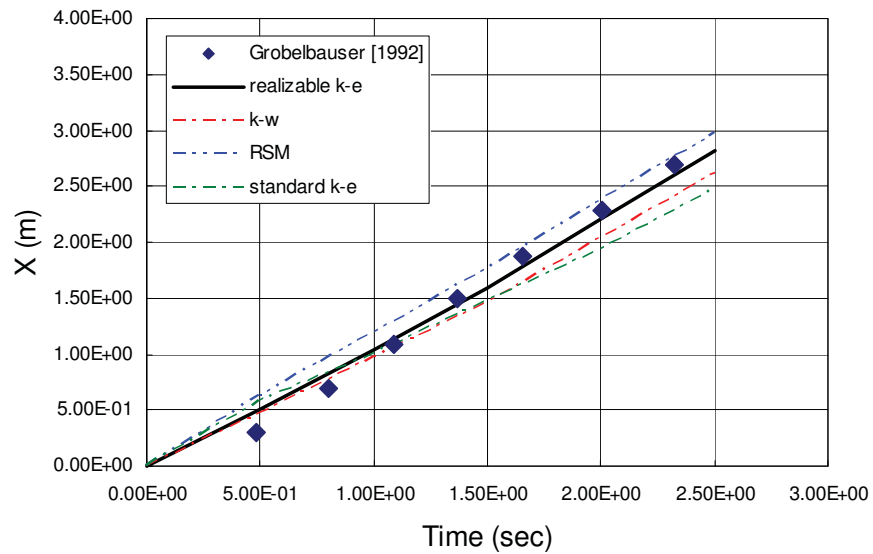


Figure 3-51. Comparisons between CFD results and experimental data (front location).

Table 3-5. Comparisons between CFD results and experimental data (current speed).

	Current Speed (m/s)	Error (%)
Experimental Data (Grobelbauer et al. 1993)	1.25	—
Standard k-e model	0.97	28.9
Realizable k-e model	1.19	5.04
k-w model	1.12	11.6
RSM model	1.20	4.2

In the above validation, heavy gas intrusion (air) into light gas (helium) has been taken into consideration, and the calculation results showed very good agreement with the experimental data. In the following section, the opposite case has been considered when the light gas (helium) is intruding into heavy gas (air). All the basic simulation set-ups are chosen to be the same as those used in the above simulation except for the initial air mass fractions. Figure 3-52 shows the initial air mass fractions assumed in the simulation. In this simulation, the left-hand side is initially filled with air while the right-hand side is filled with helium. The realizable k-e model has been selected to be the reference turbulence model. The fine mesh has been used for calculations.

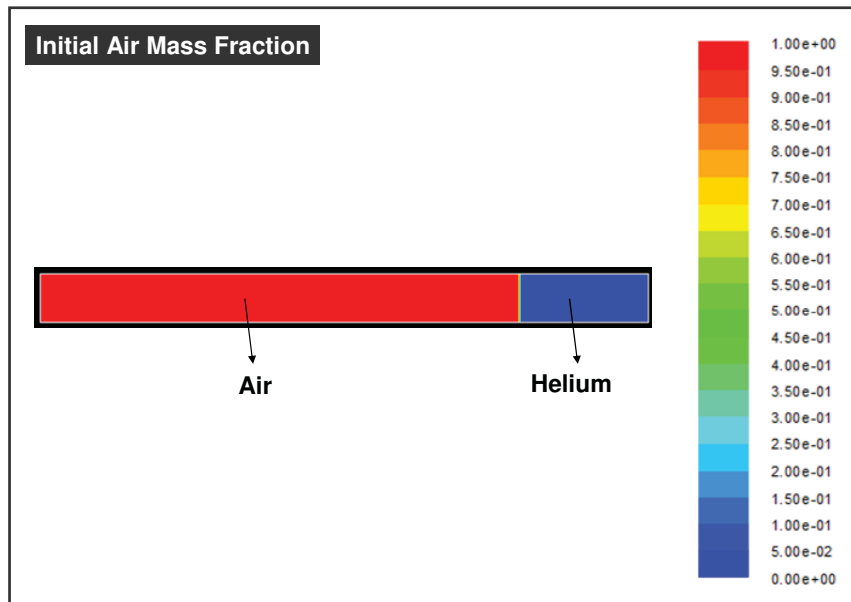


Figure 3-52. Initial air mass fraction for light gas intrusion (helium).

Figure 3-53 shows the calculated contour plots on air mass fraction for different times. The red color represents air and the blue color represents helium. Helium is smoothly intruded into the air side with almost constant speed occupying half of the channel height. It looks like the light current (helium) is showing perfect energy conserving flow satisfying Benjamin's theory. This simulation result is also consistent with the previous experimental observations by Lowe et al. (2005).

To determine current locations, the helium mass fractions on the upper plate have been plotted for different times (see Figure 3-54). The intersections between helium mass fraction curves and x-axis were chosen as the current locations.

Figure 3-55 shows the comparisons on the current locations (helium) between experiment (Grobelbauer et al. 1993) and FLUENT simulations. The calculated results showed very good agreement with the experimental data. Table 3-6 summarizes the estimated current speeds. The current speed obtained by experimental data to be 0.68 m/s and that of simulation 0.72 m/s. This result indicates that the deviation of the simulation results is only 5.56% from the experimental data.

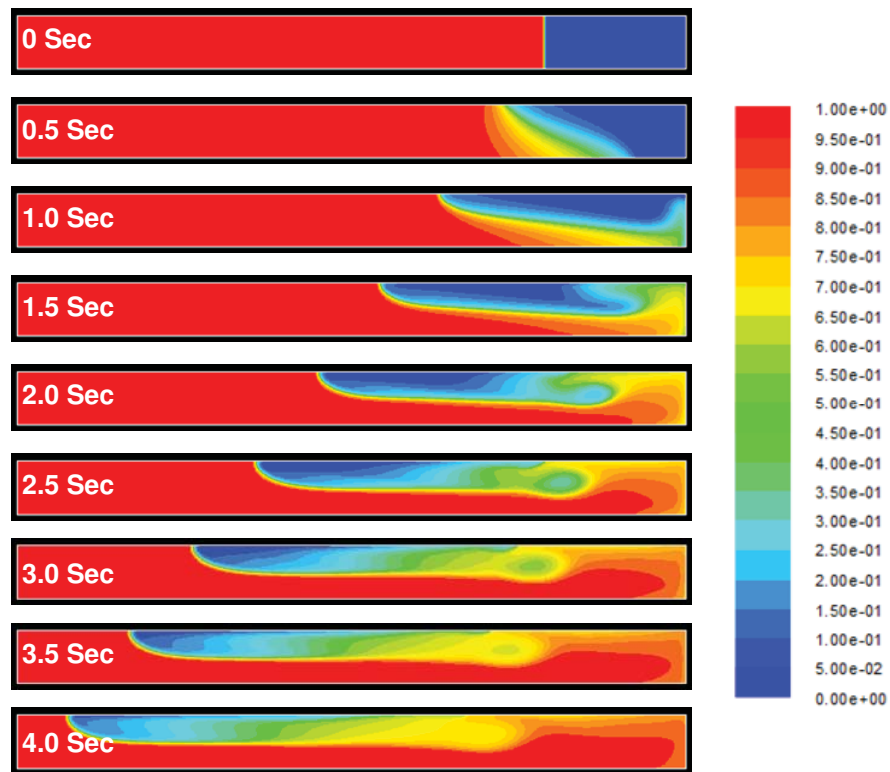


Figure 3-53. FLUENT simulation for light gas intrusion (air mass fraction, realizable k-e model, fine mesh).

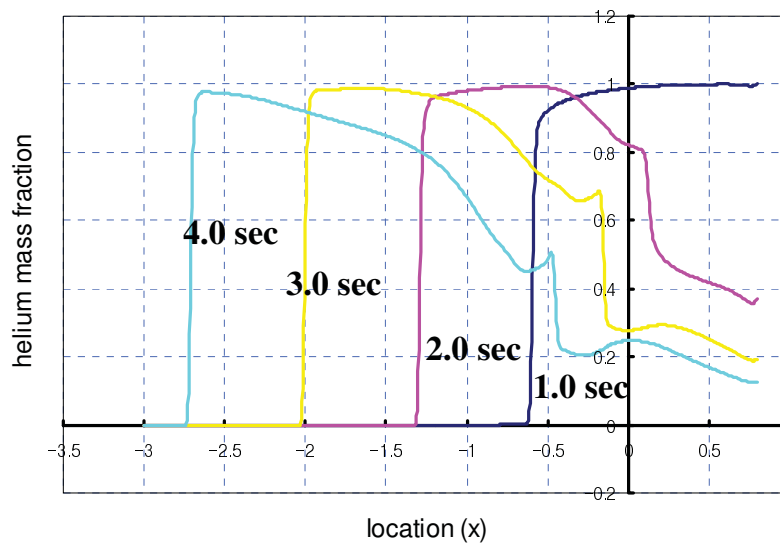


Figure 3-54. Helium mass fraction at the upper plane for light gas intrusion.

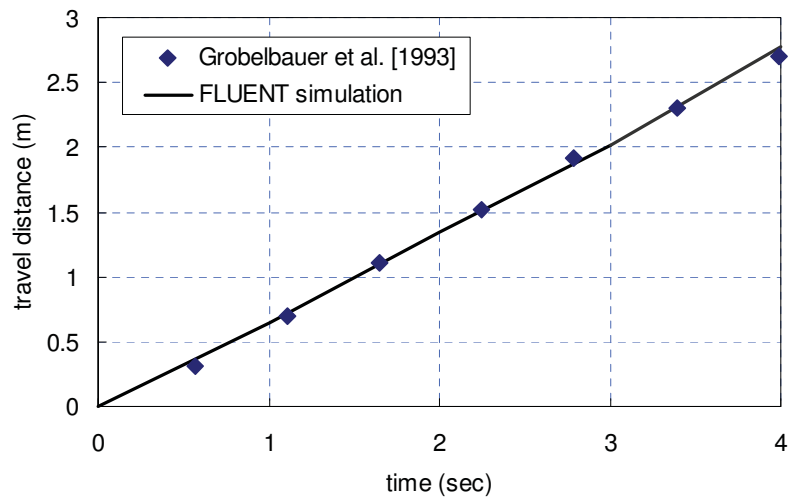


Figure 3-55. Comparisons between CFD results and experimental data (light gas intrusion).

Table 3-6. Comparisons between CFD results and experimental data (light gas intrusion).

	Current Speed (m/s)	Error (%)
Experimental Data (Grobelbauer et al. [1992])	0.68	—
FLUENT (Realizable k-e model)	0.72	5.56

4. TASK 3: ADVANCED GRAPHITE OXIDATION STUDY (INL)

4.1 Introduction

Graphite oxidation in an air-ingress accident is presently an important issue for VHTR safety because of its potential to degrade structural graphite, heat up the core, and release fission products. The oxidation process of graphite is affected by various factors, including temperature, pressure, oxygen concentration, types of graphite, graphite shape and size, flow distribution, etc. The effects of these factors have been documented by a number of previous investigations (Kim and NO 2006, Fuller et al. 1997, Moorman 1984, Ogawa 1993, Contescu et al. 2008, etc.), and good models have been developed for estimating the graphite oxidation process in an air ingress accident.

One of the main issues regarding graphite oxidation is the potential core collapse problem that may occur following the degradation of the mechanical strength of the graphite. In analyzing this phenomenon, it is very important to understand the relationship between the degree of oxidization and strength degradation. In addition, the change of oxidation rate by graphite oxidation degree (burn-off: ratio of the oxidized graphite density to the original density) should be quantified because graphite strength degradation is followed by graphite density decrease, which highly affects oxidation rates and patterns. Because the density change is proportional to the internal pore surface area, these parameters should be quantified in advance. Regarding those issues, the following tasks have been performed FY-09:

- Experiment on the fracture of the oxidized graphite and validate the previous correlations
- Experiment on the change of oxidation rate using graphite density and data collection
- Measure the surface area of the graphite using the Brunaur-Emmett-Teller method.

Based on previous results, stress and fracture analyses for VHTR core supporting structures have been performed in FY-09 by using GAMMA system analysis code and ABAQUS stress analysis code that is based on the new air-ingress scenario. In addition to this, conservative criteria for graphite burn-off have been proposed for some computational analyses and can be implemented in system analysis codes. They are summarized in this section.

4.2 Modeling of Graphite Oxidation and Fracture in Air-ingress

The inherent safety feature of the VHTR graphite core design could be compromised if the core supporting structures collapse and damage the fuel blocks, potentially leading to release of fission products. Because graphite does not easily oxidize and the amount of oxygen available in the reactor confinement structure is limited, such a failure is likely a very low probability event, perhaps well beyond design basis. But because the consequences are severe, the event does warrant some study. Graphite oxidation will occur to some extent after any air-ingress accident. Unless mitigating action is taken, the graphite support structures may gradually erode over time altering their shapes and mechanical properties. To determine the time scale of the graphite support structure failure, a computational stress analysis was performed with ABAQUS (ver. 6.75) using the transient corrosion depth, temperature and graphite burn-off predicted by the GAMMA.

4.2.1 Stress Analysis Strategy

As shown in Figure 4-1, the core is made of several layers of graphite blocks. To finish the computational analysis in a reasonable amount of time, instead of modeling the entire core, only one vertical column of the support block and plenum directly below the fuel blocks, the parts subjected to most stress and oxidation damage, was analyzed (indicated by green arrows in Figure 4-1).

As shown in Figure 4-2(b), each block is usually surrounded by six adjacent blocks. However, the presence of adjacent blocks was ignored because there is approximately 2 mm clearance between the block surfaces (GA 1997). Because of the gap, they are not exerting force on each other, so the vertical columns of the blocks were assumed to be independent of each other.

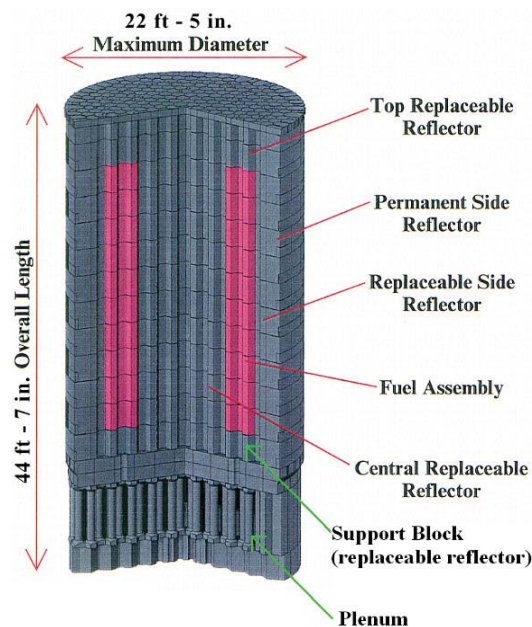


Figure 4-1. GTMHR core side view (Shenoy 2007).

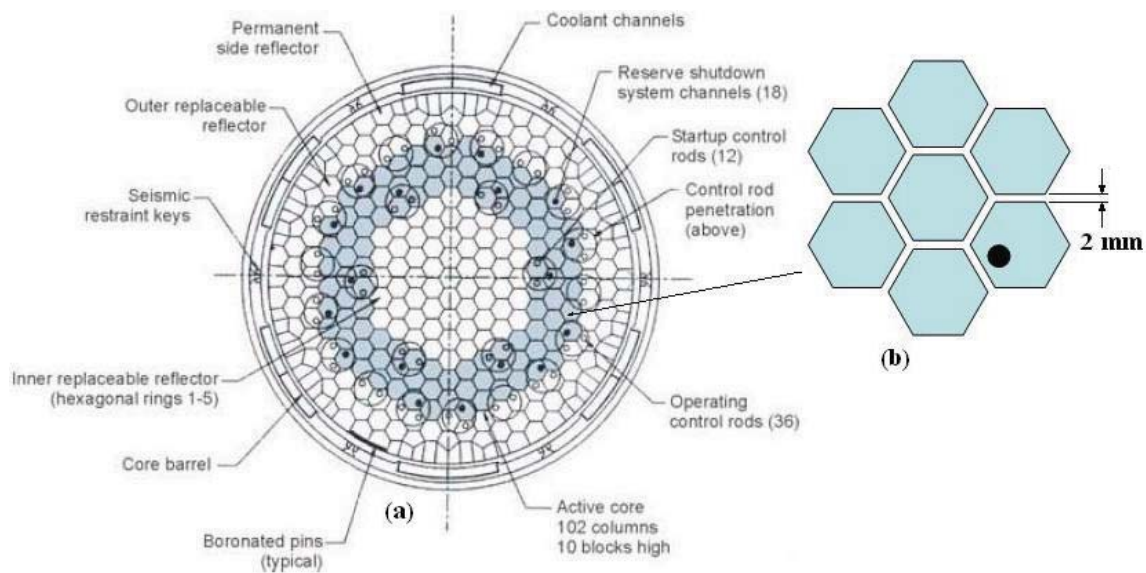


Figure 4-2. Top cutaway view of the core (Cocheme 2004).

Figure 4-3 shows the whole and cut views of the support block and the plenum that were analyzed. Oxidation damages the graphite structure by two different means: burn-off and corrosion. Burn-off refers

to the oxidation of the graphite's internal body, causing reduction of density, leading to reduction of stiffness (young's modulus) and mechanical strength. Corrosion refers to oxidation taking place on the outer surfaces of the structure exposed to airflow. The corrosion decreases the cross-sectional area available to support the weight. As corrosion continues, the cross-sectional area decreases until the stress exceeds the mechanical strength of the graphite, leading to fracture failure of the structure.

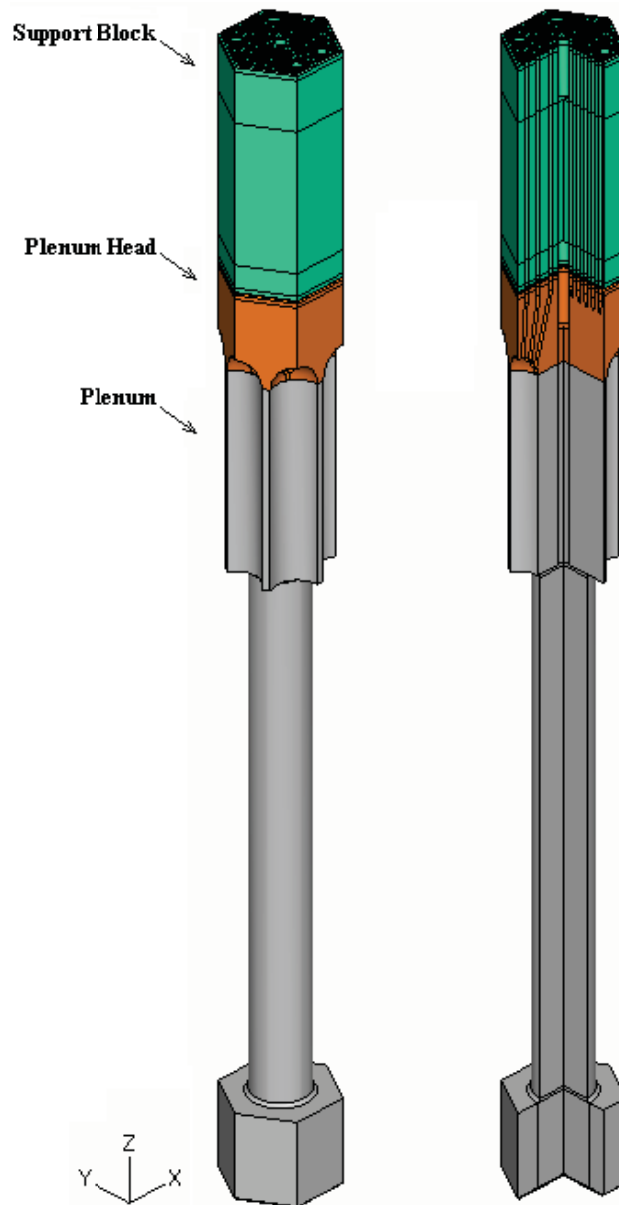


Figure 4-3. ABAQUS generated whole and cut view of the support block and plenum.

4.2.2 Structural Dimensions

4.2.2.1 Support Block Dimensions

The support block is modeled using the dimensions of General Atomics' GTMHR fuel block design shown in the Figure 4-4. The support block is almost identical to the fuel block except, the support block does not have fuel or LBP holes. Parts without exact dimensions given were approximated from the appearance of the drawing, indicated with an asterisk.

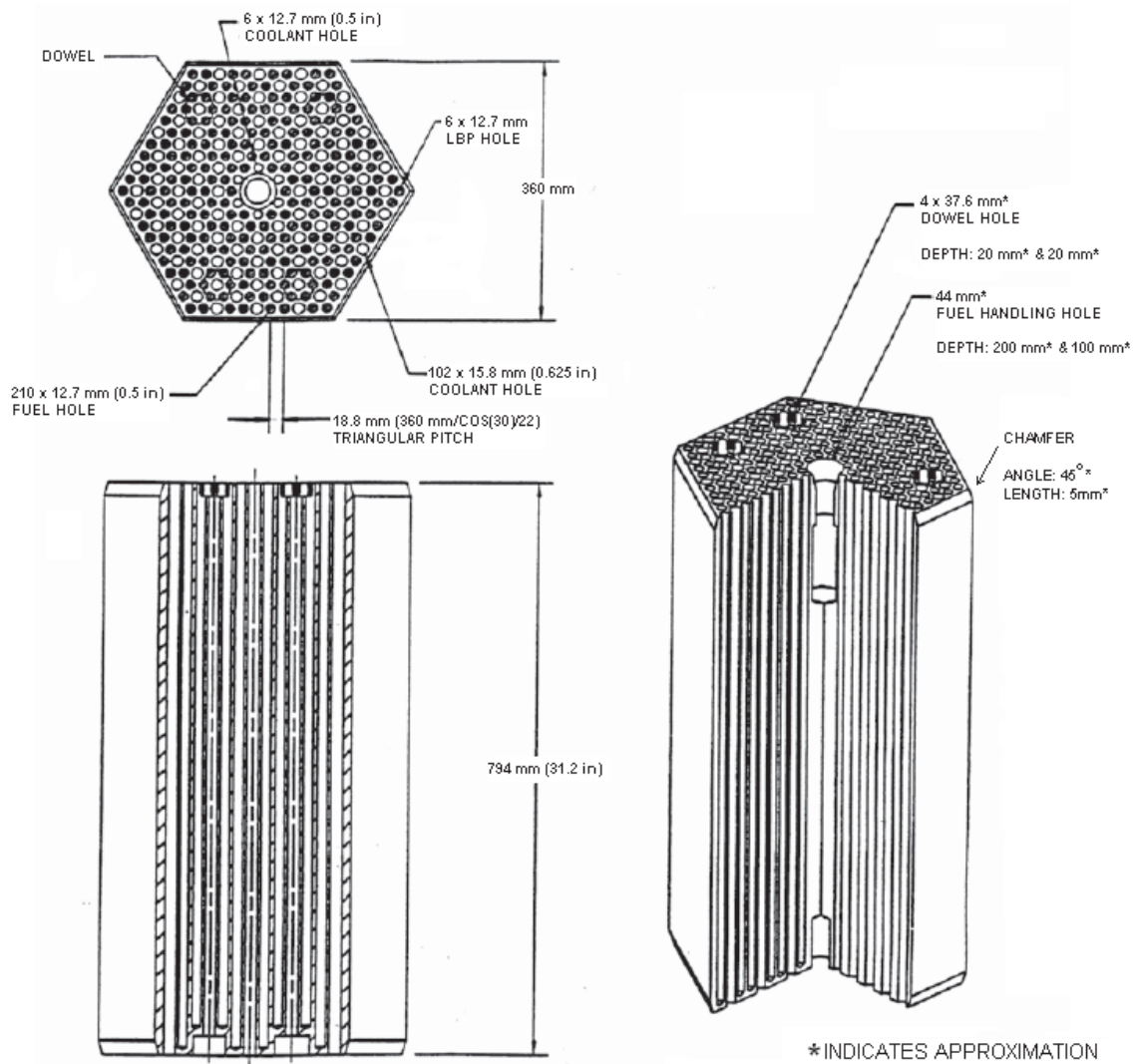


Figure 4-4. The dimensions of a General Atomics' GTMHR fuel block. (GA 1997, Cocheme 2004, GA 2003).

4.2.2.1 Plenum Dimensions

The dimensions used for modeling the plenum, shown in the Figure 4-5(a), are based on the order of magnitude estimates for geometric ratios suitable for normal operation of a 600 MWth GTMHR (McCreery 2004). The information on how the coolant channels converge into the jet hole was not available; therefore, they were personally designed using rotational symmetry such that an equal number of channels converge into each jet holes as shown in the Figure 4-4 (b).

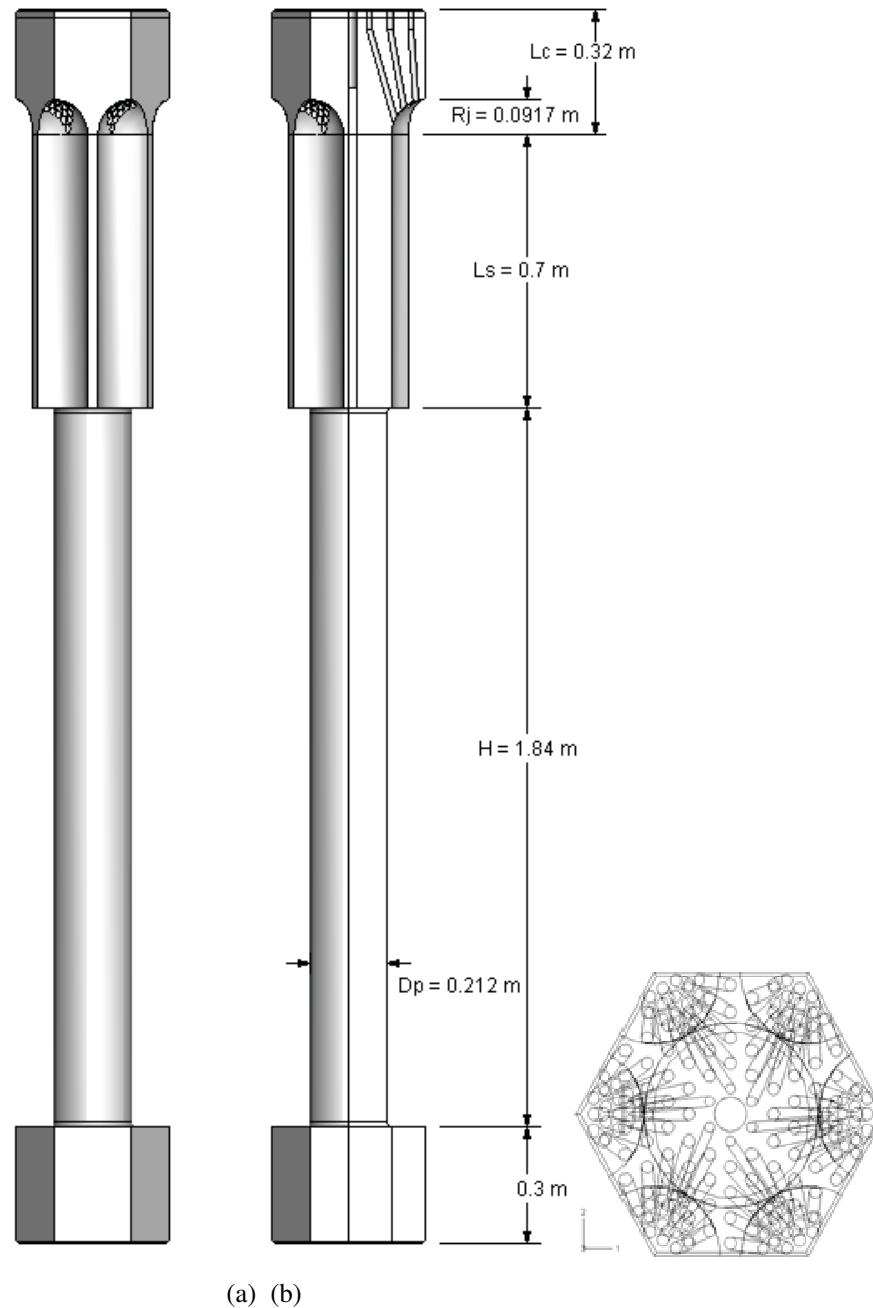


Figure 4-5. Plenum (a) side views (with dimensions), and (b) wireframe top view.

4.2.3 Change of Temperature, Burn-off, and Corrosion Thickness

The graphs in Figures 4-6, 4-7, and 4-8 show the corrosion depth, temperature, and burn-off as function of time for sections of the support block and plenum. The corrosion and burn-off start almost immediately after the LOCA because the natural convection starts almost immediately, supplying oxygen into the core. The temperature and availability of oxygen play key roles in oxidation damage. The heat from an exothermic oxidation reaction causes the temperature to rise, which also increases the oxidation rate. The corrosion is highest on the lower plenum sections because air enters from the bottom and rises up. The corrosion decreases toward higher sections because of depleted oxygen, but from section 6 and above, the temperature is significantly higher to offset this trend.

Mechanical failure occurs first in section 6 and above because these parts have numerous coolant channels, and the cross sectional area to support the load decreases significantly with corrosion on the channel walls. Even though the corrosion and burn-off is highest in lower plenum sections, they are not enough to exceed mechanical strengths or cause buckling.

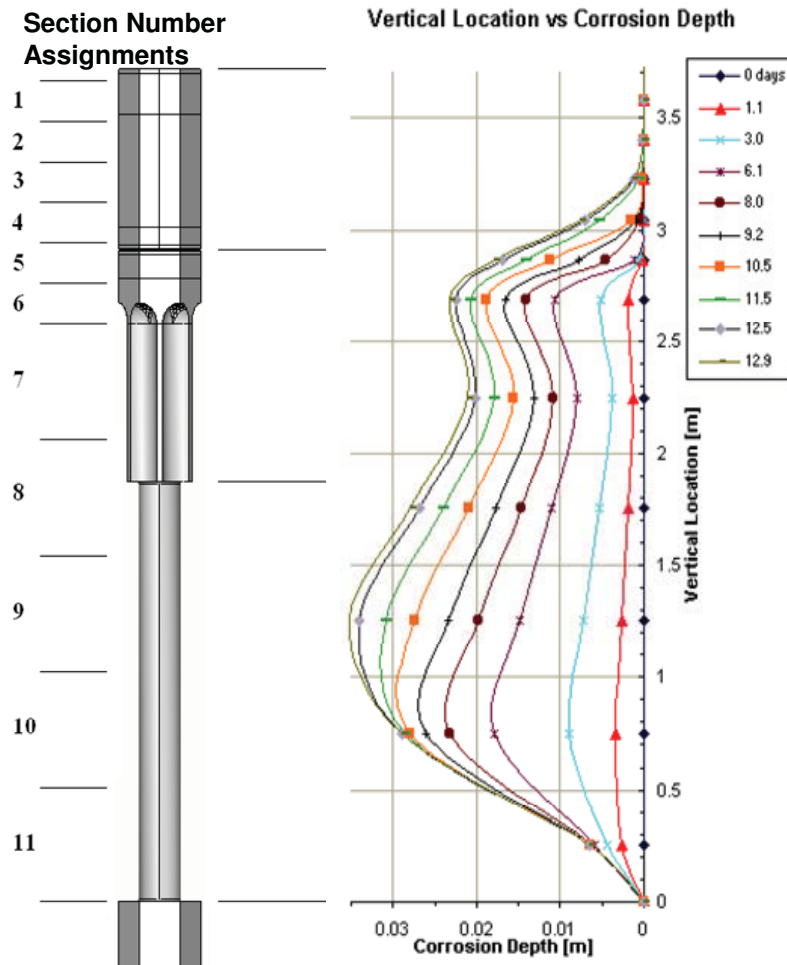


Figure 4-6. Corrosion depth and section assignments.

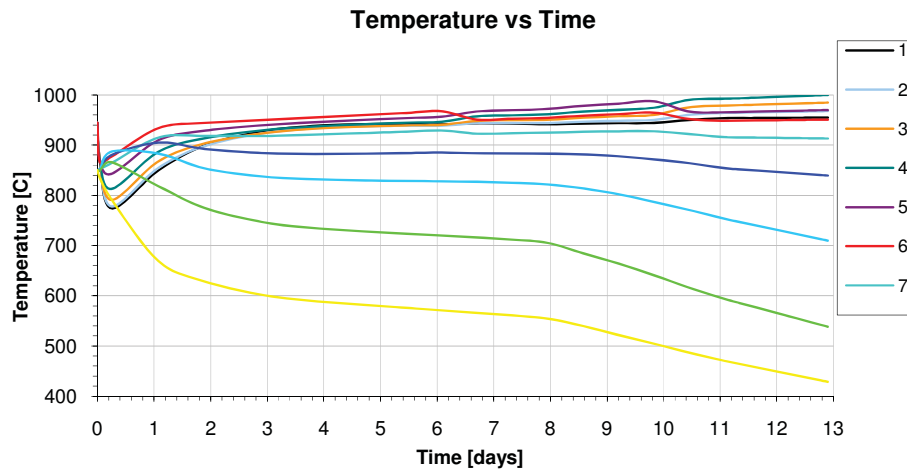


Figure 4-7. GAMMA result temperature over the time.

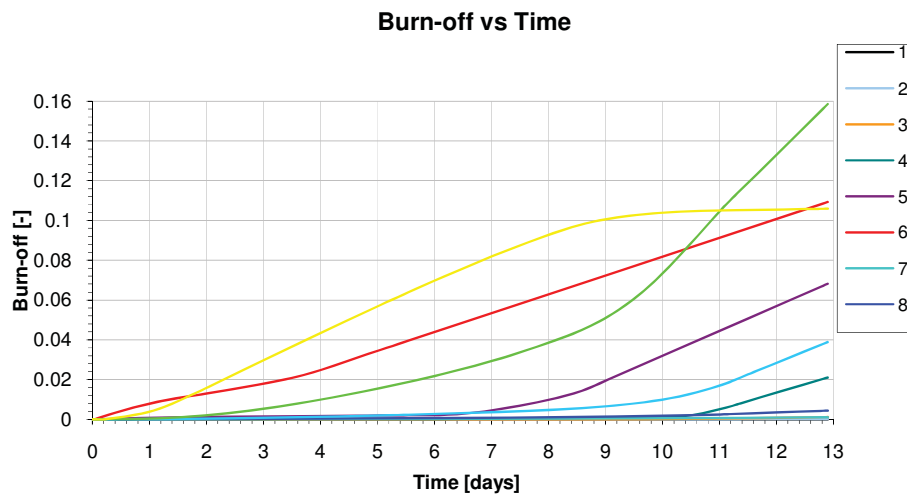


Figure 4-8. GAMMA result burn-off over the time.

4.2.4 Material Database

Mechanical properties are important to the accuracy of the analysis, so a detailed material database was built to address the effects of temperature, burn-off, and irradiation.

4.2.4.1 Properties in Standard Conditions

The GTMHR's core was assumed to be made of IG-110, a high-strength, fine-grained graphite with isotropic mechanical properties (Ishihara et al. 2004). Thermo mechanical properties of the IG-110 in its normal state are shown in Table 4-1. Because the ultimate strengths exhibit statistical variations, the minimum compressive and tensile strengths were determined from statistical treatment of the strength data such that it can be said with 95% confidence that 99% of the graphite samples survive beyond the specified values (Ishihara et al. 2004).

Table 4-1. Basic thermo mechanical properties of IG-110 at standard conditions. (Ishihara et al. 2004, Burchell 1991).

Density	1780 kg/m ³
Mean Young's Modulus	7.9 GPa
Poisson Ratio	0.14
Mean Compressive Strength	76.8 MPa
Minimum Compressive Strength	61.3 MPa
Mean Tensile Strength	25.3 MPa
Minimum Tensile Strength	19.4 MPa
Mean Thermal Expansion Coefficient (293–673°C)	4.06x10 ⁻⁶ K ⁻¹
Thermal Conductivity (600°C)	80 W/m-K

4.2.4.2 Tensile and Compressive Strength vs. Burn-off

The experimental data for the change of tensile and compressive strength because of burn-off are shown in Figures 4-9(a) and 4-9(b). The relationship between the strengths and the burn-off is exponential. Also, the ratio of the instantaneous compressive strength to initial compressive strength, S/S_0 , for both tensile and compressive strengths shows a virtually identical trend to that of function of burn-off.

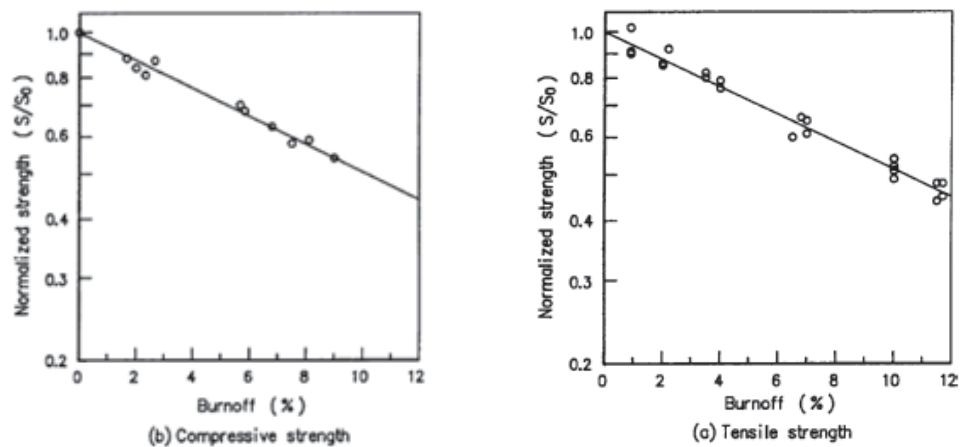


Figure 4-9. (a) Tensile strength as function of the burn-off; (b) compressive strength as function of the burn-off (Ishihara et al. 2004).

4.2.4.3 Tensile and Compressive Strength vs. Temperature

As shown in the Figure 4-10, the Young's modulus ratio appears to show square root relationship with the tensile strength. Considering that S/S₀ ratios for tensile and compressive strength behave almost exactly the same as function of burn-off, their behaviors with respect to the temperature change might be very similar with each other. Therefore, the S/S₀ ratio for compressive strength was assumed to behave the same as the S/S₀ ratio for the tensile strength as function of temperature.

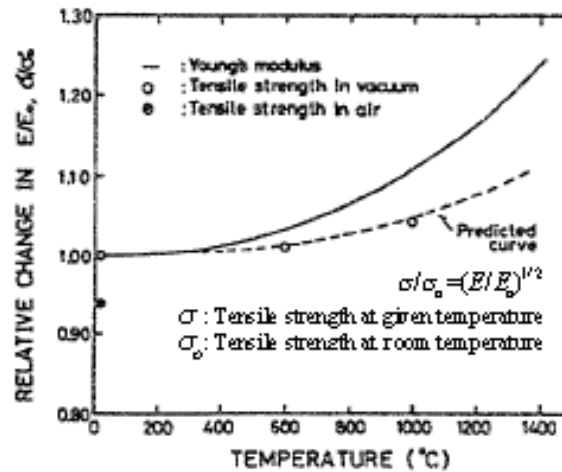


Figure 4-10. Tensile strength as function of temperature (Eto et al. 1986).

4.2.4.4 Young's Modulus vs. Temperature and Burn-off

The experimental data and coalitions for the change of Young's modulus because of temperature and burn-off are shown in the Figure 4-11.

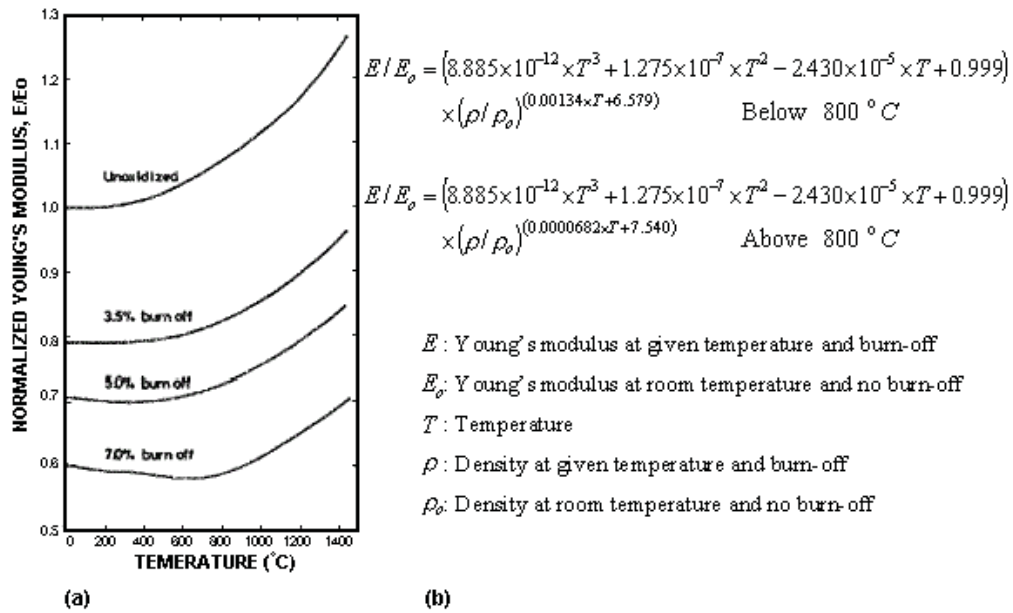


Figure 4-11. (a) The change in Young's modulus because of oxidation as a function of temperature (best fit of experiment data), and (b) the correlations for the Young's modulus as a function of temperature and burn-off (Eto et al. 1986).

4.2.4.5 Young's Modulus and Mechanical Strengths vs. Irradiation

A change of mechanical properties from irradiation is expected to be negligible because of low neutron dose experienced by the support block and plenum. Ishiyama et al. performed mechanical tests on IG-110 samples that were irradiated up to neutron fluence of 3.8×10^{22} n/cm² (neutron energy >0.05 MeV) at a temperature of 600°C, resulting in neutron dose of ~25 dpa (Burchell et al. 1996). Figures 4-12(a) and 4-12(b) show the change of Young's modulus and mechanical strength as a function of dpa.

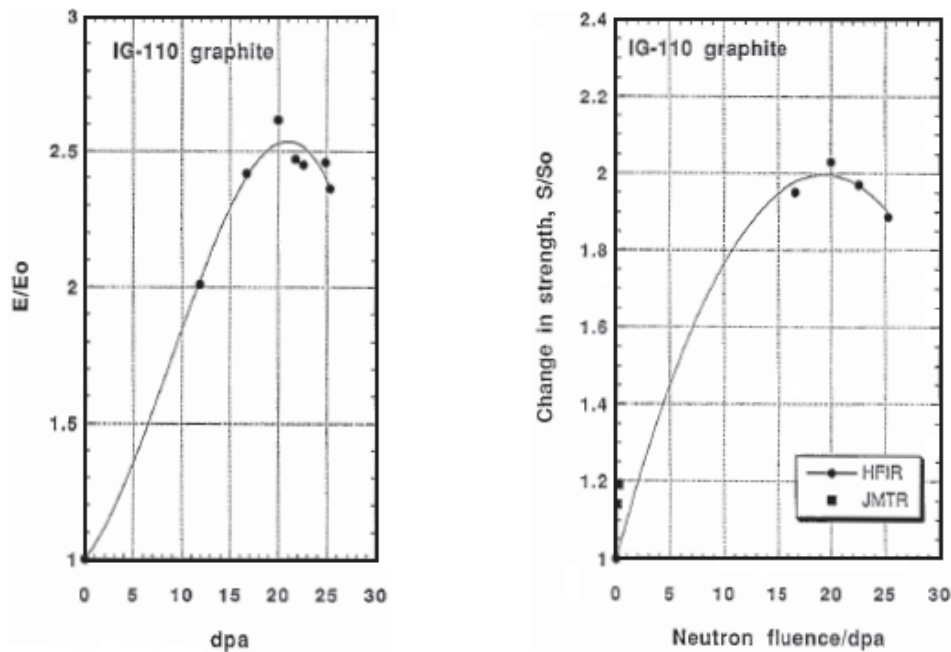


Figure 4-12. Young's modulus (a) and mechanical strength (b) as function of dpa caused by irradiation (Burchell et al. 1996).

As a reference example, the central replaceable reflectors indicated in the Figure 4-1 experience the neutron fluence of 6.7×10^{20} n/cm² per year (neutron energy > 0.1 MeV) with a neutron dose of 0.56 dpa per year (Bratton et al. 2005). In contrast, the support block and plenum experience neutron fluences of 9.1×10^{15} n/cm² per year [$E > 0.1$ MeV] and 3.7×10^{17} n/cm² per year, respectively, with negligible neutron dose in dpa for both sections (Bratton et al. 2005). Using the central reflector case as the reference and taking the neutron fluence ratio, the neutron dose received by support block and plenum are 7.606×10^{-6} and 3.1×10^{-4} dpa per year, respectively. Considering the projected plant design life is 60 years (Bratton et al. 2005), the total neutron dose received by the support block and the plenum is 4.56×10^{-4} and 1.85×10^{-2} dpa, respectively. As is apparent on Figures 4-12(a) and 4-12(b), mechanical property changes because of irradiation at these dpa are probably negligible, therefore the effect of irradiation was ignored for the stress analysis.

Normal operation temperatures for support block and plenum are about 1,000°C, and 1,000–1,200°C, respectively (Bratton et al. 2005). Because they experience irradiation at temperatures higher than the irradiation temperature in Ishiyama et al.'s experiment, the Young's modulus and strength might behave a little differently than the data shown in Figure 3-12; however, considering mechanical properties tend to recover back toward the original values at higher temperature because of the annealing effect (Burchell et al. 1996), it is most likely that the effect of irradiation on the Young's modulus and strength is less at the higher irradiation temperatures at which the support block and plenum normally operate.

4.2.5 Treatment of Material Properties during Analysis

4.2.5.1 Young's Modulus vs. Strain

The IG-110 is treated as an ideal brittle ceramic material for this application because it exhibits elastic behavior with a constant Young's modulus and does not undergo any plastic deformation before reaching the strength limit. As a relative example, Figure 4-13(a) shows the compressive stress-strain curve of UNS31803 steel, a ductile metal. As a ductile metal, its stress-strain curve is characterized by its ability to undergo plastic deformation up to a large strain value. It initially shows elastic behavior, but after about 700 MPa, starts to plastically deform until it eventually fails at the strain of 0.35. Figure 4-13(b) shows the stress-strain curve for IG-110. Please note the scale of the strain, which is 10-times smaller than that in Figure 4-13(a). Unlike the steel, IG-110, being a brittle ceramic material, is not able to handle much strain before failure and shows almost no plastic deformation. Plotting the IG-110 stress-strain curve on Figure 4-13(a) appears as almost a straight line.

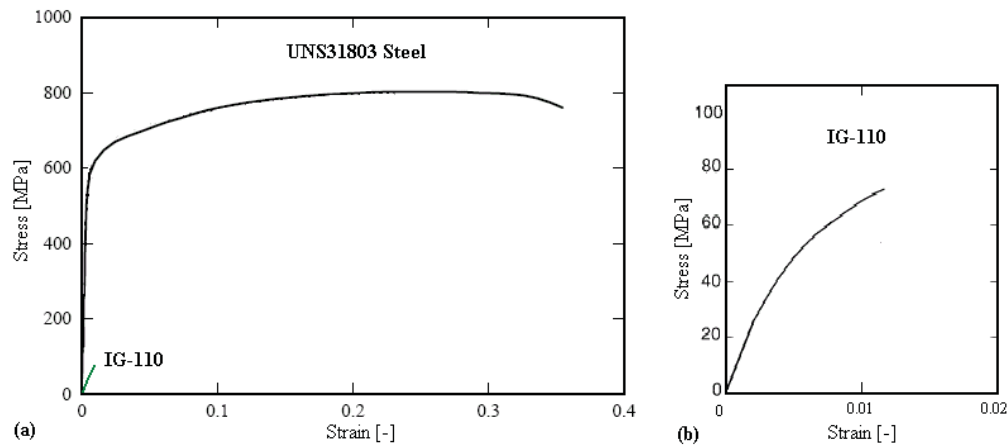


Figure 4-13. (a) Compressive stress-strain curve for UNS31803 Steel (Rasmussen 2001), and (b) Compressive stress-strain curve for IG-110 (Fuji et al. 1997).

4.2.5.2 Effect of the Temperature, Burn-off, and Irradiation

During the analysis, the young's modulus and density were estimated for the section number, the respective temperature and burn-off of the time point shown in Figures 4-6, 4-7, and 4-8, respectively, where the effect of irradiation was ignored since it is probably negligible.

4.2.5.3 Failure Criteria

For this report, the principal stress failure criterion is used as the failure criteria. The failure is assumed to occur if the minimum principal stress (maximum compressive stress) exceeds the ultimate compressive strength, or if the maximum principal stress (maximum tensile stress) exceeds the ultimate tensile strength.

4.2.6 Initial Un-oxidized State Results

4.2.6.1 Load Stress

As the first step, the support block and plenum in unoxidized condition was analyzed to understand general stress distribution. Figure 4-14 shows the maximum compressive stress distribution on the

support block and plenum in unoxidized condition, analyzed using 1/6 cyclic symmetry. As shown in Figure 4-14, the maximum stress is concentrated on the root of the plenum, indicated in red color, which corresponds to 1 MPa, far below the mechanical strength limit of undamaged IG-110. Although not shown on the figure, the maximum tensile stress is 0.1 MPa, again far below the tensile strength limit. Because the corrosion and burn-off on the lower part of the plenum and the upper part of the support block is negligible, stress distribution on these parts would be about the same on other time points, and it is unnecessary to include them in the analysis. For this reason, only the parts between points L1 to L2, indicated in the Figure 4-14, were analyzed to reduce the size of the model and computation time.

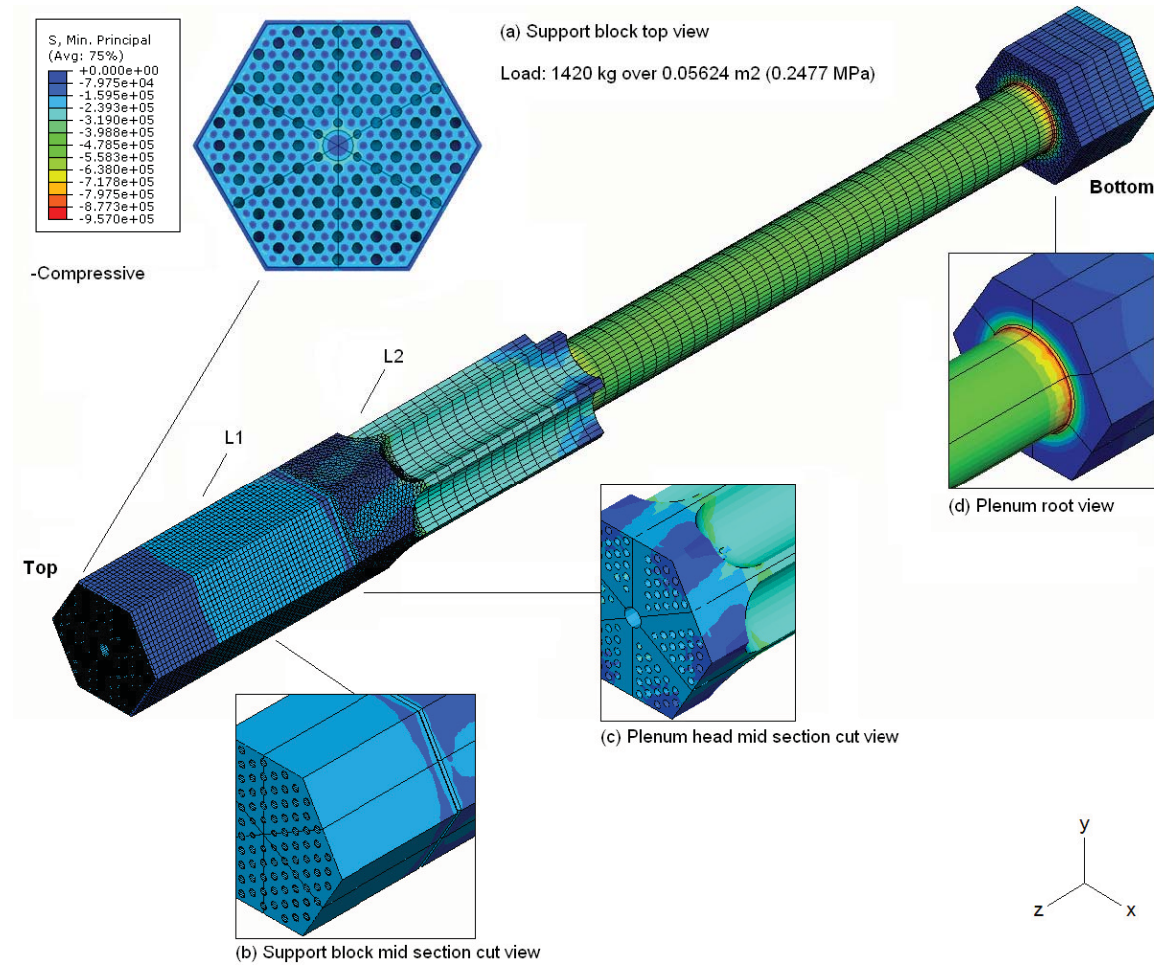


Figure 4-14. Compressive stress distribution on an unoxidized support block and plenum.

4.2.6.2 Analytical Validation

It is important to check the validity of the result obtained from finite element analysis by comparing it to the analytical estimate. For the middle of the support block and the middle of the plenum, analytical solutions to compressive stresses in z-axis direction (top to bottom) can be calculated by the simple stress relationship

$$\sigma = \frac{mg}{A} \quad (4-1)$$

where

m = Total mass of objects being supported by the area (kg)

g = The gravitational constant, 9.81 (m/s²)

A = The cross sectional area perpendicular to the loading (m²)

The two locations were chosen because the stress distribution on the cross sectional areas at these points are redistributed to be very uniform, and the loading scheme is almost uniaxial in z-axis direction such that analytical solution using the above equation should yield the same result as Figure 4-15. As shown, there are nine different stress components in 3-D principal stress that are accounted for to determine the maximum tensile and compressive stresses at a given point. However, when the loading scheme is simple, such that all of stress components except one normal stress component are negligible, the analytical solution using Equation (4-1) is approximately equal to the principal stress. At the middle of the support block and the middle of the plenum, all of stress components except the normal stress in z-axis are negligible.

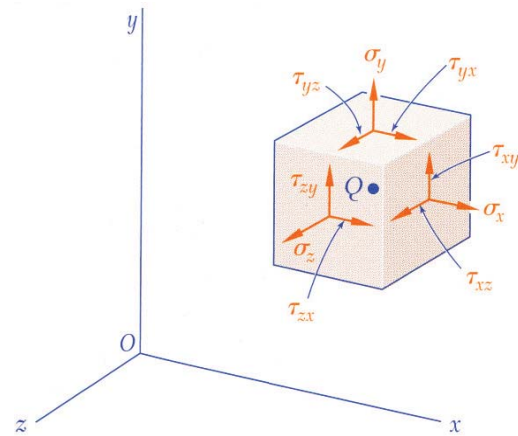


Figure 4-15. The principal stress components (Beer et al. 2006).

As shown in the Table 4-2, there is reasonable agreement between the result of the analytical calculation and the ABAQUS result, which suggests the finite element analysis was done correctly.

Table 4-2. Comparison of the analytical solution to the ABAQUS result.

Location	Supported Mass (kg)	Cross-Sectional Area (m ²)	Compressive Stress (Pa)	ABAQUS Result (Pa)
Middle of the support block	1,500	0.09148	1.636e5	1.625e5
Middle of the plenum	1,800	0.0353	5.002e5	4.915e5

4.2.6.3 Thermal Stress

Thermal stress analysis was done for a small representative part of the support including three coolant channels, indicated in Figure 4-16(a). When the coolant channel's outer surface experiences an exothermic surface oxidation reaction, this is the most likely location for the thermal stress fracture. The temperature difference between the outer surface and the inner body is expected to be in order of tens of degrees, therefore the coolant channel surface temperature of 1,300°C and internal body temperature of 1,250°C were assumed.

As apparent in the Figure 4-16(c) and 4-16(d), both the compressive and tensile stresses are below strength limits. Considering that the actual temperature difference between the coolant channel surface and the internal body is most likely much smaller than 50°C, the thermal stresses are likely smaller and thus negligible. Combined loading and thermal stress analysis was done for the nonuniform oxidation case for which the effect of thermal stress was again negligible.

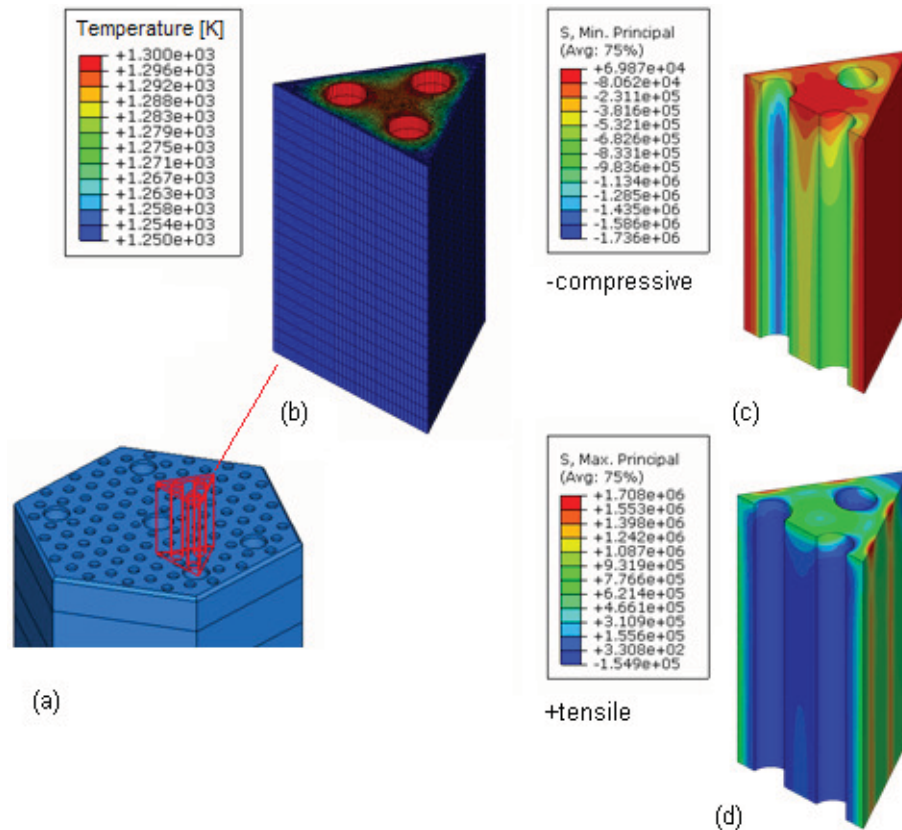


Figure 4-16. (a) Upper part of support block with triangular prism; (b) Mesh and temperature distribution; (c) Compressive stress; and (d) Tensile stress.

4.2.7 Oxidized State Results

4.2.7.1 Oxidized State Model

For oxidized states, simple modifications were made to the height of the plenum head section and support block to make them more structurally sound. Stress concentration would occur at the contact surface between the support block and plenum head (critical location in Figure 4-17), primarily because of the chamfer feature, which significantly reduces the size of cross sectional area available to support the load in heavily corroded states. The structure could last longer if the interacting surface is relocated to a higher place where oxidation damage is negligible. This is accomplished by adjusting the height of the plenum head and the support block by 25 cm.

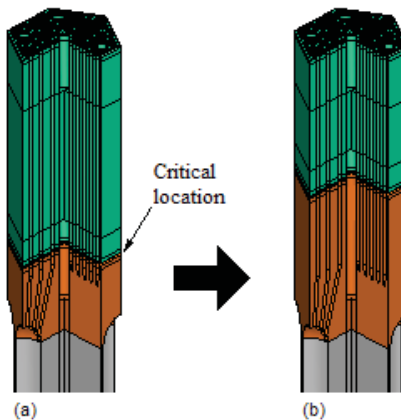


Figure 4-17. Modification of plenum head's height block by 25 cm.

Among the dimensions used for the plenum, some of them are not yet set in stone and are open to modifications, such as the height of the plenum head and support block. The plenum head's height was increased by 0.25 m, which consequently decreased the support block's height by 0.25 m. From a manufacturing standpoint, there should be no difficulty in making these modifications. Most of the fuel and support blocks have straight channel holes drilled 0.8 m long. With the height modification, instead of drilling a 0.05 m long hole from the top of plenum head, it is now increased to 0.3 m, which is still much shorter than 0.8 m. With the height of the plenum increased by 0.3 m, the chamfer and interacting surface are relocated away to a place where corrosion and burn-off are almost negligible. With the interacting surface and chamfer relocated, the cross-sectional area at the critical location is increased, which relieves the stress concentration. And because the critical location is now placed in the middle of a continuous body, it is more structurally sound.

Figure 4-18 shows the 1/6 cyclic symmetry unit of the modified plenum head at particular times during transient. As corrosion progresses and the coolant channels collapse together, the plenum head eventually develops pillars, which are the remains of the thickest parts of the plenum head. Table 4-3 shows the material properties used for each day.

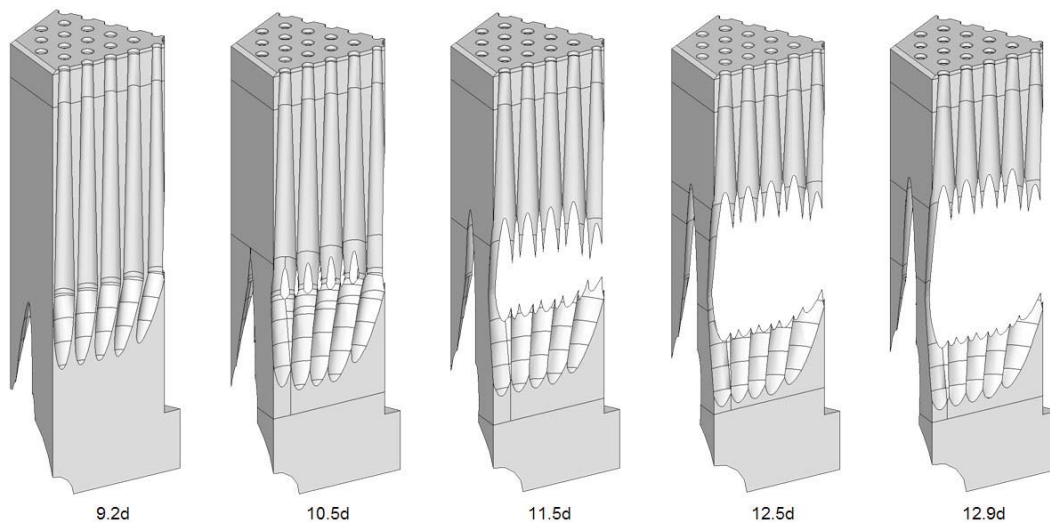


Figure 4-18. Assumed 1/6 cyclic symmetry units of the modified plenum head for each day.

Table 4-3. Material properties at each day.

Day	T [K]	Burn-off [-]	Density [kg/m ³]	E [GPa]	Compressive Strength [MPa]	Tensile Strength [MPa]
9.2	962	0.0743	1,648	4.7403	36.8721	11.6692
10.5	950	0.0861	1,627	4.2800	34.0125	10.7641
11.5	950	0.0960	1,609	3.9292	31.7850	10.0592
12.5	950	0.1050	1,593	3.6323	29.8870	9.4585
12.9	950	0.1090	1,586	3.5068	29.0802	9.2032

4.2.7.2 Oxidized State Model

Figures 4-19 and 4-20 show the maximum compressive and tensile stresses for two different locations, the edge and inside, indicated in the Figure 4-21b and 4-21c for compressive stress and Figures 4-22b and 4-22c for tensile stress. From observing Figure 4-21a and 4-21b, it can be seen that the bottom half of the pillar is slanted to the left, which creates a counter clockwise bending moment, causing compressive stress (Figure 4-21b) toward the left side and tensile stress (Figure 4-22b) toward the right side. In contrast, the top half of the pillar is straight, and because of the counter clockwise bending moment of the bottom half, the top half of the pillar is subjected to compressive stress on the right side and tensile stress on the left side. Local maximum near the edge occurs because the bending moment causes the greatest stress on the outer edge, which gets exacerbated by the decreasing cross-sectional area toward the edge because of the triangular shape. The stress is relieved toward the inner section where the cross-sectional area gets relatively larger.

Note that exceeding the strength limit on the edge does not necessarily lead to failure, because, after edge portion crumbles, the stress get redistributed to the inner section, and the inner section's cross sectional area is most likely wide enough to handle the additional loading without much change in stress concentration. But, exceeding the mechanical strength of the inner section is a definite sign of failure because failure of the inner section results in significant loss of cross sectional area to handle the load.

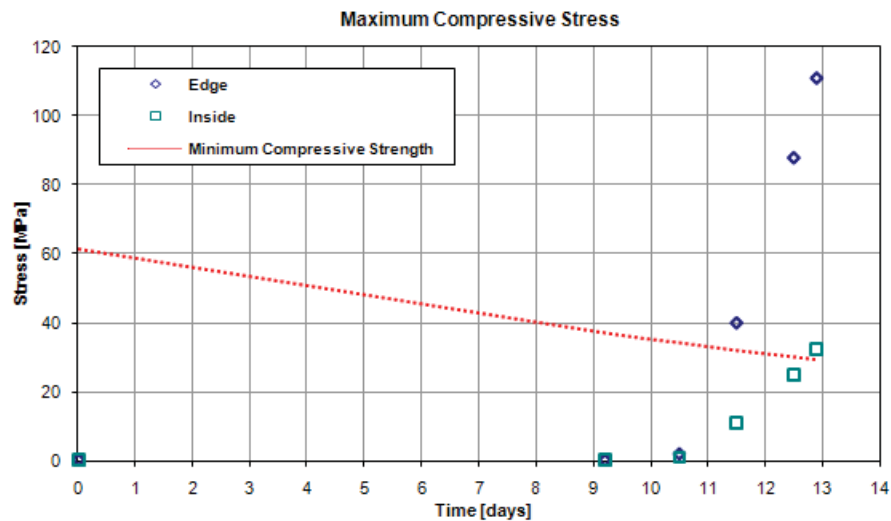


Figure 4-19. Maximum compressive stress over time.

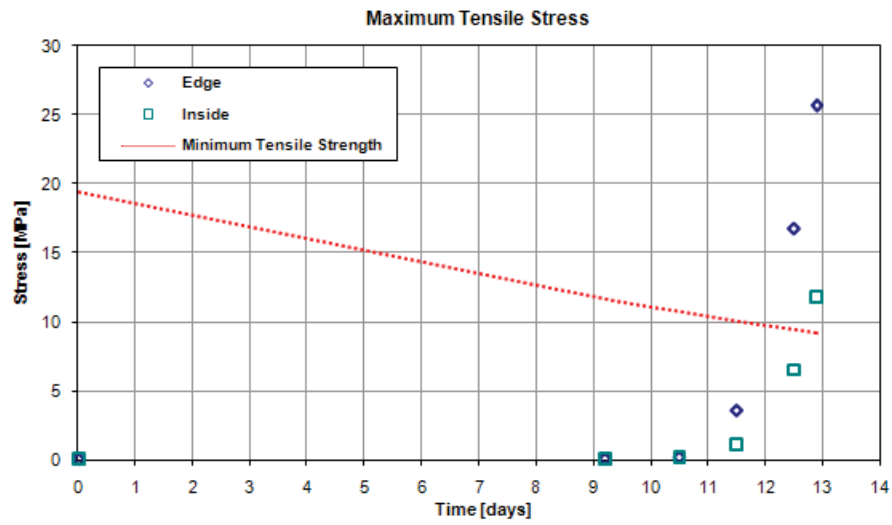


Figure 4-20. Maximum compressive tensile stress over time.

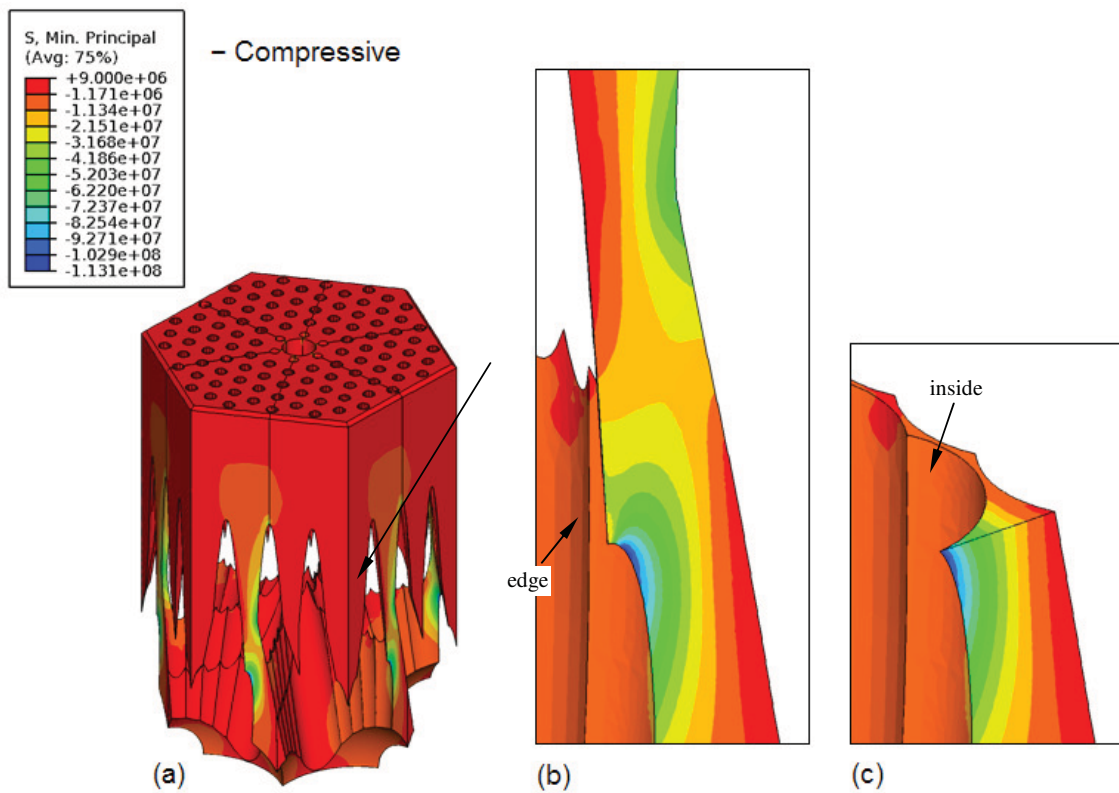


Figure 4-21. Compressive stress distribution of non-uniform corrosion model, 12.25 days after LOCA.

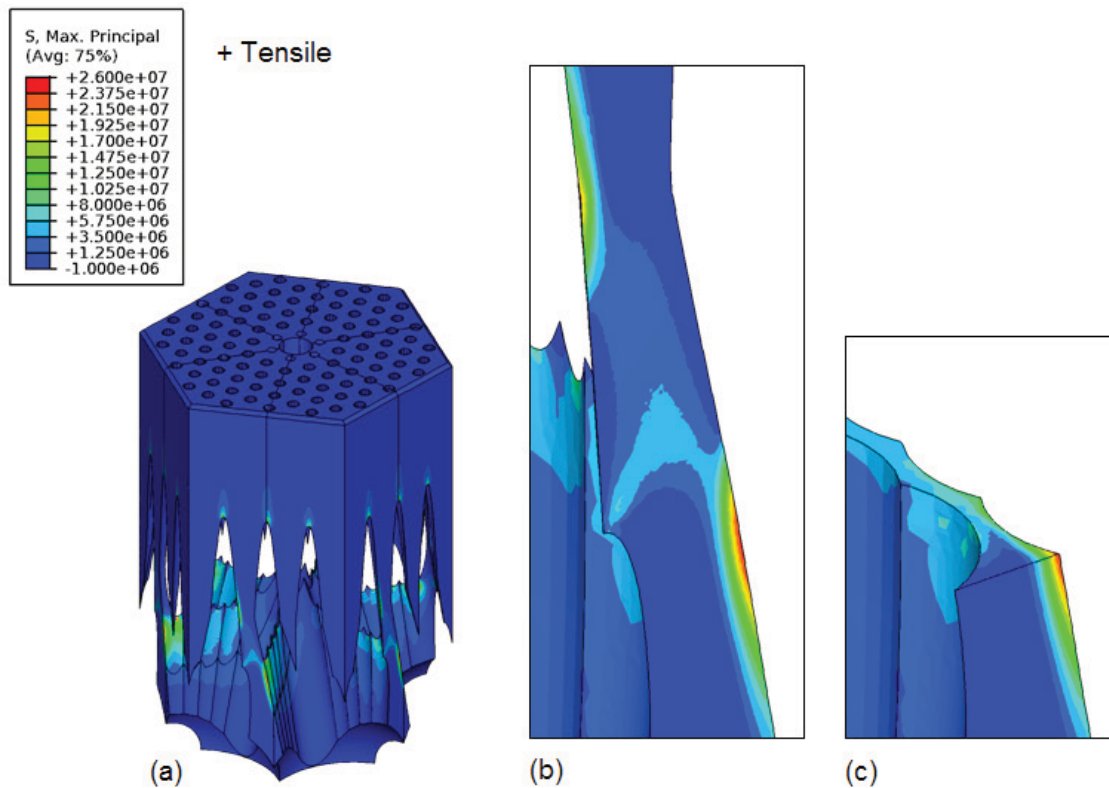


Figure 4-22. Tensile stress distribution of non-uniform corrosion model, 12.25 days after LOCA.

The stress concentrations are increasing almost exponentially over time because they are inversely proportional to the cross sectional area, which is also decreasing over time because of corrosion. The compressive strength shown in Figure 4-19 and 4-20 is exceeded first on the edge after 11.5 days, and both mechanical strengths are exceeded on the inside after 12.9 days.

4.3 Estimation of Conservative Burn-off Criteria for Graphite Structure

Degradation of graphite structural integrity by oxidation is currently subject of research in VHTR safety. The degradation is processed by two different mechanisms. Internal corrosion in the graphite pores lowers the graphite compressive strength with pore collapses, and the external corrosion leads to the stress concentration with overall size reduction. If left unabated, this degradation can result in the major failure of core structures.

In this section, simple simulations were carried out to estimate how much graphite should be burned before it fails. So, this study is aimed at providing the maximum allowed burn-off limit in certain conditions and conservatively accounts for the additional thermal energy released in the oxidation reaction. There are some advantages in this approach. First, this method provides direct estimation of structural failure in the VHTR core. The failure criteria can be directly implemented in the code. Therefore, this method is much faster and convenient than the approach used in the previous section. Second, it provides much more conservative predictions than the previous section. If the calculation result is within the criteria, there can be some confidence for the graphite structures to be secure.

The modeling and simulation in this section is based on the GTMHR 600 MWth core design, but the same methodology can be applied to the other reactor types. Figure 4-23 shows the basic pattern in the GTMHR bottom reflector, which is the most vulnerable to oxidation damage from an air-ingress accident (Kim et al. [2008]). In addition, the bottom reflector suffers from the highest mechanical stress on it.

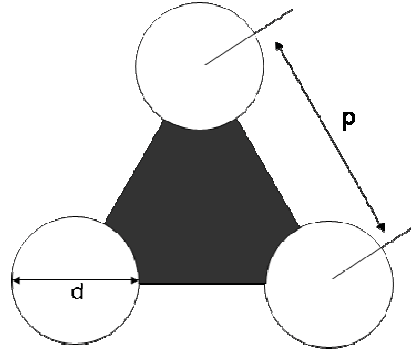


Figure 4-23. Unit block schematics.

As mentioned above, oxidation generally causes structural problems in two ways: the decrease of size will increase the stress concentration for unit surface area, and the increase of internal pore size will weaken the structure by decreasing its compressive strength. Eventually, if the stress exceeds the compressive strength, the structure can be considered fractured. Therefore, predicting graphite compressive strength and cross-sectional surface area are the essential parts of estimating graphite fracture.

The changes of graphite compressive strength can be calculated by predicting the change of graphite density because density is the main variable of graphite's compressive strength. Changes in graphite cross-sectional areas can be calculated by predicting the corrosion depths of the flow channels. In this study, the changes of the graphite density and cross-sectional area were modeled as detailed below.

First, the oxidized mass of the outside (by external corrosion) and inside (by pore oxidation) can be respectively expressed as

$$dM_{sur} = \rho \cdot (\pi r L) \cdot dr \quad (4-2)$$

$$dM_{in} = -A \cdot L \cdot d\rho \quad (4-3)$$

where

dM_{sur} = Oxidized mass change of graphite on the external surface (kg)

dM_{in} = Oxidized mass change of graphite in the inside of the pores (kg)

ρ = Density of graphite (kg/m³)

r = Radius of the flow channel (m)

L = Length of the channel (m)

A = Cross-sectional area (m²).

dM_{sur} and dM_{in} can be expressed by the total mass changes, dM_{tot} as

$$dM_{sur} = f \cdot dM_{tot} \quad (4-4)$$

$$dM_{in} = (1 - f) \cdot dM_{tot} \quad (4-5)$$

where

dM_{tot} = Total oxidized mass change of graphite at a certain time (kg)

f = Fraction of surface reaction to total reaction.

The fraction, f in Equation (4-4) and (4-5) is a very complicated function determined by oxidation and flow variables such as temperature, pressure, flow velocity, and oxygen concentration. Therefore, Equation (4-2) and (4-3) can be rewritten by

$$\frac{dr}{dM_{tot}} = \frac{f}{\rho \cdot (\pi r L)} \quad (4-6)$$

and

$$\frac{d\rho}{dM_{tot}} = -\frac{(1-f)}{A \cdot L} \quad (4-7)$$

The cross-sectional area A in Equation (4-6) and (4-7), where the load is imposed on, can be expressed by

$$A = \frac{\sqrt{3}}{4} p^2 - \frac{1}{2} \pi r^2 \quad (4-8)$$

The total graphite burn-off, B_{tot} can be defined as

$$B_{tot} = \frac{M_{tot}}{\rho_0 \cdot V_0} = \frac{M_{tot}}{\rho_0 \cdot A_0 \cdot L} \quad (4-9)$$

where

M_{tot} = Total oxidized mass of graphite (kg)

ρ_0 = Initial density of graphite (kg/m³)

L = Length of the channel (m)

A_0 = Initial cross-sectional area (m²).

Therefore, the total oxidized mass is express by

$$M_{tot} = \rho_0 \cdot A_0 \cdot L \cdot B_{tot} \quad (4-10)$$

If the density of the oxidized graphite were normalized at a certain time, it can be expressed by

$$\rho' = \frac{\rho}{\rho_0} \quad (4-11)$$

Inserting Equation(4-8), (4-10), and (4-11) into Equation(4-6) and Equation(4-7) derives two differential equations:

$$\frac{dA}{dB_{tot}} = -(A_0 f) \cdot \left(\frac{1}{\rho'} \right) \quad (4-12)$$

and

$$\frac{d\rho'}{dB_{tot}} = -(A_0(1-f)) \cdot \left(\frac{1}{A} \right) \quad (4-13)$$

By solving those two differential equations, the changes of graphite cross-sectional area (A) and normalized density (ρ') can be estimated as a function of total graphite burn-off (B_{tot}). The stress on the structure can be estimated by the information of the cross-sectional area (A), and the compressive stress can be estimated by the changes of the normalized densities (ρ'). The stress and the compressive strength can then be calculated as

$$P = \frac{W_0}{A} \quad (4-14)$$

where

$$P = \text{Stress (Pa)}$$

$$W_0 = \text{Load on the structure (N)}$$

and

$$S = S_0 \cdot \rho'^{\beta} \quad (4-15)$$

where

$$S = \text{Compressive Strength (Pa)}$$

$$S_0 = \text{Initial compressive strength (Pa)}$$

$$\beta = \text{Constant depending on the graphite types.}$$

The correlations between local density and compressive stress were obtained by Oh et al [2008]. Figure 4-24 and 4-25 show the data for IG-110 and H451, respectively. According to the research, the constants, β are 6.5 for IG-110, and 6.25 for H-451 graphite. The initial compressive strength of those graphite materials are 70.5 and 52.7 MPa, respectively.

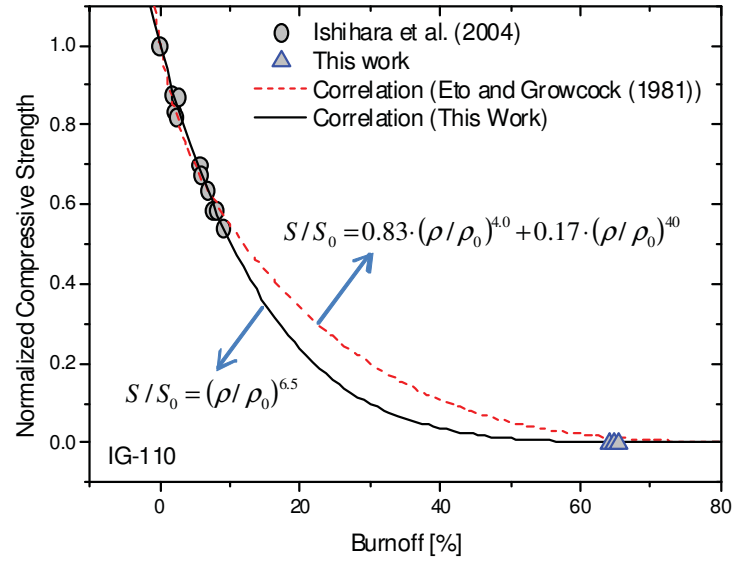


Figure 4-24. Relation between local burn-off and normalized compressive strength (IG-110).

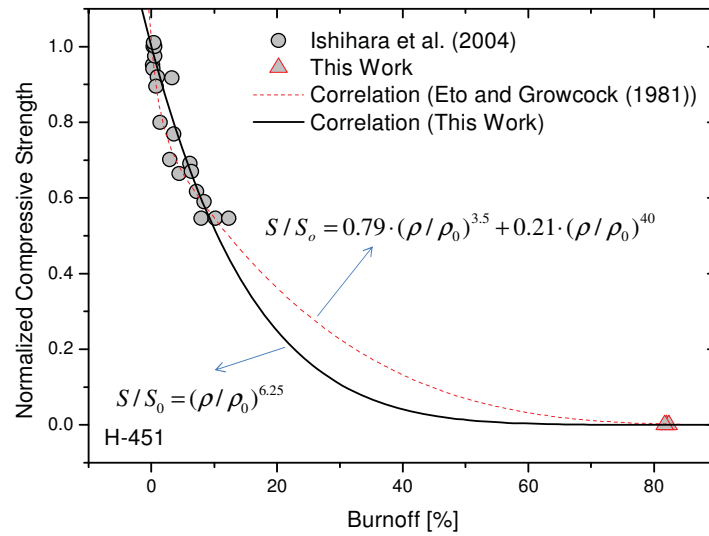


Figure 4-25. Relation between local burn-off and normalized compressive strength (H-451).

To judge the fracture of the graphite structure, the following three criteria were used in this research.

- $S > P$
- $\rho' < \rho'_{\text{limit}}$
- $p < 2r$.

Criteria (a) represents that if the stress (S) imposed on the structure exceeds the compressive strength (P) of the oxidized graphite, it will fail. Criteria (b) represents that if the normalized density (ρ') exceeds a certain limit (ρ'_{limit}), it will fail. The normalized density limit was obtained from the data measured by Oh et al. [2008]. They experimentally measured the burn-off level in which the graphite loses its mechanical strength, and provided the data for IG-110 and H451 graphite. The normalized density limits are 0.35 and 0.18 for IG-110 and H451, respectively. Criteria (c) represents that if the adjacent two flow channels are collapsed, it will fail.

To simulate the fracture of the graphite structure, MATLAB SIMULINK was selected in this research. Figures 4-26, 4-27, and 4-28 show three different models developed: constant f , randomly sampled f (uniform distribution), and randomly sampled f (Gaussian distribution). The f -value represents the ratio of the external surface reaction to the total reaction. As mentioned, this value depends on various fluid and flow conditions, and therefore varies significantly during an air-ingress accident. In this research, the f value between 0 and 1 at every time-step were randomly picked because the value cannot yet be determined. Theoretically, randomly selected f value based on uniform distribution provides the largest uncertainty because the deviation from the mean value is the largest in this distribution. However, in the uniform distribution, the average f -value converges to 0.5, which is the mean value of the probability distribution function. For this reason, the Gaussian distribution was also used with different mean values ranging from 0 to 1. Statistically, the randomly selected f -value will cover all possible scenarios of air-ingress accidents. The constant f value case, in which the f value was maintained constant at every time-step, was used for base data. Table 4-4 summarizes the input parameters used in the simulation. In this simulation, the input parameters were determined based on the GTMHR 600 MWth reactor.

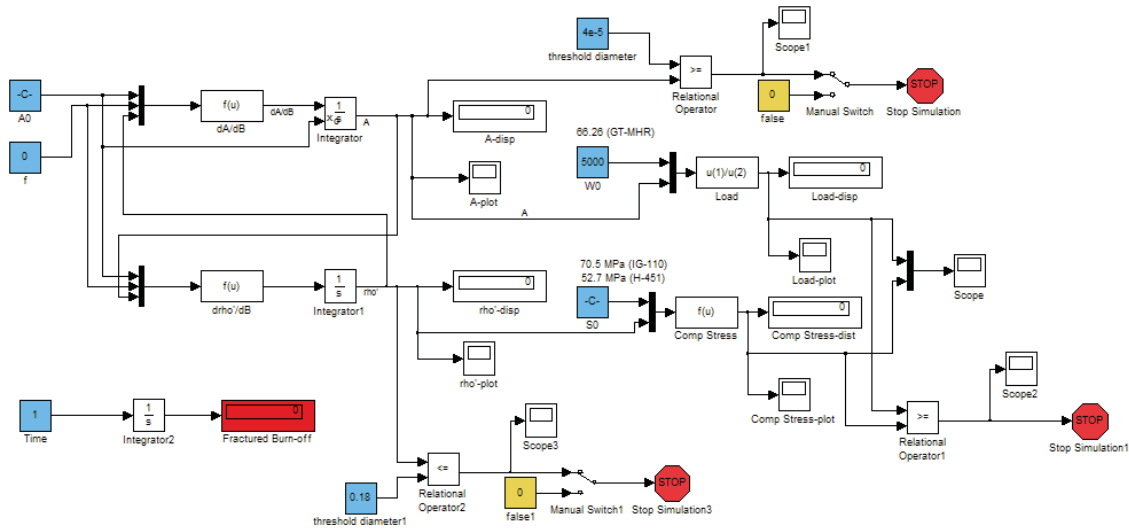


Figure 4-26. Modeling of graphite fracture by corrosion damage (constant f).

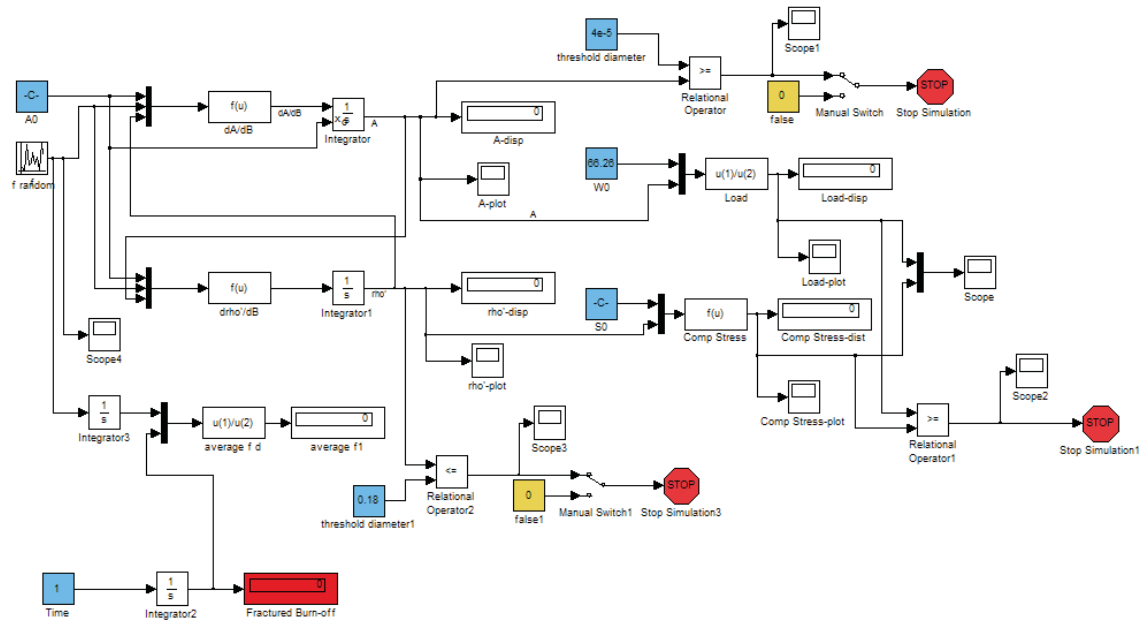


Figure 4-27. Modeling of graphite fracture by corrosion damage (randomly sampled f [uniform]).

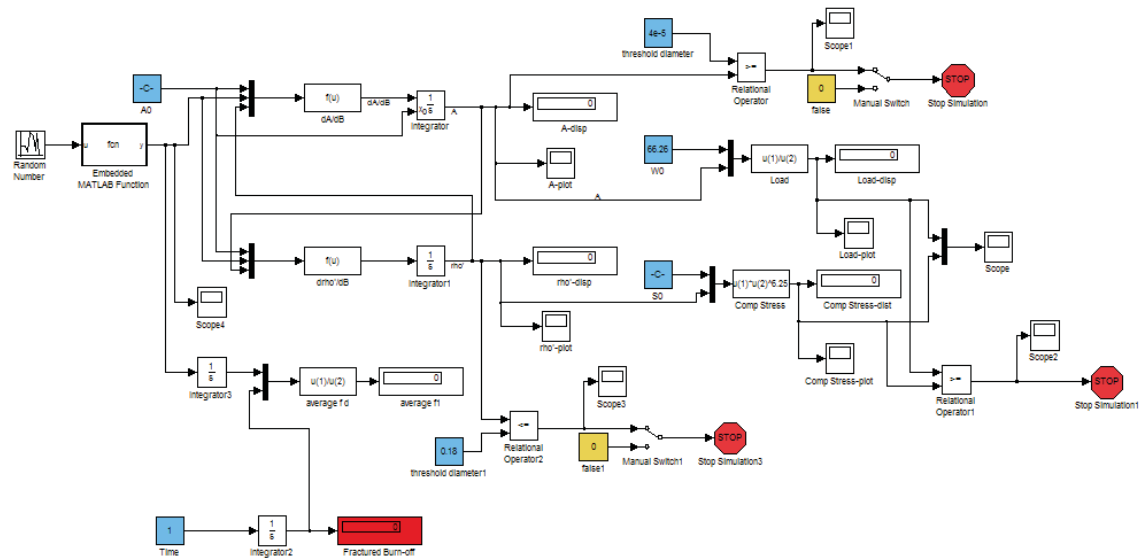


Figure 4-28. Modeling of graphite fracture by corrosion damage (randomly sampled f [Gaussian]).

Table 4-4. Input parameters for graphite oxidation and structural integrity.

Parameters	Values
Initial cross-sectional area (m^2)	0.00037
Load for a unit cell (N)	66.26
Initial compressive strength (MPa)	70.5 (IG-110), 52.7 (H451)

Figure 4-29 shows the calculated data for f -values (f) vs. total fractured burn-off (B_{tot}) based on the IG-110 graphite properties. In this calculation, the maximum allowable burn-off (0.6) was viewed at f -value = 0, meaning that the graphite becomes the most vulnerable to the oxidation damages when the whole reaction is dominated in the inside pores. As the f -value increases, the fractured burn-off also increases almost linearly. It indicates that the reduction of compressive strength by internal corrosion plays a significant role in the graphite fracture mechanism. The allowable burn-off was estimated to be 0.93 at $f = 0.8$. After $f = 0.8$, the fractured burn-off was estimated to decrease because of different fracture criteria (Criteria (c): flow channel collapsing). Thus, at large f -values, the external surface reaction plays a main role in the fracture because at even very high burn-offs, the compressive strength of the graphite has not reached the maximum stress imposed on the structure.

Figures 4-29 and 4-30 show that the data obtained from random f -value are in good agreement with those from constant f -value within 4% maximum error (red line). Therefore, conservatively, the maximum allowable total burn-off can be determined from the lowest value of the lower red line. The estimated allowable burn-off is 0.58 with 99% confidence level. It indicates that the graphite structure will not be failed at lower than 0.58 in total burn-off.

Figures 4-31 and 4-32 show the calculated results for H451 graphite. The same methodologies used in Figures 4-29 and 4-30 were applied to these analyses. The results show that the minimum allowable total burn-off for this material is 0.57, almost the same as that of the IG-110 graphite.

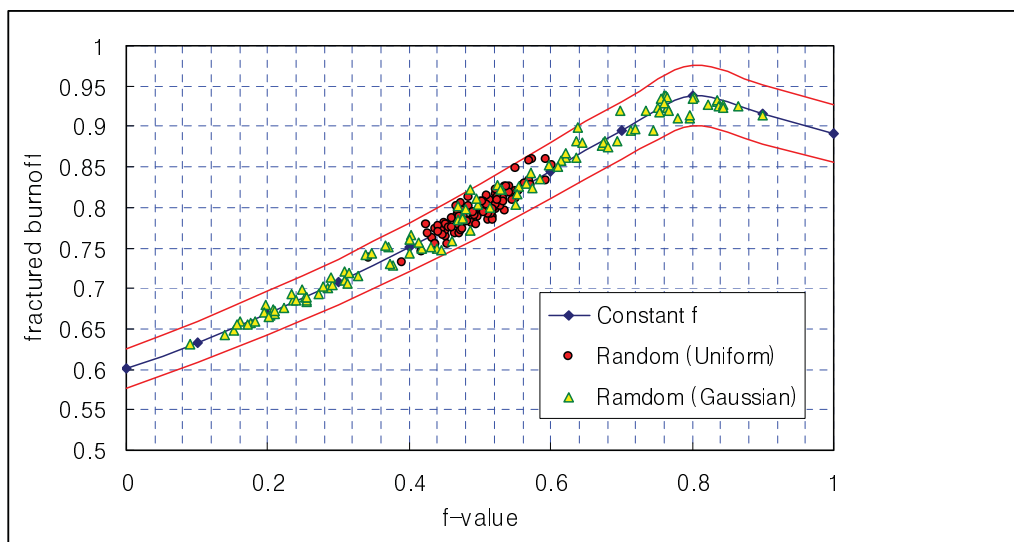


Figure 4-29. Relations between f -value (f) vs. fractured total burn-off (IG-110).

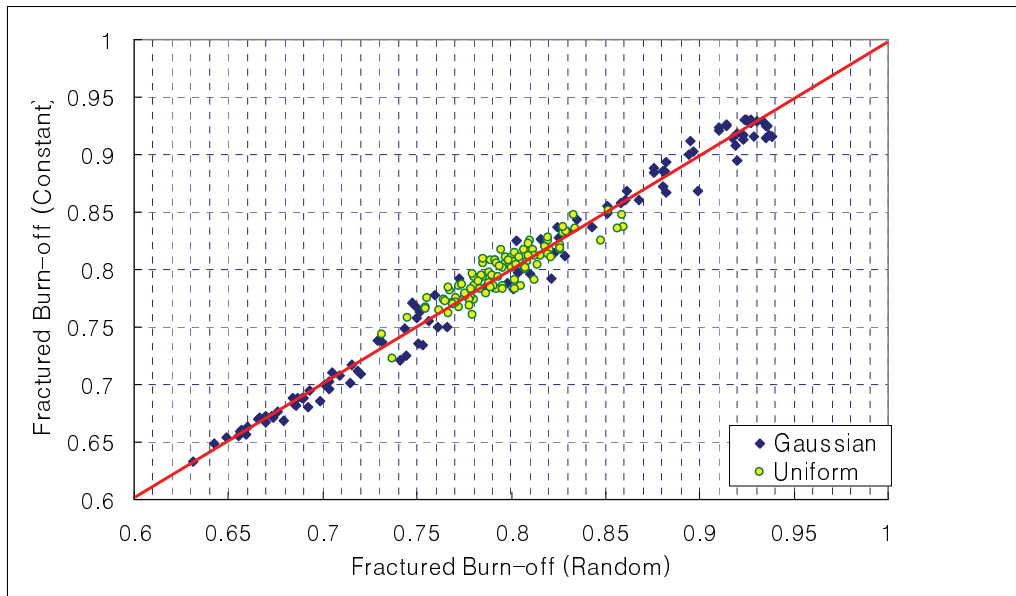


Figure 4-30. Fractured burn-off (Random f) vs. fractured burn-off (constant f) – IG-110.

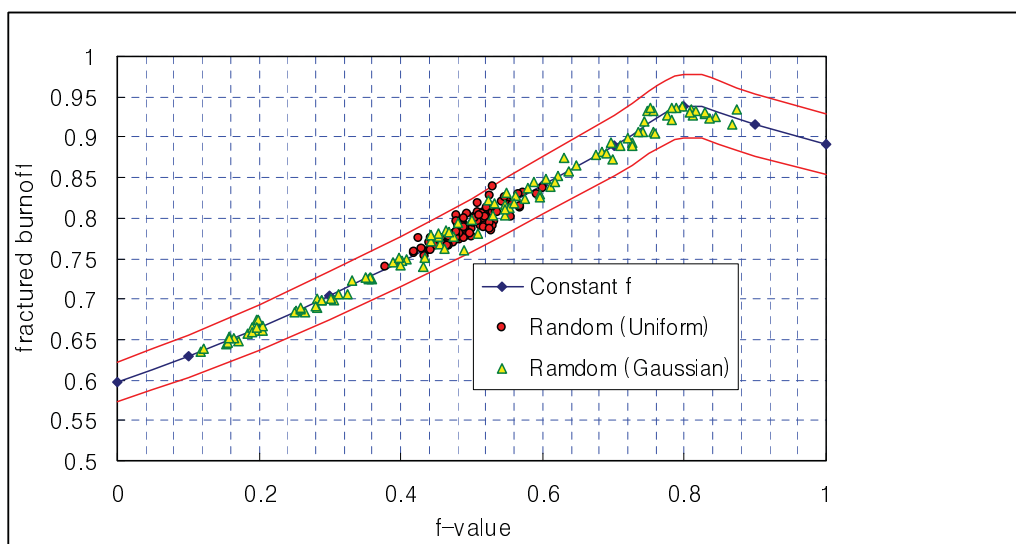


Figure 4-31. Relations between f -value (f) vs. fractured total burn-off (H451).

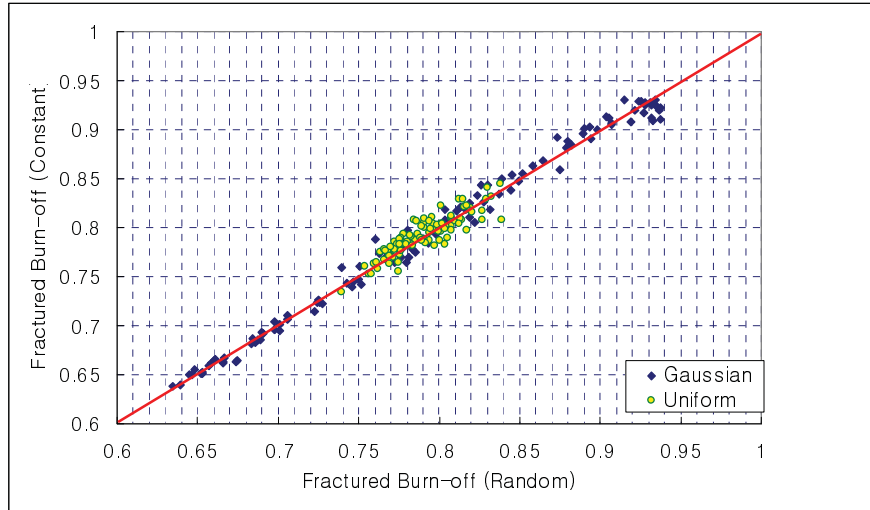


Figure 4-32. Fractured burn-off (random f) vs. fractured burn-off (constant f) – H451.

4.4 Implementation of Advanced Graphite Oxidation Model into GAMMA code and Analyses

In FY-09, the graphite oxidation models in the GAMMA code have been updated. In the updated models, the reaction kinetics, mass transfer, moisture, burn-off, and conservative failure criteria have been considered. The following summarizes the models.

The overall graphite oxidation rate is affected by two mechanisms; reaction kinetics and mass transfer. At low temperatures lower than about 700°C, the reaction kinetics dominates the oxidation rate. Therefore, the overall rate follows Arrhenius model very well at this range. However, at high temperature above about 950°C, the oxidation rate is dominated by the mass transfer of oxygen molecules in the working fluids. In the intermediate temperature ranges, the oxidation rate is affected by both kinetics and mass transfer (See Figure 4-33).

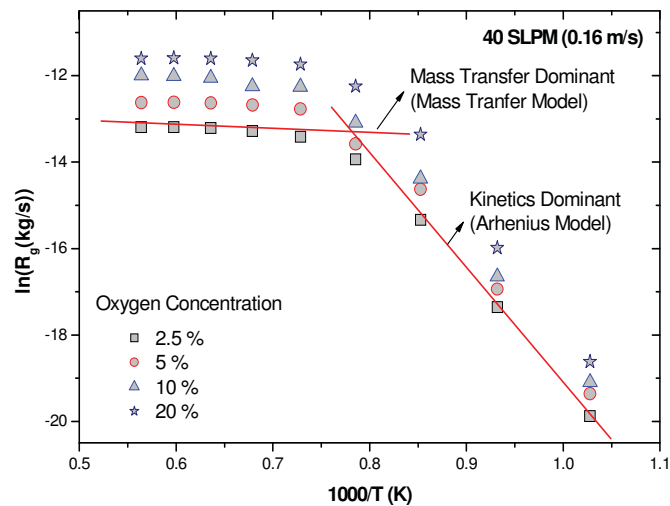


Figure 4-33. Overall graphite oxidation rate (Oh et al. 2006).

The overall graphite oxidation rate can be determined by (Oh et al. 2006)

$$\frac{1}{R_g} = \frac{1}{R_k} + \frac{1}{R_m} \quad (4-16)$$

where

- R_g = Overall graphite oxidation rate (kg/s)
- R_k = Graphite oxidation rate estimated by Arrhenius model (kg/s)
- R_m = Graphite oxidation rate estimated by mass transfer (kg/s).

R_k and R_m in Equation (4-16) can be determined by the following equations.

The oxidation rate by kinetics effect can be calculated by the Arrhenius equation form (Oh et al. 2006)

$$R_k = 2552000 \cdot \exp\left(-\frac{218,000}{R \cdot T}\right) \cdot P_{O_2}^{0.75} \cdot M_B(B) \cdot \theta_0 \cdot V \quad (4-17)$$

where

- R = Gas constant (8.315 kJ/kmol K)
- T = Graphite surface temperature (K)
- P_{O_2} = Oxygen partial pressure (Pa)
- $M_B(B)$ = Multiplication factor involved in the burn-off degree
- θ_0 = Graphite initial surface density (m²/m³)
- V = Apparent volume of the graphite structure.

The multiplication factor, $M_B(B)$ in Equation (4-17) can be determined by the relationship between the burn-off and oxidation rate shown in Figure 4-34.

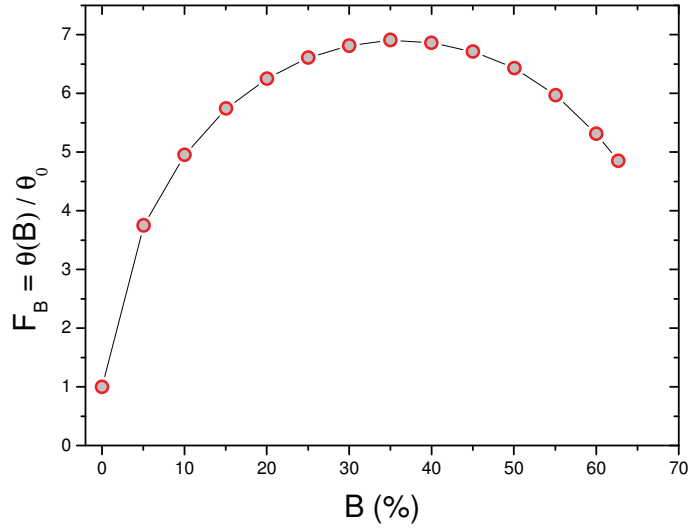


Figure 4-34. Relationship between burn-off (%) and multiplication factor (Oh et al. 2008).

The burn-off (B) in this figure is defined by

$$B = \frac{\rho_0 - \rho(t)}{\rho_0} \quad (4-18)$$

where

ρ_0 = Initial graphite density (kg/m^3)

$\rho(t)$ = Graphite density at time, t (kg/m^3).

Graphite oxidation rate by the mass transfer can be calculated by a general mass transfer model

$$R_m = 2M_c \cdot K_m (C_{O_2,\infty} - C_{O_2,0}) \cdot A \quad (4-19)$$

where

M_c = Molecular mass of carbon, C (12 kg/kmol)

K_m = Mass transfer coefficient of oxygen (m/s)

$C_{O_2,\infty}$ = Oxygen concentration in the bulk flow (kmol/m^3)

$C_{O_2,0}$ = Oxygen concentration at the graphite surface (kmol/m^3).

In the mass transfer dominant condition in which the temperature is very high, the surface concentration of the oxygen, $C_{O_2,0}$ is assumed to be zero. The mass transfer coefficient, K_m is a function of flow parameters; temperature, pressure, and velocities. When the effect of moisture is considered, the mass transfer rate is corrected as (Kim et al. 2008).

$$R_{m,moist} = 0.5 \cdot R_m . \quad (4-20)$$

The rate of graphite oxidation is affected by an oxidation history following density and overall size changes. It is therefore necessary to track the density and the size of the graphite structure in calculation. The changes of graphite overall size and density can be estimated by (Kim et al. 2008)

$$\frac{d\rho(t)}{dt} = -(1-f) \cdot R_g / V(t) \quad (4-21)$$

and

$$\frac{dz(t)}{dt} = \frac{1}{A(t)} \cdot \frac{f \cdot R_g}{\rho(t)} \quad (4-22)$$

where

f = Ratio of external reaction rate to total reaction rate

$V(t)$ = Apparent volume of graphite structure at time, t (m^3)

$z(t)$ = Corrosion depth of the graphite structure (m)

$A(t)$ = Apparent reacting surface area of graphite (m^2).

Equations (4-21) and (4-22) calculate the density changes and corrosion depth changes by oxidation, respectively. The volumes and surface areas are updated in each time-step based on the original geometries and the corrosion depth calculated. The ratio of external reaction to total reaction can be calculated by (Kim et al. 2008)

$$f = \frac{1/R_m}{1/R_k + 1/R_m} . \quad (4-23)$$

As mentioned in previous sections, one of the important issues in VHTR safety is fracture of the graphite structure by oxidation damages in the air-ingress accident. The oxidation damages generally degrade the structural integrity of graphite in two ways. Internal oxidation in the graphite inside pores degrades the graphite compressive strength, which is a resistive force under the compressive force. External oxidation in the graphite structure outside concentrates the stress on the smaller region by reducing the cross-sectional surface area where the compressive force is imposed. In Section 4.3, the minimum allowable total burn-off for IG-110 and H451 was estimated to be 0.58 and 0.57, respectively.

The total burn-off can be calculated and updated in the computer codes by

$$\frac{dM_g(t)}{dt} = -R_g \quad (4-24)$$

$$B_t(t) = \frac{\rho_0 V_0 - M_g(t)}{\rho_0 V_0} \quad (4-25)$$

where

M_g = Graphite mass in the unit cell (kg)

B_t = Total graphite burn-off.

All the graphite oxidation models were implemented into the GAMMA system analyses code. Figure 4-35 shows the flowchart of the advanced graphite oxidation models in the upgraded GAMMA code.

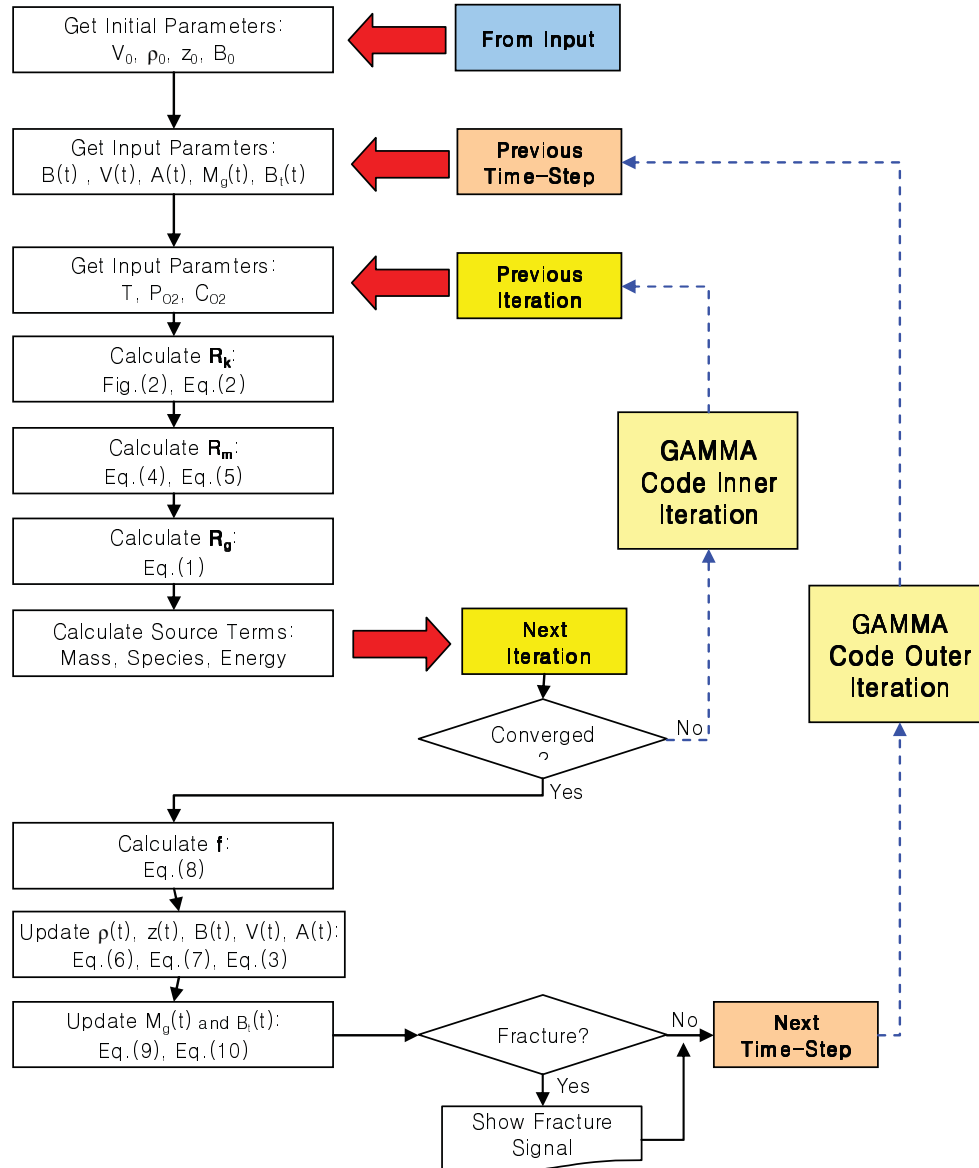


Figure 4-35. Flowchart of the advanced oxidation model.

The air-ingress analyses in this section were performed by the GAMMA code with the upgraded graphite oxidation model. The initial conditions of air-ingress after onset-natural-circulation were estimated by the FLUENT code. For this calculation, FLUENT code output data such as quasi-steady state value of air distribution, temperature and flow rate were implemented as initial GAMMA code values.

Figure 4-36 shows the code input nodalization where 2-D geometry models are used for the reactor cavity to consider the heat removal by natural convection flow, and for the solid structures including the core and reflector blocks to consider multidimensional heat conduction. Heat transport in the prismatic core is greatly complicated by the combined effect of solid conduction in the fuel, the graphite matrix and gas, and contact conduction and radiation in the fuel and fuel block gaps. In this simulation, the coolant channel and the fuel compact were separately treated by 1-D fluid equations and 2-D heat conduction equation from the graphite matrix, respectively. A porous media approach was applied to the reactor core, reflector, and plenum regions. The radiation heat exchanges were considered in every cavity and plenum. The air-cooling reactor cavity cooling system was modeled using the 1-D pipe network for the air flow loop and the 3-D tube model for the cooling tubes. Following the accident, since a reactor trips immediately, the core power is determined directly from the decay heat curves.

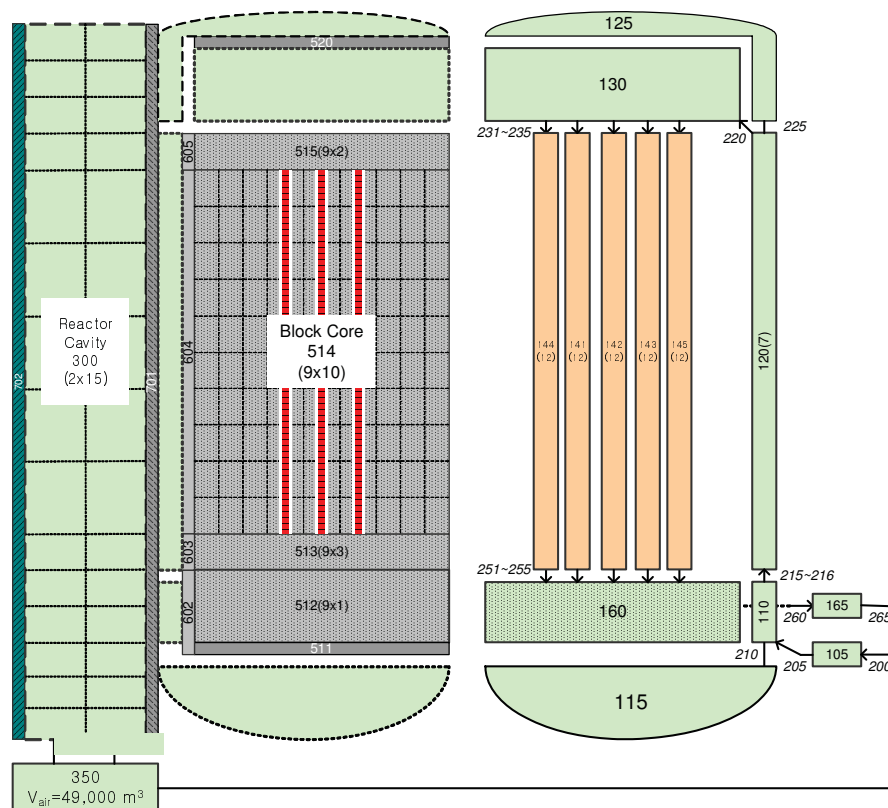


Figure 4-36. GTMHR 600 MWth code nodalization (GAMMA).

A summary of the modeling follows:

- 1-D (previous calculation) / 2-D (current) flow modeling, 2-D axi-symmetric solid modeling
- Six gas species (He, O₂, N₂, CO₂, CO, H₂O)

- Irradiation/radiosity method at the cavity and plenums
- Porous media in the core and plenum
- Natural convection in the cavity
- Infinite air inventory in the cavity.

Figure 4-37 shows the results of the core maximum temperature with time where the core maximum temperature does not exceed 1,600°C, the temperature limit in the VHTR core for fuel security. This result is consistent with that obtained in FY-08.

Figure 4-38 shows the total burn-off variations in the bottom reflector, in which the graphite is the most seriously damaged. In this analysis, the graphite was assumed to be IG-110, isotropic grade graphite produced by Toyo Tanso Co., Ltd. The red line in each figure shows the minimum allowable burn-off, which is 0.58 for IG-110. Figure 4-38 also shows that the total burn-off goes beyond the failure criteria after 88 hours. It indicates that the graphite supporting structure risks failure at about 88 hours after depressurization. Figure 4-39 shows the variations of graphite total burn-off in the lower plenum with time. According to the calculation, the lower plenum was estimated to start having a risk of failure at about 112 hours after depressurization.

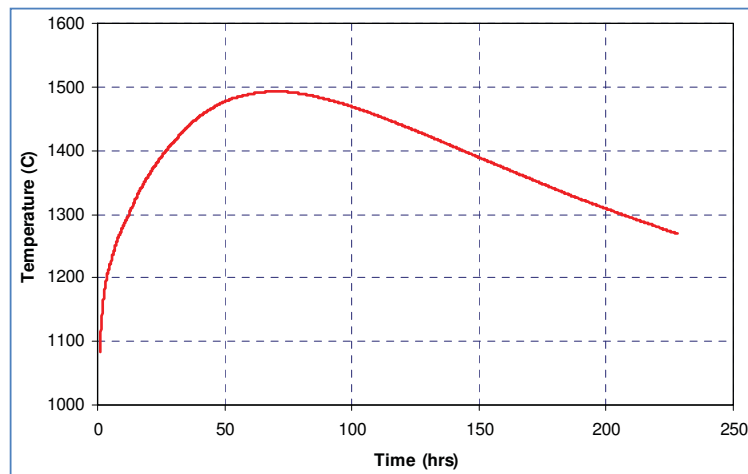


Figure 4-37. Time vs. core maximum temperature.

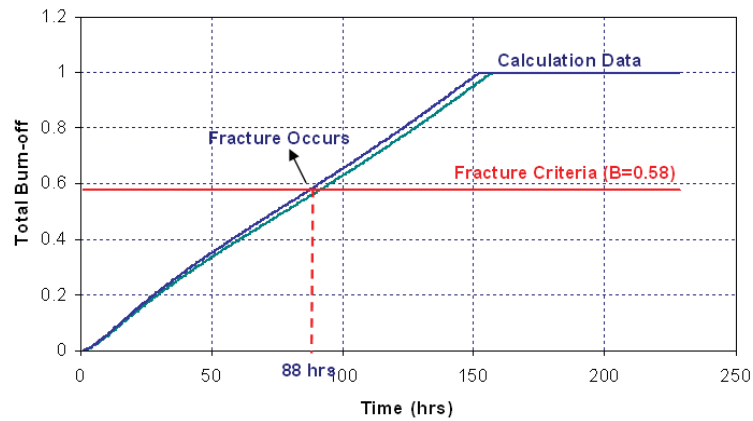


Figure 4-38. Time vs. Total Burn-off (Bottom Reflector – IG-110).

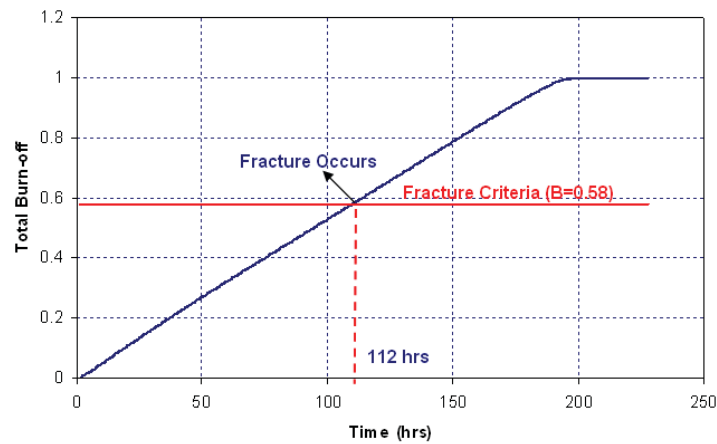


Figure 4-39. Time vs. Total Burn-off (Lower Plenum – IG-110).

Figure 4-40 shows the comparisons of failure between IG-110 and H-451 graphite. According to this figure, IG-110 and H-451 are estimated to have failed at 88 hours and 105 hours, respectively. It indicates that the H-451 graphite is a little bit more secure than the IG-110 graphite. The main reason is that H-451 is less oxidizable than IG-110 especially in the higher burn-offs.

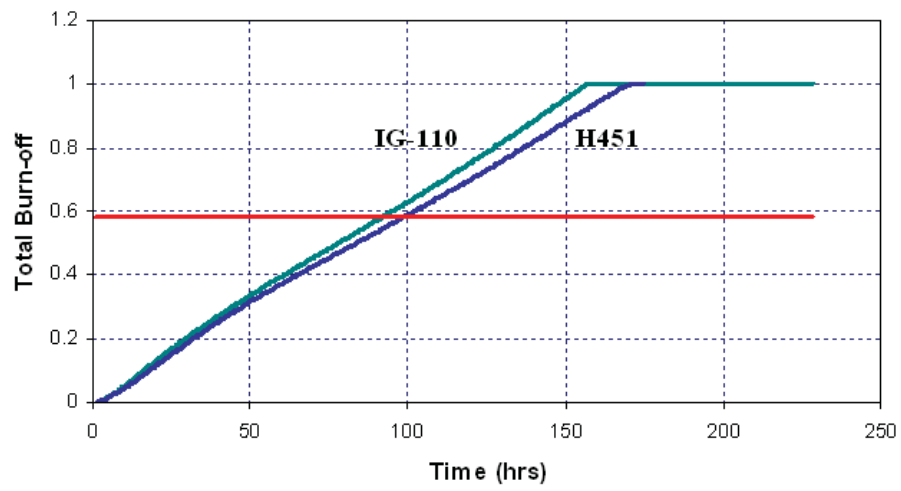


Figure 4-40. Comparisons of IG-110 and H-451 for fracture at the bottom reflector.

5. TASK 4: AIR INGRESS MITIGATION STUDY (INL)- FY-10 Task

Even though Task 4 is an FY-10 task, ideas were initiated and some scoping analysis was done on the top of the helium injection proposed and calculated by Yan et al (2008). This section summarizes the comments made on their calculations.

During operation, near-isotropic or isotropic grade graphites are subject to complex stresses such as thermal stresses and stresses caused by neutron-damage induced dimensional changes. Moreover, seismic and static forces act on the graphite component. Acting singularly or in combination, these stresses might cause microstructural cracks and fractures.

If the depressurized cooldown conduction event occurs because of a pipe and/or instrumental lines break, air ingresses into the lower plenum through the break. The supporting graphite is then exposed to oxygen, resulting in graphite oxidation. Many nuclear graphites have internal pores. For example, the fine grained IG-110 used in HTR-10 in China has many internal pores (2.19×10^{10} per m^3) and its mean pores size is $4.1 \mu\text{m}$. With the microstructural cracks and fractures described above, graphites will be more exposed to the oxygen, causing an exothermic chemical oxidation that will reduce the mechanical strength of the supporting graphite in the lower plenum and core.

Figure 5-1 shows the graphite oxidation regime map, depending on the temperature. At the high temperature (900°C and above—Zone-III), the graphite surface is too hot for oxygen to penetrate the pores. Because of the hot surface, oxygen reacts only on the graphite surface, called “diffusion limited”. At low temperatures (700°C or below), oxygen is able to penetrate the internal pores, enlarging them by oxidation and eventually combining neighbor pores. This will reduce the mechanical strength of the graphite, which is called “chemical kinetics controlled” regime (Zone-I).

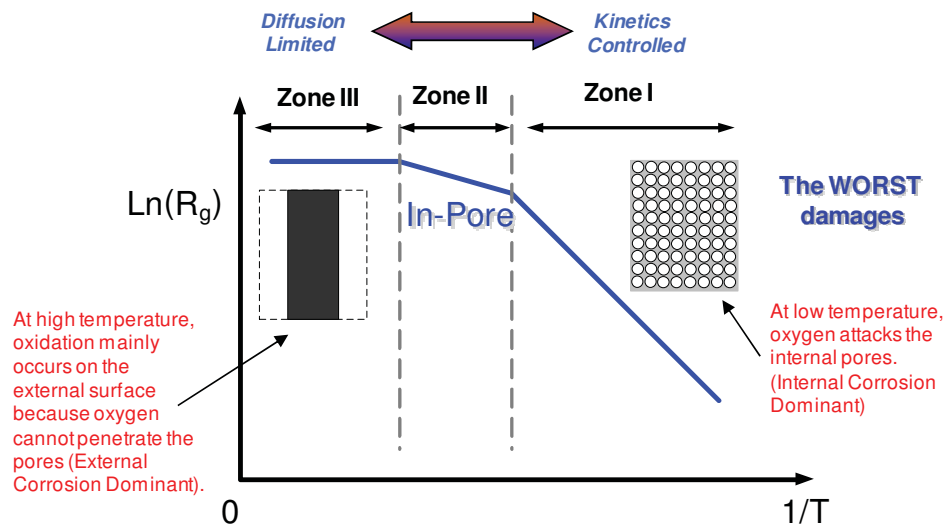


Figure 5-1. Graphite oxidation regime map.

There are several ways to mitigate air ingress and minimize graphite oxidation if the break occurs in the inlet pipe line. This work was previously performed by Yan et al (2008). Their approach was to inject helium at the top of the VHTR vessel. The helium was injected through an orifice located downstream of the helium storage tank. After investigating Yan's work, it was concluded that it does not work for a DEGB because:

- An axi-symmetry was assumed using GTHTR-300 design. As shown in Figure 5-2, the GTHTR has a large cross duct with a 2 m in diameter. When an axi-symmetric assumption was made in Yan's calculation, the inlet pipe surface did not represent the actual cross duct, therefore it was simulated based on a thin slit geometry instead of a 2 m diameter inlet pipe.
- The momentum created by the top helium injection was calculated using the following equation and the supersonic velocity helium through the orifice flow area of 0.011 mm².

$$\dot{m} = A \cdot P_o \cdot \sqrt{k \cdot \frac{I}{R \cdot T} \cdot \left[\frac{2}{k+1} \right]^{\frac{k+1}{k-1}}} \quad (5-1)$$

where

\dot{m} = mass flow in kg/hr

A = the orifice cross sectional area

P_o = the helium storage tank pressure,

k = the ratio of heat capacity at constant pressure and volume.

The value of the mass flow needs to be converted to kg/sec and multiplied by the sound velocity of helium, which is 1,134 m/s at the ambient condition.

The momentum created by the helium top injection is 0.062 Newton. The buoyancy forces created in the lower plenum of the VHTR is 155 Newton. Therefore, the buoyancy force is much larger than that of the top injected flow by a factor of 2,500, making it infeasible for the top injection to prevent air flow into the reactor core region.

Injection of an inert gas into the lower plenum could lead to air ingress mitigation and minimization of graphite oxidation as shown in Figure 5-3 by diluting the oxygen concentration and reducing the buoyancy force by lowering fluid temperature in the lower plenum. The CFD calculation has begun for this scenario, but, since the mitigation task is FY-10, more detailed calculations will be included in FY-10 report.

Outlined here how to mitigate the air ingress in terms of the change of geometry and operating condition described in Section 2.3.2. Equation 2-63 is the ratio of the buoyancy force (pressure build-up) to the hydrostatic force. Air ingress can be minimized to make the denominator term in equation 2-63 larger to make the hydrostatic force less than the pressure build-up force.

Also consider minimization of oxidation by filling/coating the graphite internal pores with either nanoparticles or an inert gas such as nitrogen. Once the internal pore surfaces of the graphite are coated with the inert gas or nanoparticles and then the oxidation will take place in the Zone-III, which is not as severe as that of the Zone-I.

The pore sizes of the IG-110 and H-451 are 3.5 micro meters and 4.1 micro meters, respectively. The size of the nitrogen atom is 65 pm in radius (130 pm in diameter = 1.3e-4 micro meter: <http://en.wikipedia.org/wiki/Nitrogen>). Therefore, the size of the graphite pore is about 2500–3100 times larger than the size of nitrogen atom. This idea of filling pores with nanoparticles was submitted to the INL patent office and was registered as IDR-1652. Therefore the details cannot be summarized in this report.

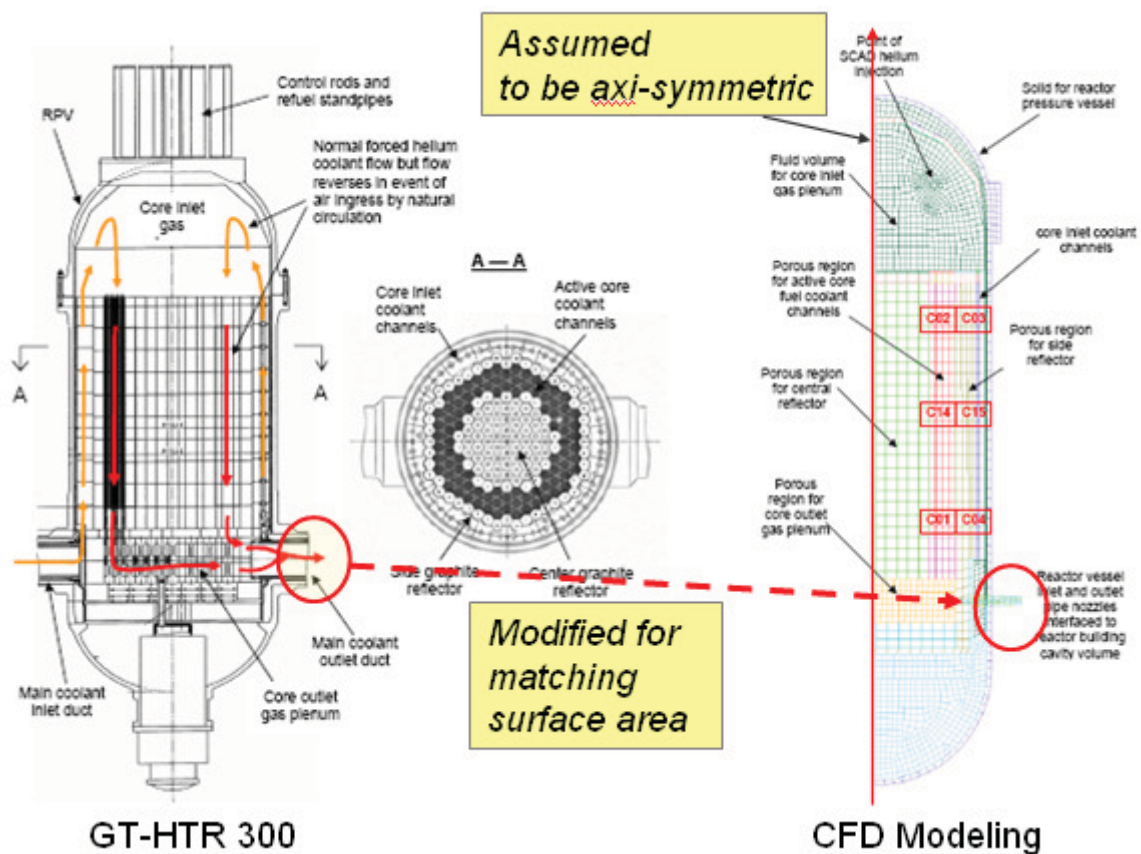
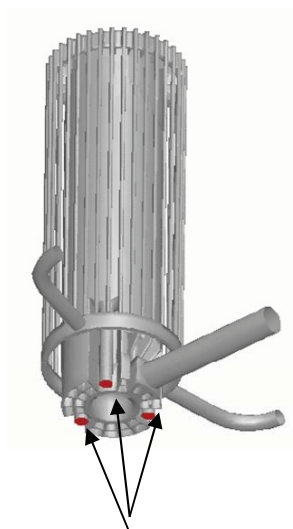


Figure 5-2. GT-HTR 300 (or GTHTR-300) Geometry and CFD model.



Injection points

Figure 5-3. Injection of Helium in the Lower Plenum via three Defuel Chutes.

6. TASK 5: EXPERIMENT OF BURN-OFF IN THE BOTTOM STRUCTURE (KAIST)

The object of this task is to measure the oxidation rate and density of the nuclear graphite and to develop oxidation models of the bottom reflector that will be directly exposed to the air-ingress event. The main parameters that affect the rate of oxidation and density of the graphite of the bottom reflector are kinetics, mass diffusion, combined effect of kinetics and mass diffusion, moisture, shape and size, and degree of burn-off. Several types of candidate graphite were selected for the experiment.

6.1 Graphite Selection

Candidate graphite materials have been proposed for the NGNP (NGNP graphite testing and qualification specimen selection strategy [Robert and Timothy 2005]). Some of the candidates are listed in Table 6-1. This year, IG-110 and IG-430, which are isotropic and fine-grained graphite produced by Toyo Tanso, were selected for the experiment. Most of the data for IG-110, except the effect of burn-off on the reaction rate, were obtained from previous research (Oh et al. 2006). General properties of IG-110 and IG-430 are presented in Table 6-2.

Table 6-1. Graphite selection matrix (Robert and Timothy 2005).

Graphite	Vendor	Proposed Use	Remarks
IG-110	Toyo Tanso	Prismatic fuel element, replaceable reflector, and core support pedestals	Historical Reference; currently being used in the HTTR and HTR-10
PCEA	Graftech International	Prismatic fuel and replaceable block Pebble bed reflector and insulation blocks	AREVA wants to construct the entire graphite core out of the same graphite
IG-430	Toyo Tanso	Prismatic fuel element, replaceable reflector, and core support pedestals	Japan Atomic Energy Agency wants to use this graphite in the GTHTTR 300
PGX	Graftech International	Prismatic large permanent reflector	AREVA may use this material; preference is to use PCEA or NBG-17 for permanent reflector. HTTR permanent structure
NBG-25	SGL	Core support candidate	Isostatic fine grain
NBG-10	SGL	Prismatic fuel element and replaceable reflector Pebble bed reflector structure and insulation blocks	pebble bed modular reactor's (PBMR) original choice for replaceable reflector Price/performance will be the basis between NBG-18 and NBG-10

Table 6-2. Properties of IG-110 and IG-430 manufactured by Toyo Tanso in Japan.

Material	IG-110	IG-430
Vendor	Toyo Tanso	Toyo Tanso
Bulk density (g/cm ₃)	1.77	1.88
Young's Modulus (GPa)	9.8	10.8
Compressive strength (MPa)	78	90
Tensile strength (MPa)	25	37
Hardness (HSD)	51	55
Thermal conductivity (W/mK)	120	140

6.2 Kinetics

Kinetics tests were performed in Zone I where the kinetics effect controls the rate of reaction. The effects of variables on the rate of reaction were experimentally investigated. A schematic of the experimental facility is shown in Figure 6-1. He/O₂ mixture gas was injected into the heated test section; injected mixture gas is controlled by a mass flow controller. A 15 kW induction heater was installed for graphite heating. Gas passing through the test section was cooled and analyzed via gas analyzers. The reaction rate was calculated by gas component analysis through two gas analyzers (Rosemount NGA2000, Yokogawa IR100).

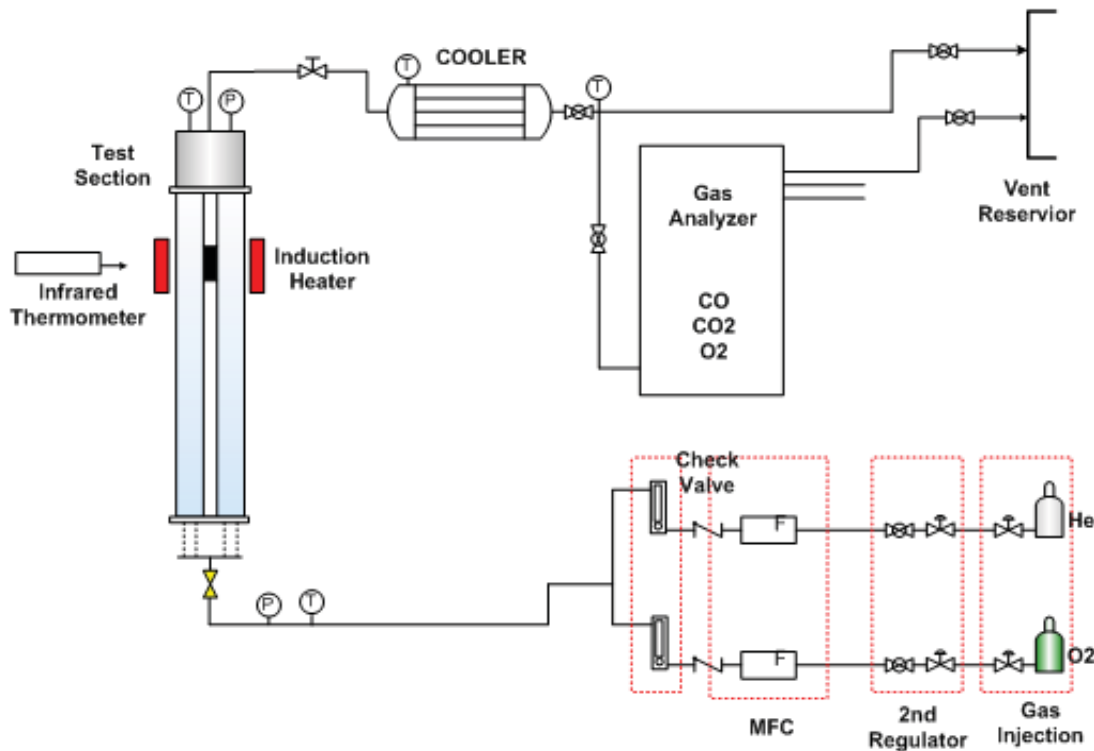


Figure 6-1. Schematic of experimental facility.

Figure 6-2 shows the picture of the experimental facility. The section was surrounded by a cylindrical quartz tube. A long entry length was designed to maintain the fully developed flow. The specimen was 2.1 cm in diameter and 3 cm in height and the test section was 7.6 cm in diameter. An induction heating method was used and the temperature was measured by an infrared thermometer (IRtext Taymatic 10, Raytec Ranger 3).



Figure 6-2. Experimental facility.

Temperature, flow rate, and oxygen concentration test conditions are summarized in Table 6-3.

Table 6-3. Test conditions.

Temperature (°C)	~540–800
Flow rate (SLPM)	~SLPM (0.04 m/s)
Oxygen fraction (%)	~34%

Data measured at 5.26% of oxygen concentration were shown in Figure 6-3. They are in good agreement with results predicted by the Arrhenius model. The sensitivity of this model was studied in the previous experiment. The activation energy was not affected by oxygen concentration (Oh et al. 2006). The reaction rate at different oxygen concentrations was measured to obtain the order of reaction. The effect of oxygen concentration on oxidation rates is shown in Figure 6-4.

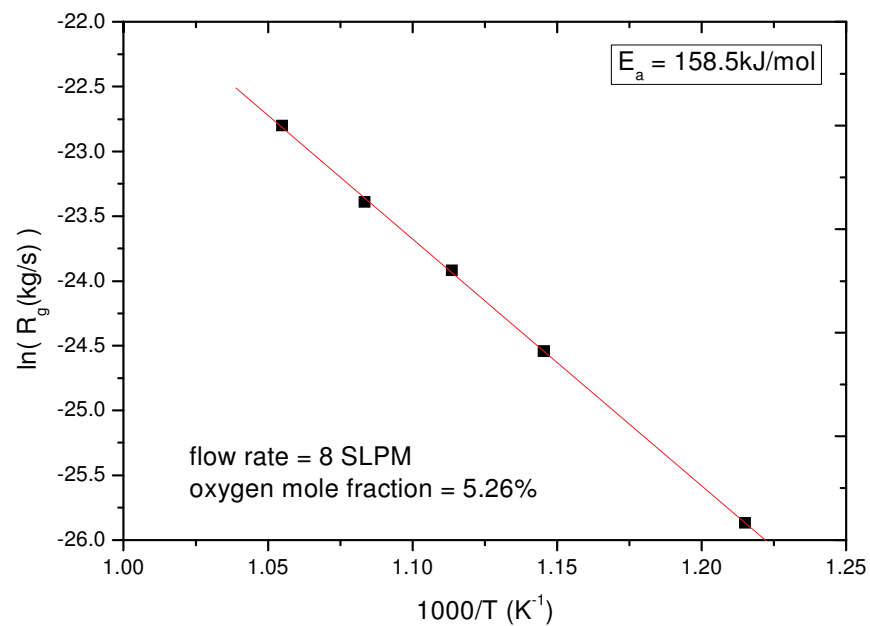


Figure 6-3. Effect of temperature on oxidation rate (IG-430).

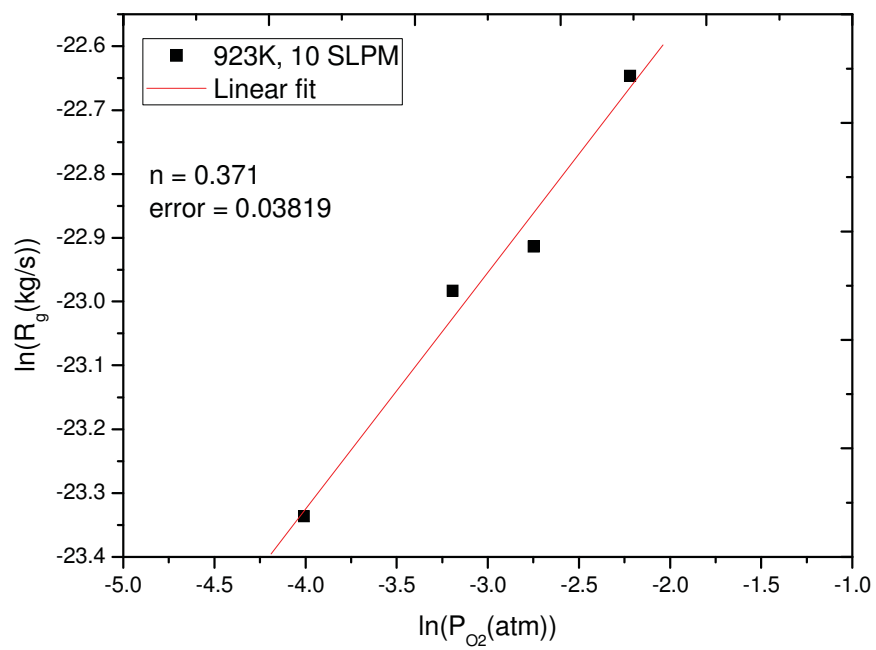


Figure 6-4. Effect of oxygen concentration on oxidation rate (IG-430).

Results are summarized in Table 6-4.

Table 6-4. Activation energy and order of reaction.

Material	IG-110	IG-430
Activation energy (kJ/mol)	218 ± 4	158.5 ± 1.5
Order of reaction, n	0.75 ± 0.15	0.37 ± 0.04

The former and our kinetics parameters for IG-110 and IG-430 are summarized in Table 6-5 and Table 6-6.

Table 6-5. Experimental results on kinetics parameters for IG-110.

Author	Temp.(°C)	Oxygen mole fraction	Flow rate (SLPM)	Ea (kJ/mol)	n	Method
Fuller (1997)	450~750	0.2	0.496	201	—	TGA
Kawakami (1987)	550~650	0.2	—	210	—	Gas analysis
KAIST	540~ 800	0.02~ 0.34	8~ 10	218	0.75	Gas analysis

Table 6-6. Experimental results on kinetics parameters for IG-430.

Author	Temp. (°C)	Oxygen mole fraction	Flow rate (SLPM)	Ea (kJ/mol)	n	Method
Chi (2008)	608– 808	0.2	10	167.4	—	TGA
KAIST	540– 800	0.02– 0.34	8– 10	158.5	0.37	Gas analysis

6.3 Mass Diffusion

Even though the rate of reaction is controlled by chemical parameters at low temperatures, the rate of reaction is limited by mass diffusion process at high temperatures. Therefore, the well- proven correlation was used in this study. The correlation developed for heat transfer through the laminar boundary layer and averaged through the whole length (Welty et al. 1984) was in good agreement with the experiment data investigated by previous study (Oh et al. 2006). The heat/mass transfer analogy is applicable for predicting the mass diffusion rate in Zone 3:

$$K_m = 0.664 \frac{D_{ij}}{L} \text{Re}_L^{1/2} \text{Sc}^{1/3} \quad (6-1)$$

This correlation is made based on the analogy of the heat transfer correlation, which was developed for heat transfer through the laminar boundary layer and averaged through the whole length.

6.4 Combined Effect of Kinetics and Mass Diffusion

A good correlation for the combined effect of kinetics and mass diffusion was suggested by the previous I-NERI program (Oh et al. 2006). The following is the correlation for the combined effect.

$$\frac{1}{R_g} = \frac{1}{R_{mb}} + \frac{1}{R_{cb}} \quad (6-2)$$

where

$$R_{mb} = K_m \cdot C_{b,O_2} \cdot A \quad (6-3)$$

$$R_{cb} = K_0 \cdot e^{\frac{Ea}{RT}} \cdot P_{O_2,b}^n \cdot A \quad (n \neq 0) \quad (6-4)$$

The mass transfer coefficient is calculated from the following Graetz solution, which includes the effect of the entrance effect

$$Sh = \frac{k_m \cdot d}{D} = 3.66 + \frac{0.0668(d/x) \cdot (Re \cdot Sc)}{1 + 0.04 \cdot [(d/x) \cdot (Re \cdot Sc)]^{2/3}} \quad (6-5)$$

The following correction was performed for high reaction rate:

$$k_m^{corrected} = \theta \cdot k_m \quad (6-6)Eq$$

where

$$\theta = \frac{\ln(B_m + 1)}{B_m} \quad (6-7)$$

$$B_m = \frac{X_{O_2,b} - X_{O_2,0}}{X_{O_2,b} - 1} \quad (6-8)$$

The following effective diffusion coefficient was used instead of a binary diffusion coefficient because of the high reaction rate:

$$D_{O_2,m} = \frac{(1 - X_1)}{\sum_{i=2}^n (X_i / D_{O_2,i})} \quad (6-9)$$

6.5 Effect of Burn-off

The reaction rate of oxidation is dependent on the level of burn-off. The effect of burn-off was experimentally investigated. The schematic of experimental facility is shown in Figure 6-5. The temperature of 600°C was maintained in the furnace. The detailed conditions are summarized in Table 6-7. The reaction rates of specimens with different volume were measured. The burn-off history is shown in Figure 6-6. The burn-off histories of IG-430 are independent of graphite dimension and volume. The relation between bulk flow and reaction rate is shown in Figure 6-6 and Figure 6-7. The effect of burn-off is independent of bulk flow. Actually, the oxidation reaction in the temperature of 600°C is in Zone 1.

The relationship between the burn-off and relative reaction rate was also obtained from the burn-off history. The internal surface area change is caused by oxidation:

$$M_B = \frac{R_g(B)}{R_g(0)} = \frac{\theta(B)}{\theta_0} \quad (6-10)$$

where R_g is the reaction rate (kg/s) and $\theta(B)$ is internal surface density (m⁻¹) at burn-off (B). According to Fuller and Okoh (Fuller and Okoh, 1997), the reaction rate with the effect of burn-off can be expressed

$$R_g = K_0 \cdot \exp\left(-\frac{Ea}{R \cdot T}\right) \cdot P_{O_2}^n \cdot \theta(0) \cdot M_B \quad (6-11)$$

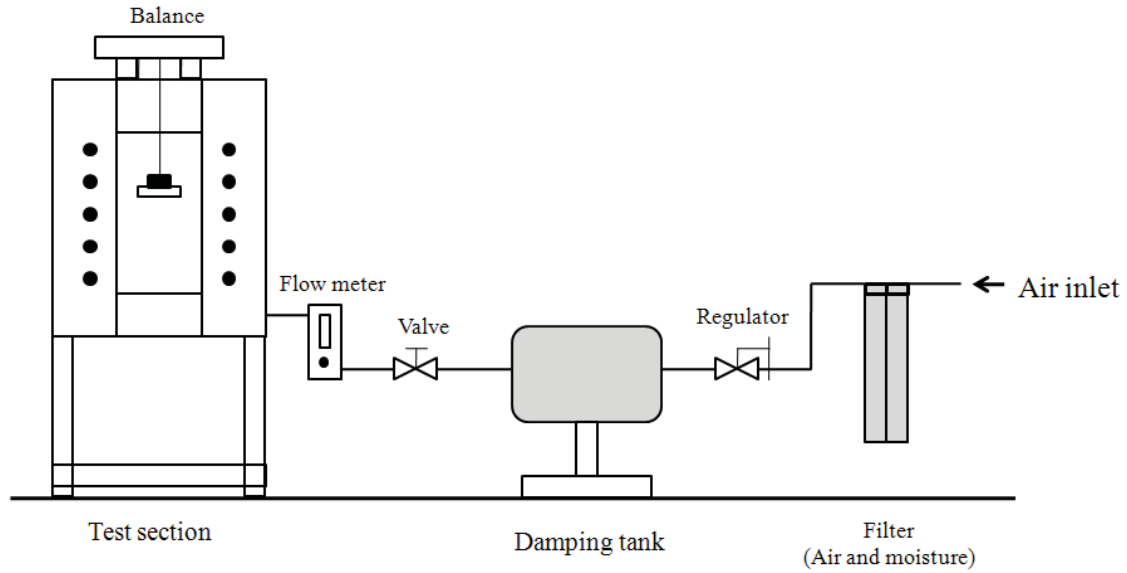


Figure 6-5. Experimental facility for burn-off tests.

Table 6-7. Conditions for burn-off tests.

Material	Air (SLPM)	Volume (mm ²)	Purpose
IG-430	5	5,126.6	Relation between graphite volume and reaction
	5	9,922.4	
IG-110	5	5,126.6	Relation between bulk flow and reaction
	2	5,126.6	

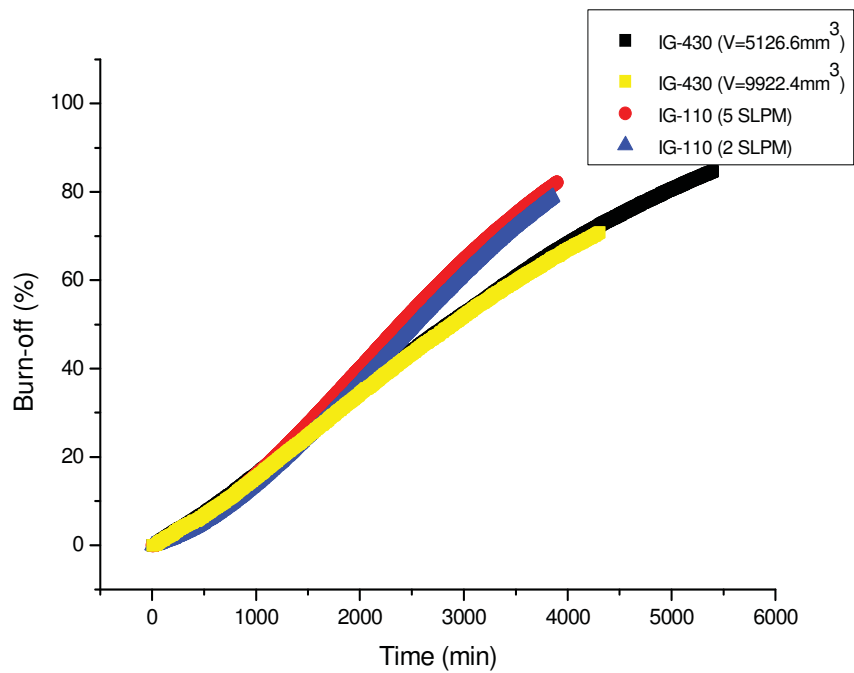


Figure 6-6. Changes of burn-off with time for different conditions.

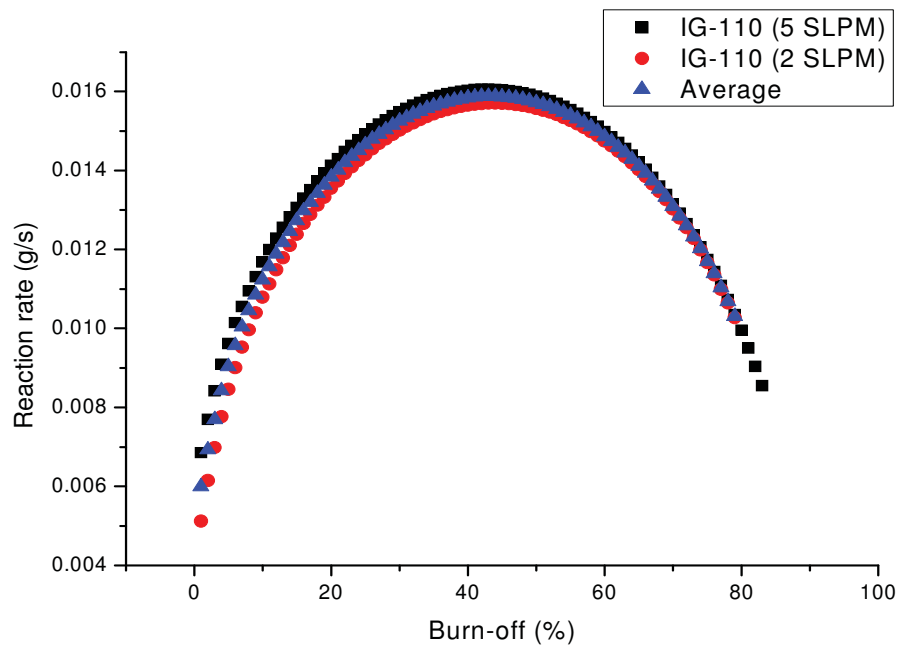


Figure 6-7. Changes of reaction rate with burn-off.

The measured M_B of IG-110 and IG-430 are shown in Figure 6-8. Both reaction rates of IG-110 and IG-430 in Zone 1 have the maximum reaction rate about 40% of burn-off. They are in good agreement with the former results. Even though the ratio of M_B has some sensitivity to initial reaction rate, the absolute value of reaction rate is almost the same as shown in Figure 6-7. The effect of burn-off on the reaction rate in IG-110 is much larger than that in IG-430.

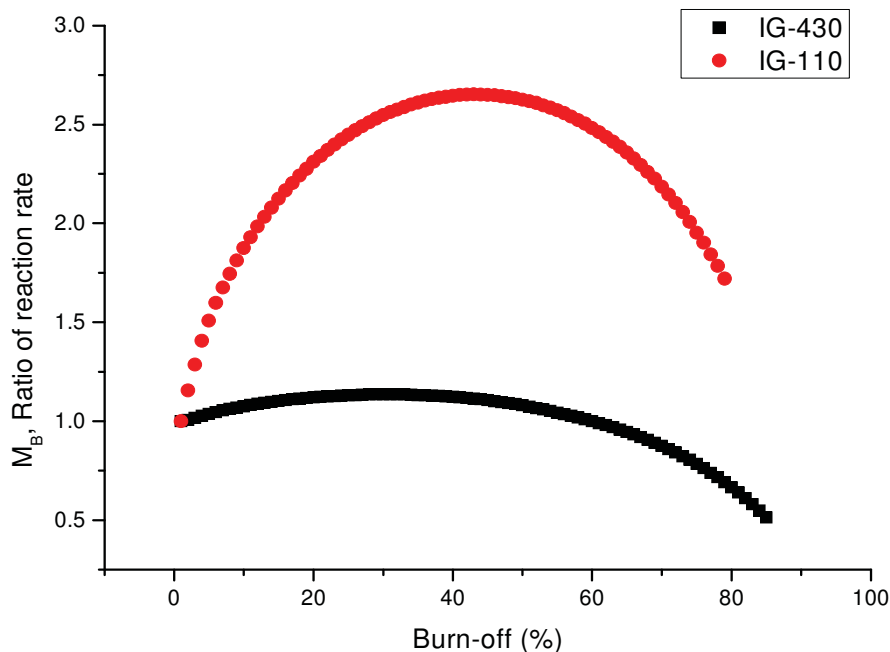


Figure 6-8. relation between burn-off and ratio of reaction rate.

6.6 Effect of Moisture

Most of the former experiments were performed in dehumidified conditions, while normal environments always have moisture. The effect of moisture in oxidation in Zone 1 and Zone 3 was tested in this section. The results of Zone 1 tests were obtained from the facility shown in Figure 6-5 above. The results of Zone 3 test were obtained from the facility shown in Figure 6-2 above. Both test facilities had an add-on water chamber to control humidity. The temperature was controlled from 600 to 1,300°C and the relative humidity was controlled from 0 to 63.6%. The test material was IG-430. The test conditions are summarized in Table 6-8.

Table 6-8. Conditions for effect of moisture tests.

Oxidation regime	Temperature	Relative humidity	Gas bulk flow (He+O ₂)	Oxygen concentration	Method
Zone 1	600°C	0– 63.6%	1 SLPM	20%	TGA
Zone 3	1000–1,300°C	0– 63.6%	8 SLPM	20%	Gas analysis

Test results in the Zone 1 reaction are shown in Figure 6-9. From the burn-off histories, the effect of moisture is negligible in Zone 1. The Internal graphite structure and chemical reaction are not affected by moisture in the gas.

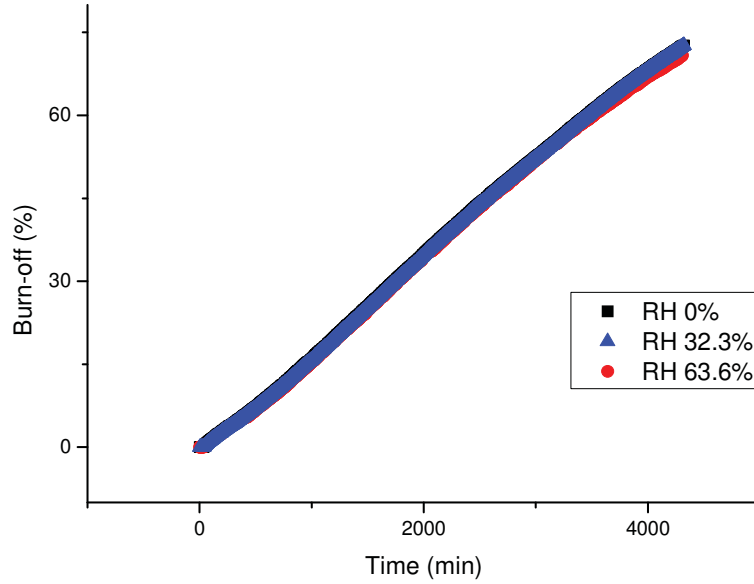


Figure 6-9. Moisture effect on the graphite oxidation in Zone 1.

Kim suggested that the mass transfer, including the moisture effect, is half of the rate without the moisture effect (Kim, 2005).

$$r_{g,moisture} = 0.5 \cdot r_{g,dry} \quad (6-12)$$

The graphite oxidation in Zone 3 is controlled by mass transfer. Therefore,

$$r_g \sim R_g \text{ (reaction rate), and} \quad (6-13)$$

$$R_{g,moisture} = 0.5 \cdot R_{g,dry} \quad (6-14)$$

The experimental results of moisture in Zone 3 are shown in Figure 6-10. They are in good agreement with those from Equation 6-14. The difference between the data was under 5%.

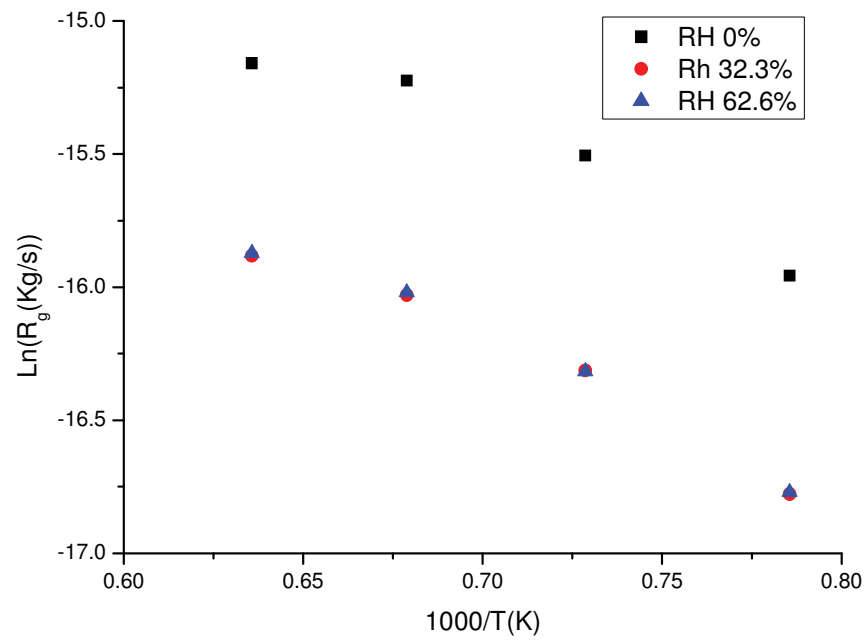


Figure 6-10. Moisture effect on the graphite oxidation in Zone 3.

7. TASK 6: STRUCTURAL TESTS OF BURN_OFF BOTTOM STRUCTURE (KAIST)

The objective of this task is to carry out the structural test of the oxidized graphite in order to develop the fracture model for the oxidized bottom reflector and lower plenum. The graphite structures of the bottom reflector and lower plenum are oxidized and damaged during an air-ingress event. The reactor core is supported by graphite columns in the bottom reflector and the lower plenum. Schematics of the GTMHR 600 MWth and graphite column are shown in Figure 7-1. As shown, the graphite column is relatively long. The slenderness ratio of the cylindrical column part is about 40. The graphite column first encounters air when the air ingress event starts. In this case, the failure prediction of oxidized graphite column in the bottom reflector is important for the reactor design and safety analysis of the VHTR because the strength and geometry of the graphite are changed by oxidation.

The oxidation of nuclear graphite is classified into Zone 1, Zone 2, and Zone 3. Zone 1 ranges in temperatures below 600°C where the nuclear graphite is uniformly oxidized with a bulk density decrease following the weight loss. The decrease of the bulk density will degrade the strength of the graphite. In Zone 3, which generally ranges in temperatures above 1,000°C, the oxidation of the graphite is dominated by a mass diffusion limit, and therefore the surface of graphite is mainly corroded resulting in the maximum stress increase of the graphite structure. In Zone 2 (600 to 1,000°C), density decreases and surface corrosion occurs at the same time.

7.1 Graphite Support Column

7.1.1 Graphite Oxidation and Failure Mechanisms

A simplified graphite column and the oxidation process, where an axial force is loaded on the graphite columns, are shown in Figure 7-1.

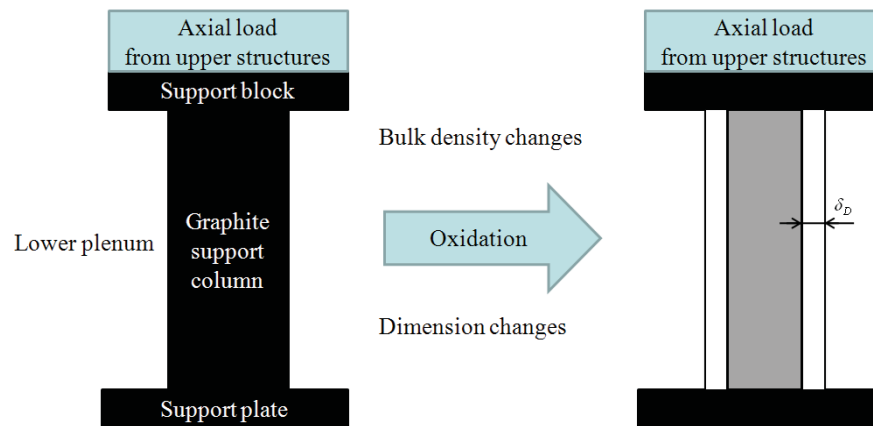


Figure 7-1. Schematic of oxidation in a graphite column.

The graphite oxidation in Zone 1 causes a decrease in bulk density. The compressive strength of the graphite is degraded with a decrease in bulk density. This is well verified by the former experiments. It is believed that the real oxidation is processed over the overall oxidation regimes during an air ingress event (Oh et al. 2006). The graphite column became slender as a result of the oxidation in Zone 3. In this case, the oxidized graphite column can fail by a different mechanism from that of the fresh graphite—buckling.

But this cannot be explained by the former experiments. Therefore, the understanding of the oxidation in Zone 3 and an approach to structural issues are needed to predict the failure of a graphite column. The graphite column becomes slender as a result of surface oxidation processed in Zone 3. If the column becomes slender, then it becomes easy for the column to fail by buckling. An analysis of the critical stress for long columns was previously developed by Leonhard Euler (Singer and Pytel 1980). The Euler formula for the fixed-fixed column is simply expressed by

$$\sigma_{cr} = 4\pi^2 EI / AL^2 \quad (7-1)$$

where I is the moment of inertia for the principal axis about which buckling occurs. When I in Equation (7-1) is replaced with the following relationship:

$$r = \sqrt{I / A} \quad (7-2) \text{Equation (7-1) becomes}$$

$$\sigma_{cr} = 4\pi^2 E / (L / r)^2 \quad (7-3)$$

where A is the cross sectional area and r is the least radius of gyration.

The ratio L/r is a nondimensional ratio called the slenderness ratio of the column. A column can be classified as either a long or short column based on the slenderness ratio. However, there are limitations to Euler's formula because this formula is only valid in estimating the strength of very long columns. For estimating the strength of a small-slenderness-ratio column, the following empirical straight-line formula was proposed by T. H. Johnson (Singer and Pytel 1980):

$$\sigma_{cr, buckling} = \sigma_{straight-line} - C(L / r) \quad (7-4)$$

where the constant $\sigma_{straight-line}$ is the intercept for L/r = 0 and the constant C is the magnitude of slope.

Three tests were performed to find the strength degradation of the oxidized graphite column in the different reaction regimes with this strategy. First, a compression test of fresh graphite was performed to measure the compressive and buckling strength of the IG-110 graphite column. Then, the compression test for a graphite column, oxidized in Zone 1, was performed to learn the relation between the compressive strength and bulk density change caused by the graphite oxidation in Zone 1. Finally, the measurement of the buckling strength of a graphite column, oxidized in Zone 3, was performed to figure out the relation between the buckling strength of the column and the dimension change caused by the graphite oxidation in Zone 3.

7.1.2 Materials

Isotropic fine-grained IG-110 and IG-430 graphite was selected as a test material. Tests, the detailed dimensions of specimens, and the objectives of experiments are summarized in Table 7-1.

7.1.3 Strength Measurements

An INSTRON Model 4204 mechanical testing facility was used for the compression test. The maximum loading of the facility was 50 kN. The apparatus and the procedures were based on ASTM Standard C695-91. The load was continuously applied to the sample at the constant rate of crosshead movement, and without shock until ultimate failure. The speed of the cross head movement was constant for all specimens. The strain rate for the shortest specimen, 15 mmΦ × 30 mm, was 1.11×10⁻⁴ sec⁻¹.

Table 7-1. Test matrix.

Diameter	Length	Slenderness ratio	Burn-off (%)	Oxidation regime	Objective
15	30	8	N/A	N/A	Compressive strength of fresh graphite was measured.
25	50	8			Buckling strength was measured. Empirical buckling strength formula was also obtained.
25	50	8			
	75	12			
	80	12.8			
	85	13.6			
	90	14.4			
	95	15.2			
	100	16			
	125	20			
	150	24			
	200	32			
	250	40			
15	30	8			The Applicability for the straight-line formula in the different diameter was confirmed.
	60	16			
	120	32			
25	50	8	0~ 24%	Zone 1	The compressive strength of oxidized graphite was measured
15	60	16	0~ 24%		The buckling strength of various oxidized graphite columns was measured. The relation between strength degradation and failure mode was found out.
15	120	32			
25	50	8			
25	100	16			
25	200	32			
15	60	16	N/A	Zone 3	Experiments for oxidation in Zone 3. Buckling strength was measured
15	120	32			
15	60	16	0~ 22 %	Zone 1	Pre-tests for support block modeling.
Annular column		15.5			
Rectangular column		15.5			

7.1.4 Oxidation Treatments

Oxidation was carried out in an electrical muffle furnace. Filtered dry air was uniformly supplied into the bottom of the furnace and gas was naturally vented out through the top of the furnace. The internal temperature of the furnace was maintained at 600°C for Zone 1 oxidation and at 1,050°C for Zone 3 oxidation. The experimental facility is shown in Figure 7-2.

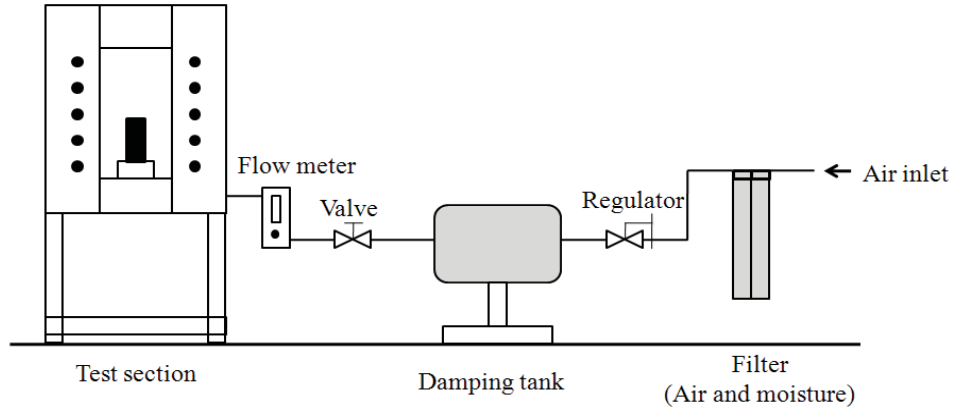


Figure 7-2. Experimental facility for oxidation tests.

7.1.5 Measurements of Compressive and Buckling Strength of Fresh Graphite Column

The measured average compressive strength of IG-110 and IG-430 were 79.46 and 89.99. It shows good agreement with typical properties of the graphite. The buckling strength of a graphite column decreases as the slenderness ratio increases. The buckling strength of IG-110 graphite columns is shown Figure 7-3.

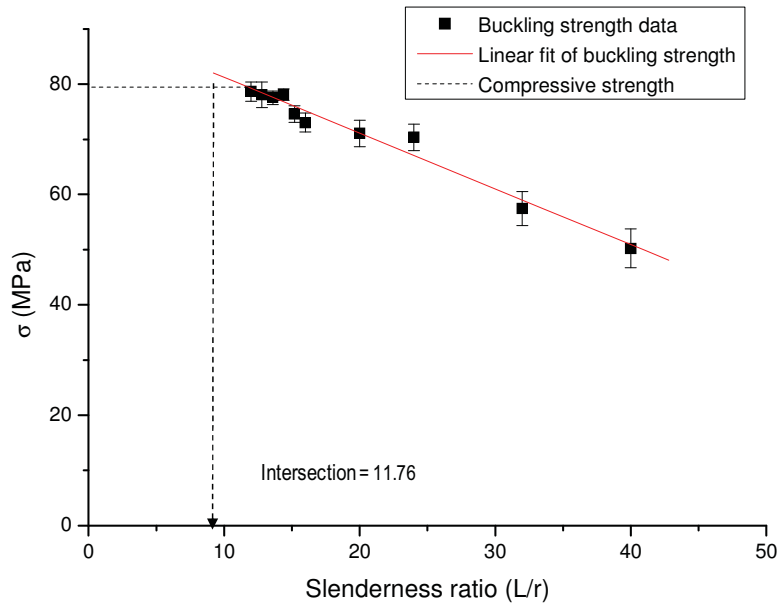


Figure 7-3. Buckling strength of IG-110 graphite columns.

The intercept and the magnitude of the empirical formula are obtained from the empirical data as

$$\sigma_{cr, buckling} = 91.34 - 1.01(L/r) \quad (7-5)$$

The buckling strength of IG-430 graphite columns is also shown in Figure 7-4.

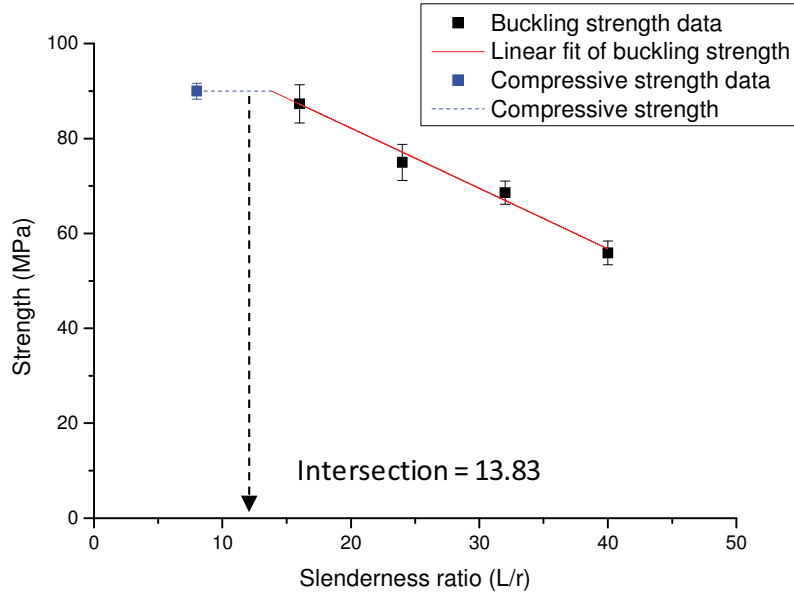


Figure 7-4. Buckling strength of IG-430 graphite columns.

The obtained empirical formula for IG-430 is

$$\sigma = 107.55 - 1.27 \cdot (L/r) \quad (7-6)$$

The differences of the 15 mm Φ columns and the empirical line are under 2%. The empirical formula applies for all columns with different diameters. Therefore, the structural strength of a graphite column under compression force can be determined by the slenderness ratio. The graphite columns that have the same slenderness ratio also have the same strength.

It is believed that the buckling failure occurs over the slenderness ratio, which is the intersection of the compressive strength and the empirical line. The intersection is 11.76 for IG-110 and 13.83 for IG-430.

7.1.6 Compressive and Buckling Strength Degradation of Graphite Column Oxidized in Zone 1

The degradation in compressive strength as a function of the decrease in bulk density is shown in Figure 7-5. The dimensions of an oxidized specimen did not change. The percentage decrease in bulk density is the same as the percentage of weight loss.

$$d = (m_0 - m) / m_0 \quad (7-7)$$

The relation between the compressive strength and decrease in bulk density can be expressed by the Knudsen relation (Neighbour 2006) as

$$\sigma / \sigma_0 = \exp(-kd) \quad (7-8)$$

$$k = 0.114$$

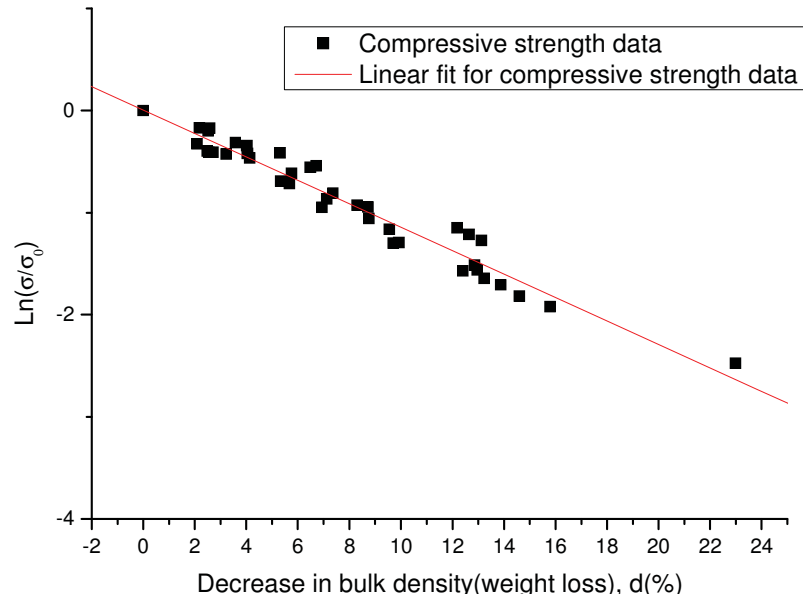


Figure 7-5. Normalized compressive strength of IG-110 oxidized in Zone 1.

The buckling strengths of the oxidized columns with various dimensions are shown in Figure 7-6. The buckling strength of the oxidized graphite column decreases as the compressive strength decreases. The relation between the buckling strength and the bulk density is expressed by the Knudsen relation

$$\sigma / \sigma_0 = \exp(-kd)$$

$$k = 0.111$$

(7-9)

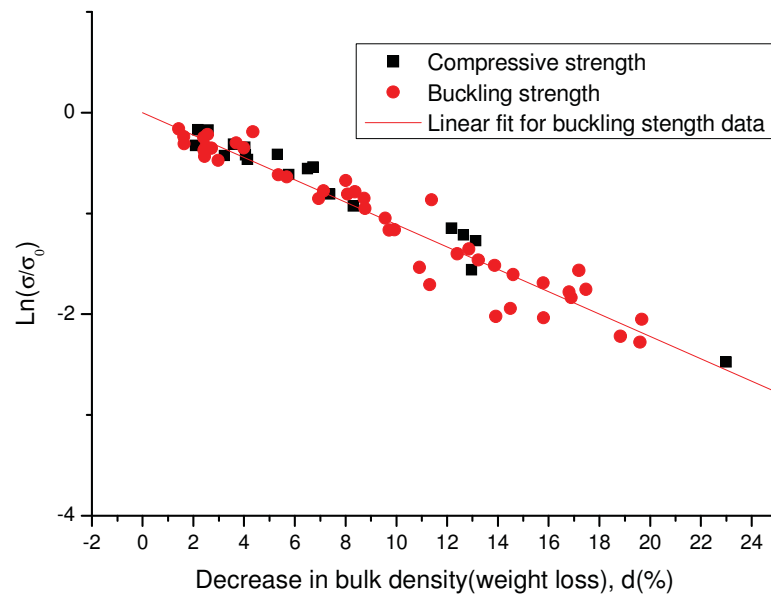


Figure 7-6. Normalized compressive and buckling strength of graphite columns oxidized in Zone 1.

The exponents of Equations (7-8) and (7-9) were almost the same. From this result, the buckling strength degradation of the oxidized graphite column is found to be independent of the slenderness ratio. The structural strength degradation of the oxidized graphite column only depends on the initial strength and a degree of the decrease in bulk density. Therefore, the strength degradation of an oxidized graphite column under axial compressive load can be expressed conservatively by Equation (7-8).

Comparison of the Knudsen relation with former researchers' data is shown in Figure 7-7. Test materials and test conditions are summarized in Table 7-2. The data obtained from KAIST is more conservative in its results. Kim (2007) obtained $k=0.089$ in the burn-off range of 0 to 7%. It is possible that the difference mainly comes from the narrow burn-off range and the use of different materials. Eto (1983) and Yoda (1985) have reported test results for IG-11. IG-110 and IG-11 are similar kinds of material, but the purity is slightly different. It is believed that the burn-off range has some sensitivity to decide exponent k from the different results of Eto's and Yoda's tests. These researchers tested the same IG-11 but the burn-off ranges were found to be different.

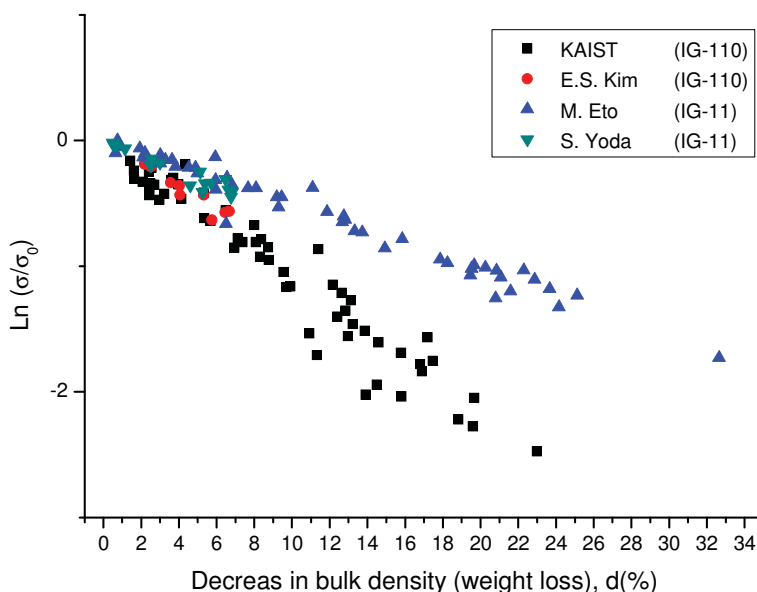


Figure 7-7. Comparison of the experimental results for the compressive strength degradation.

Table 7-2. Comparison of the Knudsen relation.

Author	Eto (1983)	Yoda (1985)	Kim (2007)	KAIST
Test material	IG-11	IG-11	IG-110	IG-110
Temperature (°C)	500	500	600	600
Burn-off (%)	0~ 6	0~ 35	0~ 7	0~ 23
k	0.060	0.053	0.089	0.114

The strength degradation of IG-430 oxidized in Zone 1 was also obtained in the same method. The results are shown in Figure 7-8.

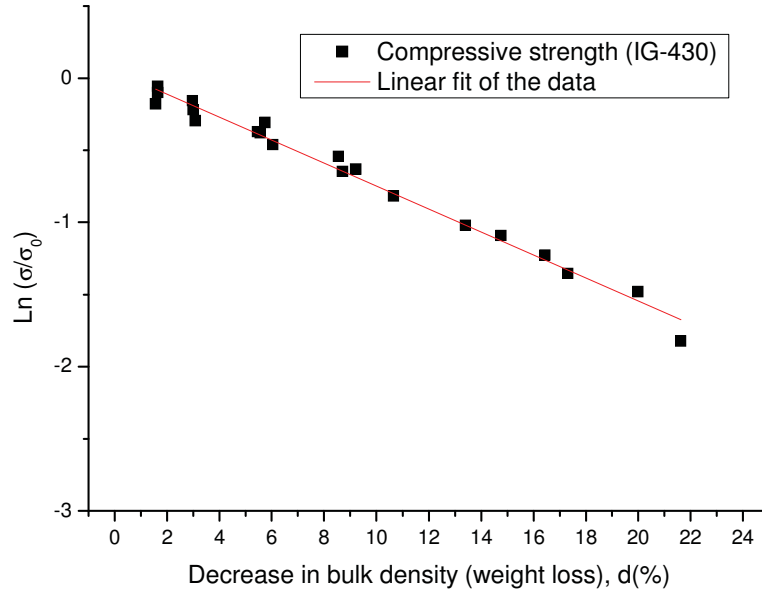


Figure 7-8. Normalized compressive strength of IG-430 oxidized in Zone 1.

The relation between the buckling strength and bulk density is also expressed by Knudsen relation as

$$\sigma / \sigma_0 = \exp(-kd)$$

$$k = 0.080 \quad (7-10)$$

7.1.7 Buckling Strength Graphite Column Oxidized in Zone 3

Three specimens were oxidized at once in the same condition. The averaged values of the strength data from the three samples are shown in Figure 7-9. The differences of slenderness ratios in each group were under 1%. The dashed line in Figure 7-9 represents the strength of a fresh graphite column as a function of the slenderness ratio. The linear fit of experimental strength data was expressed by the empirical straight-line formula

$$\sigma_{cr, buckling} = \sigma_{straight-line} - C(L/r) = 86.8 \text{ MPa} - 0.9 \text{ MPa} \cdot (L/r) \quad (7-11)$$

The deviation between the experimental data and the empirical line for the fresh graphite is about 5 MPa. From this result, it can be concluded that the surface oxidation is dominant at temperatures over 1,000°C and the strength of the graphite column oxidized at temperatures over 1,000°C can be predicted by the empirical straight-line formula of Equation (7-5).

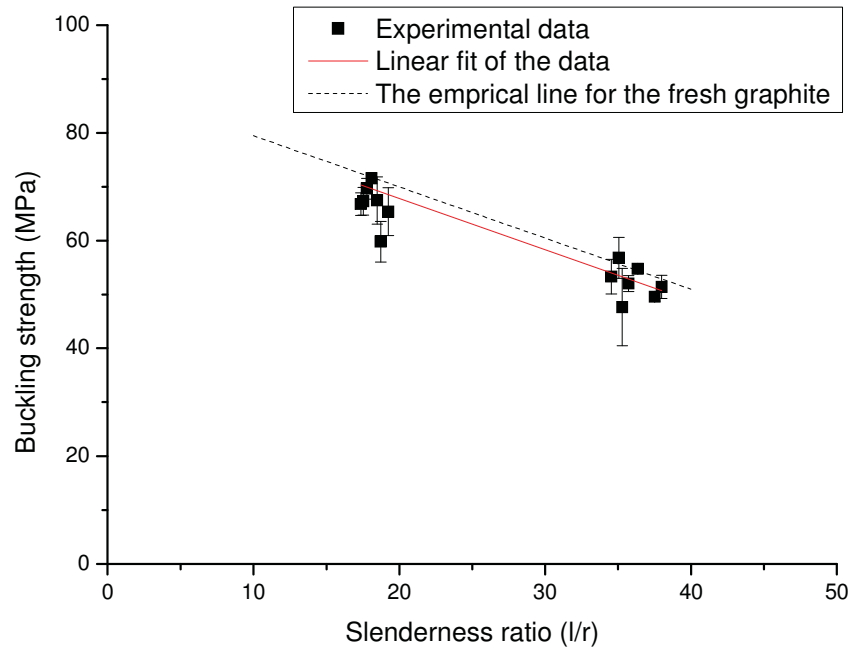


Figure 7-9. Strength of graphite columns oxidized in Zone 3.

7.2 Graphite Support Column

A graphite support block is a very complex dimension with many holes. Figure 7-10 shows a one-sixth cutaway of a graphite support block as a simplified model that can be good for an oxidation reaction, but is not good for structural tests because they have different structural parameters such as slenderness ratio. It is therefore difficult to make a chemically and structurally equivalent model. However, the graphite support block can be considered as a short column. The strength of a column is only dependent on the slenderness ratio by Euler's formula and the empirical straight-line formula. Thus, graphite columns that have the same slenderness ratio but different dimensions still have the same strength. This is confirmed by the following tests. The simplified model, which has the same slenderness ratio with a graphite support block, will then be used in analyzing a graphite support block.

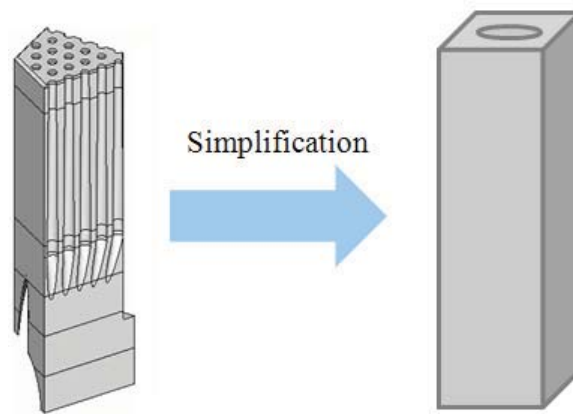





Figure 7-10. One-sixth of a graphite support block and its simplified modeling.

7.2.1 Buckling Strength Graphite Column Oxidized in Zone 3

Three specimens were measured for strength, and IG-110 and IG-430 were tested. The detailed specification presented in Table 7-3 shows that specimens B and C have the same slenderness ratio and cross-sectional area but different dimensions.

Table 7-3. Dimensions of graphite specimens for fresh graphite tests.

	A	B	C
Pictures of specimens			
Slenderness ratio (L/r)	16	15.5	15.5
Dimension (mm)	15 Φ \times 60	15 Φ \times 60 (3.8 Φ 1 hole)	13.3 \times 13.3 \times 60 (1.9 Φ 4 holes)
Cross-sectional area (mm ²)	1,76.7	165.5	165.4

An INSTRON model 4204 mechanical testing facility was also used for the compression test with the same procedures. Seven specimens were tested for each type of specimen. All the specimens failed by buckling. The strain rate was 5.55×10^{-5} sec⁻¹. The experimental results are summarized in Tables 7-4 and 7-5. The strength of specimens B and C are almost the same as expected. The experimental results show good agreement with the calculated buckling strength from the previous empirical buckling strength formulas. The empirical buckling strength relationship therefore applies for all kinds columns over the slenderness ratio tested in the previous experiments.

Table 7-4. Experimental results of IG-110 columns.

	A	B	C
Strength (MPa)	74.02 \pm 2.9	74.49 \pm 4.9	75.46 \pm 1.9
Calculated buckling strength (MPa)	75.18	75.69	75.69
Differences	1.5 %	1.0 %	0.3 %

Table 7-5. Experimental results of IG-430 columns.

	A	B	C
Strength	87.30 \pm 4.06	87.56 \pm 2.57	87.12 \pm 2.9
Calculated buckling strength (MPa)	87.23	87.85	87.86
Differences	0.1 %	0.3 %	0.8%

7.2.2 Strength Degradation of Various Columns Oxidized in Zone 1

The same kinds of IG-430 columns in Table 7-3 were oxidized at 600 °C. The strength was measured with the same compression test machine. The obtained data were also compared with the compressive strength degradation of IG-430. The normalized experimental results are shown in Figure 7-11, but they can also be expressed by Knudsen relation. The exponents for the data are almost the same. So, the strength of graphite column oxidized in Zone 1 is only dependent on the initial strength and decreases with bulk density even though the graphite columns have the different dimensions and the different failure modes. The conclusion is the same with the strength degradation in Zone 1 for IG-110, which is helpful in analyzing the graphite support block. More detailed analysis for the failure of a graphite support column will be performed in FY-10.

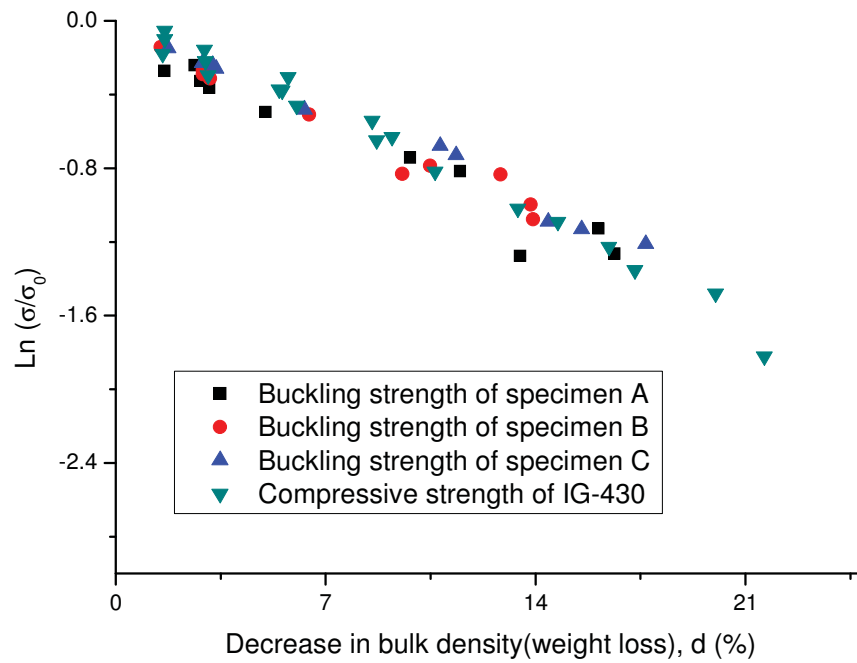


Figure 7-11. Normalized compressive and buckling strength of IG-430 columns.

8. TASK 7: COUPLING NEUTRONICS-THERMAL HYDRAULIC TOOLS (KAIST)

This task enhances the thermal-hydraulic capability of GAMMA code. To improve the reliability of thermal-hydraulic analysis, thermal power distribution is needed in the reactor core. The knowledge of accurate thermal distribution is also necessary to generate accurate cross -sections of nuclei. This task will investigate neutronics/thermal-hydraulics feedback effects and implement the feedback parameters into an upgraded GAMMA code. The activities that will be carried out are discussed below.

8.1 Coupling Procedure

The coupling procedure involves enhancing the thermal-hydraulic capability of GAMMA code. To improve the reliability of thermal-hydraulic analysis, thermal power distribution is needed in the reactor core. The knowledge of accurate thermal distribution is also necessary to generate accurate cross sections of nuclei. This task therefore investigates the feedback effects of neutronics/thermal-hydraulics and implements the feedback parameters into an upgraded GAMMA code. The following activities will be carried out in this task.

8.1.1 Set-up Parameters for Neutronics/Thermal-Hydraulics Code Coupling

The GAMMA code should transfer the following parameters to the COREDAX code:

- Node[icell].Temp0 : Fluid temperature ($^{\circ}\text{K}$)
- Node[icell].rho0 : Fluid density (kg/m^3)
- W3D[kji].Temp0 : Block temperature ($^{\circ}\text{K}$)
- Wblk[QC[m].num].grho : Block mixture density (kg/m^3)

These parameters are coupling data in the GAMMA code. They form data variable 'QC' and are sent to the COREDAX code as:

- QC[m].Tfuel : fuel temperature($^{\circ}\text{K}$)
- QC[m].Dfuel : fuel density (kg/m^3)
- QC[m].Tmod : Coolant temperature($^{\circ}\text{K}$)
- QC[m].Dmod : Coolant density (kg/m^3)
- QC[m].Prel : Node relative power

In the COREDAX code, 'QC' data are designated as either the 'Mapth' or 'Mapn' variable for the calculation node. 'Mapth' is for TH calculation node and 'Mapn' is for neutronics calculation node variable as:

- Mapth[lth].n : neutronics node number in lth TH node.
- Mapth[lth].id[lthn] : neutronics node ID in lth TH node.
- Mapth[lth].frac[lthn] : neutronics node fraction.
- Mapn[m].n : TH ndoe number in m neutronics node
- Mapn[m].id[inn] : TH node ID in m eneutronics node.
- Mapn[m].frac[inn] : TH node fraction.

In the COREDAX code, subroutine 'exdata' performs as a data transfer function.

8.1.2 Calculation Node Mapping between the COREDAX and GAMMA Code

The definitions of the calculation nodes between the COREDAX and GAMMA codes are much different. A mapping procedure should be taken node by node. This calculation node mapping is given by the following input file:

```

X Y direction Blk number
3
2 0
3 1
4 0
***** Radial Mapping *****
45
1      1  1.0
2      2  1.0
3      2  1.0
      .
      .
      .
13     3  0.5      4  0.5
      .
      .
      .
***** Axial Mapping *****
15
1      1  1.0
2      2  1.0
3      3  1.0
4      4  1.0
```

Figure 8-1. Sample Input of Calculation Node Mapping.

Radial and axial calculation nodes are determined by matching node-by-node in a sequence. Mapping is done by subroutine 'genmap' in the COREDAX code as shown in Figure 8-2.

8.1.3 Code coupling of COREDAX with GAMMA

GAMMA code, which previously calculated power distribution by subroutine 'point kinetics,' is now replaced by subroutine 'COREDAX_coupling' for both steady and transient states. The replacement is shown in Figure 8-3.

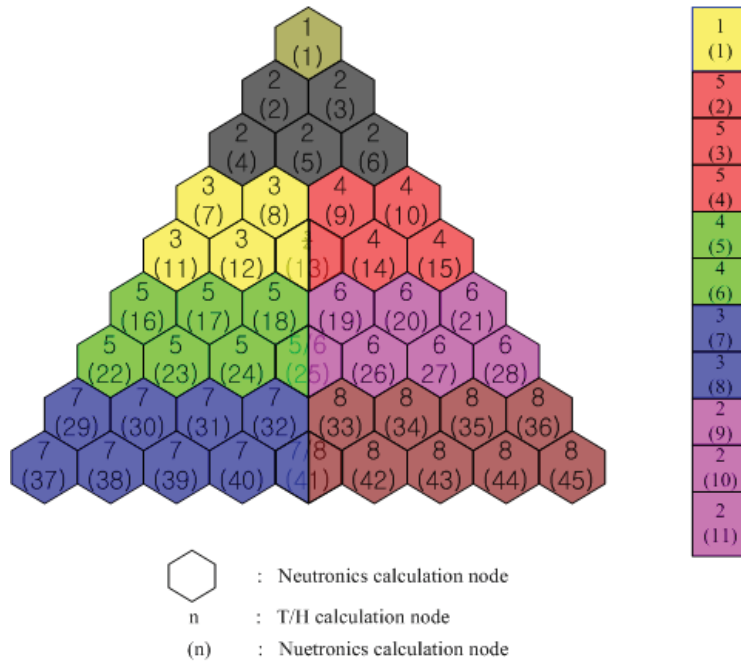


Figure 8-2. Example of calculation node mapping.

```

// set initial transport properties
set_gas_wall_prop(0, ofp[0]);

Tmax_Triso(1);

set_cblk_init(ofp[0]);

set_iter_var(ofp[0]);

simtime = Scon.ini_time;
timestep = Scon.ini_dtime; // initial time step

//-----
//COREDAX Coupling
//-----
State=0;
COREDAX_coupling();

do // loop with reduced time step
{
  get_con_blks(ofp[0]); // control elements

  get_sys_mods(ofp[0]); // time-dependent variables

  point_kinetic(ofp[0]); // point kinetics

  State=1;
  if(simtime!=0.0) COREDAX_coupling(); //COREDAX_Couple

  wall_calc_all(ofp[0]); // heat conduction, coeffi. matrix

```

Figure 8-3. COREDAX calling in the GAMMA code.

8.1.4 Calculation procedure in a coupling system

Steady state calculation is generally first done to take a transient calculation. When several coupled variables are transmitted, a proper calculation state to the neutronics code is determined. The neutronics code has four different calculation modes: (1) initialization mode, (2) steady state mode, (3) transient mode, and (4) output mode. The calculation scheme described in Figure 8-4 shows the neutronics part in an envisioned coupled code system.

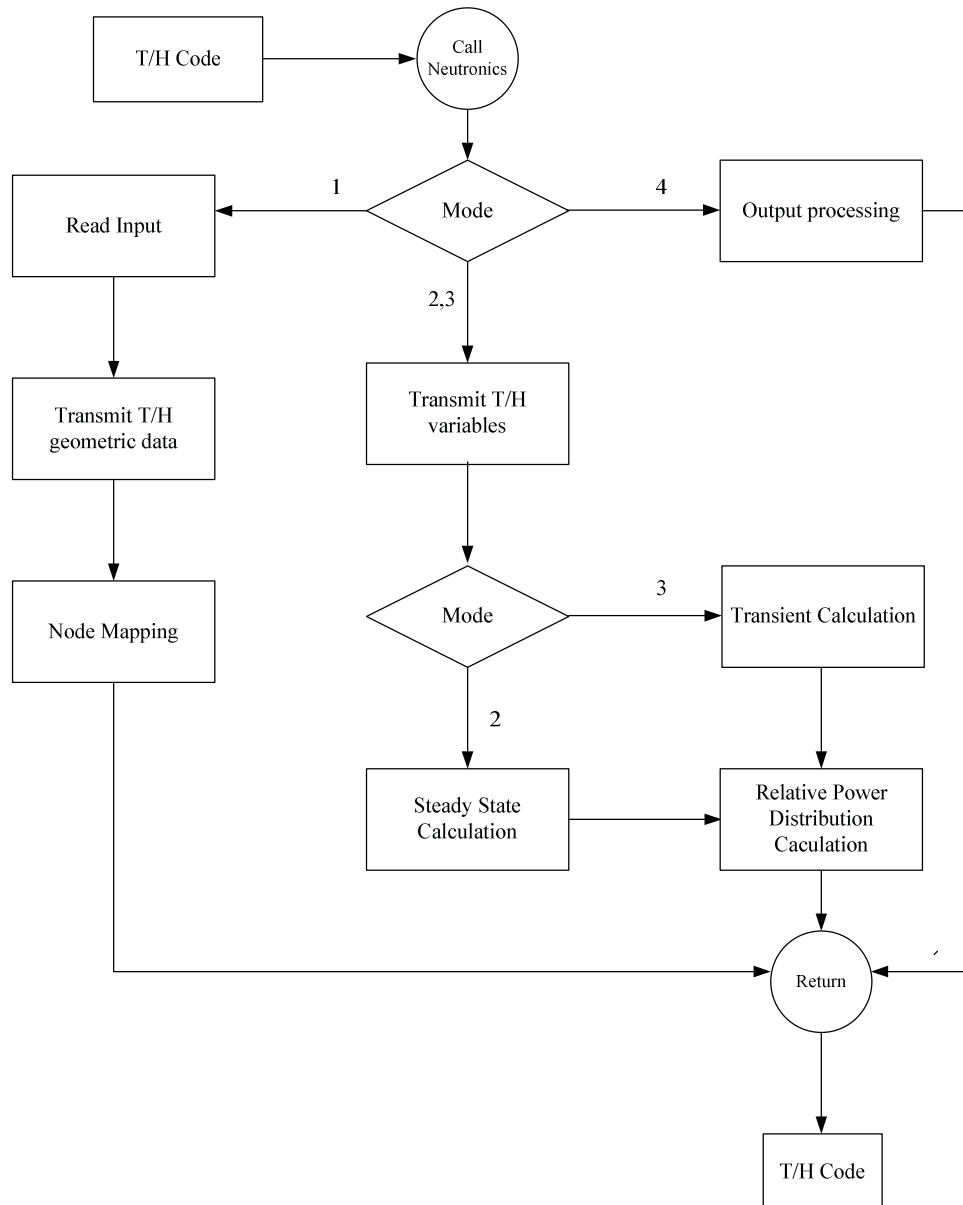


Figure 8-4. Calculation procedure in neutronics code.

8.2 Homogenized Cross-Section Table

A homogenized cross-section table is made to analyze the VHTR core. The homogenized cross section will be linearly interpolated from a precalculated TABLESET on fuel temperature, graphite temperature, and coolant density. Figures 8-5 and 8-6 show the format of the homogenized cross-section TABLESET for coupling calculation.

T_{f1}	T_{f2}	T_{f3}	T_{f4}	T_{f5}
ρ_{m1}	ρ_{m2}	ρ_{m3}	ρ_{m4}	ρ_{m5}
ρ_{m6}	Σ_1	Σ_2	...	
		...	Σ_{29}	Σ_{30}

Where:

– T_f is the Doppler (fuel) temperature ($^{\circ}\text{K}$)

– ρ_m is the moderator density (kg/m^3)

Macroscopic cross-sections are in units of cm^{-1}

Figure 8-5. Homogenized cross-section form in the COREDAX code.

```

*****
NEM – Cross-Section Table Input
*
*      T Fuel      Rho Mod.      Boron ppm.      T Mod.
*          5          6          0          0
*
***** X-Section Set #
#
*****
Group No. 1
*
***** Diffusion Coefficient Table
*
***** Absorption X-Section Table
*
***** Fission X-Section Table
*
***** Nu-Fission X-Section Table
*
***** Scattering From Group 1 to 2 X-Section Table
*
*****
Group No. 2
*
***** Diffusion Coefficient Table
*
***** Absorption X-Section Table
*
***** Fission X-Section Table
*
***** Nu-Fission X-Section Table
*
***** Xenon Absorption Cross-Section Table
*
*****
***** Inv. Neutron Velocities
*

```

Figure 8-6. Homogenized cross-section sample in the COREDAX code.

8.3 GAMMA/COREDAX Test Calculation

The GAMMA/COREDAX code coupling was tested with the simplified 600 MWth GTMHR. Problem and test results are described in the following figures. Problem core is described in Figure 8-7.

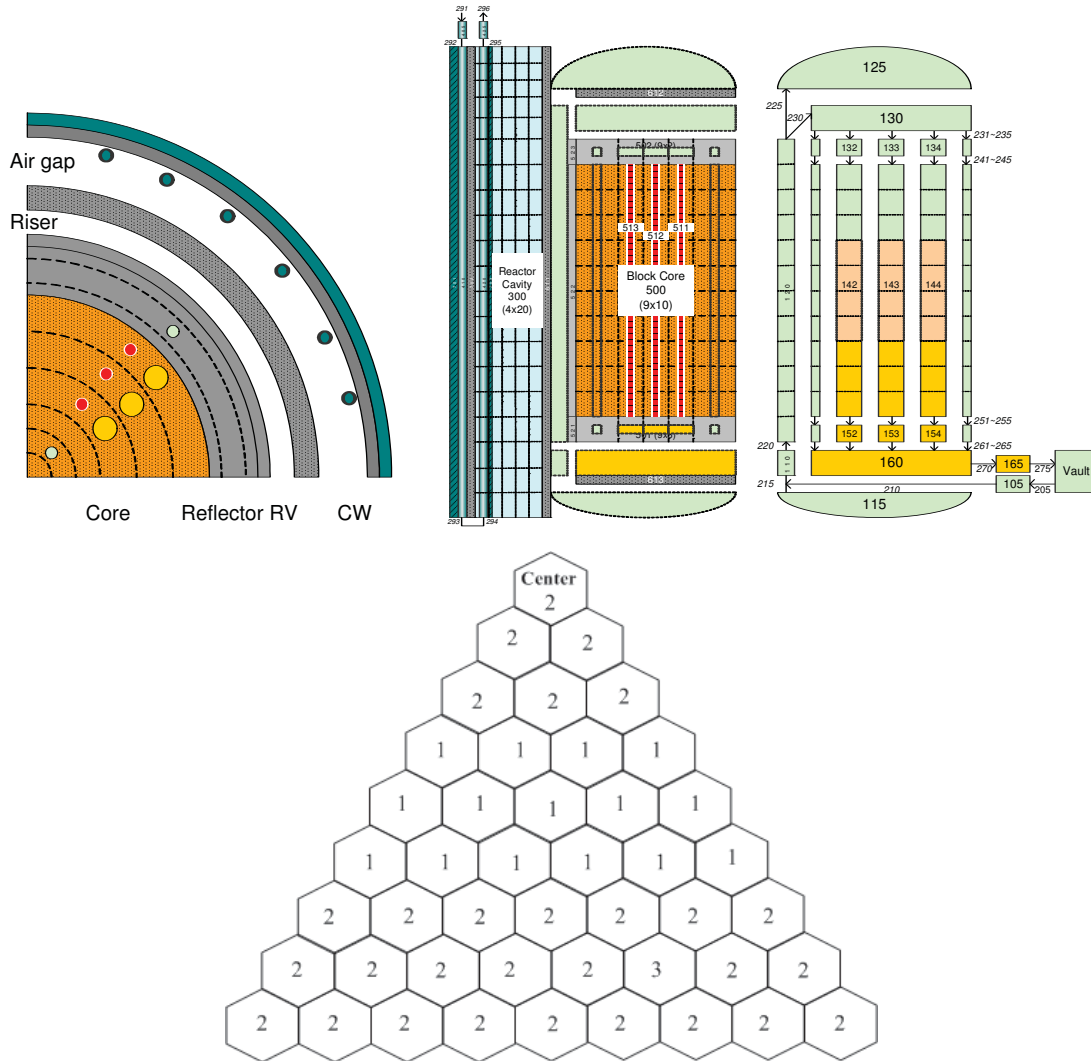


Figure 8-7. Simplified GTMHR 600 benchmark problem.

The calculation results (see Figure 8-8) show that the original GAMMA calculation is different with the GAMMA/COREDAX results and the GAMMA/COREDAX results are the same with the GAMMA results with changed input data as COREDAX results. This means that the GAMMA/COREDAX code works correctly in the coupling calculation.

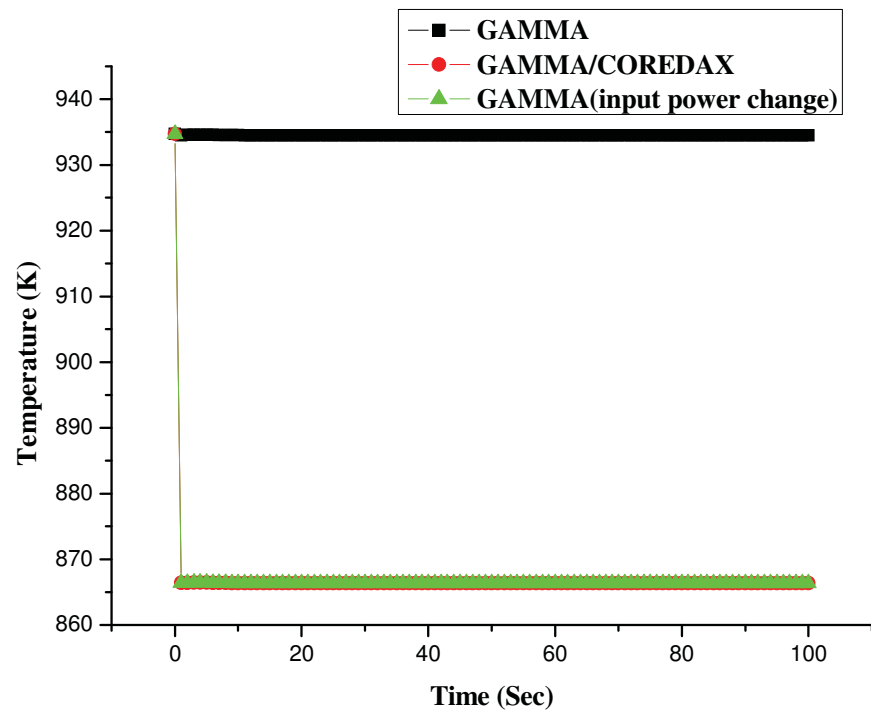


Figure 8-8. Calculation results of GAMMA/COREDAX code.

9. TASK 8: CORE NEUTRONICS MODEL

There is growing interest in making high fidelity nodal codes available in hexagonal-z geometry because of the needs of, in particular, VVER, SMART, and VHTR core analysis. The COREDAX code is a hexagonal-z 3-D diffusion nodal code based on the analytic function expansion (AFEN) nodal method. The COREDAX code consists of several unique features: (1) implementation of the AFEN method, which employs no transverse integration and represents the solution in terms of analytic solution bases; (2) inclusion of transverse gradient basis functions; (3) use of interface flux moments; (4) implementation of the CGR acceleration scheme; and (5) kinetics calculation capability based on the solution decomposition.

This report presents a research of the AFEN method in hexagonal-z geometry, multigroup formulation and CGR acceleration scheme. The COREDAX code is verified through tests of the VVER-440, a “simplified” VVER-1000, and the SNR-300 benchmark problems found in typical hexagonal-z geometry.

9.1 Basic Theory and Method

9.1.1 Nodal Unknowns and Nodal Equations

The description of the AFEN method begins with the 3-D hexagonal-z geometry multigroup diffusion equation

$$-[D]\nabla^2\vec{\phi}+[A]\vec{\phi}=\frac{\vec{\chi}}{k_{eff}}\vec{F}^T\vec{\phi} \quad (9-1)$$

where

$[D]$ = diffusion coefficient matrix

$[A]$ = removal and scattering cross section matrix

\vec{F} = fission production cross section vector

$\vec{\chi}$ = fission spectrum vector

k_{eff} = multiplication factor.

Following the AFEN methodology, the solution of the diffusion equation for nod n is expressed as

$$\vec{\phi}^n(x, y, z) = \vec{\phi}_1^n(x, y, z) + \vec{\phi}_2^n(x, y, z) + \vec{\phi}_3^n(x, y, z) + \vec{\phi}_4^n(x, y, z), \quad (9-2)$$

where

$$\begin{aligned} \vec{\phi}_l^n(x, y, z) = & \sinh(\sqrt{\Lambda^n} x_l) \vec{a}_{1l}^n + \cosh(\sqrt{\Lambda^n} x_l) \vec{a}_{2l}^n \\ & + y_l \sinh(\sqrt{\Lambda^n} x_l) \vec{b}_{1l}^n + y_l \cosh(\sqrt{\Lambda^n} x_l) \vec{b}_{2l}^n \\ & + z \sinh(\sqrt{\Lambda^n} x_l) \vec{c}_{1l}^n + z \cosh(\sqrt{\Lambda^n} x_l) \vec{c}_{2l}^n, \quad l = 1, 2, 3, \end{aligned} \quad (9-2a)$$

$$\bar{\phi}_4^n(x, y, z) = \sinh(\sqrt{\Lambda^n} z) \bar{d}_{10}^n + \cosh(\sqrt{\Lambda^n} z) \bar{d}_{20}^n, \quad (9-2b)$$

and

$$[\Lambda^n] = [D^n]^{-1} \left([A] - \frac{\tilde{\chi}}{k_{eff}} \bar{F}^T \right)^n. \quad (9-3)$$

The coordinates x_1 , x_2 , and x_3 are defined in Figure 9-1. Note that each of the 20 terms in Equation (9-2) is an analytic solution of Equation (9-1), and that Equation (9-2) includes terms of transverse gradient basis functions. Evaluation of the matrix functions is facilitated by spectral decomposition in functional theory of linear operators.

The coefficients in the Equation (9-2) flux expansion are expressed in terms of nodal unknowns, such as the node average flux, the node-interface fluxes, and the node-interface flux moments. Included are the 12 node-interface flux moments (y- and z-weighted average fluxes \times 6 radial interfaces) as nodal unknowns in this research. The six radial-interfaces are shown in Figure 9-2.

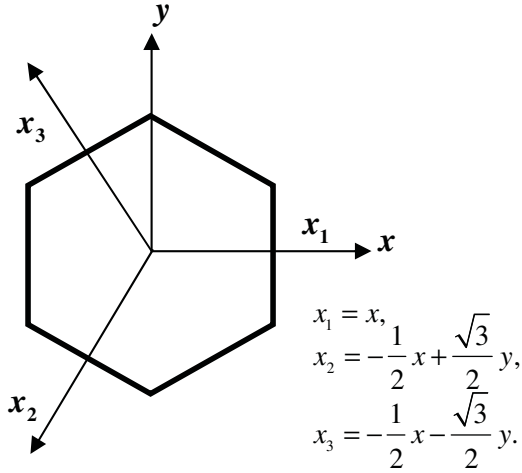


Figure 9-1. Coordinates in a hexagon.

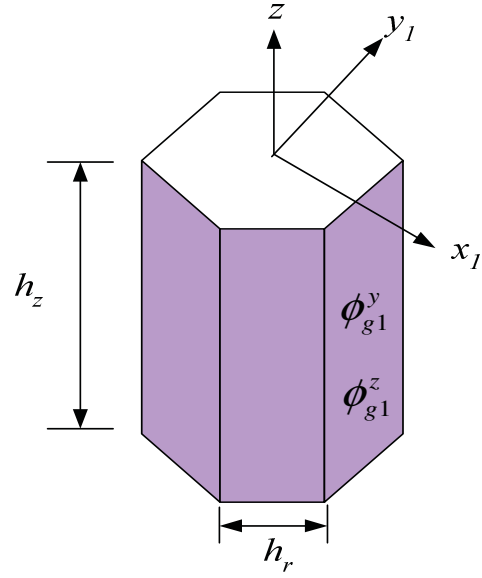


Figure 9-2. Interface flux moments on six radial interfaces.

All the nodal unknowns are defined as follows:

- One average flux

$$\phi_{gavg} = \frac{2}{3\sqrt{3}h_r^2 h_z} \int_{\frac{h_z}{2}}^{\frac{h_z}{2}} \left(\int_{-\frac{\sqrt{3}h_r}{2}}^{\frac{\sqrt{3}h_r}{2}} \int_{\frac{h_r}{2}-h_r}^{\frac{h_r}{2}+h_r} \phi_g(x, y, z) dy dx + \int_0^{\frac{\sqrt{3}h_r}{2}} \int_{\frac{h_r}{2}-h_r}^{\frac{h_r}{2}+h_r} \phi_g(x, y, z) dy dx \right) dz, \quad (9-4)$$

- Two axial interface fluxes of the form

$$\phi_{gz1} = \frac{2}{3\sqrt{3}h_r^2} \left(\int_{-\frac{\sqrt{3}h_r}{2}}^0 \int_{\frac{h_r}{2}-h_r}^{\frac{h_r}{2}+h_r} \phi_g(x, y, \frac{h_z}{2}) dy dx + \int_0^{\frac{\sqrt{3}h_r}{2}} \int_{\frac{h_r}{2}-h_r}^{\frac{h_r}{2}+h_r} \phi_g(x, y, \frac{h_z}{2}) dy dx \right), \quad (9-5)$$

- Six radial interface fluxes of the form

$$\phi_{g1} = \frac{1}{h_r h_z} \int_{-\frac{h_r}{2}}^{\frac{h_r}{2}} \int_{-\frac{h_z}{2}}^{\frac{h_z}{2}} \phi_g\left(\frac{\sqrt{3}}{2}, y, z\right) dz dy, \quad (9-6)$$

- Six y-moment radial interface fluxes of the form

$$\phi_{g1}^y = \frac{1}{h_r h_z} \int_{-\frac{h_r}{2}}^{\frac{h_r}{2}} \int_{-\frac{h_z}{2}}^{\frac{h_z}{2}} y \phi_g\left(\frac{\sqrt{3}}{2}, y, z\right) dz dy, \quad (9-7)$$

- Six z-moment radial interface fluxes of the form

$$\phi_{g1}^z = \frac{1}{h_r h_z} \int_{-\frac{h_r}{2}}^{\frac{h_r}{2}} \int_{-\frac{h_z}{2}}^{\frac{h_z}{2}} z \phi_g\left(\frac{\sqrt{3}}{2}, y, z\right) dz dy. \quad (9-8)$$

To determine nodal unknowns, as many solvable nodal equations are built as the number of these nodal unknowns. The solution procedure of the nodal equations is then usually a conventional one that involves two levels of iterative schemes: inner iteration and outer iteration.

The nodal equation for each node is composed of a nodal balance equation and associated coupling equations. The coupling equations consist of interface current continuity equations and interface current moment continuity equations. The nodal equations and interface current moment continuity equations. The nodal equations are expressed as follows:

- One node balance equation

$$\frac{1}{V} \int_V \nabla \cdot \vec{J}(r) dV + [A] \vec{\phi}_{avg} = \frac{\vec{\chi}}{k_{eff}} \vec{F}^T \vec{\phi}_{avg}, \quad (9-9)$$

- Eight interface current continuity equations of the form

$$\vec{J}_{(x,y,z)}\left(\frac{\sqrt{3}}{2} h_r\right) = \vec{J}_{(x',y',z')}\left(-\frac{\sqrt{3}}{2} h_r\right), \quad (9-10)$$

- Twelve interface current moment continuity equations of the form

$$\vec{J}_{(x,y,z)}^y\left(\frac{\sqrt{3}}{2} h_r\right) = \vec{J}_{(x',y',z')}^y\left(-\frac{\sqrt{3}}{2} h_r\right). \quad (9-11)$$

9.1.2 Multigroup Extension

The eigenvalues of Matrix in Equation (9-3) are always real in two-group problems. But in multi-group problems, the eigenvalues (and thus eigenvectors) can be complex. The AFEN method was extended to multigroup formulation using a transformation matrix defined by real and imaginary parts of a complex eigenvector. Thus, this transformation method requires the knowledge of the eigenvectors in addition to the eigenvalues. The method for multigroup problems in this research is based on the use of the spectral decomposition property in the matrix function theory. This method requires the knowledge only of the eigenvalues (the eigenvectors are not required), facilitating the computation involved in the nodal equations. The matrix function theory applied to the matrix functional evaluations of

$$f(A), \quad (9-12)$$

where f is an analytic function and A is a matrix. The matrix functions arising in the AFEN method for multigroup (G groups) problems belong to this class functions (see Equations (9-2a) and (9-2b); trigonometric, hyperbolic, or exponential functions of matrices of dimension $G \times G$).

According to the spectral decomposition property of the matrix function theory,

$$f(A) = \sum_{i=0}^{G-1} b_i A^i, \quad (9-13)$$

where the decomposition coefficients b_i can be obtained from the polynomial interpolation

$$p(\lambda_k) = f(\lambda_k), \quad k = 0, 1, \dots, G-1, \quad (9-14)$$

where λ_k 's are the eigenvalues of A (with complex conjugates allowed) and

$$p(\lambda) = \sum_{i=0}^{G-1} b_i \lambda^i. \quad (9-15)$$

Therefore, the matrix functions can be easily evaluated if the eigenvalues of the matrix A are known.

9.1.3 Coarse Group Rebalance Acceleration

To apply the CGR acceleration, the net current variables in Equations (9-9) through (9-11) above are reformulated in terms of partial currents:

$$\vec{J}_s = \vec{J}_s^{outgoing} - \vec{J}_s^{incoming}, \quad \vec{\phi}_s = 2(\vec{J}_s^{outgoing} + \vec{J}_s^{incoming}), \quad (9-16)$$

$$\vec{J}_s^{outgoing} = \frac{\vec{\phi}_s}{4} + \frac{\vec{J}_s}{2}, \quad \vec{J}_s^{incoming} = \frac{\vec{\phi}_s}{4} - \frac{\vec{J}_s}{2}, \quad (9-17)$$

where s is surface index.

Then, Equation (9-9) can be rewritten after group summation (e.g., for two group case) as

$$\begin{aligned}
& \frac{S_{xy}}{V} \sum_{d=1,6} \sum_{g=1,2} J_{0d,g}^{outgoing} + \frac{S_z}{V} \sum_{d=7,8} \sum_{g=1,2} J_{0d,g}^{outgoing} + \sum_{g=1,2} \Sigma_{ag} \phi_{av,0,g} \\
& - \frac{S_{xy}}{V} \sum_{d=1,6} \sum_{g=1,2} J_{0d,g}^{incoming} - \frac{S_z}{V} \sum_{d=7,8} \sum_{g=1,2} J_{0d,g}^{incoming} \\
& = \frac{1}{k_{eff}} \sum_{g=1,2} \nu \Sigma_{fg} \phi_{av,0,g}.
\end{aligned} \tag{9-18}$$

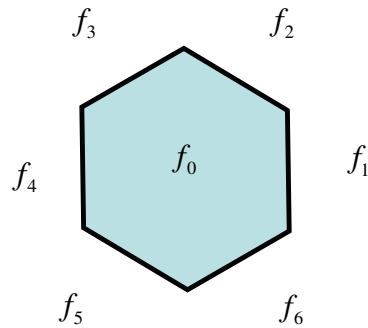
A rebalance factor per node is defined as

$$\phi_{av,d,g}^{new} = f_d \phi_{av,d,g}^{old}, \quad d=0, \quad g=1,2, \tag{9-19a}$$

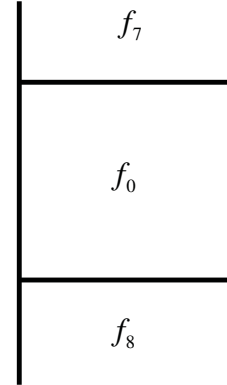
$$J_{0d,g}^{outgoing,new} = f_d J_{0d,g}^{outgoing,old}, \quad d=1,2,\dots,8, \quad g=1,2, \tag{9-19b}$$

$$J_{0d,g}^{incoming,new} = f_d J_{0d,g}^{incoming,old}, \quad d=1,2,\dots,8, \quad g=1,2. \tag{9-19c}$$

The rebalance factors are depicted in Figure 9-3.



(a) in x-y plane



(b) along z axis

Figure 9-3. Rebalance factors.

Substituting Equation (9-19) in Equation (9-18) leads to

$$R_0 f_0 - \frac{S_{xy}}{V} \sum_{d=1,6} \sum_{g=1,2} J_{0d,g}^{incoming} f_d - \frac{S_z}{V} \sum_{d=7,8} \sum_{g=1,2} J_{0d,g}^{incoming} f_d = \frac{P_0}{k_{eff}} f_0, \tag{9-20}$$

where

$$R_0 = \frac{S_{xy}}{V} \sum_{d=1,6} \sum_{g=1,2} J_{0d,g}^{outgoing} + \frac{S_z}{V} \sum_{d=7,8} \sum_{g=1,2} J_{0d,g}^{outgoing} + \sum_{g=1,2} \Sigma_{ag} \phi_{av,0,g}, \tag{9-21}$$

$$P_0 = \sum_{g=1,2} \nu \Sigma_{fg} \phi_{av,0,g}. \quad (9-22)$$

Equation (9-20) is the CGR acceleration equation with eigenvalue k_{eff} and eigenvector \vec{f} composed of rebalance factors.

9.2 Verification of the COREDAX code

To verify the improved AFEN method implemented in COREDAX, we solved the three dimensional version of VVER-440 benchmark problem, a “simplified” VVER-1000 benchmark problem, and the SNR-300 benchmark problem.

9.2.1 VVER-440 benchmark problem

The VVER-440 benchmark problem is a hexagonal-z 3-D two-group VVER-400 core. It has 1/12 reflective symmetry geometry and the outer boundary conditions are vacuum. The configuration of the core is shown in Figure 9-4. Table 9-1 shows the results, compared with those of the PARCS code, the COREDAX code, and the reference solution. Note that the COREDAX code provides very accurate nodal solutions.

Table 9-1. Results of VVER-440 benchmark problem^a

No. of planes	PARCS (k_{eff} % error) (Node power maximum % error)	COREDAX (k_{eff} % error)/ (Node power maximum % error)
24	1.010918 (-0.040)	1.01125753 (-0.0062)
60	1.010866 (-0.045)	1.01125544 (-0.0063)

a. Reference solution $k_{eff} = 1.01132$ from DIF3D-FD runs extrapolation.

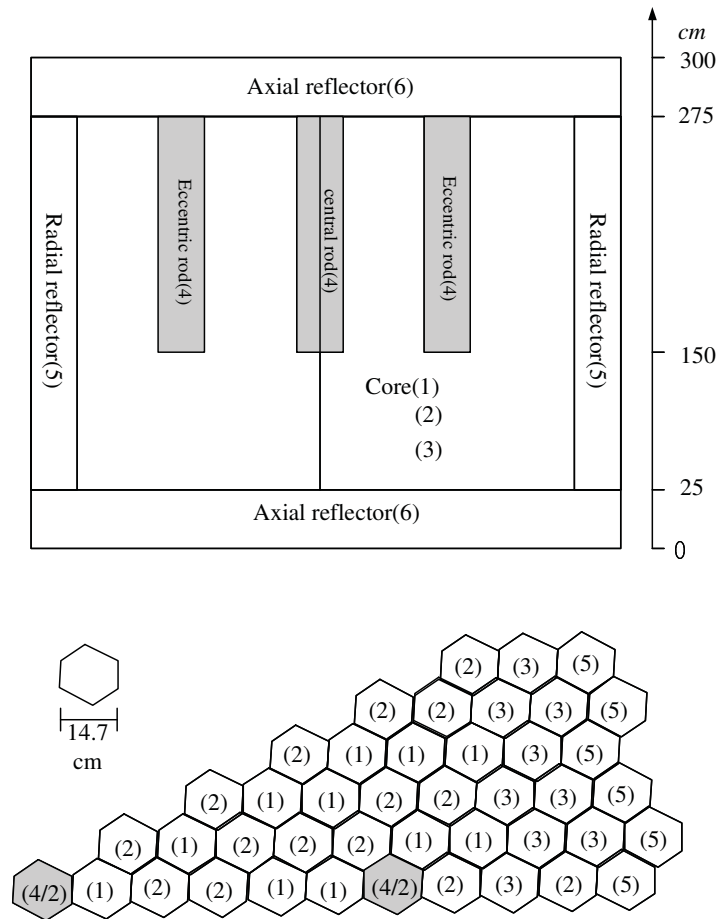


Figure 9-4. Core configuration of 3-D VVER-440.

Also in order to test CGR acceleration, we used VVER-440 benchmark problem. We tested it for 12 and 60 axial nodes. Table 9-2 shows the results. Note that CGR provides very high speed-up and accurate results.

Table 9-2: Results on CGR acceleration of VVER-440 benchmark problem^a

Number of axial nodes	Number of iterations	Computing time ^b (sec)	K_{eff} (% error)
12	3,857	144	1.01096708(0.0349)
	58	3	1.01096706 (0.0349)
60	6,599	1,130	1.01096260(0.0353)
	37	14	1.01096266(0.0353)

a. Reference solution $k_{eff} = 1.01132$ from DIF3D-FD runs extrapolation

b. Pentium IV 3.0 GHz, 2 G RAM

9.2.2 A Simplified VVER-1000 Benchmark Problem

The data of the original VVER-1000 benchmark problem (every fuel assembly has differing cross sections) is too big to fit in the VENTURE code for reference solution. A simplified core data structure was therefore constructed that maintains the same geometry. The material data numbers were changed from 283 to 7 such that the core contains five radially different nodes and 12 axial planes with two reflector and 10 fuel planes. There was no change in axial node components. The core has 1/6 reflective symmetry and the outer boundary conditions are zero flux. Sidelength of each assembly is 13.6 cm. The geometrical configuration of the core is shown in Figures 9-5 and 9-6. Core temperature is 552.15 K and coolant density is 767.1 kg/m³. Table 9-3 shows the results on k_{eff} compared with the VENTURE reference. The reference was obtained by the VENTURE code using 384 triangles \times 20 axial meshes per hexagonal prism node. Two sets of results are compared: one using flux zero boundary condition and the other using incoming current zero boundary condition. Both results show that COREDAX gives very accurate solutions. This is because the axial calculation modeling (via interface flux moments) uses an enlarged set of analytic functions to provide more accurate axial dependence.

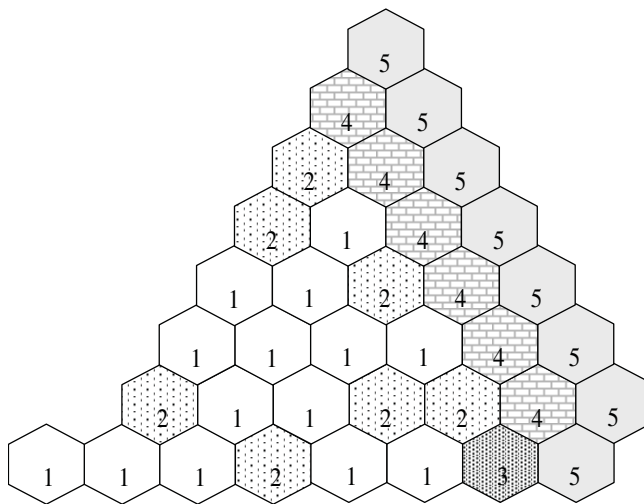


Figure 9-5. Radial core geometry of simplified 3-D VVER-100.

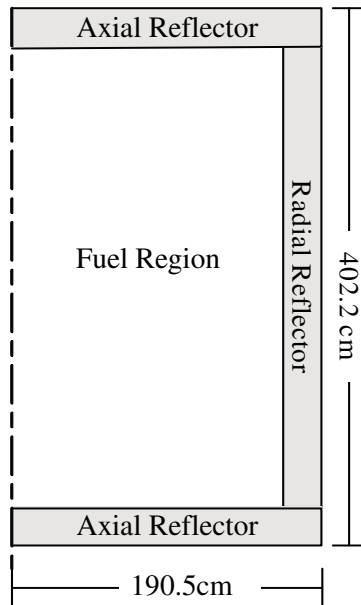


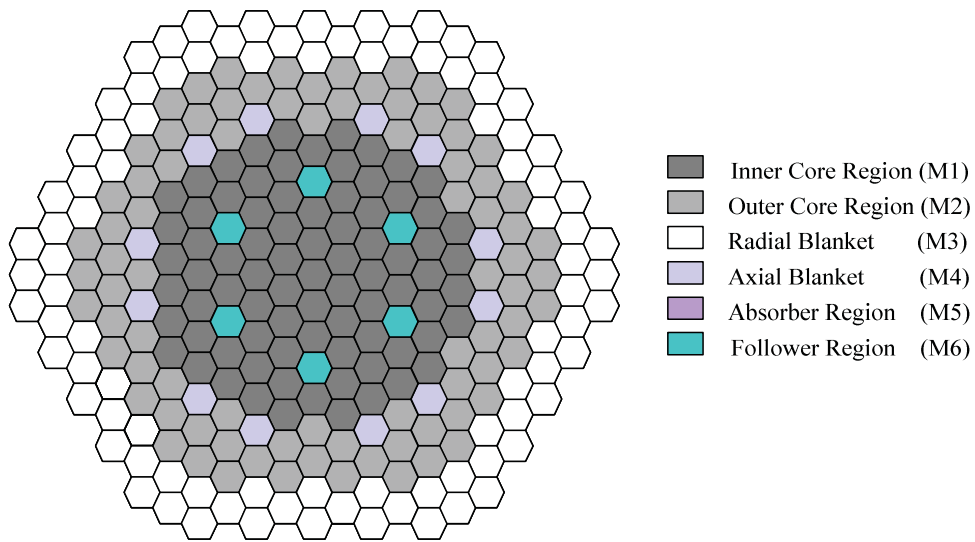
Figure 9-6. Axial core geometry of 3-D VVER-1000.

Table 9-3. Results on k_{eff} of simplified VVER-1000 benchmark problem.

Boundary conditions	VENTURE (ref.) (384×20 per node)	COREDAX (% error)
Flux zero B.C.	1.0000503	1.0000055 (-0.0045)
Incoming current zero B.C.	1.0000534	1.0000476 (-0.0006)

9.2.3 SNR-400 benchmark problem

Finally, SNR-300 was solved to test the multigroup extension in the COREDX code. SNR-300 is a four-group problem modeling a small liquid-metal fast breeder reactor core (ANL 1985). Geometry of the 3-D core is shown in Figures 9-7 and 9-8. The core has 1/6 reflective symmetry and the outer boundary condition is vacuum. The results are shown in Table 9-4. The reference solution was obtained with DIF3D-FD.



Sidelength of each subassembly
corresponds to 6.4665 cm

Figure 9-7. Radial core geometry of 3-D SNR-300.

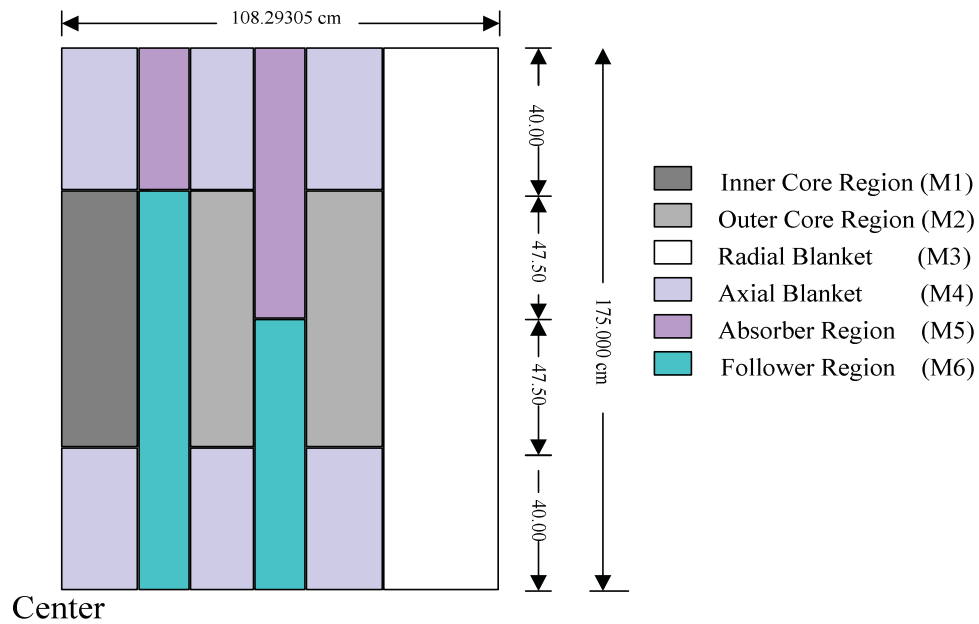


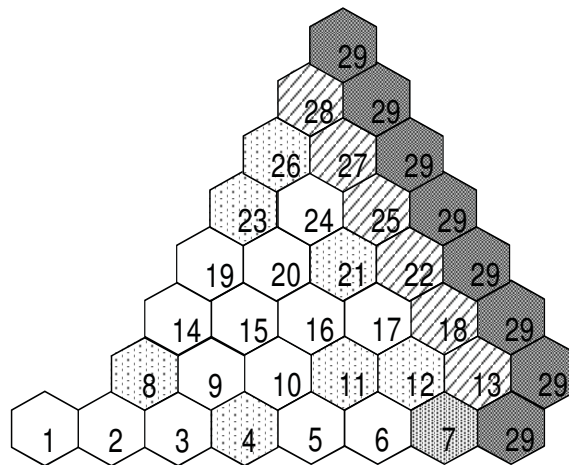
Figure 9-8. Axial core geometry of 3-D SNR-300.

Table 9-4. Results of SNR-300 benchmark problem.

Code	Number of axial nodes	K_{eff} (% error)
Reference (DIF3D-FD)	Richardson extrapolation	1.00989
DIF3D Nodal	8	1.01151 (0.160)
	18	1.01125 (0.135)
COREDAX (Transformation matrix)	8	1.01376 (0.383)
	16	1.01134 (0.185)
COREDAX (Matrix function theory)	8	1.01006 (0.017)
	16	1.01001 (0.012)

9.2.4 VVER-1000 benchmark problem

To verify the COREDAX code, the results were of the COREDAX code were compared with other participants in VVER-1000 benchmark problem. The core configuration of the 3-D VVER-1000 benchmark problem is described in Figure 9-9.



	1	2	3	4	5	6	7	8	9	10	11	12	13	14	15	16	17	18	19	20	21	22	23	24	25	26	27	28	29
1	281	281	281	281	281	281	281	281	281	281	281	281	281	281	281	281	281	281	281	281	281	281	281	281	281	281	281	281	281
2	1	11	21	31	41	51	61	71	81	91	101	111	121	131	141	151	161	171	181	191	201	211	221	231	241	251	261	271	282
3	2	12	22	32	42	52	62	72	82	92	102	112	122	132	142	152	162	172	182	192	202	212	222	232	242	252	262	272	282
4	3	13	23	33	43	53	63	73	83	93	103	113	123	133	143	153	163	173	183	193	203	213	223	233	243	253	263	273	282
5	4	14	24	34	44	54	64	74	84	94	104	114	124	134	144	154	164	174	184	194	204	214	224	234	244	254	264	274	282
6	5	15	25	35	45	55	65	75	85	95	105	115	125	135	145	155	165	175	185	195	205	215	225	235	245	255	265	275	282
7	6	16	26	36	46	56	66	76	86	96	106	116	126	136	146	156	166	176	186	196	206	216	226	236	246	256	266	276	282
8	7	17	27	37	47	57	67	77	87	97	107	117	127	137	147	157	167	177	187	197	207	217	227	237	247	257	267	277	282
9	8	18	28	38	48	58	68	78	88	98	108	118	128	138	148	158	168	178	188	198	208	218	228	238	248	258	268	278	282
10	9	19	29	39	49	59	69	79	89	99	109	119	129	139	149	159	169	179	189	199	209	219	229	239	249	259	269	279	282
11	10	20	30	40	50	60	70	80	90	100	110	120	130	140	150	160	170	180	190	200	210	220	230	240	250	260	270	280	282
12	283	283	283	283	283	283	283	283	283	283	283	283	283	283	283	283	283	283	283	283	283	283	283	283	283	283	283	283	283

Figure 9-9. Core configuration of 3-D VVER-100 benchmark problem.

The steady-state results are shown in Figure 9-10 and Table 9-5. The Hot Zero Power condition results shows that the COREDAX code results are well matched with other participants of benchmark problem and the relative power deviation from the participants' results are the smallest one in the participants.

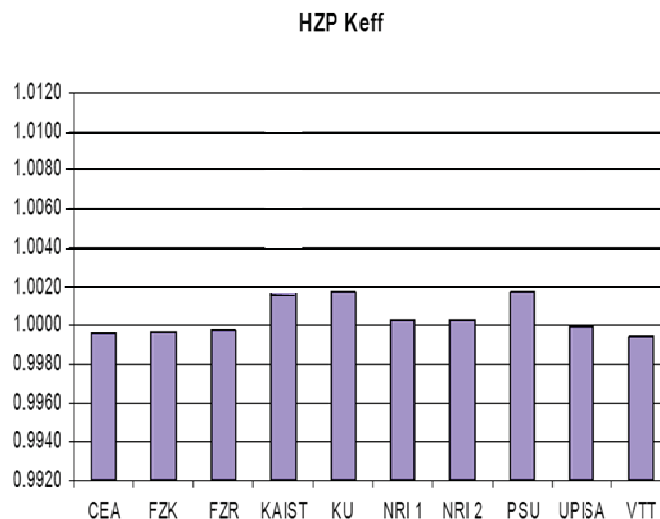


Figure 9-10. Results of VVER-100 benchmark problem.

Table 9-5. Relative power deviation from mean (%).

Part:	Max	Min
CEA	1.16	-1.0
FZK	1.07	-0.82
FZR	0.62	-0.71
NRI1	1.70	-2.17
NRI2	1.70	-2.17
UPISA	0.43	-0.86
VIT	2.20	-1.65
KAIST	0.39	-0.27

To test transient calculation ability of the COREDAX code, a transient scenario with control rod is suggested. The control rod X is withdrawn with 8 cm/sec at 0 seconds after 20 second control rod VI is inserted with 8 cm/sec for 50 sec. The control rods are described in Figure 9-11.

The results shown in Figure 9-12 mean that the power curve well follows the control rod movement and the COREDAX code is working well in transient condition.

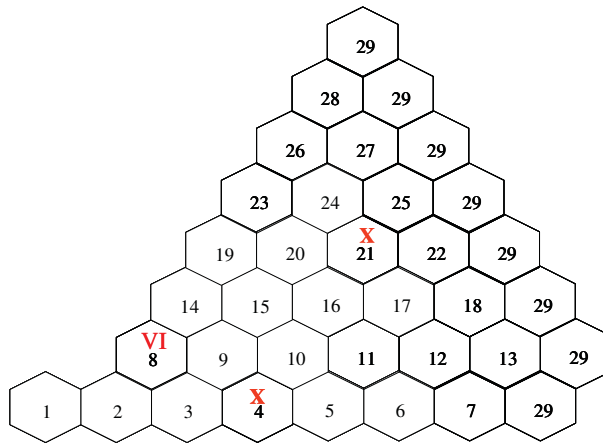


Figure 9-11. Control rod position in VVER-1000.

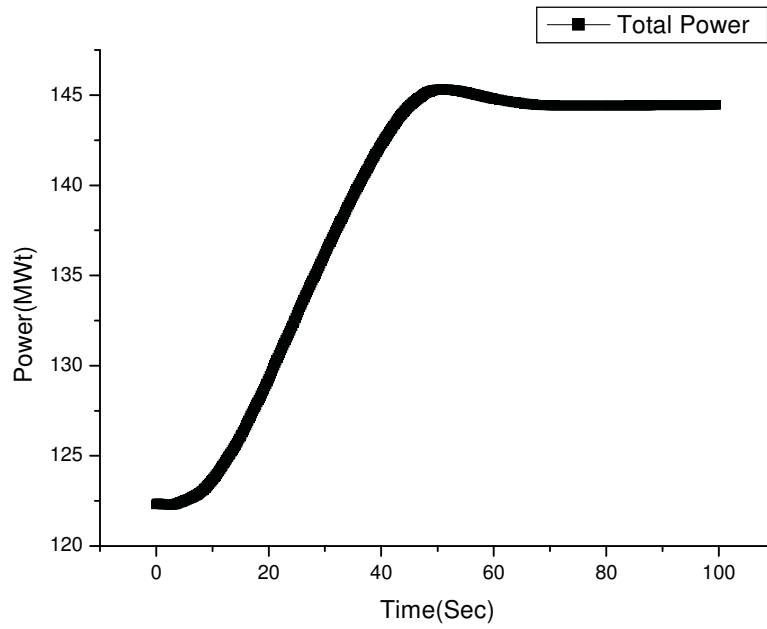


Figure 9-12. Total power change in time.

9.3 Test on GTMHR Core Model

A neutronics calculation of a simple GTMHR core model was performed as a preparation step for verification and validation (V&V).

9.3.1 Description

The GTMHR is one of the most significant HTGR gas turbine plant designs currently under investigation in various places. The GTMHR is being developed on an international basis to optimize the HTGR capabilities and resources of many countries.

The GTMHR reactor core shown in Figure 9-13 represents an annular stack of hexahedral prismatic fuel assemblies with 36 cm across flats size as shown in Figures 9-14 and 9-15, which form 102 columns 800 cm high consisting of 10 fuel assemblies stacked axially in each of these columns. The fuel assembly columns are arranged with a 0.25 cm gap to ensure performance of fuel assembly reloads during the reactor core life.

The active core is enclosed by graphite reflectors as shown in Figure 9-13. The core is surrounded by radial reflectors and the core internal surface is contiguous with internal reflectors. The upper axial reflector (UAR) and lower axial reflector (LAR) are located above and beneath the core, respectively. The upper axial reflector is 130 cm high and consists of stacks of columns assembled from hexahedral prismatic graphite blocks. These are located above the core and are separated by a gap of 0.25 cm.

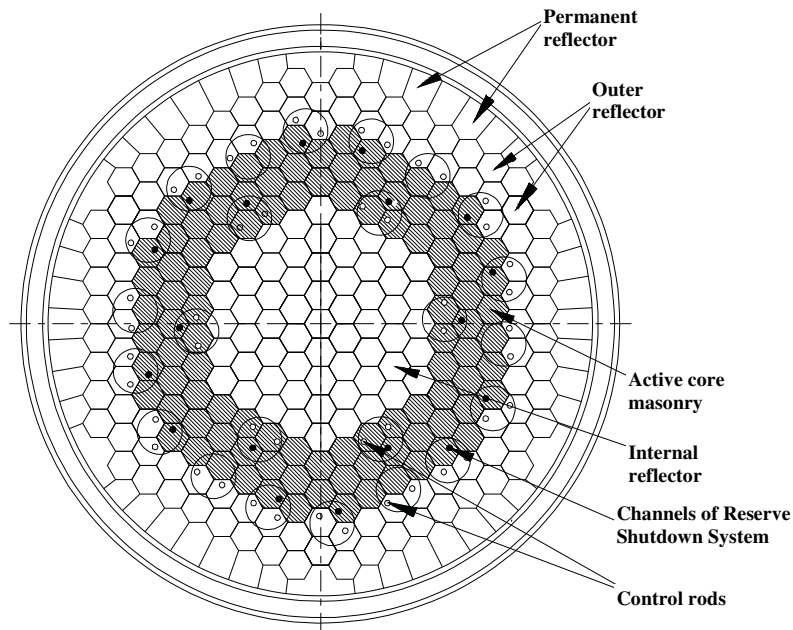


Figure 9-13. Arrangement of active core and its components.

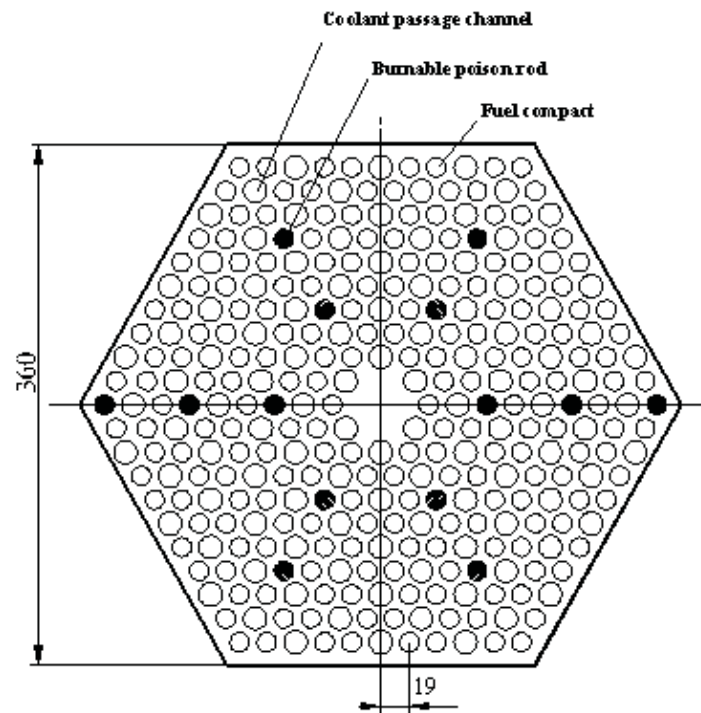


Figure 9-14. Fuel block cell, type 1 fuel assembly.

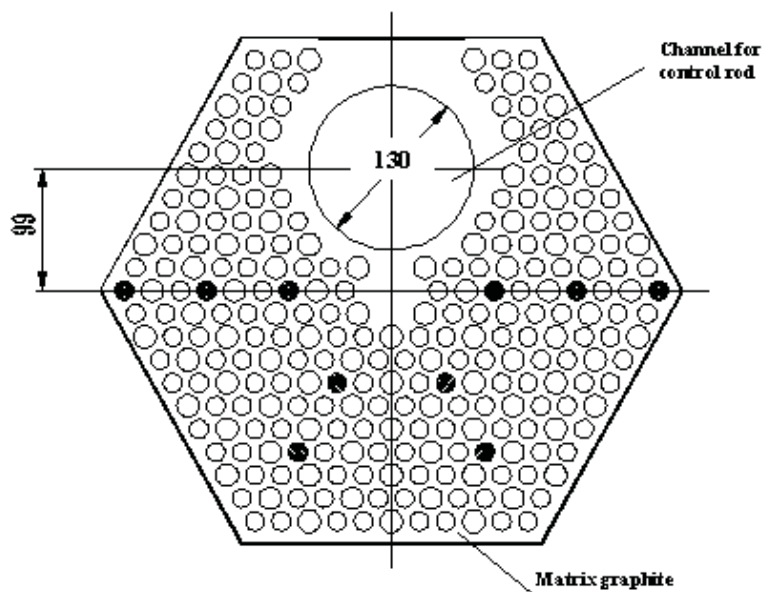


Figure 9-15. Fuel block with cavity for control rod or reserve shutdown system, type 2 fuel assembly.

9.3.2 Test results

Because the GTMHR benchmark problem gives nuclear data as nuclide density homogenized cross sections have to be generated for nodal calculation. The generation of homogenized cross sections is an involved and distinct task outside of scope in this project. This research uses simple t10-group homogenized cross sections for GTMHR fuel assemblies that are obtained informally from KAERI (and that are incomplete, e.g., cross sections for rodged blocks are not available).

The fuel assembly radial configuration is described in Figure 9-16. In the configuration fuel assembly 1 to 3 are Fuels blocks and 4,5 are graphite blocks. Test calculation results by the COREDAX code are shown in Table 9-6.

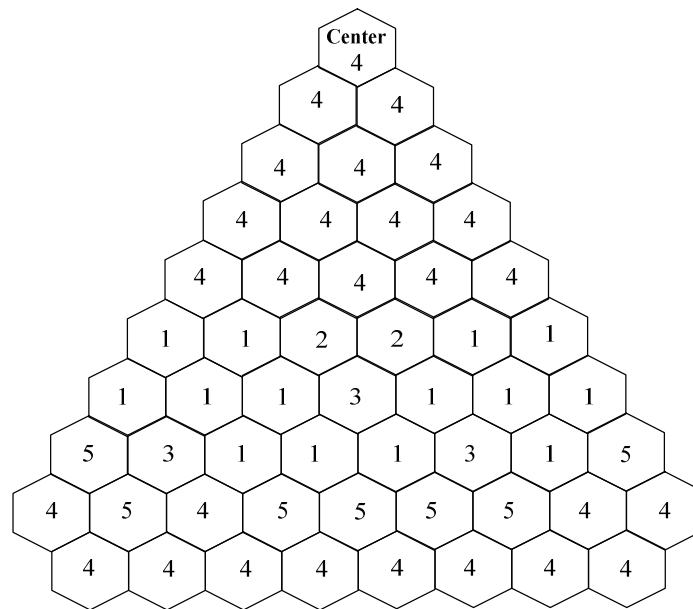


Figure 9-16. Radial core configuration of simplified 3-D GTMHR.

Table 9-6. Results on k_{eff} of simplified GTMHR benchmark problem.

Boundary conditions	COREDAX (% error)
All rods out	2.90801
Fuel region rods on	1.47786
All rods on	1.44863

10. TASK 9: COUPLED CORE MODEL V&V (KAIST)—FY-10 Task

This task involves the verification of GAMMA code coupled with COREDAX code and validation of the prediction results of thermal power distribution in the hexagonal reactor core. The following activities will be carried out in this task:

- Verification of GAMMA and COREDAX coupling
- Validation of coupled code with reference data.

This task will be performed in FY-10.

11. SUMMARY

Several important issues associated with a VHTR air-ingress accident were investigated in FY-09, the second year of this 3-year study. The tasks and notable results obtained in FY-09 are summarized below.

11.1 Task 1 (INL)

Task 1 activities consisted of both theoretical and computational work based on analytical estimations and CFD analyses. All of Task 1 results conclude that density gradient-driven stratified flow dominates the air-ingress process in the simplified model of the GTMHR, and the effect of molecular diffusion is generally negligible. The air ingress phenomena depend on the geometry, location, and size of the break. Further investigation accounting for different geometries and other conditions is recommended.

Task 1 activities and results are summarized as follows:

- A new air-ingress scenario based on the density gradient driven flow has been established. This scenario is divided into four steps: (1) depressurization, (2) stratified flow—stage 1, (3) stratified flow—stage 2, and (4) global natural circulation.

The relative importance of two air-ingress mechanisms (molecular diffusion versus density gradient driven flow) has been estimated on a theoretical basis for each step of the accident scenario. A significant decrease in the time scale of air ingress was observed.
- Time scale comparisons between stratified flow and diffusion showed that Stage 1 is clearly dominated by density gradient driven flow. The speed of the stratified flow is estimated to be about 800 times faster than the diffusion process in the GTMHR design.
- Pressure build-up and hydrostatic head in the core were compared in Stage 2 using temperature gradient as the main driving force for generating density gradient. Two different designs were considered: GTMHR 600 MWth and the NACOK experiment. The results showed that the pressure build-up in the GTMHR design was larger than the static head, but the pressure build-up in the NACOK experiment was much smaller than the static head, indicating that the GTMHR 600 MWth design will be dominated by density gradient driven flow, while the NACOK experiment will be dominated by the diffusion process in Stage 2.
- Stage 2 time scale comparisons for the GTMHR 600 MWth design also showed that the density gradient driven flow dominates air-ingress into the core. The speed of convective flow is estimated to be about 600 times faster than the diffusion in the GTMHR design.
- A detailed 3-D CFD simulation was performed by CFX for a DEGB situation. These CFD results show the density gradient driven flow to be the dominant mechanism in the whole air-ingress scenario.
- Preliminary analyses for the chemical reaction effect on air-ingress were performed with the FLUENT code using a 2-D simplified geometry based on the GTMHR design. It showed that the chemical reaction will accelerate the air-ingress process by producing CO in the flow channel.
- Preliminary analyses for the partial break accident have been performed with FLUENT using a 2-D simplified geometry based on the GTMHR design with a steam generator. This accident assumed the pressure relief line failure at the top of the steam generator. The analysis showed that the partial break is also controlled by a density gradient driven flow.

11.2 Task 2 (INL)

Task 2 activities consisted of some isothermal experiments, which were designed and pretested to validate computational and theoretical work performed in FY-08 and FY-09. All experiments were

designed to be measured by optical methods so that flow and concentration profiles could be visualized. Task 2 activities and results are summarized as follows:

- Two isothermal experiments were designed to understand stratified flow phenomena and validate previous computational analyses. One experiment is focused on a full double-ended guillotine break scenario, while the other focuses on a partial break.
- The DEGB experiment focused on the three flow characteristics unique in the VHTR air-ingress accident: (1) stratified flow in the horizontal pipe, (2) stratified flow expansion at the pipe and vessel junction, and (3) stratified flow around supporting structures. Four experimental parameters were chosen for the DEGB experiment: (1) density ratio, (2) Reynolds number, (3) initial pressure differences, and (4) supporting structure.
- The flow and concentration profiles in a DEGB were measured by PIV/PLIF method based on a laser. Front speed, current depth, concentration profile, velocity profile, and mixing parameters were considerations for this measurement.
- The partial break experiment mainly focused on identifying the three different flow regimes, depending on the break angles: (1) diffusion, (2) stratified flow, and (3) intermittent flow. Preliminary CFD simulations clearly show that the flow characteristics and air-ingress speed are highly dependent on the break angles. The maximum air-ingress speed is estimated at around 100 to 120 degrees.
- Some blind CFD calculations are ongoing in order to provide the data to compare with the experiment. The DEGB experiment is now being simulated by STAR CCM+, and the partial break experiment is being simulated by FLUENT code.
- A preliminary stratified flow experiment in the horizontal pipe was performed using water and salt water, which provided good visualization of the flow, clearly showing that the stratified flow is fast, even when the density difference is very small (~ 0.9). It also indicates that the stratified flow speed will be much faster in the two gas species, which have a larger density difference.
- Since no quality level air ingress data are currently available, the data to be collected from this study would be very valuable in validating the analytical and CFD models.

11.3 Task 3 (INL)

Task 3 activities consisted of graphite oxidation and fracture studies that focused on the integrity of supporting structures. It included both experiment and computation that produced lots of valuable results. Task 3 activities and results are summarized as follows:

- The graphite supporting structure was analyzed for the GTMHR 600 MWth design based on the new air-ingress scenario described in Task 1. Both internal and external corrosion of the graphite supports were estimated using GAMMA system analyses code, and structural stress was estimated using ABAQUS code. The graphite strength and the maximum stress were then compared for different times. The structural fracture time was defined as being when the maximum stress exceeds the strength.
- The maximum allowable burn-off for maintaining graphite structural integrity was investigated using computational methods. Both internal and external corruptions were estimated using a graphite oxidation model, and the resulting stress and strength were compared. The ratio of internal and external corrosion was randomly chosen for each time-step to cover all the possible air-ingress scenarios. As a result, the maximum allowable burn-offs for IG-110 and H-451 graphite are estimated to be 0.58 and 0.59, respectively.
- An advanced graphite oxidation model was developed that can be implemented into the system analysis codes. This oxidation model, which covers reaction kinetics, mass transfer, moisture effect,

burn-off effect, external and internal corrosion, and fracture criteria, was implemented into the GAMMA code. Air-ingress analyses were then performed based on the new model. Two different graphite materials were considered: IG-110 and H-451. The results showed that for IG-110 graphite, the bottom reflector has a risk of failing about 88 hours after depressurization, and the lower plenum about 112 hours after, and for H-451 graphite, the bottom reflector has a risk of failing about 105 hours after depressurization, which is a little bit slower than that of IG-110 because H-451 is less oxidizable than IG-110, especially in the higher burn-offs.

- NBG-18 graphite, a promising candidate for VHTR structures, was tested. The effect of burn-off at the various oxidation rates was then measured and correlated, and the characteristics were compared to those of IG-110 and H-451, which were previously characterized in FY-08. The maximum burn-off required for NBG-18 to maintain its mechanical strength, was also experimentally investigated and the resulting data implemented into the advanced graphite oxidation model in the GAMMA code.

11.4 Task 4 (INL)

Task 4 activities, which are mainly scheduled for FY-10, consisted of preliminary studies that investigated air-ingress mitigation methods. Proposed mitigation techniques for both air-ingress and graphite oxidation resulting from these studies are summarized as follows:

- The helium injection method proposed by Yan et al. (2008) was extensively investigated from various angles, which lead to the conclusion that their method is infeasible for current VHTR designs that have horizontal pipes on the side. In this design, the small injection of helium cannot prevent the buoyancy force generated in the lower plenum. Their air-ingress method only applies to vertical pipe designs in which air-ingress is dominated by molecular diffusion.
- A method for injecting helium at the lower plenum was proposed to dilute the oxygen concentration, and to reduce the buoyancy force by lowering fluid temperature in the lower plenum. A detailed CFD simulation of this model was initiated. Results and feasibility determination will be reported in the next fiscal year.
- Some methods for mitigating graphite oxidation were proposed, including nanoparticles or inert gas coating. The main purpose of these methods is to minimize the active reaction site and the oxidation reaction, which will lead to secure structural integrity of the system in such highly oxidizing conditions.
- Air-ingress mitigation studies will be in the focus of activity in FY-10.

11.5 Task 5 (KAIST)

Task 5 activities consisted of experimental works to measure the oxidation rate of the nuclear grade graphite and to develop the oxidation model of the bottom structures. The considered effects on the graphite oxidation in the reactor bottom structure are (1) kinetics, (2) mass diffusion, (3) combined effect of kinetics and mass diffusion, (4) dimension, (5) moisture, and (6) degree of burn-off. Task 5 activities and results are summarized as follows:

- Activation energies of IG-110 and IG-430 graphite have been measured to be 158.5 kJ/mol and 218 kJ/mol, respectively.
- The orders of reactions for IG-110 and IG-430 graphite have been measured and the values are 0.5 and 0.37.
- Burn-off characteristics of IG-430 and IG-110 graphite have also been compared at Zone I dominated by kinetics. The maximum reaction rates for both IG-430 and IG-110 graphite appeared at about 40% burn-off, but the trends were rather different.

- Sensitivity of burn-off on the oxidation rate was much smaller in IG-430 than in IG-110.
- The presence of moisture in the reacting gas has no influence on the oxidation or burn-off history.

11.6 Task 6 (KAIST)

Task 6 activities consisted of failure prediction studies on the oxidized graphite column in the bottom structures of the VHTRs. Mechanical testing for IG-430 graphite has been carried out for variously oxidized conditions, and the results were compared to those of IG-110 obtained in FY-08. Task 6 activities and results are summarized as follows:

- Compressive strength of the original IG-430 was measured to be 88.99 MPa, and it was about 13% higher than that of the original IG-110.
- The experiment showed that the graphite failure stress can be represented by a function of only slenderness ratio.
- The relation between graphite burn-off and buckling strength for IG-430 has been investigated by mechanical testing for the oxidized samples. This experiment showed that the mechanical degradation of IG-430 is quite a bit slower than that of IG-110, thus maintaining better structural integrity.
- The strength of the graphite columns oxidized in Zone I are only dependent on the initial strength and burn-off level, even though the graphite columns have different dimensions with different failure modes.

11.7 Task 7 (KAIST)

Task 7 activities consisted of preparatory work for determining coupling factors, mapping nodes between the GAMMA and COREDAX, and organizing calculation logic to couple T/H and neutronics codes into a system code GAMMA/COREDAX. Task 7 activities and results are summarized as follows:

- The parameters for neutronic/thermal-hydraulic coupling have been set up between GAMMA and COREDAX code.
- A mode-mapping subroutine has been developed in the COREDAX code and tested since the calculation nodes between the two codes are quite different.
- The GAMMA/COREDAX code coupling has been tested by simplified GTMHR 600MWth design, and the results showed that the calculation between GAMMA with COREDAX were exactly matched to the GAMMA/COREDAX code.

11.8 Task 8 (KAIST)

Task 8 activities consisted of development works for the COREDAX code based on the AFEN method in 3-D hexagonal geometry. Task 8 activities and results are summarized as follows:

- The COREDAX code was verified by the VVER-440 benchmark problem. As a result, the COREDAX calculation showed good agreement with the reference results by the PARCS code.
- The COREDAX code was verified by the VVER-1000 benchmark problem. As a result, the COREDAX calculation showed good agreement with the reference results by the VENTURE code.
- The COREDAX code was verified by the SNR-300 benchmark problem. As a result, the COREDAX calculation showed good agreement with the reference results by the DIF3D code.

11.9 Task 9 (KAIST)

Task 4 activities scheduled for FY-10, consist of the verifying GAMMA code coupled with COREDAX code and validating prediction results of thermal power distribution in the hexagonal reactor core.

12. REFERENCES

Executive Summary and Chapter 1 (Introductions)

Oh, C. H., Davis, C., Siefken, L., Moore, R., NO, H. C., Kim, J. , Park, G. C., Lee, J. C. and Martin, W. R., *Development of Safety Analysis Codes and Experimental Validation for a Very High Temperature Gas-Cooled Reactor*, INL/EXT-06-01362, March 2006.

Schultz et al., *Next Generation Nuclear Plant Methods Technical Program Plan*, INL/EXT-06-11804, September 2006.

Chapter 2 (Task 1)

ANSYS, *CFX-12 Manual*, 2009.

ANSYS, *ICEM CFD-11.0, Manual*, 2008.

Barr, D. I. H., “Densimetric Exchange Flows in Rectangular Channels,” *La Houille Blanche*, Vol. 22, 1967, pp. 619–631.

Benjamin, T. B., “Gravity Currents and Related Phenomena,” *J. Fluid Mechanics*, Vol. 31, 1968, pp. 209–248.

Birman, V. K., Martin, J. E., and Meiburg, E., “The Non-Boussinesq Lock-Exchange Problem. Part 2. High-resolution Simulations,” *J. Fluid Mechanics*, Vol. 537, 2005, pp. 125–144.

Britter, R. E. & Simpson, J. E., “A Note on the Structure of a Gravity Current Head,” *J. Fluid Mechanics*, Vol. 112, 1978, pp. 459–466.

Chen, G. Q., and Lee, J. H., “Turbulent Gravity Current of Lock Release Type: a Numerical Study,” *Envir. Hyd., Balkema*, 1999, pp. 449–454.

Etienne, J., Hopfinger, E. J., and Saramito, P., “Numerical Simulation Of High Density Ratio Lock-Exchange Flows,” *Physics of Fluids*, Vol. 17, 2005.

Eugeniy, V. E., and Gavrilov, N. V., A Note on the Propagation Speed of a Weakly Dissipative Gravity Current,” *J. Fluid Mechanics*, Vol. 574, 2007, pp. 393–403.

Gardner, G. C. & Crow, I. G., “The Motion of Large Bubbles in Horizontal Channels,” *J. Fluid Mechanics*, Vol. 112, 1970, pp. 459–466.

General Atomics, *Gas Turbine-Modular Helium Reactor (GT-MHR) Conceptual Design Description Report*, 910720, Rev. 1, 1996.

Grobelbauer, H. P., Fannelop, T. K., and Britter, R. E., “The Propagation of Intrusion Fronts of High Density Ratios,” *J. Fluid Mechanics*, Vol. 31, 1993, pp. 669–687.

Hartel, C., Meiburg, E., and Neckar, F., “Analysis and Direct Numerical Simulation of the Flow at a Gravity Current Head, Part 1. Flow Topology and Front Speed for Slip and Non-Slip Boundaries”, *J. Fluid Mechanics*, Vol. 269, 2000, pp. 169–198.

Hupper, H. E. and Simpson, J. E., “The Slumping of Gravity Currents,” *J. Fluid Mechanics*, Vol. 99, 1980, pp. 785–799.

Johnson, R. W., “Modeling Strategies for Unsteady Turbulent Flows in the Lower Plenum of the VHTR,” *Nuclear Engineering and Design*, Vol. 238, 2008, pp. 482–491.

Kang, H. S., “CFD Analysis for the Turbulent Flow in the 3×3 Hybrid Vane,” FLUENT User Group Meeting, Kyungju, Korea, 2006.

- Keller, J. J. and Chyou, Y. P., "On the Hydraulic Lock-Exchange Problem," *J. Applied Mathematics and Physics*, Vol. 41, 1991.
- Kim, E. S., NO, H. C., Kim, B. J., and Oh, C. H., "Estimation of Graphite and Mechanical Strength Variation of VHTR during Air-ingress Accident," INL/JOU-07-12776, *Nuclear Engineering and Design*, Vol 238, No 4, pp 837-847, 2008.
- Klemp, J. B., Rotunno, R., and Skamarock, W. C., "On the Dynamics of Gravity Currents in a Channel," *J. Fluid Dynamics*, Vol. 269, 1994, pp. 169–198.
- Kuelegan, G. H., "The Motion of Saline Fronts in Still Water, *Natl Bur. Stnd. Rep. 5813*, 1958.
- Liou, C. P., Parks, D. L., Schultz, R. R., and Williams, B. G., "Stratified Flows in Horizontal Piping of Passive Emergency Core Cooling Systems," *13th International Conference on Nuclear Engineering, ICONE 13-50450, May 16–20, Beijing, China, 2005*.
- Lowe, R. J., Linden, P. E., and Rottman, J. W., "A Laboratory Study of the Velocity Structure in an Intrusive Gravity Current," *J. Fluid Mechanics*, Vol. 456, 2002, pp. 22–48.
- Lowe, R. J., Rottman, J. W., and Linden, P. F., "The Non-Boussinesq Lock-Exchange Problem. Part 1. Theory and Experiments," *J. Fluid Mechanics*, Vol. 537, 2005, pp.101–124.
- Mok, K. M., IEONG, K. K. and Yeh, H., "Experimental Observation of the Flow Structures at Gravity Current Front," *International Conference on Estuaries and Coasts, November 9-11, Hangzhou, China, 2003*.
- NO, H. C., Lim, H. S., Kim, J., Oh, C. H., Siefken, L., and Davis, C., "Multicomponent Diffusion Analysis and Assessment of GAMMA Code and Improved RELAP 5 Code," *Nuclear Engineering and Design*, Vol. 237, 2007, pp. 997–1008.
- Oh, C. H., Davis, C., Siefken, L., Moore, R., NO, H. C., Kim, J., Park, G. C., Lee, J. C., and Martin, W. R., *Development of Safety Analysis Codes and Experimental Validation for a Very High Temperature Gas-Cooled Reactor, Final Report*, INL/EXT-06-01362, March 2006.
- Oh, C. H., Kim, E. S., NO, H. C., and Cho, N. Z., *Experimental Validation of Stratified Flow Phenomena, Graphite Oxidation, and Mitigation Strategies of Air Ingress Accident*, INL/EXT-08-14840, December 2008.
- Parson, J. D., and Garcia, M. H., "Similarity of Gravity Current Fronts," *Phys. Fluids*, Vol. 10, 1998, pp. 3209–3213.
- Schaaf, T., Frohling, W., Hohn, H., Struth, S., "The NACOK Experimental Facility for Investigating an Air Ingress into the Core of a High Temperature Reactor, *Kerntechnik*, Vol. 63, Issue 3, pp. 107–112, 1998.
- Schultz et al., *Next Generation Nuclear Plant Methods Technical Program Plan*, INL/EXT-06-11804, Rev 0.26, September 2006.
- Shin, J. O., Dalziel, S. B., and Linden, P. F., "Gravity Currents Produced By Lock Exchange," *J. Fluid Mechanics*, Vol. 521, 2004, pp. 1–34.
- Simpson, J. E., "Gravity Currents in the Environment," *PINSA*, Vol.65, No. 1, 1999, pp.1–25.
- Takeda T., *Air Ingress Behavior during a Primary-Pipe Rupture Accident of HTGR*, JAERI-1338, Japan Atomic Energy Research Institute, 1997.
- Takeda, T. and Hishida, M., "Studies on Molecular Diffusion and Natural Convection in a Multicomponent Gas System," *International Journal of Heat and Mass Transfer*, Vol. 39, No. 3, 1996, pp. 527–536.

- Takeda, T., *Air Ingress Behavior during a Primary-pipe Rupture Accident of HTGR*, JAERI-1338, Japan Atomic Energy Research Institute, 1997.
- Von Karman, T., “The Engineer Grapples with Nonlinear Problems,” *Bull. Am. Math. Soc.*, Vol. 46, 1940, pp.615–683.
- Welty, J. R., Wicks, C. E. and Wilson, R. E., *Fundamentals of Momentum, Heat and Mass Transfer*, John Wiley & Sons, Inc., 1984.
- Wilkinson, D. L., “Motion of Air Cavities in Long Horizontal Ducts, *J. Fluid Mechanics*, Vol. 118, 1982, pp. 109–122.
- Yih, C. S., *Dynamics of Nonhomogeneous Fluids*, Macmillan, 1965.

Chapter 3 (Task 2)

- ANAYS FLUENT 6.3, User Guide, 2008.
- Benjamin, T. B., Gravity Currents and Related Phenomena, *J. Fluid Mechanics*, Vol. 31, 1968, pp. 209–248.
- Birman, V. K., Martin, J. E., and Meiburg, E., “The Non-Boussinesq Lock-Exchange Problem. Part 2. High-Resolution Simulations,” *J. Fluid Mechanics*, Vol. 537, 2005, pp. 125–144.
- Britter, R. E. and Simpson, J. E., “A Note on the Structure of a Gravity Current Head,” *J. Fluid Mechanics*, Vol. 112, 1978, pp. 459–466.
- CD-adapco, STAR-CCM+ 4.02 User Manual, 2009.
- Cowen, E. A., Chang, K. A., and Liao, Q., “A Single-Camera Coupled PTV-LIF Technique,” *Experiments in Fluids*, Vol. 31, 2001, pp. 63–73.
- Crandall, S. H., Dahl, N. C., and Lardner, T. J., *An Introduction to the Mechanics of Solids*, McGraw-Hill, 2nd ed., 1972.
- Gardner, G. C., and Crow, I. G., “The Motion of Large Bubbles in Horizontal Channels,” *J. Fluid Mechanics*, Vol. 112, 1970, pp. 459–466.
- Grobelbauer, H. P., Fannelop, T. K., and Britter, R. E., “The Propagation of Intrusion Front of High Density Ratios, *J. Fluid Mech.*, Vol. 250, 1993, pp. 669–687.
- Hartel, C., Meiburg, E., and Neckar, F., “Analysis and Direct Numerical Simulation of the Flow at a Gravity Current Head, Part 1. Flow Topology and Front Speed for Slip and Non-Slip Boundaries,” *J. Fluid Mechanics*, Vol. 269, 2000, pp. 169–198.
- Keller, J. J. and Chyou, Y. P., “On the Hydraulic Lock-Exchange Problem, *J. Applied Mathematics and Physics*, Vol. 41, 1991.
- Klemp, J. B., Rotunno, R., and Skamarock, W. C., “On the Dynamics of Gravity Currents in a Channel,” *J. Fluid Dynamics*, Vol. 269, 1994, pp. 169–198.
- Lowe, R. J., Linden, P. E., and Rottman, J. W., A Laboratory Study of the Velocity Structure in an Intrusive Gravity Current, *J. Fluid Mechanics*, Vol. 456, 2002, pp. 22–48.
- Lowe, R. J., Rottman, J. W., and Linden, P. F., “The Non-Boussinesq Lock-Exchange Problem. Part 1. Theory and Experiments,” *J. Fluid Mechanics*, Vol. 537, 2005, pp.101–124.
- Martin, J. E. and Garcia, M. H., “Combined PIV/PLIF Measurements of a Steady Density Current Front,” *Exp Fluids*, Vol. 46, 2009, pp. 265–276.

- Roache, P.J., Verification and Validation in Computational Science and Engineering, Hermosa Publishers, Albuquerque, New Mexico, 1998.
- Sadanandan, R., Stohr, M., and Meier, W., "Simultaneous OH-PLIF and PIV Measurements in a Gas Turbine Model Combustor," *Appl. Phys. B*, Vol. 90, 2008, pp. 609–618.
- Sanada, Y., Suzuki, T., and Toda, Y., "Simultaneous Measurement of Velocity and Density Fields of Gravity Current," *The 1st Joint Korea/Japan Workshop on Marine Environmental Engineering*, 28-29 Dec 2003.
- Shin, J. O., Dalziel, S. B., and Linden, P. F., "Gravity Currents Produced by Lock Exchange," *J. Fluid Mechanics*, Vol. 521, 2004, pp. 1–34.
- Simpson, J. E., "Gravity Currents in the Environment," *PINSA*, Vol.65, No. 1, 1999, pp.1–25.
- Von Karman, T., The engineer grapples with nonlinear problems, *Bull. Am. Math. Soc.*, Vol. 46, 1940, pp.615–683.
- Yih, C.S., Dynamics of Nonhomogeneous Fluids, Macmillan, 1965.

Chapter 4 (Task 3)

- ABAQUS, Inc, 2007, "Getting Started with ABAQUS (Ver. 6.75)."
- Bratton, R. L., Burchell, T. D., Corwin, W. R., Hayner, G. O., Katoh, Y., Klett, J. W., *Next Generation Nuclear Plant Materials Research and Development Program Plan*, INL/EXT-05-00758, Rev. 2, September 2005.
- Burchell, T. D., Eto, M., Ishiyama, S., Strizak, J. P., "The Effect of high Fluence Neutron Irradiation on the Properties of a Fine-Grained Isotropic Nuclear Graphite," *Journal of Nuclear Materials*, Vol. 230, 1996, pp. 1–7.
- Burchell, T. D., Romanoski, G. R., "The Effects of Specimen Geometry and Size on the Fracture Toughness of Nuclear Graphites," *ORNL CONF-9109266-1*, January 1991.
- Cocheme, F. G., "Assessment of Passive Decay Heat Removal in the General Atomic Modular Helium Reactor," Unpublished master's thesis, Texas A&M University, Texas, U.S.A., 2004.
- Contescu, C., "Current R&D Activities on Graphite Oxidation at ORNL," personal communication, *NGNP R&D Technical Review Meeting, Idaho National Laboratory*, May 5–8, 2008.
- Eto, M. and Growcock, F. B., "Effect of Oxidizing Environment on the Strength of H451, PGX and IG-110 Graphites," *Carbon*, Vol. 21, No. 1, 1983, pp. 135–147.
- Eto, M., Konishi, T., Oku, T., "High Temperature Young's Modulus of IG-110 Graphite," *JAERI, Conference article from Specialists' meeting on graphite component structural design, JAERI Tokai (Japan), September 8-11, 1986*, conducted by the International Atomic Energy Agency, Vienna (Austria). International Working Group on Gas-Cooled Reactors. IWGGCR-11, 1986, pp. 133–137.
- Fuji, K., Nakano, J., Yamada, R., "Mechanical Properties of Oxidation-Resistant SiC/C Compositionally Graded Graphite Materials," *Journal of the American Ceramic Society*, Vol. 80, No. 11, 1997, pp. 2897–2902.
- Fuller, E. L., Okoh, J. M., "Kinetics and Mechanisms of the Reaction of Air with Nuclear Grade Graphites: IG-110," *J. Nuclear Materials*, Vol. 240, 1997, pp. 241–250.
- General Atomics, *International GT-MHR Project Internal Design Review Presentation Material*, 1997.
- General Atomics, *Screening Tests for Selection of VHTR Advanced Fuel*, Contract No. DE-AC03-01SF22343, Revision 0, 2003.

- Ishihara, M., Iyoku, T., Oku, T., Shibata, T., Sumita, J., “Principle Design and Data of Graphite Components,” *Nuclear Engineering and Design*, Vol. 233, 2004, pp. 251–260.
- Kim, E. S. and NO, H. C., “Experimental Study on the Oxidation of Nuclear Graphite and Development of an Oxidation Model, *Journal of Nuclear Materials*, Vol. 349, 2006, pp. 182–194.
- McCreery, G. E., McEligot, D. M., *Scaling Studies and Conceptual Experiment Designs for NGNP CFD Assessment*, INEEL/EXT-04-02502, November 2004.
- Moorman, R., Alberici, S., Hinssen, H. K., Krussenberg, A. K., Wu, C. H., “Oxidation Behavior of Carbon-based Materials Used for HTGRs and Fusion Reactors,” *Adv. Sci. Technol.*, Vol. 24, 1999, pp. 331–339.
- Ogawa, M, Mass Transfer with Graphite Oxidation in Gas Mixture Laminar Flow through Circular Tube, *J. At. Energy Soc. Jpn.*, Vol. 35, Issue No. 3, 1993, p. 245.
- Oh, C. H., Davis, C., Siefken, L., Moore, R., NO, H. C., Kim, J. , Park, G. C., Lee, J. C. and Martin, W. R., *Development of Safety Analysis Codes and Experimental Validation for a Very High Temperature Gas-Cooled Reactor*, INL/EXT-06-01362, March 2006.
- Oh, C. H., Kim, E. S., NO, H. C., and Cho, N. Z., *Experimental Validation of Stratified Flow Phenomena, Graphite Oxidation, and Mitigation Strategies of Air Ingress Accident*, INL/EXT-08-14840, December 2008.
- Rasmussen, K., *Full-range Stress-strain Curves for Stainless Steel Alloys*, Published Ph.D research, Report No R811, University of Sydney, Sydney, Australia, 2001.
- Shenoy, “Modular Helium Reactor Design, Technology and Applications,” <http://cer.ucsd.edu/SEMINARS/Shenoy.ppt>, 2007.

Chapter 5 (Task 4)

- Yan et al., “A Study of Air Ingress and Its Prevention in HTGR,” *Nuclear Technology*, Vol.163, Sep. 2008.

Chapter 6 (Task 5)

- Robert Bratton and Timothy Burchell, NGNP Graphite Testing and Qualification Specimen Selection Strategy, INL/EXT-05-00269, pp. 8-14, May 2005
- Chang H. Oh et al., Development of Safety analysis Codes and Experimental Validation for a Very High Temperature Gas Cooled Reactor, INL/EXT-06-01362, pp 112-141, March 2006
- Welty, J.R., Wicks, C.E., Wilson, R.E., Fundamentals of Momentum, Heat and Mass Transfer, John Wiley and Sons, pp. 615-618.
- E.L. Fuller, Joseph M. Okoh, 1997, Kinetics and mechanisms of the reaction of air with nuclear grade graphites: IG-110, J. Nuclear Materials, Vol. 240, pp. 241-250
- Se-Hwan Chi and Gen-Chan Kim, Comparison of the oxidation rate and degree of graphitization of selected IG and NBG nuclear graphite grades, J. Nuclear Material, Vol. 381, pp. 9-14, 2008
- KIM, E.S., Development of Graphite Oxidation Models for Air-ingress Analysis in HTGR, pp. 52, KAIST, 2006

Chapter 7 (Task 6)

- Chang H. Oh et al., Development of Safety analysis Codes and Experimental Validation for a Very High Temperature Gas Cooled Reactor, INL/EXT-06-01362, pp 112-141, March 2006

Ferdinand L. Singer and Andrew Pytel, Strength of Material, pp. 439-453, Harper & Row, New York, 1980

ASTM Int'l, Standard Test method for Compressive strength of carbon and graphite, C695-91, Reapproved 2005

G.B. Neighbour, P.J. Hacker, The variation of compressive strength of AGR moderator graphite with increasing thermal weight loss, Material Letter, 51, pp. 307-314, 2001

M. Eto, F.B. Growcock, Effect of oxidizing environment on the strength of H451, PGX and IG-11 graphite, Carbon, Vol. 21, No. 2, pp. 135-147, 1983

S. Yoda et al., Effect of oxidation on compressive deformation behavior of nuclear-grade isotropic graphite, Carbon, Vol. 23, No. 1, pp. 33-38, 1985

E.S. Kim, Y.W Kim, Effect of a thermal oxidation on the compressive strengths of selected nuclear graphites, Transactions of the Korean Nuclear Society Autumn Meeting, Korea, 2007

Chapter 8~10 (Task 7, 8, 9)

ANL, Benchmark Problem Book, ANL-7416, Suppl. 3, p. 861 (1985).

N.Z. Cho and J.M. Noh, "Analytic Function Expansion Nodal Method for Hexagonal Geometry," Nucl. Sci. Eng., 121, 245 (1995).

S.W. Woo, N.Z. Cho, and J.M. Noh, "The Analytic Function Expansion Nodal Method Refined With Transverse Gradient Basis Functions and Interface Flux Moments," Nucl. Sci. Eng., 139, 156 (2001).

D.S. Kim and N.Z. Cho, "Kinetics Calculation Under Space-Dependent Feedback in Analytic Function Expansion Nodal Method via Solution Decomposition and Galerkin Scheme," Nucl. Sci. Eng., 140, 267 (2002)

N. Z. Cho, and J. Lee, "Analytic Function Expansion Nodal (AFEN) Method in Hexagonal-Z Three-Dimensional Geometry for Neutron Diffusion Calculation," Journal of Nuclear Science and Technology, 43, 1320 (2006).

List of Computer Codes Used for This Project

Code and Version	Computer Platform	Operating System
ABAQUS 6.75	PC and HPC Cluster	Windows XP and UNIX
ANSYS CFX-12	HPC Cluster (30 parallel CPU)	UNIX
ANSYS FLUENT 6.3	HPC Cluster (20 parallel CPU)	UNIX
GAMMA Code	PC	Windows XP
ICEM-CFD 11.0	PC	Windows XP
STAR-CCM+ 4.02	HPC Cluster (60 parallel CPU)	UNIX
COREDAX	PC	Windows XP

Appendix A

DEGB Experiment Facility Schematics

Appendix A

DEGB Experiment Facility Schematics

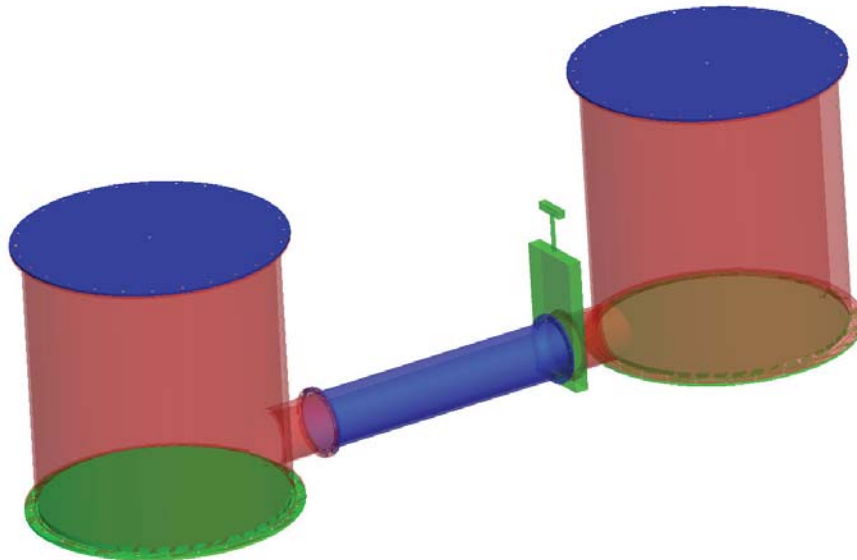


Figure A-1. DEGB facility assembly with knife gate valve.

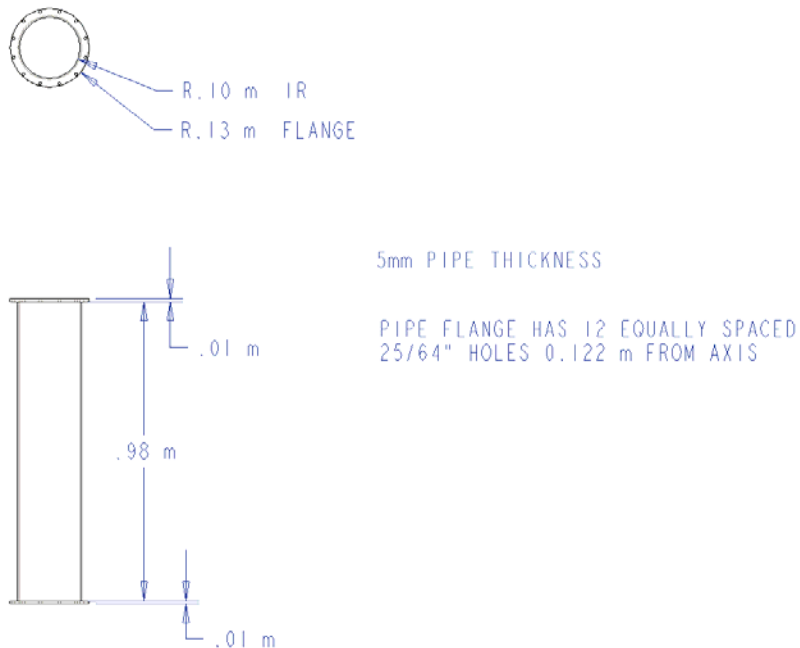


Figure A-2. Horizontal pipe dimensions.

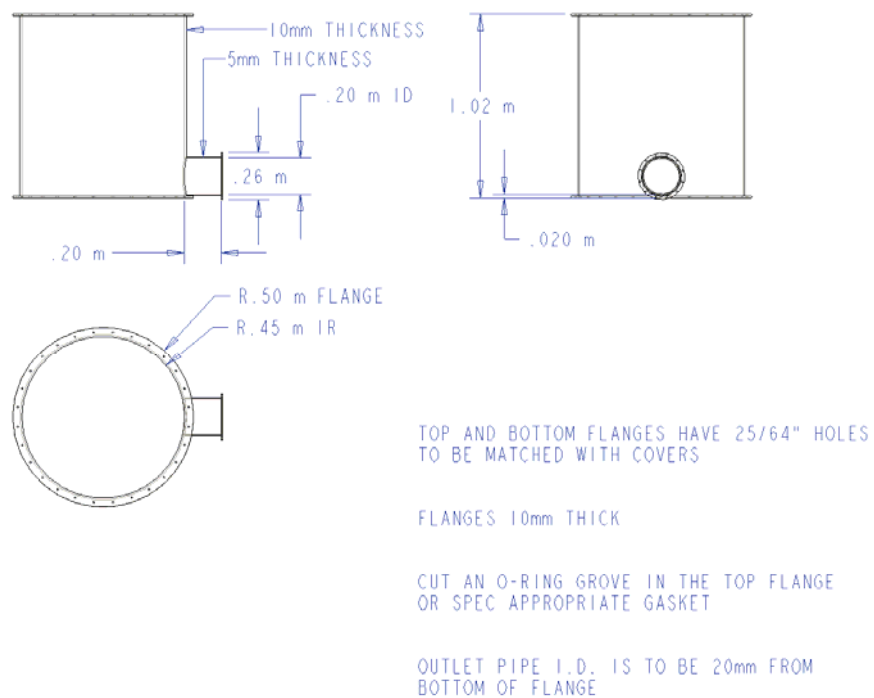


Figure A-3. Flanged tank dimensions; tanks have covers on both top and bottom to facilitate cleaning.

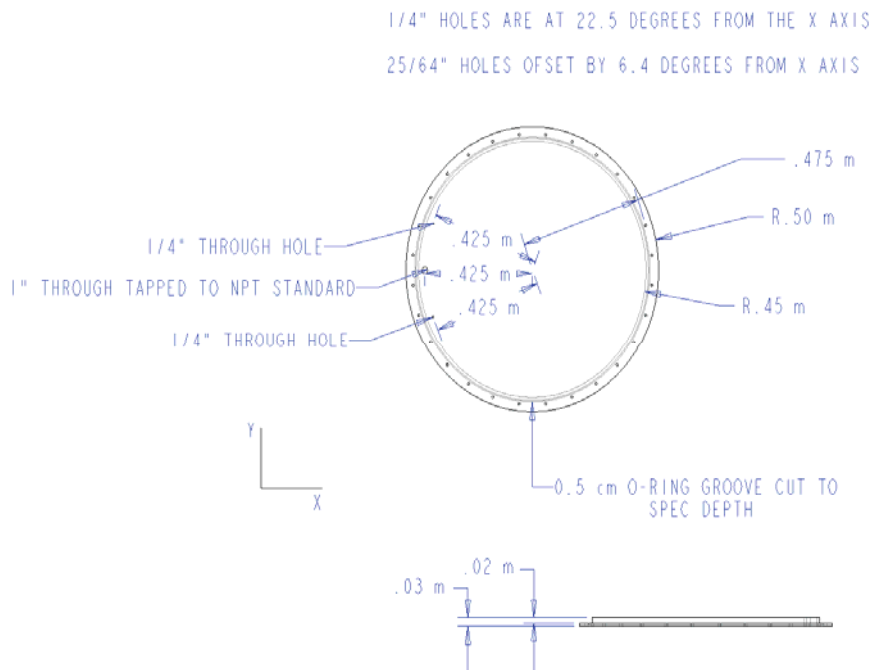


Figure A-4. Bottom tank cover.

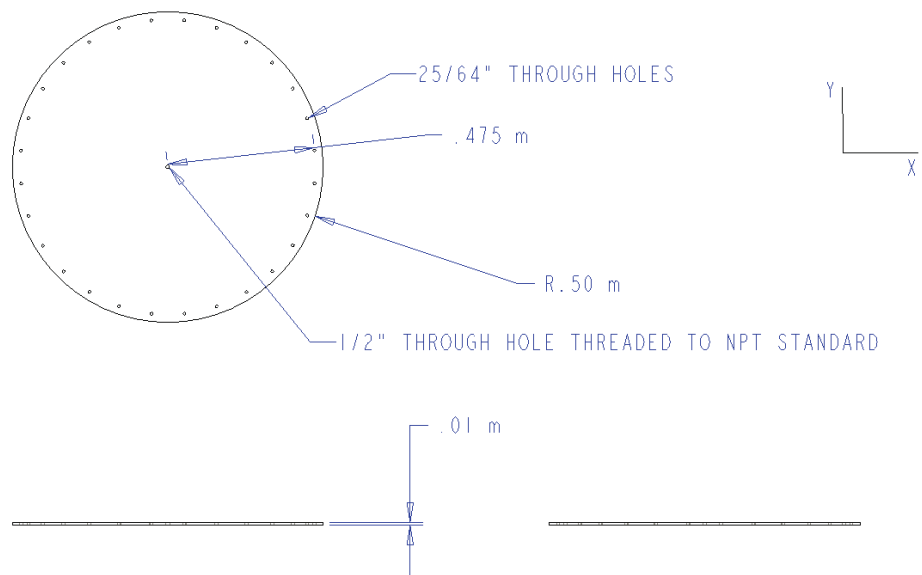


Figure A-5. Top tank cover